UTILISATION OF RESIDUES FROM BIODIESEL PRODUCTION IN FUEL CELLS

Ahmed Umar

A Thesis Submitted for the Degree of PhD
at the
University of St Andrews

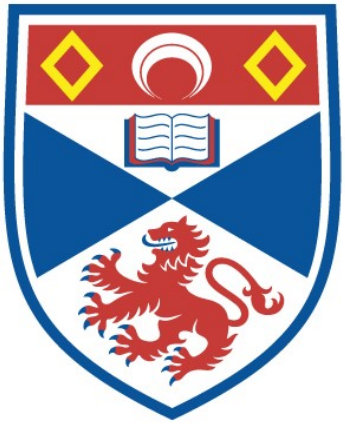

2016

Full metadata for this item is available in
St Andrews Research Repository
at:
http://research-repository.st-andrews.ac.uk/

Please use this identifier to cite or link to this item:
http://hdl.handle.net/10023/10852

This item is protected by original copyright

Utilisation of Residues from Biodiesel Production in Fuel Cells

Ahmed Umar

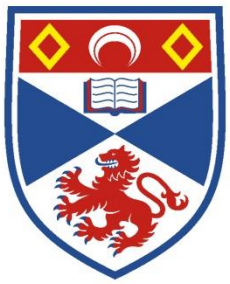

This thesis is submitted in partial fulfilment for the degree of PhD

at the

University of St Andrews

August, 2015

DECLARATION

I, Ahmed Umar, hereby certify that this thesis, which is approximately 80,400 words in length, has been written by me, and that it is the record of work carried out by me, or principally by myself in collaboration with others as acknowledged, and that it has not been submitted in any previous application for a higher degree.

I was admitted as a research student in November, 2011 and as a candidate for the degree of PhD in September, 2012; the higher study for which this is a record was carried out in the University of St Andrews between 2011 and 2015.

Date: 14th June, 2016 signature of candidate ……

I hereby certify that the candidate has fulfilled the conditions of the Resolution and Regulations appropriate for the degree of PhD in the University of St Andrews and that the candidate is qualified to submit this thesis in application for that degree.

Date: 14th June, 2016 signature of supervisor ……

In submitting this thesis to the University of St Andrews I understand that I am giving permission for it to be made available for use in accordance with the regulations of the University Library for the time being in force, subject to any copyright vested in the work not being affected thereby. I also understand that the title and the abstract will be published, and that a copy of the work may be made and supplied to any bona fide library or research worker, that my thesis will be electronically accessible for personal or research use unless exempt by award of an embargo as requested below, and that the library has the right to migrate my thesis into new electronic forms as required to ensure continued access to the thesis. I have obtained any third-party copyright permissions that may be required in order to allow such access and migration, or have requested the appropriate embargo below.

The following is an agreed request by candidate and supervisor regarding the publication of this thesis:

Embargo on electronic publication of thesis for a period of one year but access to printed copy on the following reason:

Publication would preclude future publication.

Date 14th June, 2016 signature of candidate ……..signature of supervisor……

ACKNOWLEDGEMENTS

My sincere thanks and appreciation goes to Professor John T.S. Irvine for giving me the opportunity to work in his research group as a PhD student and the privilege to explore the beauty of materials, energy and fuel cell technology. I must also acknowledge his support, understanding and magnanimity throughout the sojourn.

I would like to thank Dr Paul Connor and Dr Stephen R. Gamble who first introduced me to the rudiments of the work and been there for me all the time I needed their assistance. My gratitude also goes to Professor Frank Gunstone for the wonderful discussion we had when I came and from whose advice and Book I found a sense of direction and inspiration to this work. The effort and immense contributions of all my colleagues in the group past and present to the successful completion of this project is hereby appreciated. Particularly amongst them are Elena Stefan and Dragos Neagu for valuable discussions and collaborations, Harald Schlegl, Noor Qadri, Akshay Satapathy, Cristian Savaniu, Aida Fuente Cuesta and many others too numerous to be mentioned for their advice and inspirational discussions.

I would like to thank Sylvia Williamson for all her understanding, help with the instrumentation on BET and thermal analysis and also Ross Blackley for the SEM and TEM training and guidance. I also thank Dr Georg Haehner, Dr Richard Baker and Professor Paul Wright for advice and guidance at some point or the other.

My sincere gratitude goes to my parents, wife, children, siblings and all friends for their best wishes, moral support, patience and understanding throughout the period of this work.

I would also like to extend my appreciation and acknowledgement to the University of St-Andrews for the opportunity and hospitality and of course the Petroleum Technology Development Fund (PTDF) Nigeria for the funding and encouragements.

ABSTRACT

With the achievements recorded in the development of fuel cell technology, arguably hydrogen-driven systems would replace the combustion fossil fuel-based systems in the nearest future for safer and pollution-free environment. The much desired renewable and sustainable hydrogen infrastructure to replace or complement the fast-depleting fossil-based hydrogen fuel for the full commercialisation of fuel cell could be achieved through catalyst development and gasification of by-product glycerol glut from biodiesel production activity seen as a waste at the moment.

In this study, the development of catalysts for the conversion of biomass vegetable oil via transesterification reaction to biodiesel has been explored in parallel to the subsequent catalytic gasification of pure and by-product glycerol from biodiesel synthesis to generate hydrogen-rich gases for utilisation in fuel cells.

Reaction of tricalcium aluminate (C3A) with adsorbed water vapour under controlled hydration process at elevated temperatures was found to modify its surface morphology by formation of strongly basic hydroxide products. This was found to increase its surface basic strength and ability to catalyse transesterification reaction to biodiesel for the first time. Furthermore, basic alkaline earth metal oxides MgO, SrO and transition metal oxide ZnO that are known to catalyses transesterification reaction but suffered deactivation due to profuse leaching were doped and incorporated into the non-hydrated tricalcium aluminate (C3A) lattice structure. The doped catalysts were found to be not only active and selective to biodiesel formation but also resistant to deactivation by leaching of the doped active metals for the first time.

The rapid deactivation of the nickel-based catalyst Ni/Al_2O_3 due to carbon deposition; agglomeration and phase transformation especially during prolonged high temperature operations using feedstock glycerol in steam reforming was minimised through the use of promoters such as ceria (CeO_2) and LSCM ($La_{0.75}Sr_{0.25}Cr_{0.5}Mn_{0.5}O_{3-\delta}$) and alternative supports such as samarium-doped ceria ($Ce_{0.8}Sm_{0.2}O_{2-\delta}$) and zirconia-doped ceria ($Ce_{0.75}Zr_{0.25}O_2$). This led to the development of a new catalyst system Ni-$La_{0.75}Sr_{0.25}Cr_{0.5}Mn_{0.5}O_{3-\delta}$/ $Ce_{0.75}Zr_{0.25}O_2$ (Ni-LSCM/Ce-Zr) which was found to be very

active and offered much better suppression of carbon deposition and agglomeration minimizing catalyst deactivation. However, the work revealed that, the 'traditional' wet impregnation method does not offer sufficient control over particle size, growth and distribution. It takes time, is costly and results in weak interaction between the active phase metal catalyst particles and support leading to agglomeration, instability and deactivation at times even where a promoter was used; hence this offered poor catalytic properties.

This study has demonstrated for the first time the use of a new phenomenon called redox lattice reorganisation and already known redox exsolution as alternative methods to wet impregnation in the preparation of oxide-supported nickel-based metal catalysts in glycerol steam reforming (GSR). The work has revealed that unlike what happens with the traditional wet impregnated catalysts where metal catalyst superficially interact with the oxide support resulting in catalyst deactivation due to agglomeration and carbon deposition or phase transformation. Redox lattice reorganisation in spinel has shown that metal catalyst particles can be grown out from the support itself and firmly anchored on the spinel oxide support leaving behind elaborate macro porous channels. That provides good surface area, strong metal-support interaction and reduced tendency for catalyst deactivation by agglomeration and offered effective coking suppression and good catalytic behaviour. The work has further shown that particle size, population, metal-support interaction, size of the channels in redox lattice reorganisation can all be tailored for better catalytic behaviour by simple control of reduction temperature. The work revealed further that redox exsolution in perovskite; particle size and distribution, metal-support interaction and general morphology of the catalyst surface could be tailored for good catalytic performance through control of B-site doping, careful choice of dopant metals for both A-site and B-site cations and defect chemistry in glycerol steam reforming (GSR). The metal exsoluted catalyst systems were found to be not only active and selective toward the desired products but have also demonstrated great potentials to suppress carbon deposition.

CONTENTS

1.0 INTRODUCTION

1.1 The global energy trends and need for clean sustainable energy

Meeting the global energy needs is still a mirage and remains one of the most critical challenges facing the world today. Because of rapid industrialization coupled with the exponential growth of world population currently estimated at around 7 billion and projected to reach 10 billion in the coming decades, the demand for energy will inevitably be on the increase[1,2]. In the world over, the major source of energy is the fossil fuel (petroleum, natural gas, coal, and shale oil) formed from anaerobic transformation of buried decomposed organic materials over a long period of time. These energy resources are limited unevenly distributed and exhaustible which portends energy insecurity[3-6].

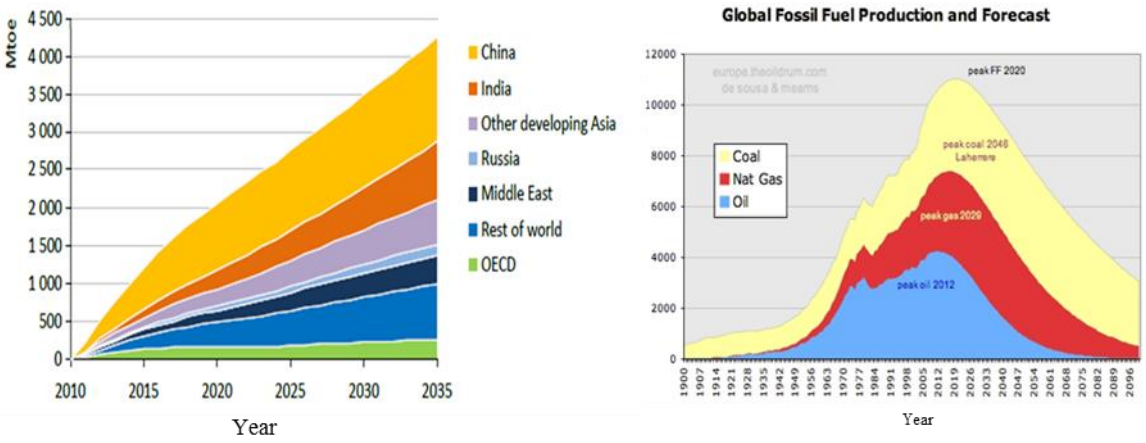

Figure 1-1 Global Energy Trend: **a,** Global Energy Demand **b**, Global Fossil Fuel Production Forecast[7,8]

Looking at the current trend in fossil fuel consumption and reserve profile, known world safe petroleum reserves estimated at 1.3 trillion barrels would be depleted in less than 40 years at the present rate of consumption[9-11]. Whilst the world energy need is expected to increase by 60% in the next 25 years, the maximum petroleum production already occurred in 2006 though some projected maximum production between 2010 and 2020. It is also expected that the world will experience increase in energy consumption of 55% between 2005 and 2030 largely by growth in China and India[1,12]. Although at the moment, the world is experiencing surge in oil supply due to the shale oil supply from North America, what is not clear is whether that would provide a succour by triggering a new era of abundance or if the uncertainties and

crisis in the Middle East being the major exporters of oil will cloud the horizon[13]. More so, fossil fuels are also associated with environmental, social and economic concerns such as atmospheric pollution, global warming, climate change, toxicity and non-biodegradability[14,15]. Other equally troubling issues are the Kyoto agreement which has to be addressed by the industrialized world through reduction of greenhouse gas emissions[16]. It is therefore risky by these prognoses for the world to depend on fossil fuel and its derivatives.

Thus, there is need for energy diversification to explore other means of clean energy sources that are more reliable in terms of supply and sustainability for transport and electricity. Such energy resources must not compromise the issues of environmental degradation, energy conservation and management. There are much renewable energy resources available which are known to be environmentally friendly some of which include wind, solar, biomass, nuclear, geothermal and hydrogen[10,17]. Technologies based on fuel cells are found most promising and seen as a near-term solution to the much desired clean energy. Basically, what informed the recent renewed interest in biomass as a long term solution are the uncertainties about the future sustainability of fossil-based fuels and environmental issues and concerns [18,19]. Essentially, biomass can be transformed to liquid, solid or gaseous products called biofuel. Such biofuels includes bioethanol, biomethanol, biobuthanol, biodiesel, biogas, biohydrogen, vegetable oil and pyrolysis oil. It is believed that oxygenated material such as biofuel burns more efficiently with cleaner emissions and environmental safety compared to fossil fuels. Technological developments based on biomass and hydrogen portends great future energy and economic potentials which are seen as a great hope for availability of future clean and sustainable energy. Biofuel potentials also offer a new economic opportunity for rural dwellers and low income earners especially those engaged in agriculture. Biofuels are therefore expected to reduce energy insecurity and over-dependency on fuel importation because biomass is everywhere[20-22].

1.2 The fuel cells

The Fuel cells are electrochemical device that utilise hydrogen and oxygen/air to produce electricity and heat in a more efficient way compared to the traditional systems of power generation. Fuel cells operate like batteries except that they do not run down to require charging but instead, they require a continuous source of fuel for sustenance of reaction. A fuel cell has great advantage of not emitting significant pollutants such as NOx or SOx because they use hydrogen as their conventional fuel and neither are they subject to Carnot cycle limitations[23]. Hydrogen is a highly reactive fuel with thermal efficiency of 35-45% when compared to 25-30% of normal petroleum fuelled engines and a maximum theoretical efficiency of fuel cell is around 83% as compared to 58% of internal combustion engine[24]. Fuel cells drive even greater efficiency when operated directly on hydrocarbon such as methanol or ethanol because of their oxygen content. Fuel cells exist in many types for different applications such as stationary, central power, auxiliary and military power systems.

Essentially, fuel cells are classified based on the electrolyte in them, the charge carrier and operating temperature such as low temperature and high temperature fuel cell. Whilst low temperature fuel cell require precious metal electro catalyst at both electrodes and uses only hydrogen to be able to function for practical purpose which are seen as its undoing, in high temperature fuel cell catalyst requirement is not stringent as non-precious catalyst such as nickel could be used and fuel flexibility increases[25]. Basically, there are five main types of fuel cells: alkaline fuel cell (AFC), proton exchange membrane fuel cell (PEMFC), phosphoric acid fuel cell (PAFC), molten carbonate fuel cell (MCFC) and solid oxide fuel cell (SOFC) as summarised in Table 1-1. Others are: direct methanol fuel cell (DMFC), direct carbon fuel cell (DCFC) and many more.

Table 1-1 Types of fuel cell and their properties

Type	Electrolyte Type	Operating temperature (°C)	Charge Carrier	Primary Contaminant	Electric out put	Efficiency (%)	Application
Alkaline Fuel Cell (AFC)	Potassium hydroxide solution	90-260	OH^-	CO, CO2 and Sulphur	300W-5KW	60-70	• Space • Military
Proton Exchange Membrane (PEMFC)	Proton Exchange Membrane	65-85	H^+	NH_3, CO and Sulphur	1KW	60	• Portable • Back up • Distributed • Transport
Phosphoric Acid Fuel Cell (PAFC)	Phosphoric Acid	160-220	H^+	CO and <1 % Sulphur	200KW	40-55	• Distributed
Molten Carbonate (MCFC)	Molten Mixture of Alkaline Metals Carbonate	650-700	CO_3^{2-}	Sulphur	2MW-100MW	45-60	• Distributed
E Fuel Solid Oxide Fuel Cell (SOFC)	Oxide Conducting Perovskite ceramic	600-1000	O^{2-}	Sulphur	100KW	60-65	• Auxillary • Distributed

Like any other device, fuel cells have their limitations and challenges which vary from one fuel cell type to another. Whilst some of the problems are material, technical and economic, some are operational. This include, sensitivity to some gases and fuel impurities such as CO, CO_2 and sulphur, expensive catalyst, long start up time, high temperature corrosions, breakdown of cell components and many others[23,25].

1.2.1 SOFC's operating principle and traditional materials

Solid oxide fuel cell **(SOFC**) is having a lot of attraction because of its high efficiency and ability to utilize different combustible fuel apart from the conventional hydrogen because unlike some others, it transports O^{2-} through the electrolyte. Another important advantage of SOFCs is its high operating temperature (600-1000 ^{o}C) which allows internal reforming and rapid kinetics. There is also possibility of recycling the heat generated or utilised in steam reforming. Furthermore, its high operating temperature makes it resistant to fuel poisoning[26,27].

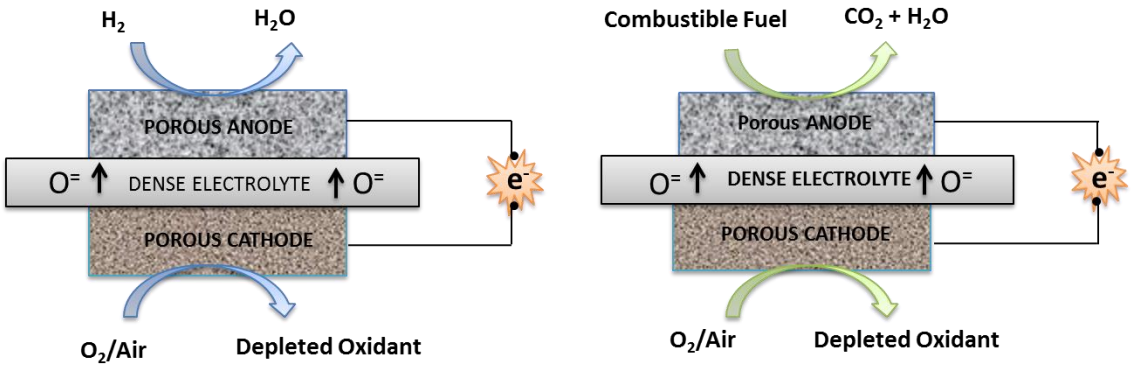

Figure 1-2 **a**, Fuel cell run on conventional fuel hydrogen and **b**, Fuel cell run on alternative combustible fuel

The solid oxide Fuel cell is characterised by four components; the anode (fuel electrode), solid ion-conducting electrolyte, cathode (air electrode) and interconnects. Molecular oxygen at the cathode is reduced during operation to ion by accepting electron supplied through the external interconnect at the porous cathode thus:

$$1/2O_2 + 2e- \rightarrow O^{2-} \qquad \text{Eqn. 1-1}$$

Migration of the oxide ions formed is driven by difference in oxygen chemical potential through the dense electrolyte to the porous anode side where they oxidize the fuel species and the electron produced moves to the cathode through the external interconnect. Depending on the fuel species used, the products are electricity, water carbon dioxide and heat. The heat is usually due to irreversible losses[25]. Assuming H_2 or CO (from hydrocarbon or oxygenated hydrocarbon) are the fuels, thus:

$$H_2 + O^{2-} \rightarrow H_2O + 2e^- + \text{Heat} \qquad \text{Eqn. 1-2}$$

$$CO + O^{2-} \rightarrow CO_2 + 2e^- + \text{Heat} \qquad \text{Eqn. 1-3}$$

It is important to note that electrochemical reaction which is the driving force in the cell occurs at a line where the electrode, the gas and the electrolyte meet known as the triple phase boundary (TPB). It extends to about 10µm from the electrolyte into the electrode[25]. All the components must remain interconnected by having their 'fingers' extended into one another for the reaction to be continuous and for effective communication between the components and hence good performance of the cell[28]. It is a requirement that the cathode must catalyse the dissociation of O_2 and be both ionic and electronically conductive at high temperature (800–1000 ^oC) in air- a property most peculiar to noble metals. Because of their prohibitive cost, instead, some oxides (perovskites) composite materials are used and the most common of them is strontium-doped lanthanum manganite $LaSrMnO_3$ (LSM) for high temperature[29-31]. It is usually used in composite form with ionic conducting ceramic yttria-stabilized zirconia (YSZ). At moderate or lower temperatures (below 800 ^oC), materials such as strontium-doped lanthanum ferro-cobaltite $LaSrFeCoO_3$ (LSFC) and strontium-doped barium ferro-cobaltite $BaSrFeCoO_3$ (BSFC) exhibit high performance than the LSM-YSZ cemets[31-33]. The electrolyte is an important component, it is required to be dense enough to separate fuel from O_2 and to retain its high ionic conductivity and zero electrical conductivity at high temperature in both air and fuel environment. The conventional material for the electrolyte is yttria stabilised zirconia- ZrO_2 + 8mol% Y_2O_3 (YSZ) for high temperature operations while samarium-doped-ceria $SmCeO_2$ (SDC) and gadolinium-doped-ceria $GdCeO_2$ (GDC) are preferred for low temperature operation[31]. The most commonly used interconnect material is

lanthanum chromate $LaCrO_3$ with electronic conductivity both in oxidizing and reducing environment at high temperature[29,30].

Just like the other components, the anode must be catalytically active to catalyses the oxidation reaction and should provide enough electronic and ionic conductivities. Excellent performance of Ni/YSZ cermet has been known as the conventional anode material. Ni provides the desired catalytic activity and electronic conductivity while the YSZ provides ionic conductivity and minimizes delamination of the composite materials at high temperature by providing thermal expansion match with the YSZ electrolyte[29-31]. Nickel was given preference against other alternative materials because it is cheap, has excellent electrical and mechanical properties and its propensity for C-C, C-O and C-H bond scission which makes it a good steam reforming catalyst especially using natural gas. However, with hydrocarbon, the performance is slow due to many side reactions that lead to formation of severe graphitic carbon and irreversible microstructural deformations which is seen from these perspectives as its inherent limitations[25,34]. Apart from nickel's susceptibility to carbon formation, other challenges are known to include cracks and delamination due to continuous exposure to redox cycles, agglomeration at high temperatures, prone to acid (HCl) and sulphur poisoning (as little as 1 ppm at high temperature)[35]. Thus, basically the structural and catalytic properties of the nickel-based materials could be improved upon through careful material and system design, choice of suitable reaction conditions and use of possible better alternative materials.

The SOFC's high operating temperature and flexibility on fuel allows it to operate on alternative fuel such as hydrocarbons other than its traditional hydrogen and ability to tolerate gases such as CO and CO_2 which are ordinarily poisons to other fuel cells which operates at low temperature[35-38]. This however requires the use of special materials to cope with high temperature operation which at the moment low cost ceramic materials are developed to suit that purpose[35]. SOFC with efficiency of 60-65% and potential power output of up to 100KW usually design in tubular or planar configurations has found application in many technologies such as auxiliary power units for transport, mobile and stationary distributed power generation, research and military applications[35].

1.3 The need for alternative fuel for fuel cells

Development of SOFC has attained a huge technical height especially in the area of anode and cathode development and it is evident that hydrogen driven systems will replace fossil fuel combustion systems in transportation, stationary and distributed power systems to reduce greenhouse gas emission and secure environment[31]. Despite all the remarkable achievements, fuel cells are not yet into full commercialisation partly due to lack of sustainable hydrogen resource, lack of efficient, affordable and reliable fuel processing systems and issues bordering on hydrogen storage in form to have density compared to that of liquid[35,39]. Hydrogen is the conventional and best option as fuel for a fuel cell, but it is a limitation in itself because its storage and transportation is quite difficult and expensive. More so, >90% of hydrogen comes from the fast depleting fossil fuel and it does not occur naturally as a gaseous fuel[26]. Therefore to keep in pace with the current energy reality, several fuel sources available has to be explored for practical fuel cells systems utilisation. Several attempts is been made to run fuel cell on alternative renewable solid, liquid and gaseous fuels. Remarkably, liquid fuels such as hydrocarbon and oxygenated hydrocarbons, natural gas, methanol, ethanol, jet fuel, biodiesel, dimethyl ether, petroleum diesel, kerosene from renewable and non- renewable sources are available for hydrogen-rich gas generation for the utilisation in fuel cell[26].

1.3.1 Liquid biofuels as alternative fuels for SOFC

Liquid biofuels for instance are not only easy to transport but are obtainable from renewable sources for sustainable hydrogen or hydrogen-rich synthesis gas production. SOFCs are versatile on fuel, having advantage of utilising different fuels directly or with minimal fuel processing due to its operating condition. Much research is on-going on different technology for hydrogen production from biomass material for SOFC's direct utilisation or by reforming processes[35,40]. Such reforming processes includes; steam reforming, catalytic partial oxidation and auto thermal reforming. Hydrocarbon and oxygenated hydrocarbon fuels studied as alternative fuels for SOFCs include Biogas (largely methane), methanol, bioethanol, diesel (both petroleum and biodiesel), gasoline and others[41]. It is interesting to note however, there is an

innovative effort recently for the utilisation of by-product glycerol phase from the biodiesel production cycle as a potential feedstock in fuel cell for energy production and development of fuel cells technology[42].

Liquid fuels have their liquid nature, high energy density, ready availability, uniform distribution all over the globe and environmentally benign as their major advantages. The major setback associated with the use of liquid fuel is deposition of carbonaceous substance on the anode surface leading to low performance and subsequent deactivation during operations. Thus, one of the prominent issues in this research area of SOFC development entails solving problems of carbon deposition, performance and robust mechanical behaviour related to the use of liquid fuel through the search for alternative electrode[31,43-46]. Interestingly, lots of progress has been made in that direction and direct utilisation of liquid fuel in fuel cell has been demonstrated with lot of success not only on SOFC but also on low temperature fuel cell such as PEMFC and direct methanol fuel cell (DMFC). Thus, suffices it to say the twin technology of biofuel processing and Fuel cell system are tools that could grantee energy security and secured environment.

1.3.1.1 Direct utilisation of liquid biofuel on SOFC

Direct utilisation of liquid fuel basically means direct addition of fuel into the anode chamber of the SOFC usually accompanied by electrochemical oxidation of the fuel decomposition products leading to hydrogen, CO and other carbonaceous products generation. These products are attracted to the anode surface by chemisorption for further reactions and conversions. In the presence of water, the CO produced is converted through water-gas-shift reaction generating more hydrogen and reduce carbon deposition[26]. Direct utilisation of liquid fuels such as hydrocarbon and oxygenated fuels on SOFC is quite a new research interest. A serious issue relating to use of hydrocarbon or oxygenated fuel is that it causes a serious deactivation and rapid disintegration of the cell structure and general performance due to huge carbon formation on the surface of the anode material. Furthermore, as a result of side reactions occurring away from the catalyst surface in the reactor, gaseous phase reaction of hydrocarbon could results to formation of tars and soot by free radicals and polymerization reactions leading to consequent fouling of the anode surface[25].

Reaction temperature, catalyst properties and anodic polarization could be regulated to mitigate the severity or otherwise of carbon deposition in direct utilisation of liquid fuel[46]. Therefore the catalytic property of the anode material is essential in determining the product composition in the anode chamber. Conventionally, Ni-based anode Ni/YSZ is used in the anode usually coupled with YSZ as the electrolyte and LSM as cathode (Ni/YSZ|YSZ|LSM). The Ni/YSZ cermet is susceptible to carbon deposition, agglomeration and evaporating of active phase at high temperature. It is also prone to sulphur poisoning, mechanical instability as a result of redox cycling which give rise to internal stress and possible delamination[25,46-48]. Efforts are being made to reduce carbon formation on fuel cells especially when a fuel other than hydrogen is used. Noble metals have done well such as Rh and Ru but are costly. Other metals brought in to replace Ni such as Cu, Co and Fe have suppressed carbon formation using methanol for instance but gave low activity when compared to Ni-based catalyst[25,49]. Ceria-based materials such as Cu/Ceria catalyst were also investigated and found to have good performance and suppress coking but less thermal stability and poor electronic conductivity[50]. Cu-Co/Ceria was found not only catalytically active but also demonstrated some improved thermal and coking stability[51,52]. Oxides of metal show some properties which give them an edge over metal catalysts. Metal oxides do not show catalytic behaviour except when reduced to their respective metals and therefore does not catalyses reactions that leads to carbon deposition. They have higher melting point but low surface energy that gives them the capacity to retain anode porosity and resist sintering respectively. In a show of flexibility and versatility, metal oxides of different properties could be combined in a single phase material rather than composite[25]. As such, Ni-based metal oxides anode materials incorporated into perovskite materials to fight deactivation and to improve performance could be a better alternative. Particularly, ceria-based materials doped with Ga_2O_3 or Sm_2O_3 were found very attractive[25,53]. Liu et el[54] tested nickel oxide (NiO) and samarium doped-ceria-SDC ($Sm_{0.2}Ce_{0.8}O_{2-\delta,}$) catalyst in the configuration NiO/SDC-SDC-SDC/SDC with methanol as fuel reported power densities of 698, 430 and 223 mW/cm^2 at 650 ^{o}C, 600 ^{o}C and 550 ^{o}C respectively. Therefore metal catalyst incorporated into the lattice structure of perovskite could offer lasting solution to the problems such as catalyst

deactivation due to carbon deposition associated with the direct utilisation of hydrocarbon or oxygenated hydrocarbon fuels.

1.3.1.2 Fuel processing

Basically a fuel processor converts commonly available fuel such biogas (largely methane) propane, oxygenated fuels such as methanol, ethanol, diesel (petroleum or biodiesel), gasoline, dimethyl ether, jet fuel, kerosene, etc. into hydrogen or hydrogen-rich gas for utilisation in fuel cells. The fuel processor is an important and integral part of fuel power providing system which has to be developed for continues supply of hydrogen or hydrogen-rich gas for fuel cell operations. Essentially, irrespective of the fuel cell, the fuel processor produces through a reforming process a mixture of oxidisable gases such as H_2, CO, CO_2, CH_4, etc[26]. Although many technologies are available in system development for continuous hydrogen production, development of reliably efficient and environmentally benign processing system is still another dimension of the global energy challenge[55].

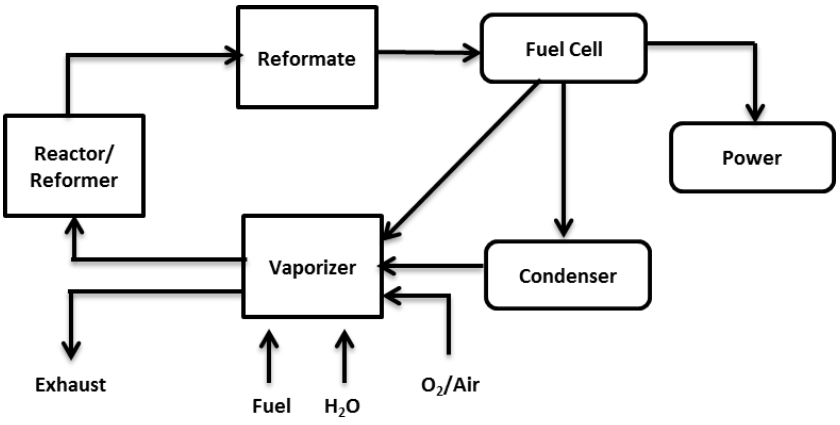

Figure 1-3 Schematic diagram showing essential steps of a typical processor

The reforming can be done with or without catalyst, but in most cases, catalytic reforming is studied because non-catalytic reforming requires high operating temperature and pressure which could lead to formation of undesirable products and the need for special material to cope with the situation[26]. Amongst the different reforming systems, the most commonly investigated include: partial oxidation

(POX)[56,57] steam reforming (SR)[58,59] and auto thermal reforming (ATR)[60,61]. The three modes are generally represented with hydrocarbons thus:

$C_xH_y + x/2O_2 \rightarrow xCO + y/2H_2$ (POX) Eqn. 1-4

$C_xH_y + xH_2O \rightarrow xCO + (x + y/2)\ H_2$ (SR) Eqn. 1-5

$C_xH_y, H_2O, O_2 \rightarrow CO, H_2$ (ATR) Eqn. 1-6

The steam reforming using hydrocarbon such as CH_4 produces CO and H_2 as seen in Eqn. 1-5 unlike with oxygenated hydrocarbon such as glycerol steam reforming(GSR) which generates CO_2 and H_2[62] (Eqn. 1-7). Partial oxidation uses oxygen/fuel mixture and highly exothermic and therefore operates at high temperature and emits lot of heat which affects its overall efficiency. Conversely, steam reforming is endothermic process and utilises fuel/water mixture and need external source of heat to operate and generate hydrogen-rich gas. Autothermal reforming represents a mixture or a hybrid of POX and SR by utilising fuel, oxygen and water mixture and therefore operates in a thermally neutral manner in such a way that the POX exothermic heat evolution is balanced by the SR endothermic heat in take. It is important to note that although these processes are very much understood and well established, they are never devoid of challenges. System design and catalyst development were identified as the major challenges[26,54]. Hydrocarbon fuel processing is associated with carbon deposition, sintering or evaporation of active phase from the catalyst surface during high temperature operations which could lead to catalyst poor performance and eventual deactivation. Therefore, there is the need for an efficient system for the processing of huge and numerous fuels available and development of catalyst that is active and selective towards the desired products. Such catalyst must be resistant to sintering or agglomeration and active phase evaporation during high temperature operations and suppresses or hinders carbon formation or sulphur poisoning[63].

1.3.1.2.1 Steam reforming (SR)

Steam reforming (SR) is quite attractive for hydrogen-rich gas production for fuel cell due to its efficiency and suitability for system integration. The process is not new, it has for long been widely used in petrochemical industries and refineries to produce

hydrogen for a number of processes such as desulphurisation of fuel or hydrocracking of heavy fractions[64]. SR is an endothermic process and therefore requires external heat supply for its operation. In glycerol steam reforming (GSR), SR occurs thus:

$C_3H_8O_3 + 3H_2O \leftrightarrow 3CO_2 + 7H_2O \quad \Delta H^o$ +ve Eqn. 1-7

It is utilised in the processing of liquid fuel and even heavy distillate provided they are desulphurised. Studies over time have identified catalyst deactivation as a result of sulphur poisoning, carbon deposition, active phase deactivation and reformer design as some of its major challenges[64-66].

Basically nickel-based materials are the most ideal catalyst for steam reforming typically supported on high surface area mesoporous materials such as alumina by wet impregnation due to its relative stability to heat, pressure and other mechanical stresses in the reformer[67]. As mentioned earlier, nickel-based catalysts in steam reforming are associated with rapid catalyst deactivation due to carbon deposition especially in liquid fuel, agglomeration and sintering at high temperatures >600 ^oC and sulphur poisoning[65,66]. The issue of carbon deposition was mitigated using alkaline metals and some transition metals such as copper as promoters or use of high steam-to-carbon ratio, though these metals are lost at high temperature which might influence their performance. They are known to enhance steam adsorption on the catalyst surface, basicity or block site that are favourable to carbon formation[26]. Steam reforming being an endothermic reaction is influenced by temperature changes. Coke formation decreases at high temperatures, but at low temperatures, the catalyst surface are more susceptible to coking activity and carbon deposition due to polymerisation of carbonaceous products chemisorbed on the catalyst surface[68].

1.3.1.2.2 Partial oxidation (POX)

Partial oxidation like steam reforming is also carried out with the aid of a catalyst otherwise high temperature typically 1200-1500 ^oC will be required which is difficult to control and special materials might be needed. POX is attractive for hydrogen-rich gas generation especially H_2 and CO production in small mobile system integrated with SOFC due to similarity in operating temperature and fuel flexibility. It requires no

water-gas-shift system hence very suitable for transport and other system where portability is required[69]. POX, an exothermic process has quick reforming ability and resists carbon deposition. It has demonstrated great potential in natural gas[70], hydrocarbon[71] and oxygenated hydrocarbon[71] reforming with lots of promising results. Like all reforming modes, catalyst deactivation due to metal sintering, active phase evaporation as a result of high temperature operations, severe carbon deposition especially on liquid hydrocarbons leading to catalyst degradation and sulphur poisoning were identified as its major challenges[72].

Equilibrium product distributions in POX of hydrocarbons and oxygenated hydrocarbons are affected by temperature, O/C (oxygen-to-carbon ratio) and gas hourly space velocity (GHSV)[69]. The catalysts mostly investigated are noble metals based such as Pt, Ru, Rh and Pb and first row transition metals like Ni, Fe and Co based catalyst typically dispersed on stable oxides such as Al_2O_3, ZrO_2, SiO_2, TiO_2 to enhance stability and resistance to deactivation[69]. Selectivity, conversion and thermal stability was often enhanced incorporating rare earth metals mostly CeO_2 and La_2O_3 and some alkaline earth metals to enhance basic properties which might alleviate carbon deposition[73]. Decomposition of $C_3H_8O_3$ for instance proceeds to generate stoichiometric gaseous products (syngas) without additional specie such as H_2O (Eqn. 2-3). The reaction is endothermic and therefore requires heat input. A possible way to enhance efficiency is to partially combust it so that the whole process becomes autothermal[74]. Partial oxidation of glycerol is an exothermic reaction (Eqn.1-9). The enthalpy of combustion generated ($\Delta H^o_{298.15}$ = -1565.0 $kJmol^{-1}$) is enough to decompose glycerol to CO and H_2. Note that water could be added to reduce the syngas ratio and increase hydrogen generation.

$$C_3H_8O_3 + O_2 \leftrightarrow CO + 2CO_2 + 4H_2 \qquad \Delta H^o \text{ –ve} \qquad \text{Eqn. 1-8}$$

$$C_3H_8O_3 + 7/2O_2 \rightarrow 3CO_2 + 4H_2O \qquad \Delta H^o \text{ –ve} \qquad \text{Eqn. 1-9}$$

Though not as good as SR in terms of hydrogen production, the product distribution is good for high temperature fuel cell such as solid oxide fuel cell. More so, its exothermic nature makes it suitable for a fast start up time in portable design since no external heat supply is required.

1.3.1.2.3 Auto-thermal reforming (ATR)

This process combines both steam reforming and partial oxidation by integrating fuel, water and oxygen and therefore operates in thermo neutral manner. The heat generated from the partial oxidation is utilised in the endothermic steam reforming and therefore require minimum heat transfer system which makes it less complicated and could therefore be smaller than the SR and POX systems. It represents a balance between SR and POX in terms of reaction condition and selection of materials for the reactor. Auto-thermal reforming operates at lower O/C ratio than POX and has advantage of quicker response and start time than SR and generates more hydrogen. It is operated at temperatures of around 700-800 ^{o}C which makes it suitable for integration with the solid oxide fuel cell[75]. ATR is a very complicated process and the equilibrium composition largely depends on the operating temperature, pressure, and feedstock composition, O/C and H_2O/C ratio as suggested by thermodynamic[75,76]. It converts hydrocarbon or oxygenated hydrocarbon to syngas containing largely of H_2 and CO. The process uses catalyst to facilitate quick attainment of equilibrium in the gas phase using Ni-based or precious metal such as Rh, Ru and Pt catalysts[77]. Performance was enhanced and carbon deposition suppressed by incorporating rare earth metals such as ceria[78]. Perovskite materials based on Ni, Co, Fe and Ce were also used due to their tendency to form oxygen vacancies, resistant to temperature which could reduce catalyst deactivation by sintering and have tendency to suppress deactivation by carbon deposition or sulphur poisoning[79]. They are often doped with alkaline metals such as Sr and Ca to improve their basic properties for enhanced resistance to carbon deposition and increase oxygen vacancies. Reactor design to mitigate issues such as heat loss, unequal distribution of reactants and catalyst design are the major challenges of this fuel processing mode[80].

1.4 Aims and objectives

1. To survey and develop heterogeneous catalysts for transesterification reaction to biodiesel and to use biodiesel yield as index for measuring catalytic activity.
2. To optimise suitable reaction conditions for using such materials as catalyst for transesterification reaction to biodiesel.
3. To develop nickel-based catalysts for conversion of glycerol and by-product glycerol phase from biodiesel synthesis to hydrogen-rich gas for utilisation in fuel cell.
4. To survey and optimise materials/catalysts structural properties, behaviour and reaction conditions for enhanced gasification of glycerol by steam reforming.
5. To explore some alternative methods of preparing nickel-based oxide-supported metal catalysts to the traditional wet impregnation method in relation to steam reforming of glycerol.

1.5 Thesis structure

Chapter 1: Introduction

Chapter 2: Research background

This chapter contains an overview of biomass as alternative sustainable energy resource, biodiesel production and by-product glycerol glut. Properties of glycerol, steam reforming of glycerol, mechanism of catalyst deactivation and carbon deposition are also reviewed.

Chapter 3: General experimental techniques

This chapter describes all the experimental procedures adopted in the research which includes sample preparation and processing, catalyst hydration, reduction and characterisation techniques. It also describes the steam reforming rig design and steam reforming procedure or catalyst test.

Materials for catalytic conversion of biomass vegetable oil to biodiesel and glycerol

Chapter 4: Tricalcium aluminate (C3A) catalyst for biodiesel production

This Investigate the structural and physicochemical changes that occurs with tricalcium aluminate (C3A) when subjected to hydration at different temperatures and how such changes influences its potentials as a catalyst for biodiesel production. The chapter also demonstrates how doping the Al site of the non-hydrated C3A in [$Ca_3Al_{2-x}M_xO_{33}$, where M= alkaline earth metal (MgO and SrO) or transition metal (ZnO) and X=0.1, 0.25 and 0.5] could enhance its Lewis basic-Bronsted acid properties as a catalyst in biodiesel production. The use of polymeric resins as catalyst for biodiesel synthesis is also investigated and compared with the synthesized ceramic catalyst.

Nickel-based catalysts for steam reforming of glycerol to hydrogen-rich gas for utilisation in fuel cell

Chapter 5: Nickel-based oxide supported catalyst: The 'traditional' wet impregnation

Influence of catalyst loading, reaction and calcination temperatures in steam reforming of glycerol over Ni/γ-Al_2O_3 prepared by wet impregnation was investigated in this chapter. It also compares the use promoters (CeO_2, and LSCM) and alternative support ($Sm_{0.2}Ce_{0.8}O_{2-\delta}$) and $Ce_{1-x}Zr_xO_2$) to enhance structural and catalytic properties of the Ni/γ-Al_2O_3 catalyst system. The carbon deposition phenomenon- as it affects and relates to different reaction conditions highlighted above was also investigated.

Chapter 6: Nickel-based oxide-supported metal catalyst: The redox lattice reorganisation and redox exsolution phenomenon

This reports the use of nickel-based spinel as catalyst and support prepared using a new phenomenon called redox lattice reorganisation and nickel-based perovskites oxides prepared using exsolution phenomenon in glycerol steam reforming (GSR). Influences of first raw transition metal (Mn, Fe, Co and Ni) B-Site doping, A-Site deficiency and defect chemistry, material processing and catalyst reduction and reaction conditions on the lattice structure, microstructure and catalytic properties in relation to steam reforming of glycerol were investigated.

Chapter 7: Summary, discussion and general conclusions

This summarises all the findings of this work.

1.6 List of publications

1.6.1 List of published articles

1. Fine-Tuning B-Site of a chromite based perovskite catalyst for steam reforming of glycerol (Mater. Res. Soc. Symp. Proc. Vol. 1735 (2015))

1.6.2 List of articles under review for publication

1. Fractal-like reorganisation of spinel oxides on reduction to yield intricate porous composites displaying good catalytic functionality (Nature Communication)

1.6.3 List of submitted drafts to supervisor

1. Lattice redox reorganisation in spinel oxides: Between reduction temperature and catalytic behaviour
2. Steam reforming of glycerol over Ni/γ-Al_2O_3 for hydrogen Production: Optimisation of processing-reaction conditions and catalyst deactivation
3. LSCM promoted nickel-based catalyst and influence of support in steam reforming of glycerol
4. Lattice defect-dopant-mediated redox exsolution of oxide supported nickel nanoparticles and its influence in steaming reforming of glycerol

1.6.4 List of proposed future articles for publication

1. Hydrated tricalcium aluminate (C3A): From cement to biodiesel synthesis
2. Tailoring structural and surface chemistry of tricalcium aluminate for catalysis of transesterification reaction to biodiesel

References

1. Asif, M. and Munir, T. Energy supply, its demand and security issues for developed and emerging economies. *Renewable and Sustainable Energy Reviews* **11**, 1388–1413 (2007)

2. Dincer, I. and Rosen, M. A. Energy, environment and sustainable development. *Applied Energy*. **64**(1-4), 427-440 (1999)

3. Bentley, R. W. Global oil and gas depletion: an overview. *Energy Policy*, **30** 189–205 (2002)

4. Demirbas, A. Biodiesel Production from vegetable oils via catalytic and non-catalytic supercritical methanol transesterification method. *Progress in Energy and Combustion Science* **31**,466-487 (2005)

5. Demirbas, A. Progress in recent trends in biofuel. *Progress in Energy and Combustion Scienc*e **33**, 1-18 (2007)

6. Dincer, I. and Rosen, M. A. A worldwide perspective on energy, environment and sustainable development. *Int. J.Energy Res.* **22**, 1305-1321(1998)

7. Angelica, A.D. A limitless Power Source for indefinite future (2011)

8. Accessed on www.solar.lynnautorepair.com

9. Bentley, R. W.; Mannan, S. A. and Wheeler, S. J. Assessing the date of the global oil peak: The need to use 2P reserves. *Energy Policy,* **35**, 6364–6382 (2007)

10. Sheehen, J.; Cambieco, V.; Duffield, J.; Garbosk, M. and Shapori, H. An overview of biodiesel and petroleum diesel life cycles: *A report by US department of agriculture and energy* pg. 35, (1998)

11. United Nation Development Programme (UNDP). Energy and the challenges of sustainability. *World energy assessment* (2000)

12. Bart, J. C. J.; Palmeri, N. and Cavallaro, S. *Biodiesel science and technology: From soil to oil*. Wood head pub series in energy and CRC Press LLC , New Delhi, USA Pg 1-820 (2010)

13. IEA (International Energy Agency): World energy outlook factsheet (2014)

14. Shafiee, S. and Topal, E. An Econometrics view of worldwide fossil fuel consumption and the role of US. *Energy and Policy* **36**,775-786 (2008)

15. Liannelos, P. N.; Zannikos, F.; loss, E. and Anastopoulos, G. Tobacco seed oil as an alternative diesel fuel, Physical and chemical properties. *Ind. Crop. Prod.* **16**, 1-9 (2002)

16. Dorian, J. P.; Franssen, H. T. and Simbeck, D. R. MD^C Global challenges in energy. *Energy Policy* **34**,15, 1984 – 1991 (2006)

17. Demirbas, A. Biodiesel fuels from vegetable oils via catalytic and non-catalytic supercritical alcohol transesterification and other methods: A survey. *Energy Conversion Management* **44**, 2093-2109 (2003)

18. Balat, M. New biofuel production technologies. *Energy Educ. Sci. Technol. Part A* **22**,147–61(2009)

19. Sims, R. E. H.; Mabee, W.; Saddler, J. N. and Taylor, M. An overview of second generation biofuel technologies. *Bioresource Technology*. **101,** 1570–1580 (2010)

20. Demirbas, C. The global climate challenge: Recent trends in CO_2 emissions from fuel combustion. *Energy Educ. Sci. Technol. Part A*. **22**, 179–93 (2009)

21. Demirbas, B. Biofuels for internal combustion engines. *Energy Educ. Sci. Technol. Part A.* **22**, 117–32 (2009)

22. Demirbas, A. Political, economic and environmental impacts of biofuels: A review. *Applied Energy* **86**, 108–117 (2009)

23. O'Hayre, R. P. Cha, S. Colella, W. and Prinz, F. B. *Fuel Cell Fundamentals*. John Wiley & Sons Inc. Pg 3-21, (2009)

24. Keigh, B. P. Polymer Electrolyte Fuel Cells: A review of recent developments. *J. Power Sources.* **51**,129-144 (1994)

25. McIntosh, S. and Gorte, R. J. Direct hydrocarbon solid oxide fuel cells. *Chem. Rev.* **104,** 4845-4865 (2004)

26. Shekhawat, D.; Spivey, J. J.; and Berry, D. A.: *Fuel Cells: Technology for fuel Processing*. Elsevier Pg1-128 (2011)

27. Sin, A.; Kopnin, E.; Dubitsky, Y.; Zaopo, A.; Arico,` A. S. La Rosa, D.; Gullo, L. R. and Antonucci, V. Performance and life-time behaviour of NiCuCGO anodes for the direct electro-oxidation of methane in IT-SOFCs. *J. Power Sources*. **164**, 300 (2007)

28. Tanner, C. W.; Fung, K. Z. and Virkar, A. V. The effect of porous composite electrode structure on solid oxide fuel cell performance .1. Theoretical analysis. *J. Electrochem. Soc*. **144**, 21–30 (1997)

29. Larminie, J. and Dicks, A. *Fuel Cell Systems Explained*. 2nd Ed.john Willey & Sons Ltd, England Pg1-406 (2003)

30. Singhel, S. C. and Kendall, K. E. High temperature solid oxide fuel cell-fundamentals design and application 1st Ed; Elsevia, Oxford, UK. Pg 405, (2003)

31. Cimenti, M. and Hill, J. M. Direct utilization of liquid fuels in SOFC for portable applications: Challenges for the selection of alternative anodes. *Energies* **2**, 377–410 (2009)

32. Baumann, F. S.; Fleig, J.; Habermeil, H. U. and Maier, J. $Ba_{0.5}Sr_{0.5}Co_{0.8}Fe_{0.2}O_{3-\delta}$ Thin microelectrode investigated by impedance spectroscopy. *Solid State Ionics*, **177**, 3187 – 3190 (2006)

33. Maguire, E. J. Gharbage, B.; Marques. L. M. B. and Labrincha, J. A. : Cathode materials for intermediate temperature solid oxide fuel cells. *Solid State Ionics.* **127**,329 – 335 (2000)

34. Kim, Y.; Kim, P.; Kim, C. and Yi, J. A novel method for synthesis of a Ni/Al_2O_3 catalyst with a mesoporous structure using stearic acid salts. *J. Mater. Chem.* **13**, 2353–2358 (2003)

35. Shekhawat, D. Spivey, J. J. and Berry, D. A. Fuel Cells: *Technologies for fuel processing*. Elsevier, 2011. 1-43

36. Lo Faro, M.; Antonucci, V.; Antonucci, P. L. and Aricò, A. S. Fuel flexibility: A key challenge for SOFC technology. *Fuel,* **102** 554–559, (2012)

37. Casas, Y.; Arteaga, L. E.; Morales, M.; Rosa, E. Peralta, L. M. and Dewulf, J. Energy and energy analysis of an ethanol fuelled solid oxide fuel cell power plant *Chem. Eng. J.* **162**, 3, 1057–1066 (2010)

38. Nobrega, S. D.; Galesco, M. V.; Girona, K.; de Florio, D. Z.; Steil, M. C.; Georges, S. and Fonseca, F. C. Direct ethanol solid oxide fuel cell operating in gradual internal reforming. *Journal of Power Sources* **213,** 156-159 (2012)

39. Edwards, P. P.; Kuznetsov, V. L.; David, W. I. F. and Brandon, N. P. Hydrogen and fuel cell: Towards sustainable energy future. *Energy Policy*, **38**, 4356-4362 (2008)

40. Valdye, P. D. and Rodrigues, A. E. Glycerol for hydrogen production; A Review. *Chem. Eng. Technol*. **32**,10, 1463 -1469 (2009)

41. Ahmed, S. and Krumpelt, M. Hydrogen from hydrocarbon fuel for fuel cells. *International journal of hydrogen energy*. **26**, 291-301, (2001)

42. Saxena, R. C.; Adhikari, D. K. and Goyal, H. B. Biomass-based energy fuel through biochemical routes: A review. *Renewable and Sustainable Energy Reviews.* **13**, 167–178 (2009)

43. Atkinson, A.; Barnett, S.; Gorte, R. J.; Irvine, J. T. S.; Mcevoy, A. J.; Mogensen, M.; Singhal, S. C. and Vohs, J. Advanced Anodes for High-Temperature Fuel Cells*. Nat. Mater.* **3**, 17-27. 105 (2004)

44. Gross, M. D.; Vohs, J. M. and Gorte, R. J. Recent progress in SOFC anodes for direct utilization of hydrocarbons*. J. Mater. Chem.***17**, 3071-3077, (2007)

45. Sun, C. Stimming, U. Recent anode advances in solid oxide fuel cells. *Journal of Power Sources* **171,** 247–260, (2007)

46. Gorte, R. J.; Vohs, J. M. and Mcintosh, S. Recent developments on anodes for direct fuel utilization in SOFC*. Solid State Ionics.* **175**, 1-6, (2004)

47. Kim, H.; Park, S.; Vohs, J. M. and Gorte, R. J. Direct oxidation of liquid fuels in a solid oxide fuel cell*. J. Electrochem. Soc.* **148**, 693-695, (2001)

48. Lin, Y. B.; Zhan, Z. L.; Liu, J.; Barnett, S. A. Direct operation of solid oxide fuel cells with methane fuel*. Solid State Ionics.* **176**, 1827-1835, (2005)

49. Brett, D. J. L.; Atkinson, A.; Cumming, D.; Ramirez-Cabrera, E.; Rudkin, R. and Brandon, N. P. Methanol as a direct fuel in intermediate temperature (500–600 ^{o}C) solid oxide fuel cells with copper based anodes. *Chemical Engineering Science.* **60**, 21, 5649–5662 (2005)

50. Kim, T.; Ahn, K.; Vohs, J. M. and Gorte, R. J. Deactivation of ceria-based SOFC anodes in methanol. *Journal of Power Sources* **164**,1, 42–48 (2007)

51. Lee, S. I.; Vohs, J. M.; and Gorte, R. J. A Study of SOFC anodes based on Cu-Ni and Cu-Co Bimetallic in CeO_2-YSZ*. J. Electrochem. Soc.* ***151***, 1319-1323. 141 (2004)

52. Lee, S. I.; Ahn, K.; Vohs, J. M. and Gorte, R. J. Cu-Co bimetallic anodes for direct utilization of methane in SOFCs*. Electrochem. Solid State Lett.* ***8*****,** 48-51 (2005)

53. Lu, C.; Worrell, W. L.; Gorte, R. J. and Vohs, J. M. SOFCs for direct oxidation of hydrocarbon fuels with samaria-doped ceria electrolyte*. J. Electrochem. Soc.* ***150***, 354-358 (2003)

54. Liu, M.; Peng, R.; Dong, D.; Gao, J.; Liu, X. and Meng, G. Direct liquid methanol-fuelled solid oxide fuel cell. *Journal of Power Sources.* **185**,188–192 (2008)

55. Song, C. Fuel processing for low-temperature and high-temperature fuel cells challenges, and opportunities for sustainable development in the 21st century. *Catalysis Today*, **77**, 17–49 (2002)

56. Ran, R.; Xiong, G.; Sheng. S.; Yang, W.; Stroh, N.; Brunner, H.: Catalytic partial oxidation of n-heptane for hydrogen production. *Catal. Lett.* **88**(1-2), 55-9, (2003)

57. Zhu, W.; Xiong, G.; Han, W. and Yang, W. Catalytic partial oxidation of gasoline to syngas in a dense membrane reactor. *Catal. Today.* 93-95, 257-61 (2004)

58. Aupretre, F.; Descorme, C. and Duprez, D. Bio-ethanol catalytic steam reforming over supported metal catalysts. *Catalysis communication* 3, 263 – 267 (2002)

59. Ming, Q.; Healey, T.; Allen, L. and Irvine, P. Steam reforming of hydrocarbon fuels. *Catalysis Today* **77**, 51-64 (2002)

60. Dauenhauer, P. J.; Salge, J. R. and Schmidt, L.D. Renewable hydrogen by autothermal steam reforming of volatile carbohydrates. *Journal of Catalysis* **244,** 238–247 (2006)

61. Geissler, K.; Newson, E.; Vogel, F.; Truong, T.; Hottinger, P. and Wokaun, A. Autothermal methanol reforming for hydrogen production in fuel cell application. *Phs. chem. chem. phys*. **3**, 289-293 (2001)

62. Wu, G.; Zhang, C.; Li, S.; Han, Z.; Wang, T.; Ma, X. and Gong, J. Hydrogen production via glycerol steam reforming over Ni/Al_2O_3: Influence of nickel precursors. *ACS Sustainable Chem. Eng*. **1,** 1052−1062 (2013)

63. Deluga, G. A.; Salge, J. R.; Schmidt, L. D. and Verykios, X. E. Renewable hydrogen from ethanol by autothermal reforming *Science*, **303**, 993-997 (2004)

64. Petterson, L. J. and Westerholm, R. State of the art of multi-fuel reformers for fuel vehicles: Problem identification and research needs. *Int. j. Hydrogen Energy*, **26**(3), 243-246 (2001)

65. Seo, Y.; Jung, Y.; Yoon, W.; Jang, I. and Lee, T. The effect of Ni content on a highly active $Ni\text{-}Al_2O_3$ catalyst prepared by the homogeneous precipitation method. *Int. j. of hydrogen energy* **36** (1) 94-102 (2011)

66. Sanchez, E. A. and Comelli, R. A. Hydrogen by glycerol steam reforming on a nickel–alumina catalyst: Deactivation processes and regeneration. *International Journal of Hydrogen Energy* **37** (19), 14740 – 14746 (2012)

67. Vaidya, P. D. and Rodrigues, A. E. Glycerol reforming for hydrogen Production: A Review. *Chem. Eng. Technol.* **32**, 10, 1463–1469 (2009)

68. Adhikari, S.; Fernando*, S.*; Gwaltney, S. R.; Filip To, S. D.; Bricka, R. M.; Steele, P. H. and Haryanto, A. A thermodynamic analysis of hydrogen production by steam reforming of glycerol. *International Journal of Hydrogen Energy* **32**, 2875 – 2880 (2007)

69. Shekhawat, D.; Spivey, J. J. and Berry, D. A. Fuel Cells: *Technology for fuel Processing*. Elsevier Pg 73-121(2011)

70. Salazar-Villalpando, M. D. and Reyes, B. Hydogen production over Ni/Ceria-supported catalyst by partial oxidation of methane. *Int. j. Hydrogen Energy* 43, 24, 9723-9729 (2009).

71. Corbo, P. and Migliardini, F. Hydrogen production by catalytic partial oxidation of methane and propane on Ni and Pt catalysts. *Int. j. Hydrogen Energy*. **32**,1, 55-66 (2007)

72. Liguras, D. K. Goundani, K. and Verykious, X. E. Production of hydrogen for fuel cells by catalytic partial oxidation of ethanol over structured Ni catalysts. *J. Power Sources* **130**, 1-2, 30-37 9 (2004)

73. Tang, S.; Lin, J. and Tan, K. L. Partial oxidation of methane to syngas over Ni/MgO, Ni/CaO and Ni/CeO_2. *Catal. Lett*. **51**, 169-175 (1998)

74. Wang, W. Thermodynamic analysis of glycerol partial oxidation for hydrogen production Fuel Processing Technology **91**, 1401-1408 (2010)

75. Authayanun, S.; Arpornwichanop, A.; Paengjuntuek, W. and Assabumrungrat, S. Thermodynamic study of hydrogen production from crude glycerol auto-thermal reforming for fuel cell applications. *Int. j. Hydrogen Energy* **35**,13, 6617-6623 (2010)

76. Wang, H.; Wang, X.; Li, M.; Li, S.; Wang, S. and Ma, X. Thermodynamics analysis of hydrogen production from glycerol auto-thermal reforming. *Int. j. Hydrogen Energy* **34**, 14, 5683-5690 (2009).

77. Youn, M. H.; Seo, J. G.; Lee, H.; Bang, Y.; Chung, J. S. and Song, I. K. Hydrogen production by autothermal reforming of ethanol over nickel catalysts supported on metal oxides: Effect of support acidity. *Appl. Catal B: Env*. **98** (1-2), 57-64 (2010)

78. Gould, B. D.; Chen, X. and Schwank, J.W. Dodecane reforming over nickel-based monolith catalysts. *Journal of Catal*. **250**, 2, 209-221 (2007)

79. Mawdsley, J. R. and Krause, T. R. Rare earth-first-row transition metal perovskites as catalysts for the autothermal reforming of hydrocarbon fuels to generate hydrogen. *Applied Catalysis A: General.* **334, 1-2,** 311–320 (2008)

80. Shekhawat, D.; Spivey, J. J.; and Berry, D. A. Fuel Cells: *Technology for fuel Processing*. Elsevier Pg. 73-129-189 (2011)

2.0 RESEARCH BACKGROUND

2.1 Biomass potentials as an alternative sustainable renewable energy resource

The dramatic growth in the world population is synonymous with the current surge for energy demand. The fossil energy reserve which is the major energy source representing 80% global energy supply is fast depleting and causing environmental degradation[1]. Considerable attention is now focused on the search and development of new energy sources that are renewable, less costly and which might guarantee environmental benefits. Biomass is found to be an attractive candidate that has full potential to serve as replacement or at least complement the depleted fossil fuel as a viable sustainable energy resource for the future[2-5]. Biomass feedstock seen as biodegradable organic matter is found on renewable, replenishing and recurring basis. Biomass has captured much interest not only because of its renewable, sustainable, biodegradable natures and being environmentally benign (having low profile of CO_2 and sulphur) but also because of its inherent potentials as great energy reserve[3].

Biomass based energy is the largest portion of renewable energy ranging from forestry to many available energy crops, which if properly utilised could significantly reduce the profile of greenhouse gas emission, guarantee energy security and realization of the Kyoto agreement[6]. Unlike fossil fuel, biomass materials are evenly distributed, it is the oldest source of energy after the sun and energy obtainable from biomass annually exceeds by several factors the world energy consumption[3]. Therefore biomass great future energy and economic potentials has never been more apt than now especially in the light of the current incessant hiking of petroleum prices, glaring catastrophe of climate change due to GHG emission, political crisis in the major oil region (Middle East and east Africa) and developing economies such as China's unstoppable thirst for energy.

Through thermochemical and biological processes, biomass can be transformed into liquid, solid and gaseous product known as biofuel[7]. Renewable biomass materials that can be converted to biofuel ranges from edible food crops to non-edible ones, agricultural and forest wastes such as crops, trees, agricultural waste, wood and wood residue, animal and animal waste[2,8,9]. Essentially, the idea of bio refinery was conceptualised in essence as an integrated system of processes and equipment to transform biomass material to more useful feedstock called biofuels. The primary

conversion processes that are being explored for biomass conversion to biofuel includes pyrolysis (gases, Char), thermolysis (char, oil gases), hydrothermolysis (Char, oil, gases), combustion (heat, CO_2 and CO), gasification (CO, H_2, CO_2 and CH_4), fermentation (ethanol, CO_2, transesterification (ethyl ester and glycerol), aerobic (CO_2, H_2O and heat) and anaerobic (CH_4 and H_2O) digestion and extraction (vegetable oil)[6,7,10,11].

2.2 Biodiesel production and by-product glycerol glut

2.2.1 Feedstock for biodiesel production

Different oil bearing crops have been identified and used as feedstock for biodiesel production, some are edible such as soybean oil, rapeseed oil, cottonseed oil, palm oil[12] etc. as well as non-edible ones such as jupati[13], Moringa oleifera oil[14], jatropha[15], algae and sea weeds[16]. Animal fat and used cooking oils are also widely used as feedstock for biodiesel production[17]. Over 75-80 % of the cost of biodiesel production lies with the feedstock and at the moment the oil crop produced can generate only 12 % of the required biodiesel. Unless more oil crops are developed especially the non-edible crops as evident in the second generation of biodiesel avoiding the use expensive foodstuff oil, it will be difficult to see biodiesel replacing completely the petroleum diesel in the nearest future[18]. Use of low-value feedstock such as tallow, crude vegetable oil, poultry fat, recovered cooking oil etc. also have the potentials to increase production and reduce cost. The issue with low-quality feedstock is they have to undergo some pre-treatments such as bleaching, filtration, deodorisation, separation, pre-esterification; distillation etc. before use which might be costly and have some environmental issues.

It is a requirement that for any feedstock to be suitable for biodiesel production it has to be readily available, cheap and have capacity to produce quality oil. Fatty acid content and its nature are important profile in the choice of feedstock for biodiesel production. Feedstock used in biodiesel synthesis differ in their fatty acid profiles ratios and chain length as seen in Table 2-1 which influences their fuel properties.

Table 2-1 some common feedstock used in biodiesel production and their fatty acid profile[19]

Oil and fat resource	Fatty acid Profile [k] (% by Weight)												
	≤ 10	12:0	14:0	16:0	16:1	18:0	18:1	18:2	18:3	20:0	20;1	22:0	22:1	24:0	24:1
Cotton Seed Oil	0.0	0,1-0.2	0.7-1.4	17.0-31	0.4-2.0	0.9-4.0	13.3-22.9	47.8-58.2	0.1-2.1	0.2-1.3	0.1-0.5	0.1-0.6	0.1-0.3	0.1-0.1	0.0
Peanut Oil	0.0	0.0	0.0	8.0-12.6	1.4	1.0-4.5	41.0-56.0	26.0-31.9	0.9	0.8-4.2	0.6-2.6	1.5-5.4	0.0	0.5-2.5	1.0
Rapeseed Oil	0.0	0.0	0.0-0.5	3.0-5.7	0.0	0.8-1.5	55.0-64.4	20.0-26.0	8.2-12.0	0.0	1.0-2.0	0.5	0.5-2.0	0.0	0.0
Palm kernel Oil	5.1-13.0	42.4-55.0	12.0-19.0	3.0-11.5	0.2	1.3-8.0	8.7-21.0	0.5-3.5	0.2	0.2	0..2	0.2	0.0	0.0	0.0
Soybean	0.0	0.1	0.1-0.4	7.0-12.7	0.1-1.0	1.4-5.9	11.5-27.2	51.5-63.1	2.9-12.1	0.3-4.0	0.1-0.4	0.1-0.8	0.4	0.0	0.0
Safflower	0.0	0.0	0.0-0.1	5.2-9.0	0.0	1.0-3.0	10.0-16.2	76.3-82.0	0.1-0.4	0.0	0.0	0.0	0.0	0.0	0.0
Sunflower Oil	0.0	0.1	0.1-0..2	2.0-9.0	0.3	1.6-6.5	14.0-39.4	48.3-74.0	0.2-0.7	0.1-1.2	0.4	0.3-1.5	0.3	0.5	0.0
Beef tallow	0.0	0.1-0.7	2.0-8.0	23.0-38.0	0.0-4.7	14.0-29.0	34.9-50.0	1.0-5.0	0.5	0.1	0.1	0.0	0.0	0.0	0.0
Poultry fat	0.0	0.0	0.0-0.5	22.2-23.0	8.4	5.1-5.4	42.3	17.0-19.3	1.0	0.0	1.0-2.0	0.0	0.0	0.0	0.0
Lard	0.0	0.1	1.4-2.3	17.3-30.0	1.9-3.0	12.0-20.0	42.5-50.0	7.0-13.0	0.4-1.0	0.3	1.5	0.0	0.0	0.0	0.0

More importantly, fuel properties of biodiesel such as heating value, cetane number, viscosity, flash point, pour and cloud point are all affected by the length of fatty acid chain, degree of unsaturation and some other functional groups attached to the triglycerides of the parent feedstock used[20]. High fatty acid profile in animal fat and used cooking oil make them more susceptible to reaction with the commonly used homogenous catalyst leading to soap formation and eventual catalyst deactivation. Geography, climate and economics are also important factors in the choice of feedstock for biodiesel production. Whilst predominantly biodiesel in America comes from soybean oil for instance in Europe, rapeseed biodiesel dominates and Indians are renowned in using used or recycled vegetable oil for biodiesel production[21]. Therefore right choice of feedstock is very important in biodiesel production as it underpins quality and fuel behaviour or properties of the biodiesel.

2.2.2 Vegetable oil fuel properties

For long, the fuel potentials of vegetable oil (a biomass material) have been recognised. Dr Rudolph Diesel, the inventor of diesel engine ran his first engine with peanut oil[22]. The glaring dangers of climate change are the driving force behind the renewed interest in biofuels. Apart from having intense energy content, vegetable oil has other desirable properties such as liquid nature, renewability, low sulphur and aromatic content, although it is costly and has limited availability.

Direct use of vegetable oil is problematic to a diesel engine basically due to its high viscosity. Despite the high viscosity, short-term use of vegetable oil recorded some success whilst prolonged use of pure vegetable oil showed problems such as injector coking, ring sticking, poor fuel atomization, carbon deposition build-up, excessive part wearing, gelling and thickening of engine lubricant, cold start etc.[23]. The high molecular weight of oil is believed to be responsible for the high kinematic viscosity (30-40 cSt at 311K) of vegetable oil which is 10-20 times high than that of petroleum diesel[23]. This implies poor atomization and injection and delayed ignition. Vegetable oil has high flash point (> 473 K) but low cetane and volumetric heating value (39 – 40 MJ/kg) relatively when compare to petroleum diesel fuel. High flash point affects volatility while low cetane number delay ignition. The structural oxygen content of

vegetable oil gives them high combustion efficiency more than the petroleum diesel. Table 2-2 summarises fuel properties of vegetable oil.

Table 2-2 some common vegetable oils used in biodiesel production and their fuel properties compared to that of petroleum diesel[24]

	Sunflower	Soybean	Rapeseed	Palm Oil	Peanut	Safflower	Tallow	Diesel (No. 2 DF)
Kinematic Viscosity at 310.8 K (mm^2/s)	33.9	32.6	37.0	39.6	39.6	31.3	51.2	2.7
Heating Value (MJ/kg)	39.6	39.6	39.7	-	39.8	39.5	40.0	45.3
Cetane number	37.1	37.9	37.6	42.0	41.8	41.3	-	47.0
Flash Point (K)	547	527	519	540	544	533	474	325
Cloud Point (K)	280.2	269.1	269.1	-	285.8	291.3	-	258.0
Pour Point (K)	258.0	260.8	241.3	304.0	266.3	266.3	-	240.0

Use of pure vegetable oil (B100) as fuel therefore might not be possible without problems but blend with petroleum diesel in different proportions up to 20-25% vegetable oil and 80% petroleum diesel (B20) is practicable without modification of engine[11,22,24-26]. In the case of emission impact, use of pure vegetable oil, blends or its derivative such as methyl esters is characterised by low or reduced hydrocarbon, particulate and CO emissions but increased NOx emissions[23].

2.2.3 The by-product glycerol glut

The successes recorded in the use of transesterification reaction for biodiesel production has led to the dramatic growth of biodiesel industry with a consequent surplus by-product glycerol and it is projected to even grow more rapidly in future. For instance, every 100 kg of biodiesel produced generates 10 kg of by-product glycerol[27]. At the moment, by-product glycerol produced has passed in many folds its demands and is being considered as a waste and virtually makes no contribution to the economics of biodiesel production[28]. This is so because by-product glycerol has very poor fuel properties and therefore not utilised or burn either in petrol or diesel engine directly. It is also not possible to use by-product glycerol for the traditional uses of glycerol in pharmaceutical, food, polymer, cosmetics and not even as lubricant because it lacks the required purity and equally serious is its disposal which constitutes a renege to the environment[27,29]. Glycerol cannot be burned in air as well because it polymerizes and due to incomplete combustion might produce the toxic acrolein[30,31]. Consequently, the search for alternative use for crude by-product glycerol has now become a 'hot' research interest in an effort to reduce cost of biodiesel production, secure environment and to make biodiesel development and commercialisation a reality[28,32]. Research studies have shown that glycerol which is non-flammable, non-toxic and non-volatile, is an enviably intense energy resource. Pure glycerol has high energy density of 6.26 $kWhL^{-1}$ when compared to 3.19 $kWhL^{-1}$ at 34.5Mpa of methane and 0.76 $kWhL^{-1}$ at 34.5 Mpa of H_2[33]. Thus, glycerol is very attractive for production of syngas or hydrogen-rich gas for utilisation in high temperature fuel cell such as solid oxide fuel cell. This is believed will help in providing the much desired sustainable hydrogen infrastructure for the full commercialisation of fuel cell. In addition to alternative new uses or application that involves direct

utilization of crude by-product glycerol, another issue is the purification processes for indirect utilisations which is costly and affects the process integrity with respect to environment. Research has shown that choice of catalyst plays a vital role in the quality of the by-product glycerol obtained from transesterification reaction. High quality glycerol is usually obtained using heterogeneous catalyst compared to homogenous catalysts[34]. Thus there is lots of interest among academics and industries in heterogeneous catalyst development for biodiesel production.

2.2.4 Properties and energy potential of glycerol

Glycerol otherwise known as propane-1,2,3-triol in its pure form is a colourless odourless and viscous liquid with a sweet taste. It has a high density and boiling point as shown in Table 2-3 compared to other simple alcohols. The high boiling point of glycerol could be attributed to formation of strong network of intermolecular hydrogen bond between the glycerol molecules which exist virtually in all phases and at all temperatures. It forms crystals at low temperatures which melt at 18 ^{o}C . It is hydrophilic and readily miscible in water due to the three hydroxyl groups in the glycerol molecule which impart some sort of polarity on the molecule comparable to what obtains in water. The calorific value of glycerol is as high as that of fossil fuel though that depends on the feedstock used to produce it[35,36].

Table 2-3 Physical and chemical properties of glycerol

Property	**Units**	**Value**
Molecular weight	g/mol	92.1
Boiling point	^{o}C	290
Melting point	^{o}C(at atm. Pres.)	18.2
Relative Density	g/cm^{3}	1.261
Viscosity	Pa s	1.5
Vapour pressure	mmHg at 150 ^{o}C	4.3
Surface tension	mN/m at 20 ^{o}C	64
Flash point	^{o}C (Closed cup)	160
Fire point	^{o}C	204
Auto flammability	^{o}C	393
Calorific value	kJ/kg (GCV)	19000
Heat of vaporisation	cal/mole at 55^{o}C	21060
Specific heat	cal/^{o}C^{-1}gm^{-1} at 26^{o}C	0.5779
Heat of combustion	kJ/mole	1662

Glycerol vapour pressure is very low just comparable to other alcohols and polar compounds such as water perhaps due to molecular association and its hydrophilic properties[35].

By-product glycerol is crude and contains some impurities from the biodiesel production process (transesterification). Such impurities include fatty acids, residual methanol and catalyst, non- separated biodiesel and non-converted vegetable oil and 60-70% glycerol depending upon the feedstock used and degree of conversion. Intermediate products such as mono-glycerides and di-glycerides may also be there depending on the level of conversion as well as catalyst efficiency[27]. Therefore glycerol by-product has impurities which make it not suitable for the traditional uses of glycerol in cosmetic, pharmaceuticals, food, and polymer industries.

Development of fuel cells for a variety of application depends on the availability of fuels- H_2 or hydrogen-rich synthesis gas infrastructure. Glycerol is a non-flammable, non-toxic, non-volatile, biodegradable and an enviably intense energy resource hence very attractive for fuel cell. By-product glycerol is therefore seen as an alternative renewable resource like ethanol which could provide the much desired sustainable hydrogen infrastructure for the development of fuel cell technology[37]. It also adds value to biodiesel production economics which might take full commercialisation of biodiesel production to reality. The global cumulative glycerol production is projected at 37 billion gallons by 2016 which translate into 42 % growth annually and expected to get to 3 megaton by 2020 largely from biodiesel synthesis. Glycerol market is projected to hit USD 2.52 Billion by 2020 largely due to growing applications, market and production of oleo chemicals in Asia[35,38,39]. These are strong indicators that the future of glycerol as sustainable energy resource is almost certain. Therefore, gasification of by-product glycerol which is one of the main products of transesterification reaction for utilisation in fuel cell will provide alternative and direct use of by-product glycerol from biodiesel synthesis. This would enhance economic viability of the transesterification process by reducing cost of biodiesel production and provide sustainable hydrogen infrastructure for fuel cell.

2.3 Development of catalyst for biodiesel production

2.3.1 Transesterification reaction

Different processes are being explored to reduce the viscosity of vegetable oil which seems to be the major problem of direct use of vegetable oil as fuel. Notable among them are: dilution, micro emulsion, pyrolysis, thermal decomposition, catalytic cracking and transesterification. The vegetable oil viscosity was lowered using dilution with solvent and micro emulsion but many engine problems such as injector coking and carbon deposit persisted. Transesterification was found to be the best because the fuel properties of the methyl esters known as biodiesel were found to be close to that of the petroleum diesel fuel and more interestingly can be burned directly on unmodified diesel engine or blended with petroleum diesel to be used directly as fuel in diesel engine for transportation[40,41].

Transesterification means transforming the free fatty acid of a triglyceride (TG) or a complex free fatty acid (FFA) with methanol to corresponding alkyl ester by abstraction of glycerine from them thus:

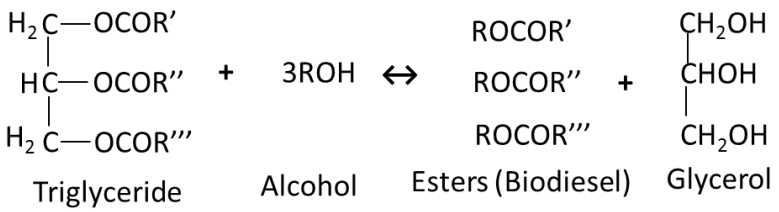

Eqn. 2-1

About 10% glycerol is obtained from each transesterification process, though the yield depends on the feedstock composition and reaction condition of the process itself such as temperature, catalyst etc. The reaction is an equilibrium one and therefore excess alcohol greater than the stoichiometric ratio of 1:3(oil: alcohol) as depicted in the equation is used to drive the conversion to the product side[42]. The conversion is done at low temperature (typically 60^{o}C) and ambient pressure using a catalyst or high temperature (200-550 ^{o}C) and high pressure (8-100 MPa) where there is no catalyst[23,43]. It requires vigorous mixing by stirring or agitation of the vegetable oil-alcohol-catalyst mixture in the reactor for certain period and at certain reaction condition typically for 2 hours at 60 ^{o}C. Two liquid phases are obtained at the end of a successful transesterification reaction: the amber yellow liquid-biodiesel at the top

and the brown viscous liquid-crude glycerol at the bottom within few hours of separation. Complete separation might take as long as 24 hours. The transesterification process can be aided in many ways such as catalytic (homogeneous and heterogeneous), non-catalytic (supercritical alcohol), enzymatic and ultrasonic assisted transesterification reactions[24,44]. In most cases, the conversion process is usually catalysed using basic or acidic homogeneous or heterogeneous catalysts to influence reaction rate and yield. The basic catalysed reaction is the most practiced due to its fast reaction rate. Parameters that affect yield in the transesterification reaction are temperature of the reaction, vegetable oil-to-methanol ratio, catalyst and catalyst concentration, water and reaction time. Choice of alcohol is an important step which influences the reaction rate among many other parameters. In theory, the choice is limited to the primary and secondary monohydric aliphatic alcohol having 1-8 carbon atoms. In practice, the choice is limited to alcohols having 1-4/5 carbon atoms. Methanol and ethanol are the most frequently used, although methanol is mostly chosen probably due to its low cost and its polar and short structure, ethanol is preferred because of its renewability and environmental benefit[41,45].

2.3.2 Homogeneous catalysis

Homogeneous catalyst may be basic or acidic. The most commonly used homogeneous acid catalysts are sulphuric acid (H_2SO_4), hydrochloric acid (HCl), phosphoric acid (H_3PO_4) and organic sulphuric acid (RSO_3H). Transesterification reaction using acid catalyst is not popular due to its slow reaction; corrosive nature and consumes lot of alcohol and therefore requires stringent reaction condition like high temperature (>150 ^oC) and high pressure (>3 bars)[46] . However some promising results were obtained using homogenous acid catalyst in biodiesel production[47-50]. Some studies revealed that homogeneous acid catalyst, however has advantages especially when using low grade oil (like used oil), or oil that has high water (≥ 1%) and free fatty acid content (≥ 0.5%), they also have ability to catalyse both esterification and transesterification reactions[46,51]. The catalyst prefers anhydrous condition as Presence of water from the vegetable oil or methanol could lead to hydrolysis of alkyl ester thus:

$$RCOOR + H_2O \rightarrow RCOOH + ROH \quad \text{Eqn. 2-2}$$

This reduces biodiesel yield, cause catalyst deactivation and increases products solubility and make glycerol recovery difficult.

Transesterification using homogeneous base catalysis is the most practiced because the reagents are cheap, offers good yield, fast reaction rate and good catalytic activity under mild condition compared to acidic homogeneous catalyst. Most commonly used basic homogeneous catalysts are; NaOH, KOH, $Ca(OH)_2$ and there alkoxide derivatives such as $NaOCH_3$, $NaOC_2H_5$, $NaOCH_2CH_2CH_3$, $KOCH_3$ and KOC_2H_5, analysis have shown that alkoxides offers better catalytic activity[47,50]. Just like the homogeneous acid catalyst, using homogeneous basic catalyst has also brought some setbacks. It also requires anhydrous condition as presence of water might results in possibilities of saponification and emulsion of product which could affect quality of product (viscosity) and cost of reaction (consumes alcohol and deactivate catalyst), a lot of washing is needed and excessive corrosion of pipeline by dissolved base. Catalyst recovery and reusability is difficult and removal of catalyst is done by neutralization which raises a lot of environmental problems[52].

2.3.3 Heterogeneous catalysis

There is a need for an alternative catalyst with a comparable performance just like the homogeneous catalyst because of the setbacks highlighted above associated with the use of homogeneous catalyst. Over the years, heterogeneous catalysts were found to have some properties that place them above homogeneous catalysts and offer exciting possibilities of changing the fortune and economics of biodiesel production. They have very little or no corrosive tendencies, more economical and have process integrity such as easy to recover and reuse high activity and selectivity and above all, environmentally benign[53]. Heterogeneous catalysis in transesterification is extensively researched as reviewed elaborately by many reviewers[54-57]. It is evident from the reviews that bulks of the catalysts used in the transesterification process are alkaline metals oxides; alkaline earth metals oxides some transition and rare earth metals oxide as bulk or supported catalysts. The supports are mostly alumina (Al_2O_3), silica (SiO_2) and alkaline earth metals. Recently, titania (TiO_2) is also being looked at. Other

materials used as catalyst are the zeolite due to their large surface area, shape selectivity and ion exchange capacity as well as the clay minerals such as hydrotalcites; non-oxide catalysts such as supported KF was also investigated as they were so classified by Hattori[58]. The catalytic activity of the metal oxides is attributable to their Lewis acid-Bronsted base site surfaces which enable them to interact favourably with alcohol generating the alkoxide ion that attack the glyceride to produce biodiesel and glycerol[54].

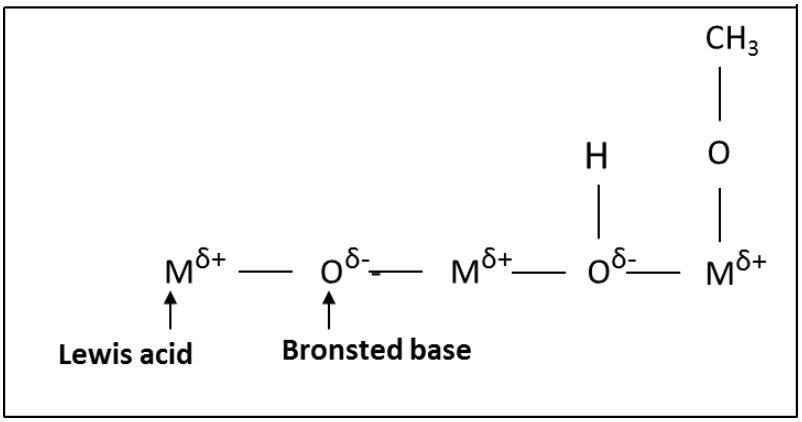

Figure 2-1 Metal oxide catalyst surface showing the Lewis acid-Bronsted base sites and their possible relationship with the suitable chemical species among the reactants for the biodiesel synthesis

However diffusion limitation due to formation of vegetable oil-catalyst-methanol triple phase (immiscible phase) in the reactor which could affect reaction rate has been identified as one of the problems associated with the use of heterogeneous catalyst. Co-solvents such as n-hexane, tetrahydrofuran, dimethyl sulfoxide enhance miscibility of the reactant and were used successfully to reduce diffusion limitation and enhance biodiesel yield[11].

The single metal oxides catalysts such as alkaline metal carbonates ($CaCO_3$, K_2CO_3, Na_2CO_3) have demonstrated good catalytic activity and selectivity towards biodiesel production. The major issue with them is that high yield is obtained only at high temperature typically >200 ^oC[59]. Bancquart et al[60] reported a comparison of catalytic activity in transesterification of glycerol with methyl stearate over single metal oxides solid base catalysts La_2O_3, MgO, CaO and ZnO and good catalytic activity was obtained at 220 ^oC with high glyceride conversion. The good catalytic activity of the catalyst was attributed to strength of their basic sites. This observation was strengthened by Yan

et al[61] in transesterification of rapeseed oil using CaO, MgO, SrO and BaO as catalyst at 64.5 ^{o}C, 18:1 methanol-oil ratio and 10wt% catalyst loading based on the weight of vegetable oil used for the transesterification for 3.5 hrs. The vegetable oil-methanol ratio was calculated based on the method shown in appendix 1. The reported catalyst performance followed the order of increasing basic strength and conversion was thus MgO < CaO < SrO < BaO or 5%, 58%, 60% and 86% biodiesel yield respectively. Amongst the alkaline earth single metal oxides catalysts used in transesterification reaction, CaO is highly studied perhaps due to its availability, low cost, minor toxicity, low solubility in methanol and good activity. Though it often suffers deactivation problems due to leaching as results of its dissolution in the reaction mixture especially alcohol and as such loses performance in subsequent reaction cycles[62,63]. Leaching of catalyst into the alcohol occurs during transesterification reaction due certain portion of the catalyst active phase forming soluble product with methanol when they react to trigger the transesterification reaction. MgO is also used extensively, but SrO and BaO are not used very often. SrO losses its activity due to formation of hydroxide with water and carbonate with CO_2 while BaO is soluble in methanol forming toxic substance[61]. Water and CO_2 also influences catalytic activity of CaO as reported in transesterification of sunflower oil. It was found that CaO is deactivated and carbonated in air but could be regenerated through thermal treatment at 700 ^{o}C[64]. Studies revealed their reaction kinetics also hinges on the strength of their basic site[60]. MgO has the weakest basic strength and high solubility in methanol among the alkaline earth metal catalysts and therefore less active. Transition metal oxides such as ZnO, ZrO_2 and WO_3 were the most investigated largely due to their acidic properties and good activity. Particularly, Zirconia was highly investigated due to its strong acid surface which could be modified to make super acids such as sulphated zirconia (ZrO_2/SO_4^{2-}) and tungstated zirconia (ZrO_2/WO_3^{2-}) which were found active in transesterification[54]. Transesterification of soybean oil using sulphated zirconia prepared by solvent-free method was reported to have yielded 98.6 % and 92 % biodiesel using methanol and ethanol respectively under 1 hour at 120 ^{o}C though the catalyst rapidly deactivated due to leaching of the sulphate active phase[65]. Other transition metal oxide catalysts such as titanium oxide and vanadium phosphate were also found to be active and promising under mild reaction conditions[54].

Generally, despite all the good activities reported in the use of single metal oxides bulk catalysts in transesterification reaction, it was noted that single metal catalysts have low reactivity at low temperature and get deactivated largely due to leaching of the active phase. Leaching for instance could lead to contamination and increase cost of production due to the need for catalyst replacement instead of reuse[66]. Therefore, a catalyst with improved properties such as; good and generous surface area, strong affinity for triglycerides, hydrophobic in nature and resistance to deactivation by leaching was sought to improve the structural properties and catalyst performance[67].

Mixed metal oxides were used to modify basic or acidic character of single metal oxides as co-catalyst or as a support. They were meant also to reduce leaching and enhance surface area. For instance, high reaction temperature requirement in the use carbonate was significantly improved by using MgO as a support. Liang et al, 2009[68] achieved 99% yield at 70 ^{o}C with methanol and K_2CO_3/MgO catalyst loading of 0.7% within 2 hours. Activity was lost only after 6 cycles. In the same work, different carriers were compared and the activity was in the order Mg > CaO > Al_2O_3 > ZnO > Activated Carbon > SiO_2 > TiO_2 > SnO_2 and conversion of 99%, 98%, 98%, 93%, 93%, 90%, 89.5%, 87% and 86% respectively. The activity of the K_2CO_3/MgO system was found better than unsupported K_2CO_3 and homogenous catalyst such as $NaOCH_3$, NaOH and KOH. It is important to note that the basic oxides supports performed better than the acidic supports. Similarly, Kawashima et al[69] compared the catalytic activities of thirteen mixed oxides based on oxides of Ca, Ba, Mg, Ti, Mn, Fe, Zr and Ce. The Ca-based oxides were the most active which was related to the strength of their basic sites. $CaZrO_3$ and CaO-CeO_2 showed better durability and reusability and were able to maintain same activity after 5-7 cycles. Both gave biodiesel yield >80% using 6:1 methanol-oil ratio at 60 ^{o}C. This illustrates that the use of ZrO_2 and CeO_2 as support has reduced the leaching tendency of CaO. In a related work, surface alkalinity, surface area of alkaline earth metal oxides (CaO, MgO, SrO and BaO) was modified by supporting them on ZrO_2. SrO/ZrO_2 exhibited the highest activity (79.7 %) in transesterification of waste cooking oil using methanol and the activity was attributed to its balanced basic/acidic sites, suitable surface area, pore volume and pore diameter[70]. In another work, leaching and stability was reduced with TiO_2 by grafting it on SiO_2 compared to using it as bulk unsupported catalyst in a study reported by Di Serio et el[71]. They compared

catalytic performance of several heterogeneous catalysts in transesterification of soybean oil by screening them in small steel vials at 180 ^{o}C simultaneously. Homogeneous contribution of each due to leaching of the active phase also studied. The behaviour of TiO_2 supported on SiO_2 was a lot more stable to leaching compared to others (PbO , PbO_2 , PbSO4 , ZnO $ZnCl_2$, ZnSO4, $Zn_3(PO_4)_2$, SnO , SnO_2 , $SnCl_2$, $SnSO_4$, Fe_2O_3 , $FeCl_3$,$Fe_3(SO_4)_3$,$FePO_4$,MgO , HT3). Use of support such as alumina has also shown significant influence in enhancing surface area and pores suitability in biodiesel production[72-74]. Recently, there was an innovative effort to use different oxides in a single phase rather than composite as catalyst in transesterification of animal fat and used cooking oil with methanol. The catalyst $Ca_{0.9}Mn_{0.1}O$ gave 92.5% against the same 92.5 % and 93.8 % from NaOH and CaO respectively after 8 hour run. Although $Ca_{0.9}Mn_{0.1}O$ had the advantage of requiring low operation temperature, there were aggregates such as Ca_2MnO_4 and Mn_3O_4 along with the $Ca_{0.9}Mn_{0.1}O$ rather than a single phase material. Leaching was also observed[75].

Generally, Surface area, Strength of basic sites, leacheability and general performance were improved using mixed oxides and support though there was still need for improvement especially surface area and leaching of impregnated active phase.

Zeolite materials were also extensively utilised as catalyst for biodiesel production with lots of promising results[76-78]. Zeolites owe their catalytic activity to their large and generous surface area, suitable chemical composition and pore size distribution as typified by the images in Figure 2-2 which can be tailored to enhance basic or acidic character or ion exchange ability. Basic or acidic character is tailored through careful selection of cation or by playing around with the Al-Si ratio to restructure the frame work[79].

Titanosilicates, zeolite-X and mesoporous silicate zeolites are the most popular in biodiesel catalysis. Engelhard titinosilicate structure (ETS) based zeolite such as ETS-4 and 10 were among the basic ion exchange zeolites that have shown great potential as catalyst for biodiesel production. Catalytic activity of ETS-10 and Zeolite-X catalysts in transesterification of soybean oil with methanol was compared by Suppes et al[80] under different reaction temperatures.

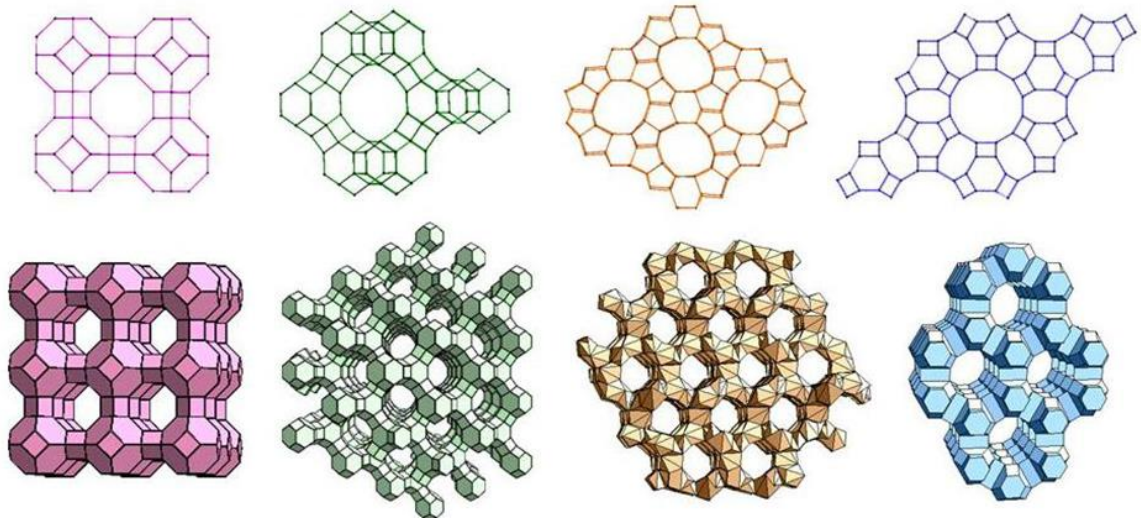

Figure 2-2 A schematic diagram showing structures of different zeolites[81]

ETS-10 gave the highest conversion compared to the Zeolite-X catalyst and the conversion increased when temperature was raised from 60 ^{o}C to 150 ^{o}C. The high performance of the ETS-10 catalyst was attributed to high basicity, large pores and effective particle diffusion. No activity loss was observed after reuse. Yan et al[61] reported a comparison in the catalytic activity of CaO on MgO, SiO_2, Al_2O_3 and acidic zeolite HY support in transesterification of rapeseed oil at 64.5 ^{o}C and oil-methanol ratio of 1:18 in which they obtained 92 %, 60 % 36 % and 23 % biodiesel conversion respectively. The results showed that the basic MgO was a better support than the acidic Al_2O_3 and zeolite HY supports. Similarly, the basic ETS-10 (Na, K) and its acidic form ETS-10 [H^+] and acidic Zeolite Hβ were compared with some basic and acidic homogeneous (NaOH and H_2SO_4 respectively) catalysts in transesterification of triacetin at 60 ^{o}C. Although the heterogeneous catalyst showed better performance when compared to the homogeneous catalysts, they exhibited some homogeneous character due to leaching. The ETS-10 (Na, K) gave 90 % conversion within I-2 hours but showed rapid deactivation by yielding only 28 % in 2 hours of the second cycle[82].

Acidity could be tailored also for good catalytic activity. Zeolite ZSM-5(HMFI) and mordanite (HMOR) with deferent Si/Al ratios were investigated for the influence of acidity and pore structure in the esterification of oleic acid of soybean oil. It was reported that conversion improved with increase of acid sites. 80 % conversion was achieved at 60 ^{o}C with HOMR zeolite and HMFI which improved with increase of acid

site[83]. Due to the problem of mass transfer with the microporous zeolite such as titanosilicate and zeolite-x, mesoporous silicate such as MCM-41 and SBA-15 were introduced and some promising results were reported[84,85].

Apart from the diffusion limitation issue, leaching of impregnated active phase resulting to decreased activity was the major problems with the use of this class of materials.

Hydrotalsites also known as layered double hydroxide (LDH) as seen in Figure 2-3 occurs naturally as an anionic clay. Their basic catalysis and surface area which can be tailored by changing the chemical composition or preparation condition has made them attractive for transesterification reaction to biodiesel[86].

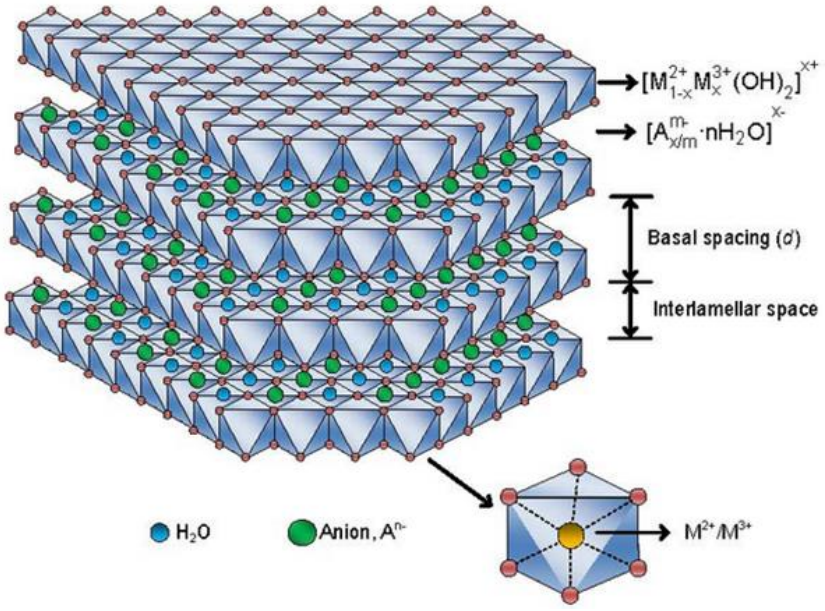

Figure 2-3 A schematic models showing the structure of layered double hydroxide[87]

Traditionally, LDH are prepared by co-precipitation by adding metal nitrates and precipitants followed by ageing or hydro treatment[88,89]. When Mg-Al based LDH is heated to high temperature (500 ^{o}C) it becomes porous with good surface due to loss of water and carbonate decomposition which makes it suitable catalyst for biodiesel production[90]. Some also reported good performance of Li-Al based LDH perhaps due to its Bronsted basic properties[91]. Impregnating some active species on the surface of the LDH could enhance catalytic activity of the LHD catalyst. Influence of catalyst amount, methanol/oil ratio, KF/HT load ratio and reaction time in transesterification

of palm oil with methanol over KF/HT was investigated. 85 % methyl ester yield was achieved using the KF/HT catalyst system at 65 ^{o}C using 12:1 methanol-oil ratio and 3 % catalyst loading within 3 hours, but conversion increased to 92 % when the reaction time was delayed to 5 hours[88]. In a related work by the same author, 90 % biodiesel yield within 10 min was obtained in transesterification of palm oil with methanol using 12:1 methanol oil ratio and 5 % catalyst loading in a CaO modified KF/Ca-Mg-Al hydrotalcite catalyst system[92].

Use of solid organic base catalysts for biodiesel production was also reported. Although the known solid basic organic catalysts operates as a homogenous catalyst, promising results were obtained and they do not form soap or emulsion like the conventional homogeneous catalysts. Guanidine had demonstrated good catalytic activity due to its high basic strength in transesterification of rapeseed oil with methanol[93]. In a related work by same author, alkyl-guanidine anchored on MCM-41 was used in transesterification of soybean oil with methanol. The result obtained was comparable to that from homogeneous catalyst, although, there was some diffusion limitation problems and instability of the catalyst frame work system[94].

2.4 Catalysis of glycerol steam reforming (GSR)

2.4.1 Glycerol steam reforming and thermodynamic consideration

Steam reforming represents a way through which glycerol or a low value feedstock such as by-product glycerol can be converted into syngas or hydrogen-rich gas for utilisation in fuel cells. Glycerol steam reforming (GSR) is believed to be a very complicated process involving so many reactions depending upon the reaction conditions. Thermodynamic analysis into the possibility of using glycerol glut to generate hydrogen for different applications especially fuel cell was studied by researchers using minimization of Gibbs free energy method. Findings from such work have revealed water to glycerol molar ratio of 9-12, temperature of 925-975K and atmospheric pressure as the optimum condition for hydrogen production[95-98]. Under these conditions, CO and CO_2 methanation reaction for instance that consumes hydrogen to produce methane is minimized and carbon deposition thermodynamically hindered. In same vein, Slinn et al[99] demonstrated the feasibility of using by-product glycerol for hydrogen production to power solid oxide fuel cell (SOFC) using steam

reforming. They reported 860 ^{o}C (1133K), 2.5 steam/carbon ratios and 0.12 mol/min glycerol flows per kg of catalyst as the optimum condition using Pt/Al_2O_3 catalyst system. They further hinted that the relatively poor performance and severe coking using glycerol by-product when compared to pure glycerol was attributed to long chain fatty acids that are hard to reform hence more likely to form carbon deposition.

Basically, when glycerol is heated to high temperatures (700-800 ^{o}C) it decomposes to yield gases (Eqn. 2-3) but at low temperatures (400-600 ^{o}C) it tends to dehydrates (Eqn. 2-4) or dehydrogenates (Eqn. 2-5) yielding liquid products as well as gaseous products. The liquid products are likely to be hydroxyacetone and 3-hydroxypropanal and glyceraldehyde and dihydroxyacetone respectively which could later decompose to yield gasses at suitable temperatures[34]. The products are chemisorbed on the catalyst surface through carbon or oxygen atoms or both leading to cleavages of C-C followed by dehydrogenation leaving CO on the catalyst surface which may desorbs, undergo water gas shift reaction or methanation reaction. Other possible reaction pathways include C-O scission or rearrangement and dehydrogenation. The former generates small alcohols and alkane while the latter give alkenes and carboxylic acids[99].

$C_3H_8O_3 \rightarrow 3CO + 4H_2 \qquad \Delta H^{o}_{298k} = +251 \text{ kJ mol}^{-1}$ Eqn. 2-3

$C_3H_8O_3 \rightarrow C_3H_6O_2 + H_2O \qquad \Delta H^{o}_{298k} = +450 \text{ kJ mol}^{-1}$ Eqn. 2-4

$C_3H_8O_3 \rightarrow C_3H_6O_3 + H_2 \qquad \Delta H^{o}_{298k} = +15 \text{ kJ mol}^{-1}$ Eqn. 2-5

In the presence of water as in the case of steam reforming, the product composition is dictated by combination of both pyrolysis and water gas shift reactions thus:

$CO + H_2O \leftrightarrow CO_2 + H_2 \quad \Delta H^{o}_{298k} = -41$ kJ mol (combined mole of CO and H_2O) Eqn. 2-6

Assuming the CO from glycerol reaction undergoes water-gas shift reaction, the overall equation for glycerol steam reforming is thus:

$C_3H_8O_3 + 3H_2O \leftrightarrow 3CO_2 + 7H_2 \qquad \Delta H^{o}_{298k} = +128 \text{kJ mol}^{-1}$ Eqn. 2-7

From Eqn. 2-3 above, every one mole of glycerol produces 4 mole of hydrogen in pyrolysis but in steam reforming, every one mole of glycerol produces 7 mole of hydrogen (Eqn. 2-7). Furthermore, from the two equations, both pyrolysis and steam reforming are endothermic processes and therefore considerable heat input favours forward reaction leading to more hydrogen or syngas production.

Reverse water gas shift reaction takes hydrogen and carbon dioxide to produce carbon monoxide and water as shown in Eqn. 2-6. Note that the reverse reaction is endothermic.

The carbon monoxide from glycerol pyrolysis might also be utilized in methanation reaction of CO, CO_2 as well as C in an exothermic manner:

$CO + 3H_2 \leftrightarrow CH_4 + H_2O \quad \Delta H^o_{298k} \ -206\ kJmol^{-1}$ Eqn. 2-8

$C + 2H_2 \leftrightarrow CH_4 \quad \Delta H^o_{298k} \ -75\ kJmol^{-1}$ Eqn. 2-9

$CO_2 + 4H_2 \leftrightarrow CH_4 + 2H_2O \quad \Delta H^o_{298k} \ -165\ kJmol^{-1}$ Eqn. 2-10

Methane steam reforming is also an important possibility for more hydrogen as shown by the reverse of Eqn. 2-8 through endothermic reaction.

Methane dry reforming is also another important reaction to hydrogen

$CO_2 + CH_4 \leftrightarrow 2H_2 + 2CO \quad \Delta H^o_{298k} \ +247kJmol^{-1}$ Eqn. 2-11

Carbon gasification reduces tendencies of carbon deposition as seen in C methanation reaction in Eqn. 2-9. Other reactions are:

$C + H_2O \leftrightarrow CO + H_2 \quad \Delta H^o_{298k} \ +131\ kJmol^{-1}$ Eqn. 2-12

$C + CO_2 \leftrightarrow 2CO \quad \Delta H^o_{298k} \ -172\ kJmol^{-1}$ Eqn. 2-13

$C + 2H_2O \leftrightarrow CO_2 + 2H_2 \quad \Delta H^o_{298k} \ +90kJmol^{-1}$ Eqn. 2-14

Methane decomposition produces hydrogen but enhance tendency for carbon deposition as shown in Eqn. 2-9.

CO disproportionation also known as Boudoard reaction also enhances tendency for carbon formation:

$2CO \leftrightarrow CO_2 + C \quad \Delta H^o_{298k} \ -171.5\ kJmol^{-1}$ Eqn. 2-15

Reactions leading to carbon deposition are mostly exothermic and reversible reactions because carbon deposition is limited by thermodynamics as seen in Eqn. 2-15. Thus,

carbon deposition during steam reforming is more severe under low temperature reaction conditions. Other reaction that leads to carbon deposition includes: Methane decomposition (Eqn. 2-9), carbon monoxide and hydrogen from glycerol decomposition may recombine to produce water and deposit carbon at low temperature (Eqn. 2-12 and Eqn. 2-14).

Using the HSC chemistry software, equilibrium product distribution and coke formation characteristic during glycerol steam reforming was examine under temperature range of 400–1000 ^{o}C and $H_2O/C_3H_8O_3$ ratio of 0-10 moles at atmospheric pressure. Using a model that assumes $C_3H_8O_3$, CO, CO_2, CH_4, H_2 and C as the only or likely products of the steam reforming of glycerol, keeping $H_2O/C_3H_8O_3$ ratio constant at 3:1 and at constant atmospheric pressure and varying the reforming temperatures, product distributions at equilibrium as a function of temperature was predicted as shown in Figure 2-4a-b. The equilibrium composition plot would enable us to see what the product distribution and composition are at equilibrium and how that changes with temperature and $S/C_3H_8O_3$ ratio. Understanding this would help to choose the best reaction condition for our catalyst test. Figure 2-4a represents equilibrium composition at constant $H_2O/C_3H_8O_3$ ratio of 3 and at atmospheric pressure as a function of temperature while in Figure 2-4b, it is at same condition but higher $H_2O/C_3H_8O_3$ ratio of 6. In Figure 2-4a, H_2 and CO_2 composition increases with temperature up to around 700 ^{o}C when H_2 starts to decrease although CO_2 start to decrease earlier around 600 ^{o}C. Simultaneously, the H_2O and CO composition decreases up to same temperature. This behaviour is attributable to water-gas shift reaction phenomenon as shown in Eqn. 2-6 which utilises H_2O and CO to generate H_2 and CO_2. Although it is an exothermic reaction, the chart indicates it strives well up to 700 ^{o}C which is also the peak of hydrogen production or perhaps due to inter play between water-gas shift reaction and pyrolysis. Beyond 700 ^{o}C, there is simultaneous increase in CO and H_2O and decrease in H_2 and CO_2. This means at high temperatures; reverse water gas shift reaction which is endothermic (Eqn.2-6) becomes thermodynamically favoured and takes H_2 and CO_2 from water gas shift reaction or pyrolysis. Furthermore, diluting the glycerol further by increasing the $H_2O/C_3H_8O_3$ ratio to 6 did not change the product distribution at equilibrium but only increased the

amount of products generated as shown in Figure 2-4b. Moles of hydrogen generated for instance increased. This is attributable to the effect of water in water gas shift reaction. The methane composition decreases with increase in temperature up to 750 ^{o}C when it becomes hindered. This agrees with the exothermic nature of the methanation reaction (Eqn. 2-8 to 2-10).

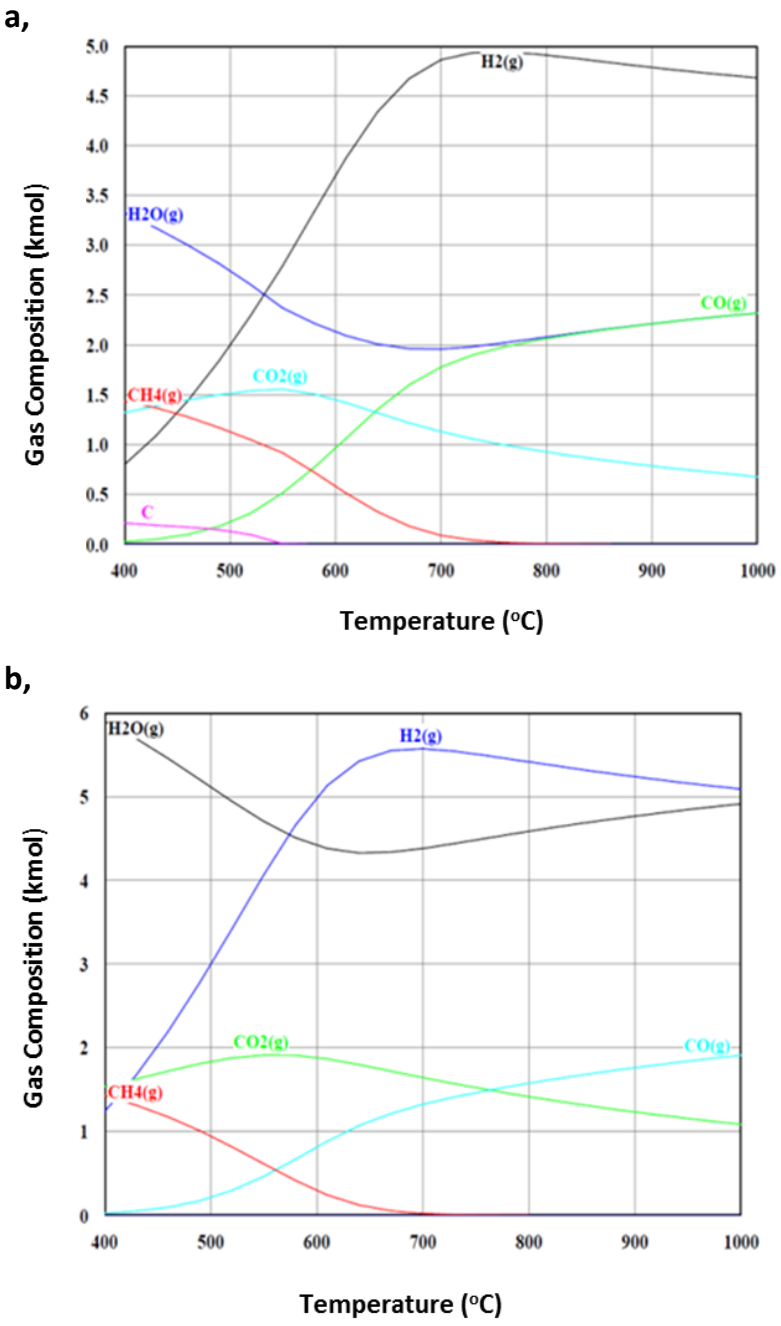

Figure 2-4 Equilibrium products distribution of steam reforming of glycerol at atmospheric pressure as a function of temperature at **a,** S/$C_3H_8O_3$ ratio = 3:1 and **b,** S/$C_3H_8O_3$ ratio = 6:1. The initial mole of reactant was 3 kmol of carbon/kmol glycerol

The mole of methane decreased as seen in Figure 2-4b compared to what is seen in Figure 2-4a which is attributable to dilution effect of water in the reforming process. Since methanation reaction produces water, any increase in water will shifts the reaction to the left. Carbon deposition ceased completely or is limited thermodynamically at 550 ^{o}C, this shows that formation of carbon products strives well at low temperature because most of the reactions leading to carbon products are exothermic (Eqn. 2-12, 2-14 to 2-15). At high $H_2O/C_3H_8O_3$ ratio and atmospheric pressure in Figure 2-4b, no carbon product was predicted at all temperatures (400-1000 ^{o}C). This portrays the combine influence of water and temperature in carbon gasification as illustrated in Eqn. 2-12 to 2-14 above. All the interpretations above agree with what other studies reported[95-97].

On the other hand, if temperature is constant and $H_2O/C_3H_8O_3$ ratio changes, the product distribution changes as illustrated in Figure 2-5a-b. Figure 2-5a, shows product distribution at equilibrium at constant temperature of 550 ^{o}C and at atmospheric pressure for different $H_2O/C_3H_8O_3$ ratio. H_2 and CO_2 continue to increase with increase in $H_2O/C_3H_8O_3$ ratio accompanied by simultaneous decrease in CO due to WGSR which is slightly exothermic. Methane increases to the stoichiometric composition due to methanation reaction which is exothermic therefore does well at moderate temperatures. But at dilution beyond 3:1 ratio the methane decreases. This as explained above is due to the fact that methanation reaction produces water so increase in water will shift the reaction backwards. This observation is even more evident in Figure 2-5b at relatively high temperature (700 ^{o}C), the total methane content is lower due to the exothermic nature of methanation reaction couple with the influence of dilution. Carbon deposition disappears at all dilution beyond the 3:1 ratios at 500 ^{o}C which is due to the role of water in carbon gasification as seen in above equations. At 700 ^{o}C, no carbon products were predicted at all dilutions. This corroborates what was seen above-inter play of dilution and temperature.

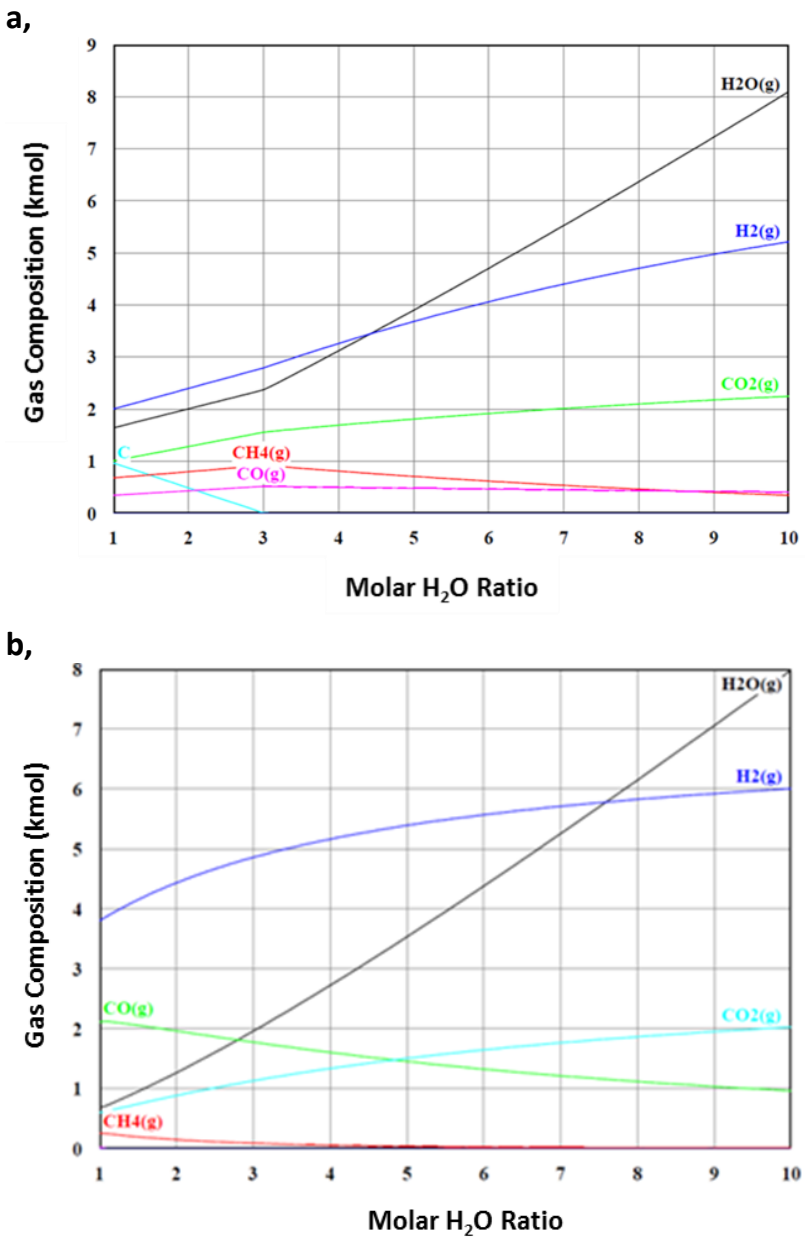

Figure 2-5 Equilibrium products distribution of steam reforming of glycerol at atmospheric pressure as a function of $S/C_3H_8O_3$ ratio at **a,** 550 ^{o}C = 3 and **b,** 700 ^{o}C. The initial mole of reactant was 3 kmol of carbon/kmol glycerol

Generally, the amount of hydrogen increased at all points when temperature increased from 550 ^{o}C in Figure 2-5a to 700 ^{o}C in Figure 2-5b. At relatively high temperature of 700 ^{o}C as in Figure 2-5b, mole of H_2 and CO increased due to combined influence of steam reforming and pyrolysis of glycerol since both are endothermic processes. Methane content decreased at high temperature due to exothermic behaviour of the methanation reaction and endothermic behaviour of steam reforming as well as dry reforming of methane. Water gas shift reaction is not

favoured at high temperature because no increase in CO_2 is observed. It remains constant perhaps due to increase in water content.

Thermodynamic study of hydrogen production from glycerine steam reforming using Gibbs free minimization method has shown that process yield of products such as hydrogen depends not only on reaction condition such as temperature and S/C ratio but also pressure. Hydrogen yield increases with temperature to 702 ^{o}C, water/glycerol molar ratio of 9-12 at atmospheric pressure and is considered condition suitable for hydrogen generation. But high temperature of >762 ^{o}C, and water/glycerol molar ratio of 2 to 3 and high pressure of 20-50 atm is considered suitable for syngas generation[100,95]. Hydrogen production is best at low pressure (atm. pressure) but decline at high pressure[95,96]. Moles of hydrogen produced remain the same for different pressure value at high temperature. At high temperature and pressure, methane yield through methanation reaction increased[96]. However, supercritical water has been shown to be a promising medium for hydrogen generation at high pressure (24 bars) and temperature 700-800 ^{o}C from hydrocarbon and alcohols. At high pressure (24 bars) reaction time can be shorten to enhance hydrogen yield and reduce methane formation [101,102,103]

It is evident from the foregoing that product distribution in glycerol steam reforming (GSR) is dictated by certain conditions such as water gas shift reactions, reverse water gas shift reaction, methnation, methane reforming and pyrolysis. Other sundry reactions equally important include carbon gasification, methane steam reforming, dry reforming and methane decomposition. Hydrogen production is favoured by high reaction temperatures, high glycerol/water ratio and low pressure[98]. Therefore glycerol steam reforming (GSR) though quite complicated process is efficient hence suitable for hydrogen production for fuel cell application.

2.4.2 Catalyst development for steam reforming of glycerol

Effective utilisation of by-product glycerol as a hydrogen source for fuel cells largely depends critically on the discovery of new catalysts with high selectivity and sufficient activity. It is a requirement that such catalyst should be able to hinder, suppress or tolerate carbon deposition which is synonymous with the use of biomass feedstock or

biofuels for hydrogen generation especially under mild reaction conditions**.** It should also guarantee process integrity and environmental safety. Over the years, lots have been done towards achieving this noble objective of developing effective and efficient catalysts[29,32]. Substantial part of the work was dedicated to development of catalyst that facilitate the breaking of C-C, C-H and C-O bonds associated with hydrocarbons or biomass materials such as glycerol feedstock most of which were Ni-based catalyst system typically supported on metal oxides such as mesoporous alumina. Essentially, nickel is cheap, readily available and has strong affinity to catalyses C-C, C-H and H-O bond cleavages and selective towards syngas. Gamma alumina, is a good material widely used as a catalyst support or adsorbent due to its mesoporous, ordered sponge-like pore structure and large surface area. These could enhance surface reaction and morphology of the active nickel catalyst, reduce coke formation and enhance diffusivity of reacting species and resulting products[34,104,105].

Though this area of research is quite new, a lot has been reported on the use of nickel-based catalysts for hydrogen production from glycerol. Dou et al[106] for instance using Ni/Al_2O_3 catalyst system for the steam reforming of both pure and by-product glycerol reported glycerol conversion of 62-100 % depending upon reaction condition. They attributed the short fall in performance from crude glycerol to thermally resistant residue from decomposition of organic impurities which agrees with what Slinn et al[99] reported. Much earlier, Czernik et al[107] reported 70% H_2 yield (method of calculation not specified) from the use of commercial Ni in catalytic steam reforming of biomass liquid. They observed gradual increase in methane over time which they attributed to catalyst deactivation. Buffoni et al[108] observed and reported CO, CO_2, H_2 and CH_4 as the only gaseous product of glycerol steam reforming using Ni-based catalyst. They also found that 550 ^oC is the minimum temperature required to obtain hydrogen with high selectivity (see Eqn. 4A-1 of appendix 4). Cheng et al[109] reported that although surface of Ni/Al_2O_3 catalyst appears to have a net acidity, it is populated by combination of acidic and basic sites on which glycerol and steam undergoes associative and dissociative adsorption. Mechanism of glycerol steam reforming (GSR) over Ni/Al_2O_3 suggests that glycerol dissociatively adsorbs on the nickel site while water dissociatively adsorbs on the Al site forming hydroxide. Metal catalysed

dehydrogenation of glycerol results into formation of glycerol-based products which reacts with hydroxyl group from the support at metal/support interface to generate H_2 and oxides of carbon[34,109]. Despite successes recorded in the use of Ni-based catalyst system, some major setbacks such as deactivation due to carbon deposition and sintering or evaporation of nickel and possible phase transformation at high temperature operations were reported[104].

Metal oxides were used as promoters and alternative supports with the aim of stabilizing the nickel-based catalyst system. Noble metals such as Ru, Rh and Pt despite their prohibitive cost were also used as replacement for Nickel due to their activity and ability to tolerate carbon deposition. Iriondo et al[110] studied the influence of Ce, La, Mg and Zr as promoters to Ni/Al_2O_3 catalyst system and concluded that the promoters enhanced hydrogen production. The promoters modified the surface properties such as interaction of the nickel and support thereby enhancing the catalyst activity and selectivity (method of calculation not specified) towards H_2 and CO_2. While La and Ce enhanced thermal stability, Mg promoted surface nickel concentration and Zr stimulated steam activation. Adhikari et al[111] compared the influence of MgO, CeO_2 and TiO_2 as alternative supports to Ni-based catalyst and reported MgO and TiO_2 as the best supports at high temperature of 650 ^oC achieving 65.65 % and 62.29 % hydrogen selectivity (see Eqn. 4A-1 of appendix 4) respectively, while CeO_2 was found the best at lower temperature achieving a maximum hydrogen selectivity of 66.9% at 550 ^oC. Generally, MgO was the overall best of all with hydrogen yield of 56.5% (see Eqn. 4A-2 of appendix 4) equivalent to 4 moles of the 7 moles from the stoichiometric equation. In a related work by the same author, influence of reaction temperature, feed flow rate and water/glycerol ratio on glycerol conversion and hydrogen selectivity in steam reforming of glycerol using same catalyst i.e Ni/MgO, Ni/TiO_2 and Ni/CeO_2 was investigated. Ni/CeO_2 was adjudged the best achieving a maximum hydrogen selectivity of 74.7% (see Eqn. 4A-1 of appendix 4) and glycerol conversion of 99% at 600 ^oC and 12:1 water-glycerol molar ratio and feed flow rate of 0.5 ml/min. The robust performance of the Ni/CeO_2 was attributed to enhanced surface area and good metal dispersion[112].

Noble metals as promoters and replacement for nickel were also investigated. Adhikari et al[113] investigated fourteen catalyst systems involving Ru, Ir, Rh, Pd, Pt, Ce and Ni on ceramic monolith Al_2O_3 and SiO_2 as supports. In terms of H_2 selectivity and glycerol conversion, Ni/Al_2O_3 and $Ru/CeO_2/Al_2O_3$ were adjudged the best. Ni/Al_2O_3 recorded hydrogen selectivity of 80% (see Eqn. 4A-1 of appendix 4) which dropped to 71% in $Ru/CeO_2/Al_2O_3$ at 900 ^oC, 9:1 water/glycerol ratio and 15300 GHSV. The work also revealed that glycerol conversion and product composition was affected by catalyst loading and flow rates. Complete conversion of glycerol by steam reforming over Ru/Y_2O_3 and 90% hydrogen yield (method of calculation not specified) at 500-600 ^oC which increased up to 3% Ru loading was reported by Hirai et al[114]. Beyond 3% to 5% Ru loading, hydrogen yield was not affected. The reaction was carried out at 600 ^oC and steam-to-carbon ratio of 3:1. Zhang et al[115] compared the catalytic activity of some ceria supported transition metals (Ni and Co) and noble metal (Ir) catalysts in steam reforming of glycerine and ethanol. The noble metal Ir/CeO_2 had the best performance recording 100% glycerol conversion and hydrogen selectivity >85% (method of calculation not specified) at 400 ^oC which was attributed to combine influence of the active metal and support redox properties and also enhanced water-gas shift reaction. Despite the efficiency of noble metals in tolerating coking, at times steam reforming is marred by carbon deposition even with the help of promoters except where addition of oxygen helps in the gasification of carbon or use of high steam to carbon ratio to enhance water gas shift reaction[116].

Basic or acidic property of a support tends to influence or dictate the reaction pathways during glycerol steam reforming (GSR). Acidic surfaces such Al_2O_3, SiO_2 and ZrO_2 courses dehydration of glycerol which results in the formation of undesired products that could lead to carbon deposition and subsequent catalyst deactivation. Basic surfaces such as MgO, SrO on the other hand did not proved better. This was demonstrated in a work reported by Soares et al[117] in Steam reforming of glycerol over Pt catalyst supported on Al_2O_3, CeO_2/ZrO_2, C, ZrO_2 and MgO/ZrO_2. The work revealed that the most basic catalyst support MgO/ZrO_2 deactivated faster while the most acidic support Al_2O_3 exhibited some stability. The C-supported catalyst was the most stable. Several efforts were made to enhance such behaviour or tendency

through the use of promoters which have yielded promising results in many studies[29,34].

Perovskites despite their suitable properties such as good micro structures, ionic and electronic conductivity, existence of oxygen ion vacancies and their mobility in the lattice and defect chemistry, not a single work to the best of my knowledge has been reported on the use of those materials as catalyst in steam reforming of glycerol but were used with other feedstock and different fuel processing mode with a promising results[118,119]. Redox properties of perovskites is known to create defect which enhance their oxygen release and storage capacity that could promote water dissociation, methane oxidation or steam reforming, enhance water gas-shift reaction and carbon gasification. Therefore, perovskites properties could be tailored to provide promising result and address issues of durability and carbon deposition in glycerol steam reforming (GSR)[120].

2.5 The catalyst deactivation mechanisms

Catalyst deactivation results when a catalyst losses performance or activity on stream overtime. Deposition of carbonaceous substance on the surface, pores and voids of catalyst known as coking or poisoning by contaminant in the feedstock leading to low performance and subsequent catalyst deactivation has always been a major problem in steam reforming of hydrocarbon or oxygenated biomass feedstock. Other processes that lead to catalyst deactivation include thermal degradation or sintering and agglomeration of active phase of a catalyst during high temperature operation, masking of catalyst surface by hydrocarbon stuff thereby creating a barrier between the reactants and the catalyst active sites. Deactivation could also results due to structural transformation, loss of active phase by volatilisation, attrition and erosion[121,122]. It is important to note that these processes could be physical or chemical and they occur side by side with the main reactions. Consequences of catalyst deactivation can be serious and may cost industries billions of dollars per year due to process shutdown and catalyst replacement; therefore, understanding their nature will help in catalyst design that could help to minimize, ameliorate or hinder them.

2.5.1 Catalyst poisoning

Catalyst poisoning occurs when an impurity from the feedstock is chemisorbed at the active sites on the surface of a catalyst leading to its blockage or obstruction to the main reactants by means such as electronic effect, structural modification of the active site or formation of new species irreversibly. Catalyst poisoning could be uniform on the catalyst surface usually known as *non-selective* poison and the performance of the catalyst will depend on the amount of poison chemisorbed or could also be specific or *selective* only to some active sites. Poison could also be 'reversible' when it is weakly chemisorbed on the surface and could be regenerated by simple removal of the poison. Catalyst poisoning due to adsorption of H_2O molecule and COx species on the catalyst surface during ammonia synthesis for instance hinders nitrogen adsorption which could be regenerated by removal of those chemical species and reduction of the adsorbed oxygen. However, poisoning could lead to permanent changes which are 'irreversible'.

Table 2-4 Common poison of some industrial catalysts[121,122]

Catalyst	Process	Poison
Fe, Ru	Ammonia Synthesis	CO, H_2O, C_2H_2, S, O_2
Ni/Al_2O_3	Steam Reforming	H_2S, As, HCl
Cu	Methanol Synthesis, Low-T CO shift	H_2S, AsH_3, PH_3, HCl
SiO_2-Al_2O_3, Zeolite	Catalytic cracking	Organic bases, NH_3, Na, Heavy metals
Ni, Co, Fe	CO hydrogenation (Fisrscher-Tropsch synthesis)	H_2S, COS, As, HCl, metal carbonyls
V_2O_5	Oxidation	As
Pt, Pd	Automotive Catalytic Converters (Oxidation of CO and HC, NO reduction)	Pb, P , Zn, SO2, Fe
Hydrocracking	Noble Metals on zeolite	NH3, S, Se, Te, p
Ag	Methanol Oxidation to formaldehyde	Fe, carbonyl, Ni, C
Ag	Ethylene to ethylene oxide	C_2H_2
Transition metal oxides	Many	Pb, Hg, As, Zn

Poisoning may affects overall activity without affecting the selectivity of the catalyst depending on the nature of the catalyst. In Pt/Al_2O_3 catalyst system for instance, adsorption of basic nitrogen on the acidic Al_2O_3 could affect its cracking and isomerization catalysis but might not affect the tendency of the Pt to perform its dehydrogenation activity[121,122]. Table 2-4 above summarises common industrial poisons.

Metal oxides are more resistant to poisoning than the metal catalysts relatively. Acidic cracking catalyst could be poisoned by adsorption of basic chemical species on its surface. Metal catalyst are poisoned by adsorption via the orbitals of the surface atoms any chemical species in the reactant stream with right electronic structure such as unoccupied orbitals or unshared electron or multiple bonds[121]. Catalyst poisoning could be avoided by reducing the concentration of the poison from the feedstock prior to its use such as hydrodesulphurization to remove sulphur compounds. Furthermore, catalyst design incorporating chemical species that are resistant to poisoning and optimization of the catalyst properties such as surface area, pore size distribution, particle size, etc. and operating conditions could also help to mitigate poisoning.

2.5.2 The coking phenomenon (carbon deposition)

A primary issue in the use of hydrocarbons or oxygenated hydrocarbons like glycerol in steam reforming to generate syngas is the fouling of the catalyst surface or pores by physical deposition of carbon residues known as coking which might lead to catalyst loss of performance or deactivation. In severe case, it might lead to disintegration of catalyst particles[121,122]. Cracking, decomposition and reaction of biomass feedstock on the catalyst surface leave behind carbonaceous residue that block active site, pores and deactivate catalyst. Tars also deposit on the catalyst surface largely from polymerization and free radical cracking reactions of biomass feedstock in the gas phase which occurs away from the catalyst surface[123]. Because of good understanding of these phenomena, it is possible to map out region of carbon stability based on thermodynamic calculations in both reforming and gasification in an equilibrium phase diagram. Figure 2-6 below show in a CHO phase diagram that above the dashed line (the carbon deposition boundary), carbon residue exist in equilibrium with the gaseous products while below it carbon exist as CO, CO_2 and CH_4. Hydrocarbon fuels largely sit above the dashed line due to their low oxygen content and therefore require addition of chemical species such as H_2, air, O_2 and H_2O in order to avoid carbon formation at equilibrium and achieve complete gasification of carbon[19]. Interestingly, in the diagram, glycerol sits on the carbon boundary because its oxygen content balanced the number of carbon atoms in it and therefore may not need

addition of such chemical species to decompose it; hence glycerol is suitable for steam reforming and water-gas shift reaction to generate hydrogen or hydrogen rich gas.

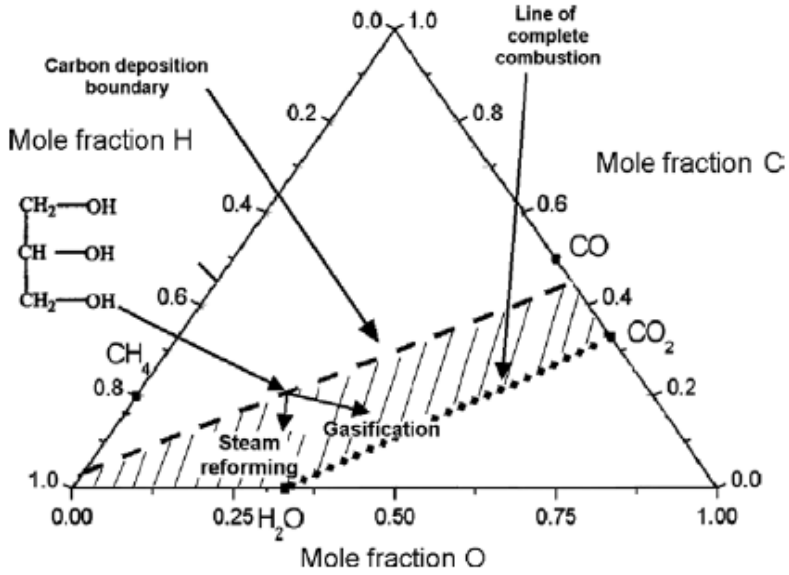

Figure 2-6 CHO phase diagram showing region of carbon stability[19]

The mechanism of carbon formation from feedstock decomposition product such as CO was reviewed by many workers[34,123,124]. Assuming CO dissociation to be the rate determining step, different forms of carbon was identified depending upon the feed stock, reaction condition and type of catalyst. It is important to note that structure, type, location and mechanism of formation of coke are important to catalyst deactivation than the quantity of coke deposited and they largely depends on the catalyst i.e metal or metal oxide catalyst bulk or supported[122,125].

Table 2-5 Types of carbon and their corresponding temperature of formation[122]

Structural type	Designation	Temperature of Formation (^{o}C)	Peak temperature (^{o}C) for reaction with H_2
Adsorbed, atomic (surface Carbide)	C_α	200-300	200
Polymeric, amorphous films or filaments	C_β	250-500	400
Vermicular filaments, fibres and/or whiskers	C_v	300-1000	400-600
Nickel Carbide (bulk)	C_γ	150-250	275
Graphitic (crystalline) platelets or film	C_c	500-550	550-850

With nickel based catalyst, atomic carbon (Cα), amorphous carbon (C_β), vermicular carbon (C_v), bulk Ni carbide (C_γ) and the graphitic carbon (C_c) were identified as illustrated in Table 2-5. Looking at the metal supported catalyst for instance; carbon is chemisorb forming a monolayer or a multiple layers by physical adsorption or may encapsulate metal particles or block reactant access to the pores of the catalyst and deactivate it. The mechanism of catalyst deactivation by carbon deposition is due to precipitation of dissolved carbon fibres deposited in Nickel surface layers to a certain depth in the bulk. It may accumulate at low or high temperature on the metal surface and deactivate the surface by blocking access to reactants. But at intermediate temperatures the precipitated carbon fibres form filament at the rear side of the metal particle which grow to separate the metal from the support. Filament growth might be sufficient enough to cause severe deactivation[122,126].

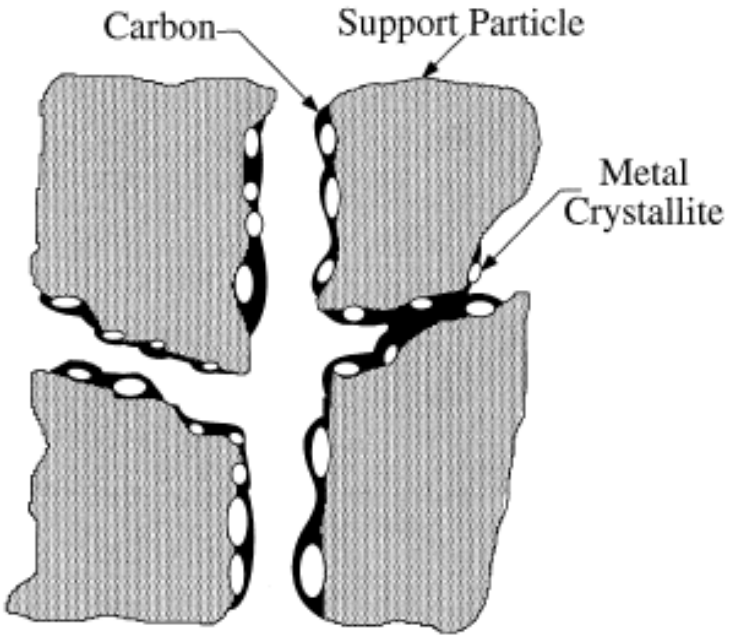

Figure 2-7 A modelled structure showing fouling of catalyst surface, pore blockage and crystallite encapsulations by the activities of carbon deposition[122]

Not all carbon deposition that results into deactivation, at low temperatures of 300-375 ^oC the carbon are polymeric while at high temperature <650 ^oC encapsulating graphitic carbon dominates the metal surface of methanation or steam reforming catalysts. Deactivation rate could depend on the rate of formation of coke and its gasification in some instances and is given by:

$$r_d = r_{cf} - r_{cg} \qquad \text{Eqn. 2-15}$$

Where r_d is rate of deactivation, r_{cf} is rate of coke formation and r_{cg} is the rate of coke gasification. If the rate of coke formation is balanced by the rate of gasification no coke formation occurs. The structural properties of catalyst such as metal type, crystallite size and use of support or promoters play an important role in the control of rate of carbon deposition. For instance addition of Pt to Co, Fe and Ni or addition of Cu to Ni might prevent them from being active towards the formation of filamentous carbon because Pt for instance has tendency to reduce dissolution and mobility of coke on its surface and Cu lower carbon formation in steam reforming[121,122]. Therefore such properties could be tailored in catalyst design to develop catalyst that is highly resistant to catalyst deactivation by carbon deposition.

2.5.3 Sintering

Sintering is physical structural deformation of catalyst particles especially during higher temperature operations (>500 ^{o}C). If not checked, sintering could results into stresses due to particle size growth, reduced surface area, disintegration and consequent loss of performance and catalyst deactivation. Sintering of metal catalyst particles which is both physical and chemical may occur in metal and metal oxides, bulk and supported catalysts. A theory developed to explain mechanism of sintering in metal supported catalyst suggests that sintering could be due to *atomic migration* or *crystallite migration*. At very high temperature, sintering might also occur due to vapour pressure[121,122]. In the atomic migration model, it is believed that detachment of atom from the lattice and its migration across the support and formation of a bigger crystallite from its collision with another crystallite is responsible for the sintering phenomenon as depicted in the model by 'A' of Figure 2-8. Since smaller particle always prefer to grow large due to the stability of the latter, the smaller particle tends to decline overtime. The crystallite migration model looked at sintering as results of binding together of two smaller crystallites to form a bigger one[121] perhaps due to the reason highlighted above as illustrated by 'B' in Figure 2-8.

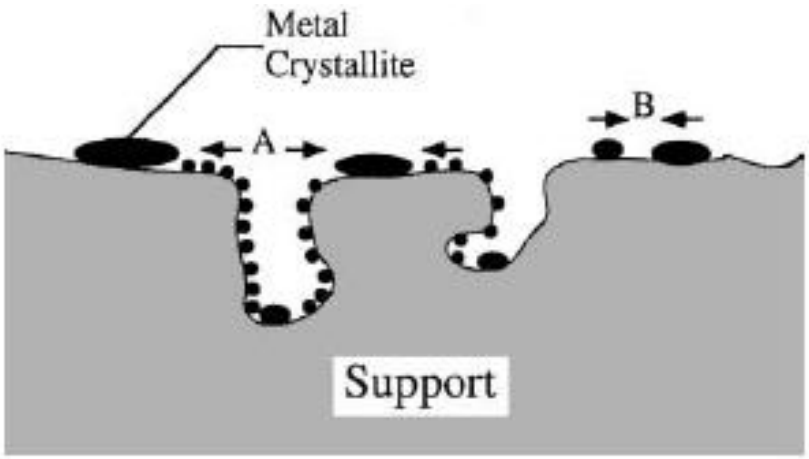

Figure 2-8 A model showing depicting particle growth by 'A' atomic migration and 'B' crystallite migration concepts[122]

However, how fast the above processes leads to sintering largely depends on how fast the detachment, migration, collision etc. occurs which in turn depends on the reaction conditions such as temperature and the environment or atmosphere. The strength of metal-support interaction and dispersion of metal particles on a support also influences the extent of sintering in a supported catalyst[122]. Metal catalysts weakly bound on support or crowded metal particles are more susceptible to sintering. Just like carbon deposition or coking, sintering in metals, metal oxides, bulk or supported catalysts could be minimised or completely hindered by tailoring some properties of the catalyst such as particle size and distribution, surface area, pore size, support surface, etc or incorporates some chemical species in the catalyst active phase or support system that are known to be robust, rugged and resistant to sintering. For instance, some additives such as Ca, Ce, Ba, C, O_2 are said to decrease metal mobility and F, Cl, Pb, Bi and S increase it and CeO_2 and La_2O_3 enhance metal-support interactions and thermal stability of Al_2O_3 > SiO_2. Surface defect in support or pores are known to obstruct metal mobility[121].

2.5.4 Structural transformation

In a severe case of sintering, crystallite particle fusion may results into complete transformation of the fused particles leading to the formation of new chemical species during high temperature operation which might not be catalytic. This might lead to reduced surface area and performance and subsequent deactivation of catalyst. The extent of the structural transformation defers from metal to metal or from metal

oxide to another metal oxide or type of support used. At high temperature (<900 ^{o}C) reaction of Ni with Al_2O_3 in Ni/Al_2O_3 catalyst system might lead to the formation of a spinel species $NiAl_2O_4$ which causes decrease in surface area, particle size growth and poor catalyst performance, or formation of Rh_2AlO_4 from Rh_2O_3/Al_2O_3 catalyst system used in car exhausts[121,127]. It is also observed that during high temperature operations, support such as γ-Al_2O_3 may undergo successive transformation from being amorphous with high surface area to a crystalline low surface area α-Al_2O_3. The successive products formed at different temperature as seen in Eqn. 2-16 possesses different properties, this could also affects performance and could lead to catalyst deactivation[128].

$$\gamma\text{-}Al_2O_3 \xrightarrow{900\ oC} \delta\text{-}Al_2O_3 \xrightarrow{1000\ oC} \theta\text{-}Al_2O_3 \xrightarrow{1200\ oC} \alpha\text{-}Al_2O_3 \qquad \text{Eqn. 2-16}$$

Other deactivation mechanism includes volatilisation or erosion of active phase during high temperature operations due to the active phase forming a volatile chemical species. For instance volatile $Cucl_2$ is formed from Cu where chlorine is available likewise volatile RuOx forms from Ru where oxygen is available[121]. All these could erode the active phase and subsequent catalyst deactivation. Masking of active site by some chemical species might also cause catalyst deactivation. Basic active site might be masked by acidic hydrocarbons which block the active site and pore preventing the main reactant from those sites which could lead to low performance and possible catalyst deactivation. Washing or burning could help get rid of those substances. Water could also have a negative effect on the systems when used in much quantity. At low temperature for instance, CH_4 is a major product through methanation reaction. The methanation reaction produces water (Eqn. 2-8 and 2-10) as described above and much dilution with water will shift the equilibrium reaction to the left favouring less methane production.

2.6 Research gaps and challenges

2.6.1 Research gaps and challenges in biodiesel production and catalyst development

It is evident that use of heterogeneous catalysts in transesterification for biodiesel production has potential in reducing the menace of corrosion and make the process environmental friendly. It also reduces downstream activities associated with the use of homogenous catalysts thereby increasing the quality of biodiesel produced. Research over time highlighted issues associated with the use of heterogeneous catalysts such as low activity at low temperature and use of high vegetable oil-methanol ratio, effect of water and high FFA in transesterfication of some oil and recycled oil. Others are low surface area, catalyst deactivation due poisoning of active site by adsorption of acidic hydrocarbons on the active sites and leaching of impregnated active phase. Those issues were addressed to certain level; however, there is still need for more to be done. There is need to develop catalysts that give good yield under mild reaction condition such as low temperature and methanol-oil ratio especially derivatives of CaO. Deactivation of catalyst due to leaching of active phase still persists. To the best of my knowledge, there has been little work addressing these problems especially leaching of active phase by way of incorporating the active phase directly into the lattice structure of the parent material as a single phase material rather than composites using impregnation.

2.6.2 Research gaps and challenges in glycerol steam reforming and catalyst development

From the review above is evident that glycerol steam reforming (GSR) has the potential to generate the much desired sustainable hydrogen for utilization in fuel cells. It also highlighted the role a catalyst could play in achieving such task of which the Ni-based catalysts are the most frequently used. A lot has been achieved in the development of efficient catalyst. Such catalysts were desired to be structurally stable and to resist, suppress or tolerate carbon deposition and gas poisoning in steam reforming of glycerol. However, structural stability to high temperature operations, carbon deposition and gas (sulphur) poisoning are still major issues to address. The

use of impregnation or assembly techniques offers only weak interaction between the active phase metal particles and support resulting in agglomeration, instability and deactivation, hence offers poor catalytic properties[128]. Alternatively metal catalyst particles grown from the bulk itself under redox influence, by redox lattice rearrangement or redox exsolution could provide enhanced structural properties and good catalytic behaviour[129].

In this work, nickel based oxides-supported metal catalysts prepared by the traditional wet impregnation will be compared to chromium-rich spinel oxide supported metal catalyst particles prepared for the first time by a new phenomenon called redox lattice rearrangement/reorganisation. Attempt would also be made to look at the influence of B-site substitution in a chromite-based perovskite with some transition metals and the exsolution of B-site metal particles, structural properties and catalytic behaviour in relation to steam reforming of glycerol. Correlation would also be made between defect chemistry, B-site metal particle exsolution and catalytic behaviour in an A-site deficient titanate perovskite for glycerol steam reforming.

References

1. Alexander, G. and Boyle, G. *introducing renewable, in renewable energy* (G. Boyle Ed), Oxford University Press, New York, NY (2004)

2. Ture, S.; Uzun, D. and Ture, I. E. The Potential use of sweet sorghum as non-pollution source of energy. *Energy* **22 (1)**, 17-19 (1997)

3. Mohan, D.; Pitmann Jr., C. U. and Steele, P. H. Pyrolysis of wood for bio oil: A critical review. *Energy and Fuel,* **20**, 848-889 (2006)

4. European Commission: Communication from the commission: Energy for the Future: Renewable sources of energy – white paper for community strategy and action plan, Brussels, 1997.

5. International Energy Agency: World energy outlook 2000, IEA, Paris 2000

6. Vasudevan, P.; Sharma, S.; Kumar, A. Liquid fuel from biomass: An Overview. *J.Sci.Ind.Res.* **64**, 822-31(2005)

7. Bridgwater, A. V. Renewable fuels and chemicals by thermal processing of biomass. *Chemical Engineering Journal*. **91**, 87-102 (2003)

8. Artigues, A.; Puy, N.; Febregas, E. and Batroli, J. Bio oil characterization to obtain a second generation biofuel and added-value products. *9th Green Chemistry Conference.* Alcala de Henanes – Spain, 2011

9. Dermirbas, A. Hydrogen rich gas from fruit shells via supercritical water extraction. *Int. J. Hydrogen Energy*. **29**, 316 – 21 (2004)

10. Bala, B. K. Studies on biodiesels from transformation of vegetable oils to diesel engines. *Energy Edu. Sci. Technol.* **15**,1-45 (2005)

11. Bart, J. C. J.; Palmeri, N. and Cavallaro, S. *Biodiesel science and technology: from soil to oil*. Woodhead pub. limited pg 1-49 (2010).

12. Sharma, Y. C. and Singh, B. Development of biodiesel: Current scenario. *Renewable and Sustainable Energy Reviews***, 13**, 1646 – 1651 (2009)

13. Da Conceino, L. R.; da Costa C. E. F.; da Rocha Filho, G. N. and Zamian, J. R. Obtaining and characterization of biodiesel from Jupati (Raphia taedigera mart) Oil. *Fuel*. **90**,9, 2945-2949 (2011)

14. Da Silva, J. P. V.; Sera, T. M. P.; Gossmann, M.; Worlf, C. R.; Meneghetti, M. R. and Meneghetti, S. M. P. *Moriger Oleifera Oil:* Studies of characterization and biodiesel Production. *Biomass and Bioenergy* **34**(10), 1527-1530 (2019).

15. De Oleiveira, J. S.; Leite, P. M.; de Souza, Z. B.; Mello,V. M.; Silva, E. C.; Rubin, J. C.; Meneghetti, S. M. P. and Suarez, P. A. Z. Characterization and composition of jatropha gossyphilia and jatropha caucas L. oil and application for biodiesel Production . *Biomass and Bioenergy*. **33**, 3, 449-453 (2009)

16. Demirbas, M. F. Biofuel from algae for sustainable development. *Applied Energy* **88**(10), 3473-3480 (2011)

17. Ali, Y.; Hanna, M. A. and Cuppett, S. L. Fuel properties of tallow and soya bean oil esters. *Journal of the American Oil Chemists Society* **72**(12), 1557-1564 (1995)

18. Schenk, P. M.; Thomas-Hall, S. R.; Stephens, E.; Marx, U. C.; Mussgnug , J. H.; Posten, C.; Kruse, O. and Hankamer, B. Second generation biofuels: High-efficiency microalgae for biodiesel production. *Bioenergy. Res*. **1**, 20–43 (2008)

19. Bart, J. C. J.; Palmeri, N. and Cavallaro, S. *Biodiesel science and technology: from soil to oil*. Woodhead pub. limited pg 1-49 (2010)

20. Slinn, M.; Kendall, K.; Mallon, C. and Andrews, J. Steam reforming of biodiesel by-product to make renewable hydrogen. *Bioresourse Technol*. **13**, 5851-5858 (2007)

21. Sivasamy, A.; Cheah, K. Y.; Fornasiero, P.; Kemausuor, F.; Zinoviev, S. and Miertus, S. Catalytic applications in the production of biodiesel from vegetable oils. *ChemSusChem* **2**, 278 – 300 (2009)

22. Shay, E. G. Diesel fuel from vegetable oils status and opportunities. *Biomass and Bioenergy* **4**(4), 227-242 (1993)

23. Demirbas, A. Biodiesel fuels from vegetable oils via catalytic and non-catalytic supercritical alcohol transesterifications and other methods: A survey. *Energy Conversion and Management* **44**, 2093–2109 (2003)

24. Bart, J. C. J.; Palmeri, N. and Cavallaro, S. *Biodiesel science and technology: from soil to oil*. Woodhead pub. limited pg 1-49 (2010)

25. Schlick, M. L.; Hanna, M. A. and Schinstock, J. L. Soybean and sunflower oil performance in a diesel engine. *Trans*. ASAE **31**, 1345 – 1349 (1998).

26. Mazed, M. A.; Summer, J. D. and Batchelder, D. J. Peanut, soybean and cottonseed oil as diesel fuel. *Trans. ASAE* **28**, 1375-1377 (1995).

27. Thomson, J. C. and He, B. B. Characterization of crude glycerol from biodiesel production from multiple feedstocks. *Applied Engineering in Agriculture* **22**(27), 261-265 (2006)

28. Gruerrero-Perez, M. O.; Rosas, J. M.; Badia, J.; Redriguez-Mirasol, J. and Cordero, T. Recent intervention in glycerol transformation and Processing. *Recent Patent in Chemical Engineering* **2**,11-21 (2009)

29. Valdye, P. D. and Rodrigues, A. E. Glycerol for hydrogen production; A review. *Chem Eng. Technol*. **32**(10), 1463 -1469 (2009)

30. Alhanash, A.; Kozhevnikova, E. F. and Kozhevnikov, I. V. Gas-Phase dehydration of glycerol to acrolein catalysed by caesium hetropoly salt. *Applied catalysis A: General* **378**, 11-18 (2010)

31. Ulgen, A. and Hoelderich, W. F. Conversion of glycerol to acrolein in the presence of WO_3/TiO_2 catalyst. *Applied catalysis A: General*, **400**, 34-38 (2011)

32. Adhikari, S.; Farnando, S. D. and Haryanto, A.: Hydrogen production from glycerol: An update. *Energy Conversion and Management* **50**, 2600-2604 (2009)

33. Lo Faro, M.; Minutoli, M.; Monforte, G.; Antomui, V. and Arico, A. S. Glycerol oxidation in solid oxide fuel cells based on Ni – perovskite electro catalyst. *Biomass and Bioenergy* **35**,3,1075-1084 (2011)

34. Lin, Y. Catalytic volarization of glycerol to hydrogen and syngas. *Int. j. hydrogen energy*. **38**, 2678-2700 (2013)

35. Quispe, C. A. G.; Coronado, C. J. R. and Carvalho Jr., J. R. Glycerol: Production, consumption, prices, characterization and new trends in combustion. *Renewable and Sustainable Energy Reviews*. **27**, 475–493 (2013)

36. Pagliaro, M. and Rossi, M. *The Future of glycerol: New uses of a versatile raw material*. RSC Green Chemistry Book Series, 1-18 (2008)

37. Kamonsuangkasem, K.; Therdthianwong, S. and Therdthianwong, A. Hydrogen production via oxidative steam reforming of biodiesel by-products over Ni/CeO_2-ZrO_2/Al_2O_3 catalyst. *International Conference on Chemistry and Chemical Process*. **10,** 107-113 (2011)

38. Grand view research inc. August, (2014) access on www.grandresearch.com

39. Fan, X. Burton, R. and Zhou, Y. Glycerol (by product of biodiesel production) as source for fuels and chemicals—mini review. *The Open Fuels & Energy Science Journal* **3**, 17–22 (2010)

40. Ziejewski, M. and Kuafman, K. R. Laboratory endurance test of a sunflower oil blend in a diesel engine*. J. Am. Oil Chem. Soc*. **60,** 1567 -1573 (1983).

41. Demirbas, A. Biodiesel production from vegetable oils via catalytic and non-catalytic supercritical methanol transesterification method. *Progress in Energy and Combustion Science.* **3**, 466-487 (2005)

42. Ma, F. and Hanna, M. A. Biodiesel Production: A Review. *Bioresource Technology*. **70**(1), 1-5 (1999)

43. Da Silva, C. and Oliveira, J. V. Biodiesel production through non-catalytic supercritical transesterification: Current state and perspectives *Brazilian Journal of Chemical Engineering* **31**(2), 271-285 (2014)

44. Dizge, N.; Aydiner, C.; Imer, D. Y.; Bayramoglu, M.; Tanriseven, A. and Keskinler, B. Biodiesel production from sunflower, soybean, and waste cooking oils by transesterification using lipase immobilized onto a novel microporous polymer, *Bioresource Technology* **100**, 1983–1991 (2009)

45. Clark, S. J.; Wagner, L.; Schrock, M. D.; Pinnar, P. G. Methyl ethyl esters as renewable fuels for diesel engine. *J.A.Oil Chem.Soc*. **61**, 1632 – 8 (1984)

46. Georgogianni, P. J.; Katsoulidis, A. K.; Pomonis, P. J.; Manos, G. and Kontomias, M. G. Transesterification of rapeseed oil for the production of biodiesel using homogeneous and heterogeneous catalysis. *Fuel Processing Technology*. **90** (7-8), 1016-1022 (2009)

47. Freedman, B.; Pride, E. H. and Mounts, T. L. Variable affecting the yields of fatty esters from transesterified vegetable oils. *JAOCS.* **61**,10, 1638-4 (1994)

48. Canakci, M. and Van Gerpen. J. Biodiesel production from oil and fats with high free fatty acids. *Transaction of the American Society of Agricultural Engineers*. **44**,6,1429-36 (1999)

49. Bechmans, H. J. and Hirata, S. Biodiesel production crude Jatropha curcus L. seed oil with high content of free fatty acid. *Bioresource Technology* **99**,6,1716-21 (2008)

50. Koh, M. Y. and Mohd Ghazi, T. I. A. Review of biodiesel production from jatropha curcus L. oil. *Renewable and Sustainable Energy Reviews* **15** (5), 2240-2251(2011)

51. Canakci, M. and Gerpen, J. V. Biodiesel production via acid-catalyst. *Trans. Autom. Sci. Eng*. **42**, 1203-1210 (1999)

52. Abreu, F. R.; Lima, D. G.; Hamu, E. A. Wolf, C. and Suarez, P. A. Z. Utilization of metal complexes as catalyst in the tranesterification of Brazilian vegetable oil with different alcohol. *Journal of molecular catalysis* **206**, 122, 29-33 (2004)

53. Puppan, D. Environmental evaluation of biofuels. *Periodica Polytechnica. Ser. Soc. Man Sci*. **10**,1, 95-116 (2002)

54. Zabeti, M.; Ashri, W. M. and Aroua, M. K. Activity of solid catalysts for biodiesel production: A review. *Fuel Processing Technology* **90**, 770-777 (2009)

55. Leung, D. Y. C.; Wu, X. and Leung, M. K. H. A Review on biodiesel production using catalysed transesterification. *Applied Energy* **87**, 1083- 1095 (2010)

56. Rafaat, A. A. Biodiesel production using solid metal oxide catalyst: A Review paper. *Int.J. Environ. Sci* . Tech. **8** (1) 203-221(2010)

57. Okwonkwo, M. U.; Galadima, A. and Leke, L. Advances in biodiesel Synthesis: From past to resent. *Applied Chemistry*. **3**, 6924-6945 (2012)

58. Hattori, H. Solid based catalyst: Generation of basic site and application to organic synthesis. *Applied catalysis A: General*. **222**, 247-259 (2001)

59. Suppes, G. J.; Bockwinkel, K.; Lucas, S.; Botts, J. B.; Mason, M. H. and J. A. Heppert, J. A. Calcium carbonate catalyzed alcoholysis of fats and oils. *JAOCS*, **78**, 2, 140-146 (200)

60. Bancquart, S.; Vanhove, C.; Pouilloux, Y. and Barralt, J. Glycerol transesterification with methyl stearate over solid base catalyst I: Relationship between activity and basicity. *Appl. Catal A. Gen*. **218**, 1-2, 1-11(2001)

61. Yan, S.; Lu, H. and Liang, B. Supported CaO catalysts used in the transesterification of rapeseed oil for the purpose of biodiesel production. *Energy and Fuels* **22**, 1, 646-651 (2008)

62. Boey, P.; Maniam, G. P. and Abd Hamid, S. Performance of calcium oxide as a heterogeneous catalyst in biodiesel production: A review. *Chemical Engineering Journal.* **168** 15–22 (2011)

63. Lee, D.; Park, Y. M. and Lee, K. Heterogeneous base catalyst for transesterification in biodiesel synthesis. *Catalysis Survey From Asia* **13**, 63–77 (2009)

64. Granados, M. L. ; Poves, M. D. Z.; Alonso, D. M.; Mariscal, R.; Galisteo, F.C.; Moreno-Tost, R.; Santamaría, J. and Fierro, J. L. G. Biodiesel from sunflower oil by using activated calcium oxide. *Applied Catalysis B: Environmental* **73**, 317–326, (2007)

65. Garcia, C. M.; Teixeira, S.; Marciniuk, L. L. and Schuchardt, U. Transesterification of soybean oil catalysed by sulphated zirconia. *Bioresource Technology.* **99**, 6608–6613 (2008)

66. Di Serio, M.; Tesser, R.; Pergmei, L. and Satacesaria, E. Heterogeneous catalyst for biodiesel Production. *Energy Fuel*. **22**, 1, 207-217 (2008)

67. Lotero, E.; Liu, Y.; Lopez, D. E.; Sawaanakarn, K.; Bruce, D. A. and Godwin Jr, J. G. Synthesis of biodiesel via acid catalysis. *Industrial and Engineering Chemical Research*. **44**, 14, 5353-5363 (2005)

68. Liang, X. Gao, S.; Wu, H. and Yang, J. Highly efficient procedure for the synthesis of biodiesel from soybean oil. *Fuel Processing Technology* **90**, 701–704 (2009)

69. Kawashima, A.; Matsubara, K. and Honda, K. Development of heterogeneous base catalyst for biodiesel production. *Bioresource Technology* **99**, 9, 3439-3443 (2008)

70. Wan Omar, W. N. N. and Amin, N. A. S. Biodiesel production from waste cooking oil over alkaline modified zirconia catalyst. *Fuel Processing Technology* **92**, 2397–2405 (2011)

71. Di Serio, M.; Tesser, R.; Casale, L. and D'Angelo. A.; Trifuoggi, M. and Santacesarria, E. Heterogeneous catalyst in biodiesel production : The influence of leaching. *Topics Catal.* **53**, 811–819 (2001)

72. de Caland, L. B.; Santos, L. S. S.; de Moura, C. V. R. and de Moura, E. M. Preparation and study of bimetallic compounds efficiency in the synthesis of biodiesel fuel. *Catal. Lett.* **128**, 392-400 (2009)

73. Kim, H. J., Kang, B. S.; Kim, M. J.; M. J.; Park, Y. M.; Kim, D. R.; Lee, J. S. and Lee, K. Y. Transesterification of biodiesel using heterogeneous base catalysts. *Catalysis Today*. **93**, 95, 315-320 (2004)

74. Macedo, C. C. S.; Abreu, F. R.; Tavares, A. P.; Alves. M. B.; Zara, L., Rubim J. C. Suarez, P. A. Z. New homogeneous metal oxides based catalyst for vegetable oil transesterification, *J. Baz. Chem. Soc.* **17**,1291-6 (2006)

75. Dias, J. M.; Alvim-Ferraz, M. C. M.; Almeida, M. F.; Díaz, J. D. M.; Polo, M. S. and Utrilla, J. S. Biodiesel production using calcium manganese oxide as catalyst and different raw materials. *Energy Conversion and Management* **65**, 647–653 (2013)

76. Leclercq, E.; Finiels, A. and Moreau, C., Transesterification of rapeseed oil in the presence of basic zeolites and related solid catalysts. *J. Am. Oil Chem. Soc.* **78**, 1161–1165 (2001)

77. Xie, W.; Huang, X. and Li, H. Soybean oil methyl esters preparation using NaX zeolites loaded with KOH as a heterogeneous catalyst. *Bioresource Technology* **98,** 936–939 (2007)

78. Kim, H. J.; Kang, B.; Kim, M.; Park, Y. M.; Kim, D.; Lee, J. and Lee, K. Y.; Transesterification of vegetable oil to biodiesel using heterogeneous base catalyst. *Catal. Today* **93–95**, 315–320 (2004)

79. Fathizadeh, M. and Aroujalian, A. Synthesis and characterization of nano particle crystals of NaX zeolite. *Int. J. Ind. Chem*. **2**, 3, 140-143 (2011)

80. Suppes, G. J.; Dasari, M .A.; Doskocil, E. J.; Mankidy, P. J. and Goff, M. J. Transesterification of soybean oil with zeolite and metal catalyst. *Applied catalysis A: General.* **257**, 213-223 (2004)

81. Zheng, Y.; Li, X. and Dutta, P. K. Exploitation of unique properties of zeolites in the development of gas *Sensors,* **12**, 5170-5194 doi:10.3390/s120405170 (2012)

82. Lo´pez, D. E. Goodwin Jr., J. G., Bruce, D. A. Lotero, E. Transesterification of triacetin with methanol on solid acid and base catalysts. *Applied Catalysis A: General*. **295**, 97-105 (2005)

83. Chung, C.; and Park, B. Esterification of oleic acid in soybean oil on zeolite catalyst with different activity. *Journal of Industrial and Engineering Chemistry* **15**, 3, 388-392 (2009)

84. Li, E. and Rudolph, V. Transesterification of vegetable oil to biodiesel over MgO-functionalised mesoporous catalysts. *Energy and Fuels* **22**, 145-149 (2008)

85. Albuquerque, M. C .G.; Jime'nez-Urbistondo, I.; Santamary a-Gonza'lez, J.; Me'rida-Robles, J. M.; Moreno-Tost, R.; Rodry'guez-Castello'n, E.; Jime'nez-Lo'pez, A.; Azevedo, D. C. S.; Cavalcante, Jr. C. L. and Maireles-Torres, P. CaO supported on mesoporous silica as basic catalyst for transesterification reactions. *Applied Catalysis A: General* **334**, 35-43 (2007)

86. Díez, V. K.; Apesteguía, C. and Cosimo, J. I. Effect of the chemical composition on the catalytic performance of MgyAlOx catalysts for alcohol elimination reactions. *J. Catal*. **215,** 220-223 (2003)

87. Tronto, J.; Bordonal, A. C.; Naal, Z. and Valim, J. B. Conducting Polymers / layered double hydroxides intercalated nano composites, *Materials Science - Advanced Topics*, DOI: 10.5772/54803 (2013)

88. Gao, L.; Xu, B.; Xiao, G. and Lv, J. Transesterification of palm oil with methanol to biodiesel over a KF/hydrotalcite solid catalyst. *Energy Fuels* 2008, **22**, 3531–3535

89. Wang, Y.; Zhang, F.; Xu, S.; Yang, L.; Li, D.; Evans, D. G.; and Duan, X., Preparation of macro spherical magnesia-rich magnesium aluminate spinel catalysts for methanolysis of soybean oil. *Chemical Engineering Science* **63**, 17, 4306-4312 (2008)

90. Cantrell, D. G.; Gillie, L. J.; Lee, A. F. and Wilson, K., Structure reactivity correlations in MgAl hydrotalcite catalysts for biodiesel synthesis, *Appl. Catal. A: Gen*. **287**, 183–190 **(2005)**

91. Shumaker, J. L.; Crofcheck, C.; Tackett, S. A.; Santillan-Jimenez, E.; Morgan, T.; Ji, Y.; Crocker, M. and Toops, T. J. Biodiesel synthesis using calcined layered double hydroxide catalysts. *Applied Catalysis B: Environmental*. **82,** 120-130 (2008)

92. Gao, L.; Teng, G.; Lv, J. and Xiao, G. Biodiesel synthesis catalysed by the KF/Ca-Mg-Al hydrotalcites base catalysts. *Energy Fuels*. **24**, 646–651 (2010)

93. Gelbard, G.; Brès, O.; Vargas, R. M.; Vieulfaure, F. and Schuchardt, U. 1H Nuclear magnetic resonance determination of the yield of the transesterification of rapeseed oil with methanol, *J. Am. Oil Chem. Soc*. **72**, 1239–1241 (1995)

94. Sercheli, R. Vargas, R. M. and Schuchardt, U. Alkylguanidine-catalyzed heterogeneous transesterification of soybean oil. *JAOCS*, **76**, 10 1207-1210 (1999)

95. Adhikari, S.; Fernando, S.; Gwaltney, S. R.; To, S. D. F.; Bricka, R. M.; Steele, P. H. and Haryanto, A.: A Thermodynamic analysis of hydrogen production by steam reforming of glycerol. *Int. j. Hydrogen Energy* **32**, 14, 2875-2880 (2007)

96. Dieuzeide, M. L. and Amadeo, N. Thermodynamic analysis of glycerol steam reforming *Chem. Eng. Technol.* **33**, 1, 89–96 (2010)

97. Da Silver, A. L. and Muller, I. L. Thermodynamic study on glycerol-fuelled intermediate temperature solid oxide fuel cell (IT-SOFC) with different electrolyte. *Int. J. hydrogen energy* **35**, 5580-5593 (2010)

98. Wang, W. Thermodynamic analysis of glycerol partial oxidation for hydrogen production. *Fuel Process Technol.* **91**, 1401-1408 (2010)

99. Slinn, M.; Kendall, K.; Mallon, C. Andrews, J. Steam reforming of biodiesel by-product to make renewable hydrogen. *Bioresourse Technol* **13**, 5851-5858 (2007)

100. Wang, X.; Li, S.; Wang, H.; Liu, B. and Ma, X. Thermodynamic Analysis of glycerine steam reforming *Energy and Fuels* **22,** 4285-4291 (2008)

101. Byrd. A. J.; Pant, K. K. and Gupta, R. B. Hydrogen production from glycerol by reforming in supercritical water over Ru/Al_2O_3 catalyst. *Fuel* **87**, 2956-2960 (2008)

102. Kersten, S. R. A.; Potic, B.; Prins, W. and Van Swaaiji, W. P. M. Gasification model compounds and wood in hot compressed water. *Ind Eng Chem Res* **45,** 4169-4177 (2006)

103. Gadhe, J. B.; Gupta, R. B. Hydrogen production by methanol reforming in supercritical water: Suppression of methane formation. *Ind Eng Chem Res* **44,** 4577-4588 (2005)

104. Sanchez, E. A. and Comelli, R. A. Hydrogen by glycerol steam reforming on a nickel–alumina catalyst: Deactivation processes and regeneration. *International Journal of Hydrogen Energy* **37**, 19, 14740-14746 (2012)

105. Niesz, K., Yang, P. and Somorjai, G. A. Sol-gel synthesis of ordered mesoporous alumina. *Chemcomm, Royal Society of Chemistry.* 1986-1987 (2005)

106. Dou, B.; Rickett, G. L.; Dupont, V.; Williams, P. T.; Chen, H. Ding, Y. and Ghadiri, M. Steam reforming of crude glycerol with in situ-CO_2 sorption. *Bioresour Tecnol*. **101**, 7, 2436-2446 (2010)

107. Czernik, S.; French, R.; Feik, C. and Chornet, E. Hydrogen by catalytic steam reforming of liquid by-products from biomass thermo-conversion processes. *Ind Eng Chem Res***. 41**, 4209-4215 (2002)

108. Buffoni, I. N.; Pompeo, F.; Santori, G. F. and Nichio, N. N. Nickel catalysts applied in steam reforming of glycerol for hydrogen production. *Catalysis Communications* **10** 1656–1660 (2009)

109. Cheng, C. K.; Foo, S. Y. and Adesina, A. A. Steam reforming of glycerol over Ni/Al_2O_3. *Catalysis Today* **178**, 25-33 (2011)

110. Iriondo, A.; Barrio, V. L.; Cambra, J. F.; Arias, P. L.; Gu¨emez, M. B.; Navarro, R. M.; Sa´nchez-Sa´nchez , M. C. and Fierro,J. L. G. Hydrogen production from glycerol

over nickel catalysts supported on Al_2O_3 modified by Mg, Zr, Ce or La. *Top Catal.* **49**, 46–58 (2008)

111. Adhikari, S. Fernado, D. and Haryanto, A. Hydrogen production from glycerine by steam reforming over nickel catalysts. *Renewable energy* **33**, 5, 1097-1100 (2008)

112. Adhikari, S. Fernado, D. Filip To, S. D. Bricka, R. M. Steele, P. H. and Haryanto, A. Conversion of glycerol to hydrogen via steam reforming process over nickel catalysts. *Energy and Fuels* **22**, 1220-1226 (2008)

113. Adhikari, S.; Fernando, S. and Haryanto, A. Production of hydrogen by steam reforming of glycerine over alumina-supported metal catalysts *Catalysis Today* **129,** 355–364 (2007)

114. Hirai, T.; Ikenaga, N. O.; Miyake, T. and Suzuki, T. Production of hydrogen by steam reforming of glycerine on ruthenium catalyst*. Energy and Fuel*. **19**, 1761-1762 (2005)

115. Zhang, B.; Tang, X.; Li, Y.; Xu, Y. and Shen, W. Hydrogen production from steam reforming of ethanol and glycerol over ceria-supported metal catalysts. *International Journal of Hydrogen Energy* **32**, 2367 – 2373 (2007)

116. Swami, S. M. and Abraham, M. A. Integrated catalytic process for conversion of biomass to hydrogen. *Energy Fuel* **20**, 2616-2622 (2006)

117. Soares, R.R. Simonetti, D.A. and Dumesic, J.A. Glycerol as a source for fuels and chemicals by low-temperature catalytic processing*. Angew. Chem. Int*. Ed. **45**, 3982 – 3985 (2006)

118. Li, C-L. and Lin Y-C. Methanol partial oxidation over palladium-, platinum- and rhodium-integrated $LaMnO_3$ perovskites. *Appl Catal B.* **107**, 284-293 (2011)

119. Li, C-L.; Wang, C-L. and Lin, Y-C. Pd-integrated lanthanum transition metal perovskites for methanol partial oxidation. *Catal Today* **174**, 135-140 (2011)

120. Royer, S.; Duprez, D.; Can, F.; Courtois, X.; Batiot-Dupeyrat, C.; Laassiri, S. and Alamdar, H. Perovskites as substitutes of noble metals for heterogeneous catalysis: Dream or reality. *ACS Chem. Rev*. **114**, 10292-10368 (2014)

121. Forzatti, P. and Lienti, L. Catalyst deactivation. *Catalysis Today* **52**, 165-181 (1999)

122. Bartholomew, C. H. Mechanism of catalyst deactivation. *Applied Catalysis A: General* **212**, 17-60 (2001)

123. Cheng, C. K.; Foo, S. Y.; and Adesina, A. A. Carbon deposition on bimetallic Co–Ni/Al_2O_3 catalyst during steam reforming of glycerol. *Catalysis Today* **164** 268–274 (2011)

124. Pompeo, F.; Santori, G. F. and Nichio, N. N. Hydrogen production by glycerol steam reforming with Pt/SiO_2 and Ni/SiO_2 Catalysts. *Catalysis Today* **172**, 183-188 (2011)

125. Menon-, P.G. Coke on catalyst- harmful, harmless, invisible and beneficial types. *J. Mol. Catal.* **59**, 207-220 (1990)

126. Rostrup-Nielsen, J. Mechanism of carbon formation on Ni-containing catalysts. *J. Catal*. **48**, 1-3, 155-165 (1977)

127. Kim, Y.; Kim, P.; Kim, C. and Yi, J. A novel method for synthesis of a Ni/Al_2O_3 catalyst with a mesoporous structure using stearic acid salts. *J. Mater. Chem.* **13**, 2353–2358 (2003).

128. Perego, C. and Villa, P. Chapter 3 Catalyst preparation methods. *Catalysis Today* **34**, 281–305 (1997)

129. Neagu, D.; Tsekouras, G.; Miller, D. N.; Me´nard, H. and Irvine, J. T. S. In situ growth of nanoparticles through control of non-stoichiometry. *Nature Chemistry* **5,** 916-923 (2013)

3.0 EXPERIMENTALS

3.1 Reagents used

S/No	Name	Chemical formulae	% Purity	Manufacturer
1	Aluminium Oxide	γ-Al_2O_3	99.97	Alfer Aesar
2	Lanthanum Oxide	La_2O_3	99.99	π-Pi-KEM
3	Cerium (IV) Oxide	CeO_2	99.90	ACROS
4	Samarium Oxide	Sm_2O_3	99.99	Alfa Aesar
5	Strontium Carbonate	$SrCO_3$	99.90	Alfa Aesar
6	Calcium Carbonate	$CaCO_3$	99.50	Alfa Aesar
7	Titanium (IV) Oxide	TiO_2	99.60	Alfa Aesar
8	Aluminium Nitrate Nonahydrate	$Al(NO_3)_3.9H_2O$	98.00	Sigma-Aldrich
9	Calcium Nitrate Tetrahydrate	$Ca(NO_3)_2.4H_2O$	99.00	Sigma-Aldrich
10	Magnesium Nitrate Hexahydrate	$Mg(NO_3)_2.6H_2O$	99.00	Sigma-Aldrich
11	Strontium Nitrate Hexahydrate	$Sr(NO_3)_2.6H_2O$	99.00	Sigma-Aldrich
12	Nickel (II) Nitrate Hexahydrate	Ni $(NO_3)_2.6H_2O$	99.00	ACROS
13	Cerium Nitrate Hexahydrate	$Ce(NO_3)_3.6H_2O$	99.00	Aldrich
14	Iron (III) Nitrate Nonahydrate	$Fe(NO_3)_3.9H_2O$	98.0	Alfa Aesar
15	Cobalt (II) nitrate Hexahydrate	$Co(NO_3)_2.6H_2O$	98.0	Sigma-Aldrich
16	Chromium (III) Nitrate Nonahydrate	$Cr(NO_3)_3.9H_2O$	99.0	Sigma-Aldrich
17	Lanthanum (III) Nitrate Hexahydrate	$La(NO_3)_3.6H_2O$	99.90	Alfa-Aesar
18		$Sr(NO_3)_2$	99.90	Alfa-Aesar
19	Manganese (II) Nitrate Tetrahydrate	$Mn(NO_3)_2.4H_2O$	99.98	Alfa-Aesar
20	Zinc Nitrate Hexahydrate	$Zn(NO_3)_2.6H_2O$	98.00	Sigma-Aldrich
21	Zirconyl Chloride Octahydrate	$ZrOCl_2 \cdot 8H_2O$	98.00	Sigma-Aldrich
22	Citric Acid	$C_6H_8O_7.H_2O$	99.60	Fisher Sci.
23	Ethylene glycol	$C_2H_6O_2$	99.00	Fisher Sci.
24	Amberlyst-A26	OH^- Form	-	Aldrich
25	Amberlyst-36	H^+ Form	-	Aldrich
26	Poly(Ethylene glycol)-block-Pol(propylene glycol)-block-Poly(ethylene glycol) (P-123)	$(C_3H_6O.C_2H_4O)X$	-	Aldrich
27	Hypermer KD-1 Dispersant (polyester/polyamide copolymer)	-	-	Richard E. Mistler
28	Sodium Hydroxide	NaOH	97.00	Fisher Sci.
29	Sulphuric Acid	H_2SO_4	95.00	Fisher Sci.
30	Nitric Acid	HNO_3	70.00	Fisher Sci.
31	Ammonium Hydroxide	NH_4OH	35.00	Fisher Sci.
32	Deuterated Chloroform	$CDCl_3$	99.80 atom D	Aldrich
35	Methanol	CH_3OH	99.70	Sigma-Aldrich

3.2 Catalyst preparation and processing

3.2.1 The solid state synthesis

A modified solid state synthesis which involves the use of oxides; carbonate and nitrates of some metals instead of oxides or carbonates only was used in the synthesis of some titinate perovskite[1]. The oxides and carbonate were pre dried at 300-800 ^{o}C at heating/cooling ramp rate of 5^{o}/min for 2-3 hrs in air atmosphere depending upon the compound and weighed hot at 300 ^{o}C. Stoichiometric oxides (such as La_2O_3, CeO_2,) or carbonates (such as $SrCO_3$, $CaCO_3$) and nitrates (such as $(Ni(NO_3)_2.6H_2O$, $Fe(NO_3)_3.9H_2O$, $Co(NO_3)_2.6H_2O$, $Cr(NO_3)_3.9H_2O$) of the active components were carefully weighed into a beaker. An amount (~0.05 wt.% amount) of polymeric Hypermer KD-1(polyester/polyamide copolymer) dispersant based on the total weight of the sample was added to aid dispersion of the active component and to avoid agglomeration. Using an ultrasonic probe, the mixture was elaborately but carefully homogenised in little acetone (~0.1 wt.%). The mixing obtained from the ultrasonic probe results in the eventual formation of fine particle powder and was a lot better than hand mixing using agate mortar and pestle. The homogenised solution was then stirred continuously until dried. The fine powder was then transferred to alumina crucible quantitatively and calcined in furnace at 1000 ^{o}C and heating ramp rate of 5^{o}/min and dwelled for 12 hours to decompose the carbonate and remove moisture and to trigger the nucleation that would later lead to the formation of pure phase perovskites. The sample was then homogenised using a planetary ball miller at the speed of 300 rph for 1.5 hr hours in acetone. After the ball milling the samples were dried pelletised to a spherical shape of about 2 mm thick using a pellet press at 2 bar pressure and calcined at temperatures of 1350-1430 ^{o}C and heating ramp rate of 5^{o}/min depending on the material for 12 hours in air atmosphere then ground to fine powder after cooling with agate mortar and pestle.

3.2.2 The sol-gel method

The tricalcium aluminate ($Ca_3Al_2O_6$) catalyst for biodiesel synthesis was prepared by sol-gel synthesis using citric acid as chelating agent and organic fuel. Basically this method restricts diffusion and segregation of the chemical species involved in the

synthesis by holding them together in a homogenized gel. The initial solution containing the active components and citric acid is usually transformed to gel by continuous heating and evaporation to dryness and later heated more rapidly to decompose it to the desired oxides[2].

In this work, desired stoichiometric amount of $Ca(NO_3)_2.4H_2O$, $Al(NO_3)_3.9H_2O$ and $C_6H_8O_7$ (citric acid) were dissolved and homogenised in a beaker at 100 ^oC until gel was formed. The temperature was then increased to 130 ^oC until the gel dried and transformed to a cake-like material. The material was transferred to oven at 80 ^oC and allowed to dry further. The dried sample was crushed with agate mortar and pestle and heated in a furnace to 900 ^oC at ramp heating rate of 1^o/min for 12 hours. It was ground and homogenised to a fine powder with agate mortar and pestle, pelletised and heated again at 1350 ^oC at ramp heating rate of 5^o/min for 18 hours. All the samples were rapidly quenched to room temperature by removing them from the furnace in alumina boat at 1350 ^oC and kept outside by the furnace. The samples were then ground to fine powder after cooling. In the case of $Ca_3Al_{2-x}M_xO_6$ (where M= Mg, Sr and Zn), $Mg(NO_3)_2.6H_2O$, $Sr(NO_3)_2.6H_2O$ and $Zn(NO_3)_2.6H_2O$ were added alongside $Ca(NO_3)_2.4H_2O$ and $Al(NO_3)_3.9H_2O$ and $C_6H_8O_7$ (citric acid) and homogenised to form gel. All other processes were the same.

The catalyst $Ca_3Al_2O_6$ powder was pelletised and arranged in alumina boat. Hydration was done at different temperature of 900-1200 ^oC at heating/cooling ramp rate of 5^o/min for 5 hours by passing argon through a water bubbler into the tubular furnace containing the samples.

3.2.3 The combustion method

Basically, this method involves gelling of the active components using organic polymers as complexing or gelling agents. The pecchini method utilizes polymeric precursor citric acid (CA) and poly ethylene glycol (EG) as chelating agent and organic fuel respectively. Other complexing/chelating agent that could possibly be used are urea ($CO(NH_2)_2$ and glycine $(NH_2CH_2COOH)_3$. They help in complexing, gelling and homogenising of the metal cation in the solution by forming a CA-EG-metal ion polymer chain to avoid segregation or crystallization of the metal nitrates during

evaporation of solvent. The burning behaviour of the dried sample largely depends on the ratio of the organic fuel (EG) or reductant used to the metal cation or oxidizer (NO_3) and usually a high ratio is favourable. At the right temperature the system auto-ignites forming a fluffy mass which results in the formation of fine particles and large surface area.

In this work, the catalyst systems $La_{0.75}Sr_{0.25}Cr_{0.5}Mn_{0.5}O_{3-\delta}$ (LSCM), $La_{0.75}Sr_{0.25}Cr_{0.5}Fe_{0.}5O_{3-\delta}$ (LSCF) and $La_{0.75}Sr_{0.25}Cr_{0.5}Co_{0.5}O_{3-\delta}$ (LSCC) were all prepared by the combustion method using nitrates of the metals, ethylene glycol and citric acid as organic fuel and complexing agents respectively. The nitrates solution of the metals were prepared separately in deionised water and each transferred to an already homogenised ethylene glycol and citric acid and stirred overnight at 100 ^{o}C. Temperature was increased gradually until the thick gel dries up and allowed to burn to ash. The ash was then transferred to a furnace and fired to 1100 ^{o}C at 1 ^{o}C/min and dwelled at that temperature for 7 hours. The samples were ground to fine powder and kept for further analysis. The metal ion-CA-EG ratio of 1:4:16 was adopted in the synthesis.

The nickel impregnation into the pre-reacted LSCM, LSCF and LSCC was done by adding the pre-reacted oxide supports (LSCM, LSCF and LSCC) into 5% nickel nitrate solution and stirred vigorously for several hours and dried at 80 ^{o}C on hot plate. The powders were homogenised and calcined at 1100 ^{o}C for 7 hours.

3.2.4 The wet impregnation

The supported nickel catalysts were prepared by wet impregnation which involves interaction of a solid (support) with a solution containing the chemical species (active components) to be deposited on its surface. The deposition leads to selective adsorption of those chemical species by Van der Waals, hydrogen or columbic forces. In this method, volume of solvent beyond what the material requires to look wet is used. The metal-support interaction in this method is usually week and a time, the particles deposited is greater than the number of adsorption site on the support surface[2].

In this work, the Ni/γ-Al_2O_3 catalyst system was prepared from commercial γ-Al_2O_3 powder and Ni $(NO_3)_2.6H_2O$ precursors of good purity. The γ-Al_2O_3 powder was first degassed at 700 ^oC at the heating ramp rate of 5^oC/min for 5 hours to remove adsorbed moisture and gases. The degassed powder was weighed to get the required amount and gradually added to aqueous solution containing the desired amount of Ni $(NO_3)_2.6H_2O$ to give the required catalyst loading at 60 ^oC under stirring. The stirring continued for 5 hours and dried at 80 ^oC on hot plate and further dried overnight at 80 ^oC in oven. The samples were ground and homogenised to powder and then air calcined at different temperatures of 500-1000 ^oC for 5 hour. After cooling, the powder was ground to fine powder and kept for further tests and analysis.

The Ni-LSCM/Al_2O_3 and Ni-CeO_2/Al_2O_3 catalyst systems were prepared in same manner except that pre reacted LSCM (lanthanum strontium chromium manganese-$La_{0.75}Sr_{0.25}Cr_{0.5}Mn_{0.5}O_{3\pm\delta}$) from combustion synthesis (as described above) and $Ce(NO_3)_3.6H_2O$ respectively were added along with the Ni $(NO_3)_2.6H_2O$ solution and subsequent treatments were same as described above in this section.

The Ni-LSCM/Ce-Zr was also prepared as in above by depositing both Ni and LSCM on pre reacted Ce-Zr ($Ce_{0.75}Zr_{0.25}O_2$) support. The mesoporous $Ce_{1-x}Zr_xO_2$ (X=0.25, 0.5 and 0.75) support was prepared by evaporation induced self-assembly (EISA) using a template as a pore former to optimize doping and surface area for better properties and catalytic performance. Pore former P123 was dissolved in the required volume of ethanol and then stoichiometric amount of $Ce(NO_3)_3{\cdot}6H_2O$ and $ZrOCl_2{\cdot}8H_2O$ were added and stirred vigorously at room temperature for 2 hrs. The sol-gel was allowed to evaporate slowly at 60 ^oC and later calcined at 400 ^oC at 1 ^oC/min for 4 hours to remove the organic template[4].

In the case of Ni-LSCM/SDC catalyst system, samarium doped ceria (SDC- $Sm_{0.2}Ce_{0.8}O_{2-\delta}$) support was prepared by co-precipitation method. Stoichiometric amount of Sm_2O_3 was dissolved in suitable quantity of nitric acid and then allowed to near-dryness at 80 ^oC and then dissolved in deionised water. Solution of $Ce(NO_3)_3{\cdot}6H_2O$ was also prepared in deionised water separately containing stoichiometric amount. The two solutions were mixed homogenised then NH_4OH was used to raise the pH to around 9-10 at which point the product precipitated out. The precipitate was allowed to settle,

filtered and dried in the oven at 80 ^{o}C for several days. The dried powder was calcined at 800 ^{o}C for 7 hours and was then ground to fine powder and kept for further use and analysis. The Ni-LSCM/SDC catalyst system was prepared by gradual addition of the samarium doped ceria (SCD- $Sm_{0.2}Ce_{0.8}O_{2-\delta}$) support and pre reacted LSCM into the nickel nitrate solution and all other processes were the same for stirring and drying as described above in this section.

3.2.5 Catalyst reduction for exsolution

The nickel containing perovskites prepared by solid state and combustion method and the spinels were reduced for nickel exsolution under controlled atmosphere in tubular furnace and in TORVAC. The controlled atmosphere furnace reduction consists of a Lenton furnace and a dense alumina tube fitted with gas-tight connections at both ends. In this case the samples are pelleted to circular pellets of about 2mm thick using pellet press at 2 bar pressure and placed in an alumina boat and inserted to the centre of the tube in the furnace. The setup allows controlling the flow rates and selection between 5% H_2/Ar gas and pure H_2. For safety, heating and cooling up to and down from 650 °C is always performed in 5%H_2/Ar. The reduction was done at 900 ^{o}C for 30 hours. The TORVAC furnace employs tungsten elements for heating and generating a strongly reducing environment. The samples were placed on yttria-stabilised zirconia pellets individually supported on carbon paper shelves and stacked in a carbon crucible. The furnace was operated at pressure values of 2 - $5\cdot10^{-2}$ mbar (“vacuum”) or under 0.1-0.2 bar of 5%H_2/Ar to achieve different reducing conditions. Different reduction temperatures of 900-1200 ^{o}C were used for 1-2 hrs. Molecular sieves were deployed in the cold zones of the furnace as water traps to help maintain a stable vacuum and ensure a low p_{O_2} is achieved[5,6].

3.2.6 The ion-exchange resins activation

Ion exchange resins have a micro porous polymeric structure commonly made from styrene, polyvinyl benzene monomers with suitable surface area and acidic (sulphonic) or basic (hydroxyl) groups which could provide Bronsted acid or Lewis base surfaces for transesterification of vegetable oil to biodiesel without leaching tendency. Ion-exchange resins owe their catalytic properties to their ability to swell thereby making their active sites accessible to reactants[7].

In this work, commercial Amberlyst-A26 was ion exchanged in 1M NaOH while Amberlyst-36 was ion exchanged in 1M H_2SO_4 overnight to get them activated. Physically adsorbed NaOH and H_2SO_4 were washed off using methanol and filtered.

3.3 Catalyst characterization

3.3.1 Surface area, pore size and pore volume determination

The BET surface area determination depends on the concept that physical solid adsorption and desorption of gases increase with decreasing temperature and increasing pressure. Therefore absorbing gas is admitted onto the samples continuously at different concentration or volume at constant temperature, the pressure due to the accumulated gas is measured and a plot of quantity of gas adsorbed against partial pressure at a particular temperature at equilibrium gives the so-called adsorption isotherm which describes much about the surface and structure of absorbing material[8]. The gas adsorption occurs on the surfaces of the adsorbent and pores usually from monolayer to multilayer adsorption. The BET surface area is mostly based on the physical adsorption of inert gas nitrogen at 77.35 K while pore size and volume is based on capillary condensation of the gas resulting in filling of the pores which depends on the nature of the pores. Two theories are prominent in surface area calculation, the Langmuir theory which assumed that the adsorption is physical; no interaction between layers, collision between the molecules is elastic and that only a monolayer adsorption occurs. The Branuer-Emmet-Teller (BET) is an extension of Langmuir theory incorporating the multilayer adsorption. Langmuir calculated the surface area by relating it to the amount or volume of gas adsorbed by adsorbent (test sample) and the mass of the adsorbent[8]. Thus:

$$S = \frac{V_m \sigma N}{m V_G} \qquad \text{Eqn. 3-1}$$

Where:

S = specific surface area ($m^2\ g_{cat}^{-1}$)

V_m = volume of gas adsorbed by surface covered by monolayer

σ = area occupied by single gas molecule adsorbed

N = Avogadro's constant

m = mass of the adsorbent (test sample)

V_G = molar gas volume constant

In contrast, the BET theory calculates surface area based on multilayer physisorption by relating the volume of gas adsorbed physically to the area of the adsorbent, thus:

$$\frac{P}{V\,(Po-P)} = \frac{1}{CV_m} + \frac{(C-1)P}{CV_mPo} \qquad \text{Eqn. 3-2}$$

P = gas pressure

Po = saturation pressure of the gas

V = volume of the gas adsorbed at pressure p

C = constant characteristic of the adsorbent

V_m = volume of gas adsorbed at S.T.P by surface covered by monolayer

A plot of P/V(Po-P) vs P/Po gives straight line with intercept $1/CV_m$ and slope as $C-1/CV_m$. From the straight line plot Values of C and Vm can then be calculated, hence the surface area of the sample can be determined thus:

$$S_a = \frac{V_m\, a_m\, N}{m \times 22400} \qquad \text{Eqn. 3-3}$$

S_a = specific surface area

a = cross sectional area of the adsorbate molecule in square meter (0.162 nm^2 for nitrogen).

m = mass of the test powder in grams

22400 = volume occupied by 1 mole of the adsorbate gas S.T.P.

Vm and N as defined above.

Total volume of the pour is related to the amount of vapour adsorbed at relative pressure approximately equal unity at which point the pores are completely filled with nitrogen. Volume of liquid adsorbed $V_{liq.}$ is given by:

$$V_{liq.} = \frac{V_{ads}\, V_m\, p}{RT} \qquad \text{Eqn. 3-4}$$

The pour size is estimated from pore volume assuming cylindrical pore geometry, thus:

$$r_p = \frac{2V_{liq.}}{S_a}$$ Eqn. 3-5

Samples are usually heated to certain temperature before measurement to get rid of adsorbed atmospheric gases or moisture on the material then the system is purged with nitrogen or helium as non-absorbing gases.

In this work, Micromeritcs TriStar II 3020 model was used in the determination of Brunauer-Emmett-Teller (BET) surface area, Barret-Joyner-Halenda (BJH) pore volume and size using nitrogen adsorption/desorption at 77.35K. Required amount of each sample was put into a quartz sample tube and heated to 120 ^{o}C for 2-3 hours under vacuum to remove adsorbed moisture and atmospheric gases before the analysis. Then the sample was transferred to the main instrument for the surface area analysis. The temperature was reduced to liquid nitrogen boiling point (77.35 K) so that the gas vapour absorbs. The isotherm was obtained by injecting series of known volumes of nitrogen into the sample at constant temperature and measuring the pressure due to it at equilibrium. The pressure was lowered and the nitrogen desorption was taken for the desorption isotherm.

3.3.2 X-Ray diffraction (XRD)

The XRD is an analytical tool used for the identification of phase purity of materials such as single-phase and multiple-phase in microcrystalline mixtures, structural identification and unit cell calculations, crystallite shape and size determination from analysis of peak broadening and many more. Basically, little amount of randomly arranged sample with no preferred orientation is ideal for XRD analysis. Conceptually, XRD is based on the fact that atomic arrangement of atoms or crystals is assumed to exist in layers or planes, X-ray incident on these layers are reflected off the plane giving rise to diffraction pattern depending on weather interference was constructive or destructive. Each substance has a peculiar arrangement of these layers hence give characteristic diffraction pattern which serves as finger print for the identification or characterization of materials. Commonly, Cu is used for inorganic materials as a source coherent monochromatic X-rays by striking it with high-energy electrons in a sealed vacuum tube. Different X-rays are generated but the strongest Cu radiations are Kα, $K\alpha_2$ and Kβ of which Kα is used with a wavelength of approximately 1.54 Å and others

removed or filtered[9]. Other anode materials used as source of X-ray radiation includes Cr (Kα 2.29 Å), Fe (Kα 1.94 Å), Co (Kα 1.79 Å) and Mo (Kα 0.71 Å).

The distance between the planes 'd' and incidence angle 'θ' are related in an equation known as the Bragg's equation. Note that one of the incident rays has to travel extra distance called path distance 'Δ' before coming in phase with the first one thus Δ= dsinθ. Combining incident and reflected rays we have 2Δ = nλ and therefore, 2dsinθ = nλ thus:

$$n\lambda = 2d\sin\theta \quad \text{(Bragg's Equation)} \qquad \text{Eqn. 3-6}$$

Where n is an integer i.e. 1, 2, 3, 4…., λ is the wavelength of the X-ray, d = interplanar spacing producing the X-ray diffraction and θ is the angle of diffraction.

In this work, Crystallographic studies were carried out on the samples by room temperature powder diffraction technique using Pan-Analytical Empyrean X-Ray Diffractormeter operating in reflection mode using Cu-$K\alpha_1$ radiation at λ = 1.5406 Å. Each fine ground sample was filled in the sample holder and levelled which was then placed in multiple sample holders before it was introduced into the machine. Diffraction angle 2θ was taken in the range of 10-90 for 1hour. The crystallographic data obtained was refined and analysed using STOE WinXPOW and some further analysed using the Rietveld refinement on Fullprof software. The Rietveld refinement was carried out by comparing the XRD data from some samples obtained experimentally to a model structure for authentication. Rietveld refinement was mainly used to obtain unit cell parameters in this study, a simpler method would have sufficed but using Rietveld is okay also. The materials in this study are phase pure with large crystal and therefore no strain would be observable. The quality or accuracy of the refinement or otherwise was checked using statistical indicators R_p, R_{wp} and R_{exp} as well as X^2 called refinement fit parameters or residues. Good result should have R_{wp} of 2-10% depending on the detailed profile and crystallographic refinement. For unit cell parameter comparison, the esd values are a better guide to accuracy. [10].

Crystallite size was determined by analysis of peak broadening and calculated using Scherrer's equation:

$$D = \frac{K\lambda}{\beta Co S\theta} \qquad \text{Eqn. 3-7}$$

Where D = crystallite size

K = Constant = 0.94

λ = Wavelength of X-ray

β = line broadening at half the maximum intensity or full width at half maximum (FWHM)

θ = Diffraction angle

3.3.3 Thermal analysis

3.3.3.1 Thermo gravimetric analysis (TGA)

In TGA, few milligrams of sample is heated up at a certain rate (commonly between 1-20 ^{o}C/min) under a certain atmosphere such as reducing (hydrogen), oxidising (oxygen, air) or inert atmosphere such as argon, helium or nitrogen to a chosen temperature or time to monitor how weight changes as a function either of those chosen variables i.e. temperature or time[9]. Usually correction run is made first before the main test using empty crucible with the same programme meant for the main test to guard against the interference of the instrument buoyancy. The instrument subtracts that from the main run. The instrument precision was about 0.01-0.05 mg.

In this work, physical or chemical behaviour of the sample under the influence of temperature was monitored to investigate weight change due to possible decomposition, structural changes or thermal instability/stability, phase segregation in different atmosphere such as air, hydrogen, O_2 and argon using NETZSCH STA449C and NEZSCH TG209 analysers. Samples were run in air or 5% H_2/Ar only or in air then after cooling then run in 5% H_2/Argon using the same sample to temperatures of 750-950 ^{o}C and ramp rate of 3-10^{o}C/min in alumina crucible.

3.3.3.2 Temperature programmed desorption (TPD)

In TPD, gas desorption from the surface of materials is monitored under various condition of temperature. The data obtained from such temperature programmed experiment, relates the energy of desorption to the strength of relationship between the adsorbed gas and the material which in turn is related to the strength and number of the active site on the desorbing material surface as a function of the reaction condition.

In CO_2 TPD, a solid surface previously equilibrated with CO_2 at room temperature is subjected to a programmed temperature increase which overcomes the adsorption energy of the adsorbed gas and desorption occurs. The generated gas is channelled to a mass spectrometer for detection and quantification by argon carrier gas. There is a direct relationship between the temperature at which the CO_2 desorbs under a linear temperature increase and activation energy of desorption and the basic strength of the desorbing surface. The instrument precision based on area was 0.0036×10^{-9}-0.012×10^{-9} A.

In this work, appropriate amount of sample was placed in the crucible and 10 % CO_2/Ar mixture was used for the surface coverage of the catalyst sample to determine the strength of its basic site at 50 ^{o}C for 1 hour using NETZSCH STA 449C trigravimetric analyser equiped with Thermostar mass spetrometer. The system was then purged with argon at same temperature to get rid of physically adsorbed CO_2. That was followed by a temperature programmed desorption at steady heating rate of 5^{o}/min to 900 ^{o}C and an isotherm for 1 hour. The desorbed CO_2 was monitored on mass spectrometer in parallel with the weight change due to the CO_2 desorption on TGA. The sample was then cooled to 50 ^{o}C.

3.3.3.3 Temperature programmed oxidation (TPO)

The TPO is used to monitor the reaction of carbonaceous substance on the surface of a used catalyst with oxygen under different condition of temperature. There is a correlation between the temperature at which bulk of the carbon oxidises and the location, nature or type of coke deposited. The desorbs CO_2 is monitored in parallel with the weight loss due to gassification of carbon on TGA. Therefore data obtained

from such analysis is used as as index for assessing or characterizing the coking phenomenon and to evaluate the extent of coking during the catalyst activity.

In this work, used catalyst were analysed for carbon deposition using NETZSCH STA 449C trigravimetric analyser equiped with Thermostar mass spetrometer. After putting a known weight of the used catalyst in alumina crusible, then MS-TGA system was pugged with argon to get ride of any other gas in the system. Oxidation of the surface carbon to carbon dioxide was done using O_2 gas by gradually increasing temperature from room temperature to 900 ^{o}C . Uder this condition, oxidation of the carbonaceous substance was monitored using the mass spectrometer in parallel with the weight change due to oxidation of carbon on the TGA. A plot of weight change and ion current against temperature was used to characterize and quantify carbon deposition.

3.3.4 Scanning electron microscopy (SEM)

SEM designed based on reflection provides information about the morphology (such as topography, texture) and microstructure and surface features of the powder or pellet material under investigation over wide range of magnification, the technique is based on the interaction between the particles of the material and beam of electrons. Electron from a source (Gun) is focused on certain spot on the surface of the material under examination and scanned systematically which generates secondary electron from the sample that is used to produce three dimensional images[9]. X-rays used for chemical analysis are also generated alongside the secondary electrons.

In this work, dispersion, particle size and morphology of catalyst materials were investigated using Field Emission Scanning Electron Microscopy (FESEM) JEOL JSM6700F. Micrographs were taken using secondary electrons and back scatter. The surfaces of some samples were coated with gold using Quorum Technologies Q150R prior to introduction into the machine to enhance electronic conductivity and reduce accumulation of charge on the sample that might cause blurring of the image.

3.3.5 Gas chromatography (GC)

Gas chromatography is an analytical tool used for the seperation and quantification of complex mixtures of chemical species. It consists of two essential features; a mobile phase of usually an inert gas such as helium, nitrogen or argon and a very thin liquid or

polymeric inert material anchored on inert solid support and enclosed in a metal or glass tubing known as column as the stationary phase. Usually helium is prefered as mobile phase because it does not appear in the chromatogram. The sample in a carrier gas intracts with the stationary phase and seperates or elutes at a time known as retaintion time characteristic of each chemical substance in the mixture. The samples are detected by either thermal conductivity detector (TCD) or flame ionisation detector (FID) and the result or output appears as a series of peaks known as chromatogram as shown by the schematic in Figure 3-1.

Sample can be introduced to the GC by direct injection through the external inlet to the column using a micro syringe. Alternatively and more repeatably, samples are introduced to the the GC by flowing it through gas switching valves and a loop. The use of gas switching valve or loop is to ensure accuracy and reproducibility of gas sampling from the continuous gas flow from the experimental process into the GC hence better than manual injection.

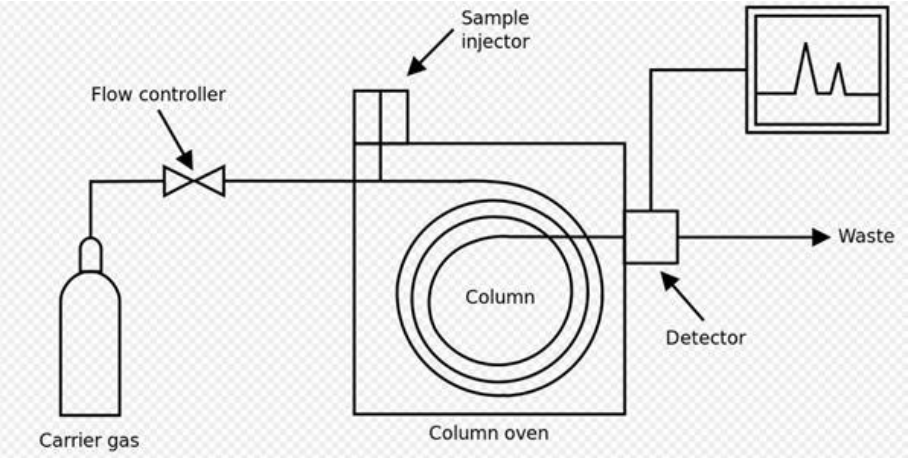

Figure 3-1 Schematic diagram of GC showing the essential componets[11].

The loop is filled with gas in an off-line position with respect to the GC column by automatic pump which then thereafter switch to an on-line position and become connected in series with column and the gas sample is emptied into the column by the mobile phase as shown in the schematic diagram of Figure 3-2. The area of the peaks is proportional to the concentration of the gas sample. The gas concentrations and their corresponding areas were used for the calibration plot (see appendix 2).

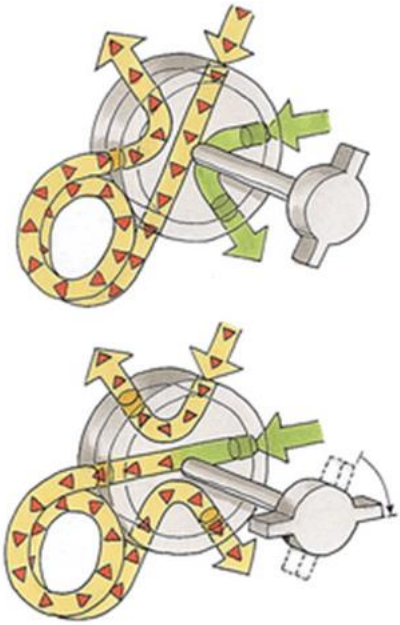

Figure 3-2 Schematic diagram of gas exchanging valve system showing the loop is filled in off-line position with respect to the column and emptied thereafter into the column when the loop is in an on-line position with respect to the column[12].

In this work, the glycerol water mixture was injected into a vaporizer and the vapour conveyed to a reactor by helium carrier gas and the reformate directed to the GC for seperation and quantification. The glycerol dilution used in this study was kept at S/C ratio of 1-3 or Water/glycerol ratio of 3-9 and 0.01-0.019 ml/min glycerol solution flow rate. The vaporized reactant mixture was conveyed to the reactor in a micro furnace by carrier gas (Helium) at flow rate of 40 ml/min. The gaseous products CO, CO_2 and CH_4 from the steam reforming of glycerol were analysed using gas chromatography HP 6890 series equiped with thermal conductivity detector (TCD) under the following reaction condition:

Table 3-2 GC set parameter and conditions

Set Parameter	Set point condition
Column type	HP 19095p-CO_2, HP-PLOT carbon plot (25.0m x350µm x 25.0µm nominal)
Carrier gas	Helium at 40 ml min^{-1}
Oven/column temperature	100 ^oC
Inlet temperature	60 ^oC

The retaintion time for the products in the GC as recorded during the anaysis was CO-3.5 min, CH_4- 5.6 min, and CO_2-11.2 min respectively. The water product resulting

from the experiment was trapped in a condenser and never allowed into the the GC. To quantify each product, the GC was calibrated using standard gases as shown in appendix 2, and concentration of those standard gases were related to the area of the peak on the GC chromatograph which was correlated to unknown samples from the steam reforming. Since the amount of the gases in the gas pipe (loop) to the GC is related to the P-V-T properties, the molar concentration was obtained from molar gas equation as shown in appendix 2.

3.3.6 Mass specroscopy (MS)

Mass spectrometer measures masses and relative concentration of atoms and molecules based on their different charge-to-mass ratio and relative abundance hence is used for both qualitative and quantitative analysis. Mass spectrometer is essentially made of three important components; the ion source, mass analyser and a detector. Because ions are short-lived and reactive, the process is usually done under vacuum. Gases or volatile liquids are bomberded with electrons from heated flament as ion source which knock off electron from them and the cation generated are propelled by a charge repeller and accelerated towards a magnetic field. The ions may further breaks to smaller ions and neutral fragment. In the magnetic field the ions are deflected based on their charge-to-mass ratio giving rise to array of ions registred as separate entities on the detector. The out put is a plot of relative abundance of each ion against their respective mass-to-charge ratio (m/z) known as mass spectrum[13]. Mass spectrum also appear as a plot of relative abundance in ion current/A against time. The ion current level could be related to the amount (concentration) of the ion and therefore mass spectrometer can be callibrated with standard gases and the ion (gas) current could be related to the concentration of the gaseous analyte which could also be related to the concentration of unknown sample from steam reforming for quantitative analysis. The calibration drifted quite a lot and I needed to recalibrate regularly.

In this work, H_2 was monitored and quantified by mass spectrometer because we are unable to see hydrogen on the GC or it appears as small negative peak. Different concentration of the gas and their corresponding ion current was used to obtain the calibration plot as shown in appendix 2. Then, the corresponding ion current of the

gas from the experiment was compared on the standard as explained above to obtain the corresponding concentration of the sample. The molar concentration was obtained by relating the concentration with molar gas volume (see appendix 2).

3.3.7 Proton nuclear magnetic resonance spectroscopy (^{1}H NMR)

The sensitvity of NMR to unique molecular environment and ability to yield a unique molecular spectra for different molecule was seen as a powerful tool for quantitative analysis in biodiesel characterisation. In this concept, integrals of resonances from ^{1}H NMR was used to relate the amount of fatty acid in oil to the methyl ester or biodiesel to determine the biodiesel yield[14].

The Figure 3-3 shows how the chemical shift for proton were assigned to the methyl esters and triglycerides respectively for the quantification of the biodiesel yield from transesterification reaction.

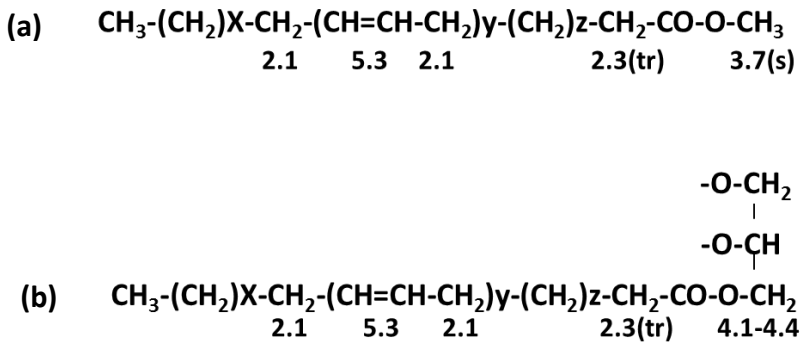

Figure 3-3 chemical shift assignment to the **a**, methyl ester and **b**, triglycerides

From the proton NMR spectrum for a typical progressing transesterifcation as seen in Figure 3-4 below, two suitable or relavant peaks were integrated-the one at 3.7 ppm corresponding to methoxy group in the biodiesel (methyl ester) and at 2.3 ppm corresponding to α-carbonyl methylene group fond in all fatty acid of vegetable oil triglyceride[14]. They are related in equation used for the calculation of biodiesel yield thus:

$$C = \left[2A_{CO2CH3}/3A_{\alpha\text{-}CH2}\right] X\ 100 \qquad \text{Eqn. 3-8}$$

Where C = Conversion or yield of vegetable oil to biodiesel (methyl ester)

$A_{\text{-}CO2CH3}$ = integration value of the proton of biodiesel (methyl ester) methoxy group

$A_{\alpha\text{-}CH2}$ = integration value of the proton of the methylene moiety from vegetable oil

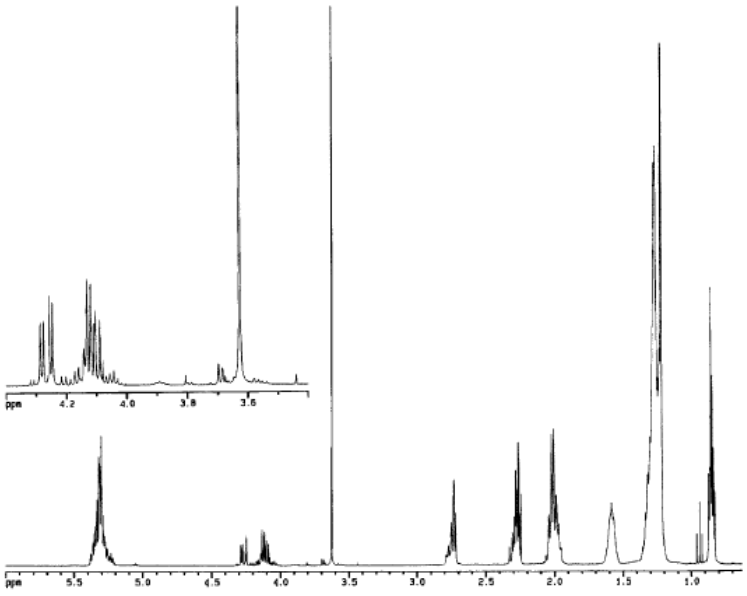

Figure 3-4 proton NMR spectrum for a typical progressing transesterifcation reaction[15]

In this work, about 2.5 µml was withdrawn from each progressing transesterification reaction and transferred to 1 ml deuterated chloroform ($CDCl_3$) in a vial. The vial was shook to dissolve the sample and ensure homogeneity. The dissolved sample was then transferred to clean and dried NMR tube using a syringe. Quantitative 1H NMR was run for each sample using 300 or 400 MHz NMR spectrometer.

3.4 Reforming rig design

The steam reforming rig designed in a top-bottom flow configuration essentially consists of three parts; the water-glycerol mixture injection system, the vaporizer and a reactor concealed in a micro furnace. The water-glycerol mixture injection system has a programmable syringe pump Harvard Instrument 55-2222 pump model with a provision for two syringes to handle two immiscible liquids. The liquid feed mixture is injected to a $1/8^{th}$ stainless steel pipe wrapped with heating tape at 250 ^{o}C. The pipe is to function both as vaporizer and mixer. It is connected to gas sources controlled by appropriate Brooks mass flow controllers and suitable size gas $1/8^{th}$ plastic pipes. The vaporised liquid with aid of a carrier gas is conveyed to a quartz tube reactor (8mm internal diameter and 10mm outer diameter) concealed in a micro furnace controlled by Eurotherm programmable controller. To ensure that the reactants are vaporised

and not recondensed from natural cooling or insufficient tape heating before the reformer, the outlet from the vaporizer was kept right on top of the furnace connected to the reactor. So as soon as it comes out it enters the hot reactor. Required amount of catalyst is usually imbedded at the centre of the reactor using quartz wool. There is provision at the top of the reactor for thermocouple to be inserted down to the catalyst bed to monitor its temperature. The generated reformate is channelled through a cold trap to separate gaseous products from condensate to GC and MS for analysis while excess gas is discharged through by-pass exhaust.

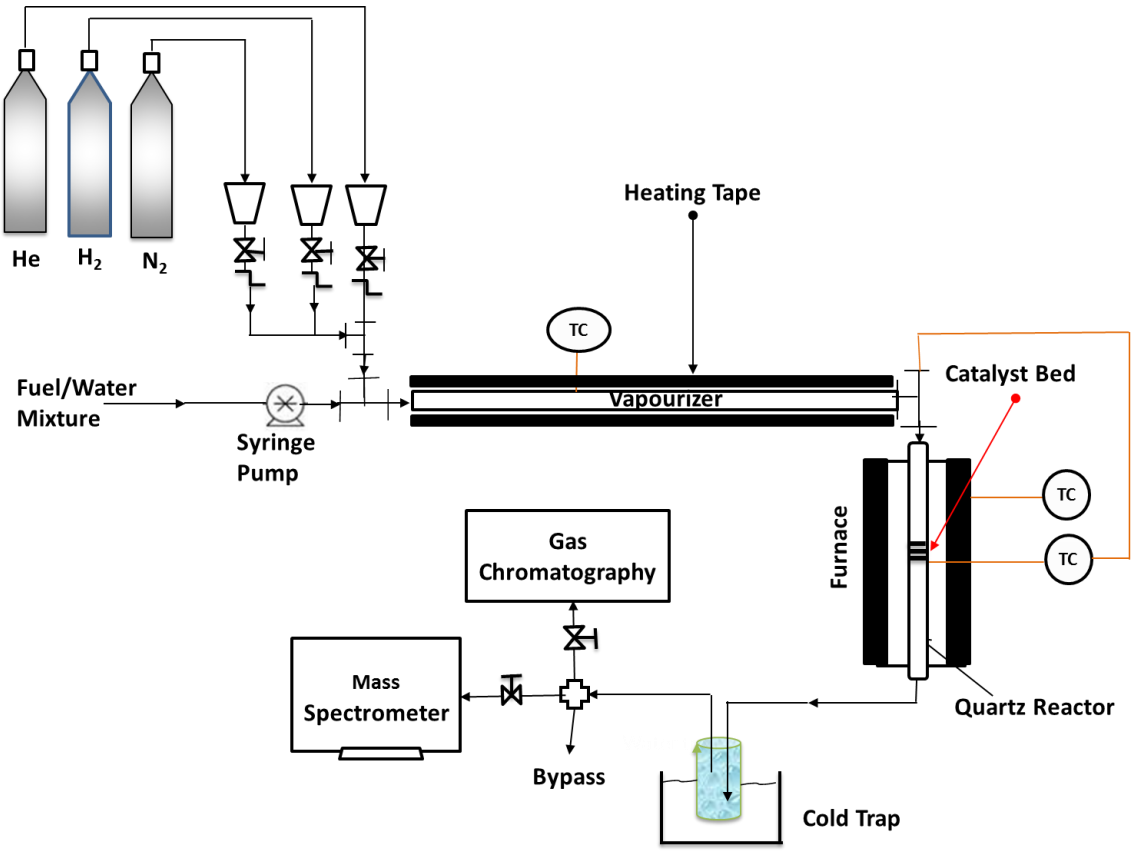

Figure 3-5 Schematic diagram of the steam reforming rig showing all the three essential units

3.5 Catalyst testing

3.5.1 Catalysis of transesterification reaction to biodiesel

3.5.1.1 The traditional synthesis

In this work, about 1-2.5 % weight of the catalyst based on the weight of the vegetable oil was mixed with 10 g of soybean oil in a three-necked round bottom flask (250 ml) caped with glass stoppers and equipped with reflux condenser to guard against loss of methanol. Magnetic stirrer was used to keep the mixture agitated on hot plate at the desired rate. When the desired temperature was attained, suitable amount of catalyst and methanol was added and kept stirring. Samples were collected at specific intervals into small vials using pastures pipette and dried in the hood to remove dissolved methanol. NMR samples were prepared by dissolving about 2.5 µml of biodiesel into 1 ml deuterated chloroform and conversion or yield was measured by ^{1}H NMR using 300 or 400 MHz NMR spectrometer. At the end of the reaction, catalyst was removed and the product allowed overnight for effective separation of biodiesel and glycerol. After each run, catalyst recovered was washed with both methanol and ethanol for reuse. Both the inorganic catalysts and the resin catalysts were run in same manner. Different factors as they affect biodiesel yield such as reaction time and temperature, vegetable oil-to-methanol ratio and catalyst amount were explored. Vegetable oil-to-methanol ratio was calculated based on the method shown in appendix 1. Because of the variation in the molecular mass of oil, in this analysis an average value of 880 g/mol was used as the near average molecular mass of the sunflower oil obtained from TESCO used for this work. Typical molar weight of sunflower oil is 876.16 g/mol based on the molecular weights of triglycerides-palmitic, stearic, oleic and linoleic corresponding to the fatty acid methyl esters of the oil[16]. Molecular weight of used sunflower oil containing olive was determined to be 882 g/mol[17] and sunflower oil mixed with olive and palm oil was found to be 875 g/mol respctively[18]. Whilst 856 g/mol was determined for waste oil, 882 g/mol were obtained for vegetable oil[19]. According to British pharmacopoeia, sunflower oil largely contains 90% as oleic and linoleic acid with total molar mass of 870 g/mol (ignoring minor fat (<10% as palmitic and stearic acid)[20]. Therefore typical oil may have molecular weight of 876 ± 6 g/mol.

3.5.1.2 The autoclave synthesis

Autoclave biodiesel synthesis entails keeping the oil and catalyst udder high pressure and temperature to cause both chemical and physical transformation. Under high pressure and temperature in the autoclave environment, triglyceride bond breakage is enhanced and helps in the methyl ester conversion. The pressure would mainly be due to the vapour pressure of methanol[21].

In the autoclave synthesis, 1-3g of the resin catalyst was added to 10g of oil in the autoclave reactor followed by required amount of methanol. The autoclave rector was inserted into a steel container and kept in the oven at required temperature under the methanol vapour pressure (3-10 bars) for 24hrs.

3.5.2 Catalytic glycerol steam reforming (GSR)

The glycerol steam reforming was carried out on a fixed bed quartz tube (8 mm inner diameter (ID), 10mm outer diameter (OD) and 24cm long) reactor at different temperatures of 300-900 ^{o}C and atmospheric pressure. The nickel-based catalyst systems prepared by wet impregnation were reduced *in situ* at 500 ^{o}C for 1 hour using 10% H_2, while the perovskite catalysts were pre reduced as described in section 3.2.5 above before the catalyst test. 50-100 mg catalyst was sandwiched between two quartz wools and kept at a position in the reactor such that it will always remain at the centre of the furnace which is the hottest point of the furnace. Thermocouple was inserted thorough the reactor to the top of the catalyst bed to monitor temperature. The glycerol-water mixture was supplied using syringe Harvard apparatus 55-2222 infusion pump at the flow rate of 0.010-0.019 ml/min to a stainless steel pipe wrapped with heating tape at 250 ^{o}C for vaporization. The vaporized reactant mixture was conveyed into the reactor by carrier gas (Helium) at flow rate of 40 ml/min. Steam-to-carbon ratio (S/C) of 3:1 and 1:1 using both pure and by-product glycerol was investigated. Gaseous products were analysed using GC equipped with TCD (HP 6890 series) and mass spectrometer residual gas analyser.

3.5.2.1 Catalyst performance evaluations

The performance of all the catalysts investigated in this work was evaluated based on parameters such as glycerol conversion to gaseous product, yield, selectivity etc. Those parameters were defined as follows:

Glycerol conversion to gaseous products (X_G):

$$X_G = \frac{(CO + CO_2 + CH_4) \text{ mol. Produced}}{3 \text{ x molar flow rate of glycerol solution}} \text{ x } 100$$

Hydrogen yield (Y_{H2}):

$$Y_{H2} = \frac{H_2 \text{ mol. produced}}{3 \text{ x } 7 \text{ x glycerol soln molar flow rate}} \text{ x } 100$$

Where 1/7 is from the mole of H_2 in the stoichiometric equation of steam reforming of glycerol.

Hydrogen Selectivity (S_{H2}):

$$S_{H2} = \frac{H_2 \text{ mol. Produced}}{\text{Total mol C products produced}} \text{ X } \frac{1}{RR} \text{ X } 100$$

Where RR is the ratio of H_2/CO_2 and in glycerol it is 7/3[22,23]

Selectivity for carbon containing species in the gaseous phase (S_i)

$$S_i = \frac{\text{mol. In specie i Produced}}{\Sigma \text{ i mol. produced}} \text{ X } 100$$

Where i is CO, CO_2 and CH_4

COx selectivity (S_{COx}):

$$S_{COx} = \frac{(CO + CO_2) \text{ mol. Produced}}{\text{Total C atom in feedstock}}$$

Turnover number (TON):

$$TON = \frac{\text{mole of desired product formed}}{\text{BET Surface area of the catalyst}}$$

BET surface area was used instead of active site because not all site are active and are not same as such calculating or determining active site correctly would be problematic. But since surface sites depends on surface area which is also related to particle size and easy to measure accurately, then surface area was used to calculate TON.

Turnover frequency (TOF):

$$TOF = \frac{TON}{\text{Contact time (sec)}}$$

References

1. Neagu, D. Tsekouras, G. Miller, D. N. Me´nard, H. and Irvine, J. T. S. *In situ* growth of nanoparticles through control of non-stoichiometry. *Nature Chemistry* **5**, 916-923 (2013)

2. Haber, J.; Block, J. H. and Delmon, B. Manual of methods and procedures for catalyst characterisation*. Pure and Appl. Chem***. 67** 1257-1306 (1995)

3. Sutka, A. and Mezinskis, G. Sol-Gel auto-combustion synthesis for spinel-type ferrite nanomaterials. *Front Mater. Sci.* **6**, 2, 128-141 (2012)

4. Yuan, Q.; Li, L. Lu, S.; Duan,H.; Li, Z.; Zhu, Y. and Yan, C. Facile synthesis of Zr-based functional materials with highly ordered mesoporous structures. *J. Phys. Chem. C*. **11,** 4117–4124 (2009)

5. Stefan, E. and Irvine, J. T. S. Synthesis and characterization of chromium spinel as potential electrodes support materials for intermediate temperature solid oxide fuel cell. *J Mater Sci* **4**, 7191-7197 (2011)

6. Stefan, E. Connor, P. A. and Irvine, J. T. S. Development and performance of $MgFeCrO_4$ – based electrodes for solid oxide fuel cells. *J. Mater. Chem. A*, **1**, 8262-8269 (2013)

7. Feng, Y.; He, B.; Cao, Y.; Li, J.; Liu, M.; Yan, F. and Liang, X. Biodiesel production using cation-exchange resin as heterogeneous catalyst*. Bioresource Technology* **101**, 1518–1521 (2010)

8. Webb, P.A and Orr, C. *Analytical methods in fine particle technology*. Micromeritics Inst. Corp. Norcross, GA, USA. (1997)

9. West, A. R. *Solid State Chemistry and its Applications*. John Wiley and Sons, Pg 102-115 (1984)

10. Kniess, C. T.; de Lima, J. C. and Prates, P. B. The quantification of crystalline phase in materials: Applications of Rietveld method sintering-methods and products, Dr Volodymyr Shatokha (Ed.) ISBN: 978-953-51-0371-1, InTech, Available from: http://www.intechopen.com/books/sintering-methods-and-products/the-quantification-of-crystalline-phases-inmaterials-pplications-of-rietveld-method (2012)

11. https://en.wikipedia.org/wiki/Gas_chromatography#/media/File:Gas_chromatograph-vector.svg

12. http://hiq.aga.com/international/web/lg/spg/likelgspg.nsf/docbyalias/anal_gaschrom

13. Williams, D. H. and Fleming, I. *Spectroscopic methods in organic chemistry*. McGraw-Hill Int. London. Pg 170-224 (1966)

14. Gelbard, G.; Brès,O.; Vargas, R. M.; Vielfaure, F. and Schuchardt, U. F. 1H nuclear magnetic resonance determination of the yield of the transesterification of rapeseed oil with methanol. *J. Am. Oil Chem. Soc.* **72**, 10, 1239-1241 (1995)

15. Knothe, G. Analytical methods used in the production and fuel quality assessment of biodiesel. *Transactions of the ASAE* **44**,2, 193-200 (2001)

16. Sanchez, A.; Maceiras, R.; Cacela, A. and Rodriguez, M. Influence of n-hexane on *in situ* transesterification of marine macroalgae *Energies* **5**, 243-257 (2012)

17. Encinar, J. M.; Gozalez, J. F. and Rodriguez-Renares, A. Ethanolysis of used frying oil. Biodiesel preparation and characterization Fuel Process Technol 88, 513-522 (2007)

18. Lapuerta, M.; Herrero, J. M.; Lyons, L.; Garcia-Contreras, R. and Briceno, Y. Effect of the alcohol type used in the production of waste cooking oil biodiesel on diesel performance and emissions Fuel 87, 3161-3169 (2008)

19. Leung, D. Y. C. and Guo, Y. Transesterification of neat and used frying oil: Optimization for biodiesel production. *Fuel Process Technol* **87**, 883-890 (2006)

20. https://en.wikipedia.org/wiki/Sunflower_oil

21. Di Serio, M.; Tesser, R.; Casale, L.; D'Angelo, A.; Trifuoggi, M. and Santacesaria, E. Heterogeneous catalysis in biodiesel production: The influence of leaching. *Top Catal* **53**, 811–819 (2010)

22. Adhikari, S.; Fernando, S. and Haryanto, A. Production of hydrogen by steam reforming of glycerine over alumina-supported metal catalysts *Catalysis Today* **129,** 355–364 (2007)

23. Chiodo, V.; Freni, S.; Galvagno, A.; Modello, N. and Frusteri, F. Catalytic features of Rh and Ni supported catalysts in the steam reforming of glycerol to produce hydrogen Applied Catalysis A: General **381**, 1-7 (2010)

MATERIALS FOR CATALYTIC CONVERSION OF BIOMASS VEGETABLE OIL TO BIODIESEL

4.0 Tricalcium aluminate (C_3A) catalysts for biodiesel production

4.1 Introduction

Tricalcium aluminate (C3A) being one of the essential crystalline interstitial phases in Portland cement has attracted much research due to its strategic role in the early stages of hydration process in cement and strength development of concrete[1-4]. Essentially its chemical composition is $Ca_3Al_2O_6$ but in cement chemistry it is abbreviated as C3A from $3CaO.Al_2O_3$. Tricalcium aluminate is a stable solid phase at temperature 1300-1350 ^oC but melt and forms a liquid phase at around 1400-1542 ^oC. It also shares some properties with mayenite ($12CaO.7Al_2O_3$) as shown by the phase diagram below. As such it facilitates the formation of desired silicate phases by providing liquid at the peak of kiln processing temperature of 1400-1450 ^oC[1,5].

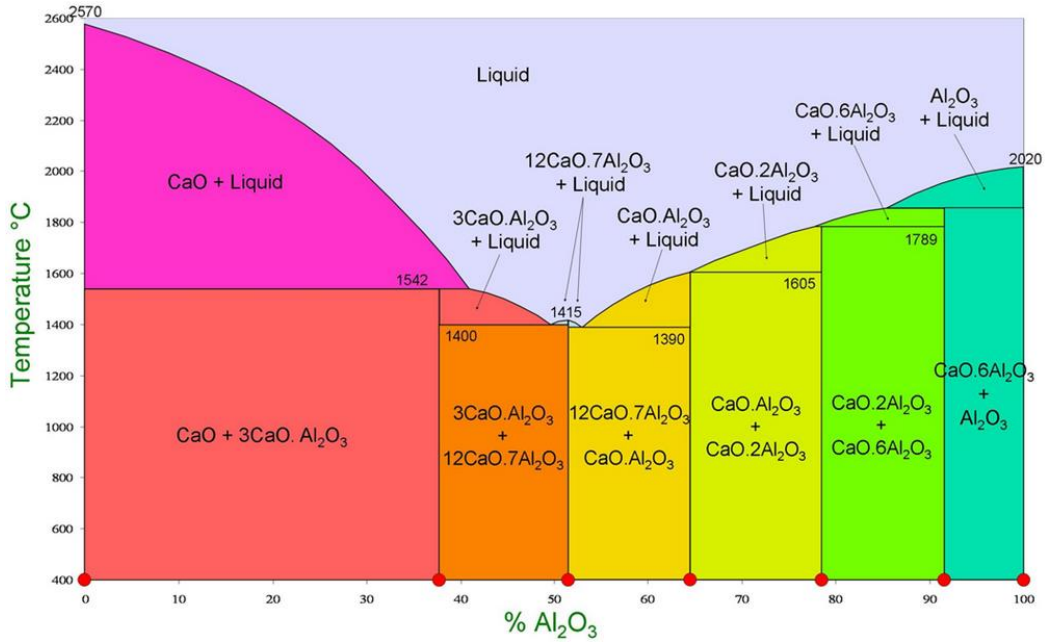

Figure 4-1 Phase diagram showing different stable phases of calcium aluminate compounds[5]

The Crystal structure of tricalcium aluminate consists of corner 6 sharing AlO_4-tetrahdra with linkage via Ca forming 8-cyclic $Al_6O_{18}^{18-}$ anions in a unit cell. It has a body centred cubic symmetry with *Pm*3*m or Pa*3 space group and has a lattice parameter of a = 15.263(3) Å and cell volume of 3555.66 A^3 characterized by surrounding holes of radius 1.47 Å at 1/8 1/8 1/8[6,7]. It was observed that tricalcium

aluminate shares some crystallographic resemblance of its XRD pattern especially the strongest line which occurs in same position as that of the perovskite such as $CaTiO_3$ (a = 3.8 Å) and the silicate such as Na_2CaSiO_4 [8,9].

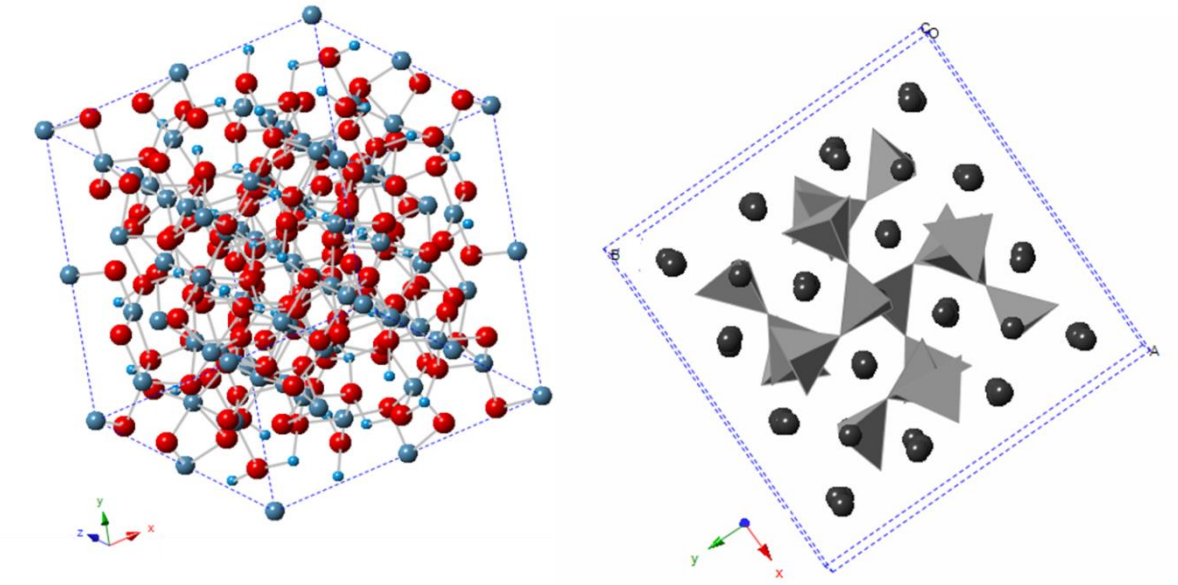

Figure 4-2 Crystal Structure of tricalcium aluminate showing Al-Ca-O frame work in ball-stick as well as the polyhedral model

The renewed interest in calcium aluminate compounds has attracted application in catalysis such as gasification of organic compounds[10-13]. In biodiesel production, no literature is available on the use of basic calcium aluminate compounds such as tricalcium aluminate as catalyst for transesterification reaction of oil to biodiesel to the best of my knowledge. However, the only pioneering work is where calcium aluminate compound mayenite was used in composite formulation with CaO i.e. (CaO-$Ca_{12}Al_{14}O_{33}$) to enhance its basic properties for transesterification of *Argemone Mexicana* oil for biodiesel production. The catalyst showed good conversion of the oil, reusability and suppression of leaching[14].

Furthermore, studies have revealed that tricalcium aluminate reacts with water due to its basic properties exothermally forming calcium aluminate hydrate[4,15]. The water molecule protonates one of the oxygen atoms on the C3A rings leading to the formation of strongly basic calcium hydroxide thus[4]:

$$Ca_3Al_2O_6 + 4H_2O \rightarrow CaAl_2O_2(OH)_4 + 2Ca(OH)_2 \qquad \text{Eqn. 4-1}$$

It is interesting to note that for every tricalcium aluminate molecule, 2 Ca(OH)2 molecules are generated. This has resultant influence on the basic properties of the material as evident in Eqn. 4-1 above. Such transformation to basic products could be harnessed in catalysis of biodiesel synthesis. Alternatively, tricalcium aluminate has shown some versatility and stability to doping for enhanced properties especially with strongly basic alkaline and alkaline metals and transition metals[16-18]. This property could be harnessed to develop strongly basic tricalcium aluminate-based compounds for utilization as basic catalyst for transesterification reaction to biodiesel.

The aim of this section is to for the first time enhance basic properties of tricalcium aluminate through 'controlled' hydration to hydroxide products at elevated temperature for utilisation as a basic transesterification reaction catalyst for biodiesel production. However, the hydration or water uptake needs to be controlled to prevent agglomeration or 'wetting' of the powder which is not desired in transesterification reaction catalysis. As such, the hydration temperature was optimized by hydration of the samples at different temperatures of 900-1200 ^{o}C. In parallel, the Al-site of non-hydrated C3A would be doped with oxides of alkaline earth metals (MgO and SrO) and a transition metal (ZnO) to enhance surface basic, hygroscopic properties and chemistry to catalyse transesterification reaction. More so, the dopants are known for good catalytic activity in biodiesel synthesis but lose activity rapidly due to leaching. Therefore integrating them into the C3A crystal lattice could help to prevent catalyst deactivation by leaching.

4.2 Hydrated tricalcium aluminate (C3A): A novel catalyst for biodiesel production

4.2.1 Thermal analysis of the hydrated samples

4.2.1.1 Investigation of degree of hydration

Thermo-gravimetric analysis (TGA) and Differential thermal analysis (DTA) was carried out to measure weight loss due to dehydration or decomposition of the hydrated products as well as their corresponding temperature ranges. To measure the kinetics or influence of temperature on the degree of hydration, C3A samples were hydrated at different temperature i.e. 900 ^{o}C, 1000 ^{o}C, 1100 ^{o}C and 1200 ^{o}C. The thermal

analysis was performed in Argon atmosphere at ramping rate of 5°/min to 1300 °C on the pre hydrated samples. Figure 4-3 shows the weight change when the pre hydrated samples of C3A were heated from room temperature to 1300 °C. There are three important points of weight loss identified and marked as 1, 2 and 3 in the chart corresponding to different dehydration processes.

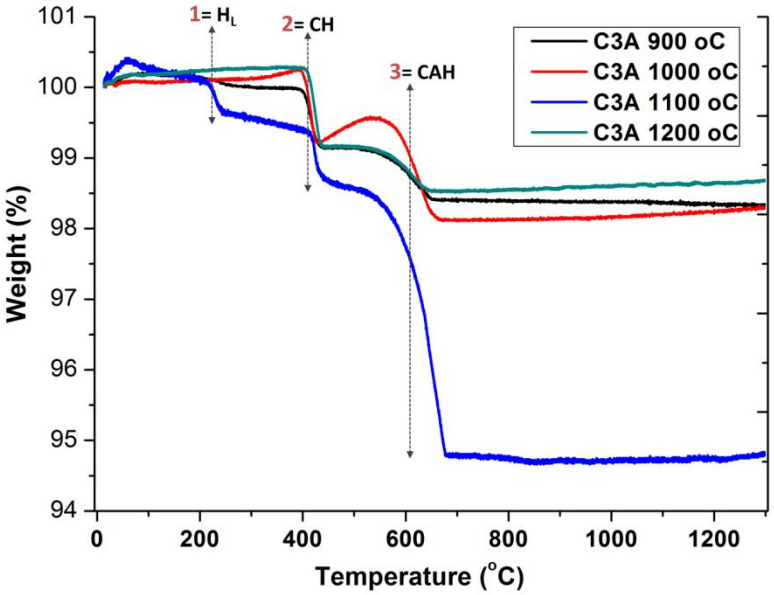

Figure 4-3 Thermal analysis of the hydrated C3A samples showing weight loss due to dehydration of the pre-hydrated samples at different temperature. The 1st weight loss is due to chemical water or lattice water (H_L), the 2nd stage is due to dehydration and decomposition of $Ca(OH)_2$ and the 3rd correspond to the decomposition of $4CaO.3Al_2O_3.3H_2O$

When tricalcium aluminate was treated in the gas stream at elevated temperature, hydrolysis occur leading to the formation of products; calcium hydroaluminate in the ratio 4:3:3 ($4CaO.3Al_2O_3.3H_2O$) and calcium hydroxide ($Ca(OH)_2$. Dehydration of the hydrated products occurs in stages as seen in Figure 4-3. The first stage '1' occurs at temperature ~200-278 °C as shown by the DTA Plot in Figure 4-4b corresponding to the loss of chemical water or lattice water (H_L) marked as 'H_L' in the Figure. This particular process is most notable with the C3A sample hydrated at 1100 °C which suggests more water uptake by the sample. The sample hydrated at 900 °C (C3A 900 C) seems to have recorded the least water uptake. The second stage '2' is the weight loss corresponding to the dehydration due to loss of chemically bound water and decomposition of $Ca(OH)_2$ (CH)[19-22]. The last stage '3' corresponds to the weight loss

due decomposition or dehydration of $4CaO.3Al_2O_3.3H_2O$ (CAH)[19-22]. It is clear the hydration process was effective and formation of basic products has occurred on the surface of the materials. Judging by the level of weight loss in the 2nd and 3rd stages, it is clear also sample hydrated at 1100 ^oC had more of the basic hydration products while sample hydrated at 900 ^oC had the least. This observation is supported by the IR analysis result shown in Figure 4-4a.

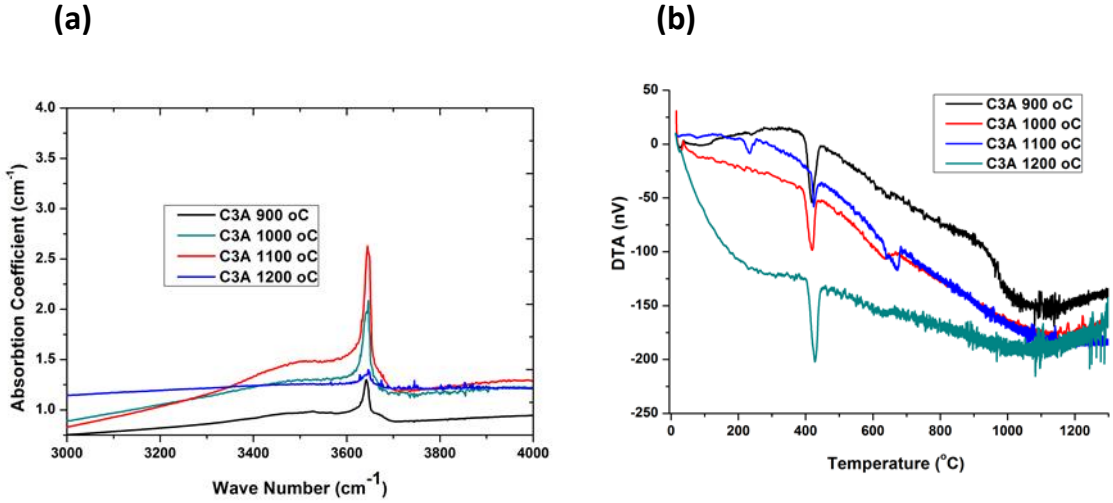

Figure 4-4a-b IR and DTA analysis of the hydrated C3A samples. **a,** is the IR result showing absorption peak at around 3650 cm^{-1} corresponding to absorption peak for hydroxyl ion (OH^-)-stretching band which indicates the samples are hydrated and formation hydration hydroxide products. b, DTA peaks showing the temperature or energy range corresponding to the weight loss from dehydration process in Figure 4-3

The figure shows a peak at 3650 cm^{-1} corresponding to absorption peak for hydroxyl ion (OH^-)-stretching band which further confirms water vapour uptake and subsequent formation of basic hydroxide products. To further investigate the extent or degree of hydration and its influence on structure of the materials, the amount of water molecule/C3A as a function of hydration temperature was calculated for each sample. The calculation considered the weight loss due to dehydration of chemical water as well as decomposition of the products. Table 4-1 shows the water molecule corresponding to each stage of the dehydration process.

Table 4-1 Variation of degree hydration with hydration temperature

	Water molecule loss at each stage/C3A		
Sample	1	2	3
C3A 900 ^oC	-	0.24	0.105
C3A 1000 ^oC	-	0.32	0.18
C3A 1100 ^oC	0.85	0.79	0.59
C3A 1200 ^oC	-	0.27	0.10

The result suggests that the sample hydrated at 1100 ^{o}C (C3A 1100 ^{o}C) contains more water at the entire stages while the sample hydrated at 900 ^{o}C (C3A 900 ^{o}C) had the least amount of water. This confirms that there is relationship between the hydration temperature and the degree of hydration and formation of hydration product hence possibly catalytic behaviour. It suffices to add that all things be equal, is likely C3A-1100 ^{o}C will be more active for transesterification reaction to biodiesel because of its strong basic behaviour except if its higher water content relatively portends a counter negative influence to its catalytic behaviour. This hydration behaviour of C3A resembles the behaviour of another calcium aluminate compound mayenite ($Ca_{12}Al_{12}O_{33}$) samples hydrated in a wet TGA as reported by Irvine and West, 1989[23] and Hayashi et al, 2005[24].

In the subsequent section, we will investigate how degree of hydration influenced structural properties such as lattice parameter and the optimum hydration temperature that will give maximum biodiesel yield.

4.2.1.2 Basic strength of the C3A catalyst surface

Basically, temperature programmed desorption (TPD) of CO_2 was carried out to investigate the strength of basic sites on the hydrated C3A surface by equilibrating the C3A surface with CO_2 at low temperature as explained in section 3.3.3.2. This was done by relating the strength of the basic sites to the temperature at which the biding force between the basic site and acidic CO_2 breaks and the CO_2 desorbs. The temperature programmed desorption result shown in Figure 4-5 gives only one distinct CO_2 peak at high temperature in all the samples which indicates high basic strength. There is no significant CO_2 peak at much lower temperatures below that point (600 ^{o}C) to indicate corresponding weak basic sites[25]. The strong peaks are attributable to the formation of basic hydroxide products due to hydration of the samples which is indicative of likely good catalytic activities with the samples. This analysis has also interestingly shows that there is a relationship between the hydration temperature and the strength of the basic sites. This corroborates earlier observation regarding the basic character of the C3A hydrated samples.

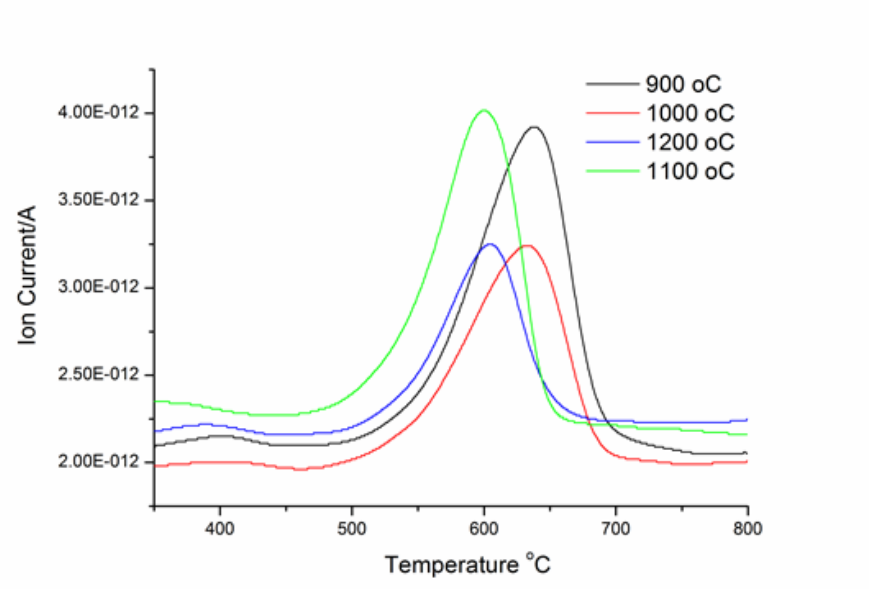

Figure 4-5 The CO_2 temperature programmed desorption profile of the different temperature pre hydrated C3A samples showing the temperature at which bulk of the CO_2 desorbs in each sample. The CO_2 desorption occurred at high temperature confirming the high basic strength of the samples.

4.2.2 Crystallographic and micro structures in relation to hydration temperature

Diffraction patterns from room-temperature powder crystallographic data for the non-hydrated and hydrated C3A samples at different hydration temperature are shown in Figure 4-6a with the characteristic cubic most intense peak at 33.169^{o}. Other major peaks at 40.924, 47.616, 59.260, 69.625, 79.331 and 88.739 respectively are also typical cubic peaks as indicated in Figure 4-6a. A part from the major peaks, other smaller peaks are also all due to C3A and no extra peaks observed as corroborated by refinement data below and the peak fitting with C3A XRD pattern from literature[7] in Figure 4-6b which confirms that the materials synthesized are in pure phase.

Magnified 8 0 0 peaks in Figure 4-7 shows a slight shift to bigger 2theta in the position of the peaks or a shift to a smaller d-spacing in the hydrated samples with respect to non-hydrated sample attributable to variation in degree of hydration with hydration temperature. This shows that the lattice water influences the structural properties of the materials.

(a)

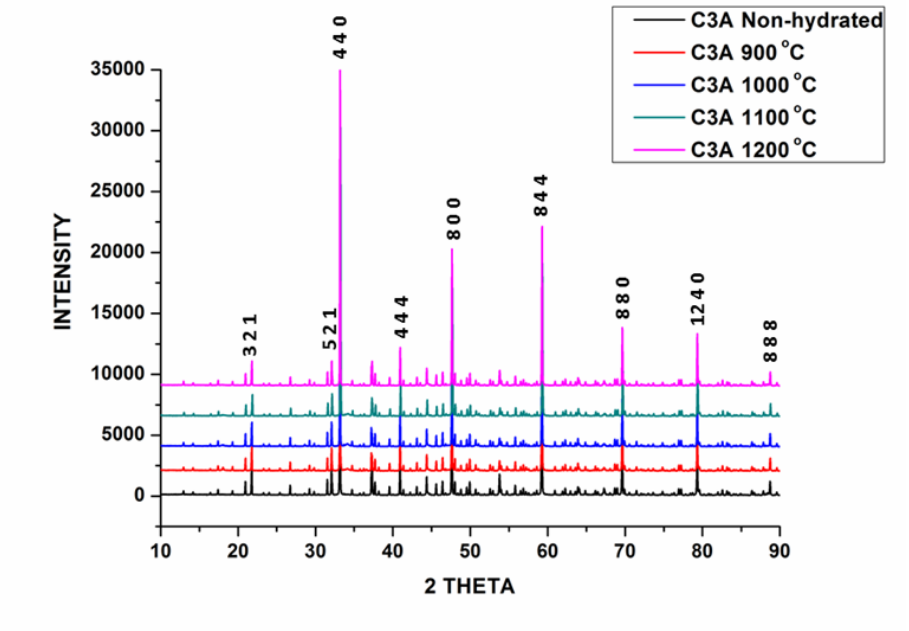

(b)

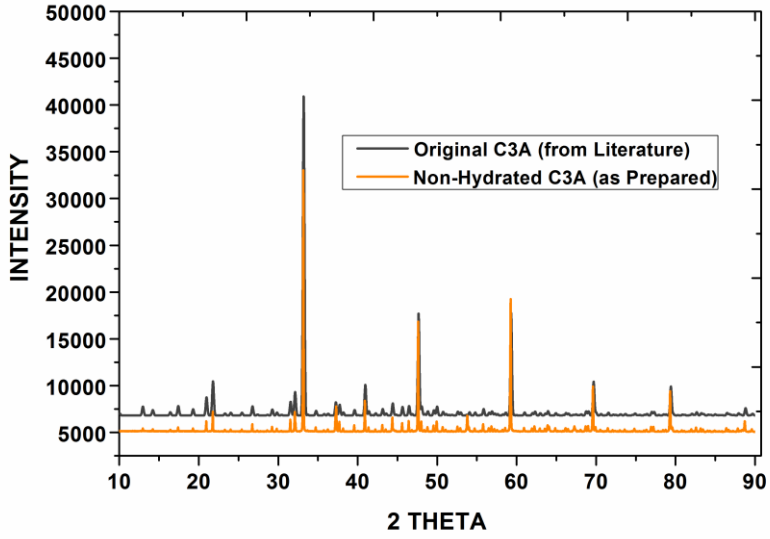

Figure 4-6 Crystallographic studies: **a,** XRD pattern of the hydrated C3A samples at different temperatures compared to that of the host non-hydrated C3A sample and also reflecting the major indexed peaks **b,** comparison of XRD pattern of the C3A sample as prepared before hydration with that of the original C3A from literature[7] confirming the phase purity of the prepared samples.

Interestingly, there is also slight shift among the hydrated samples as the hydration temperature increases with sample hydrated at 1100 ^{o}C showing a greater shift

relatively. This further correlates degree of hydration and formation of hydroxide products with hydration temperature.

It is also interesting to note that the hydrated C3A samples were stable after the hydration as shown by the XRD pattern of the hydrated samples. This implies the hydration and water uptake was controlled and the transformation occurred as aimed in the surface which is good for the catalysis.

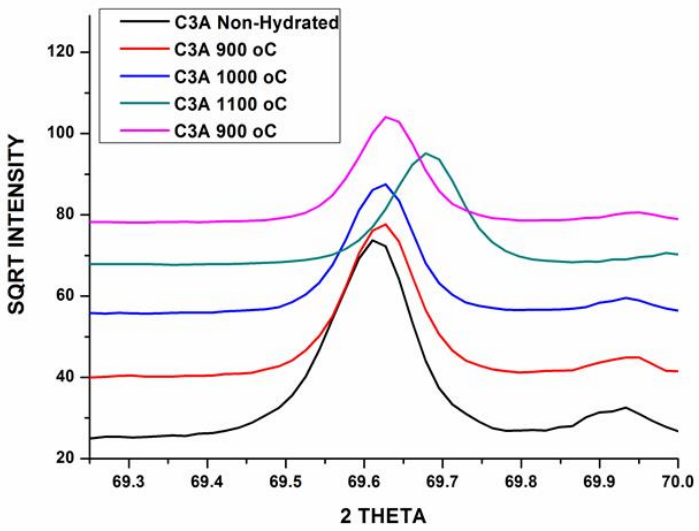

Figure 4-7 Magnified 8 8 0 peaks showing a shift towards a bigger 2θ angle or smaller d-spacing from non-hydrated C3A sample to hydrated sample. It also shows a slight shift in same direction as the hydration temperature increases though not regularly

The refinement of the XRD pattern of the non-hydrated and hydrated samples with STOE WinXpow software using ICSD No.205 has proved them to be cubic with *Pm*3*m* space group. The refinement data in Table 4-2 shows that lattice parameter (a) and cell volume closely agrees with the 15.263(3) Å and 3555.66 A^3 respectively from the literature[7].

Table 4-2 Showing variation of refinement data amongst the C3A samples

Sample	Cell Parameter (a)	Cell Volume (A^3)	2thetha zero point
C3A-Non-Hydrated	15.2652(4)	3557.16(15)	-0.0107(17)
C3A-900 ^oC	15.26488(22)	3556.97(9)	-0.0048(16)
C3A-1000 ^oC	15.26511(21)	3557.13(8)	-0.0034(9)
C3A-1100 ^oC	15.26640(13)	3558.10(5)	0.0420(3)
C3A-1200 ^oC	15.2650(3)	3557.08(13)	0.0073(14)

The cell parameter (a) and cell volume plotted against hydration temperatures as shown in Figure 4-8 reflects similar variation observed in Figure 4-7. This suggests a relationship between the hydration temperature, water uptake or degree of hydration and those parameters. These variations could only be due to change in hydration temperature since that is the only difference among them which might have influenced the water uptake and possible formation of hydroxide products. Because the sample responds differently to hydration at different temperatures that also implies the optimization of the hydration temperature investigated is essential to help ascertain the optimum hydration temperature that will give maximum yield.

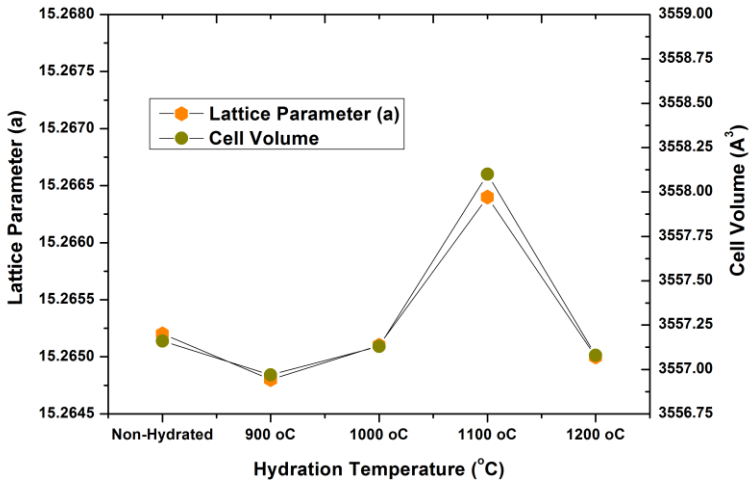

Figure 4-8 comparison of lattice parameter to cell volume as a function of hydration temperature

The C3A 1100 ^{o}C sample has the largest cell parameter (a) which clearly confirms its behaviour from the TGA analysis especially degree of hydration. Excitingly, a plot of lattice parameter and number of water molecule bound to a molecule of C3A against hydration temperature proved this relationship as seen in Figure 4-9a. It is clear there is a linear relationship between the structural properties of the materials and hydration temperature as shown in Figure 4-9b which justifies the shift observed in Figure -7 as well as the aim of the research.

Particle size was also investigated to further characterize the samples to understand possible influence of the hydration temperature on particle size which is an essential property in catalysis. The calculation was done using the Scherrer's equation and the result is as shown in Table 4-3.

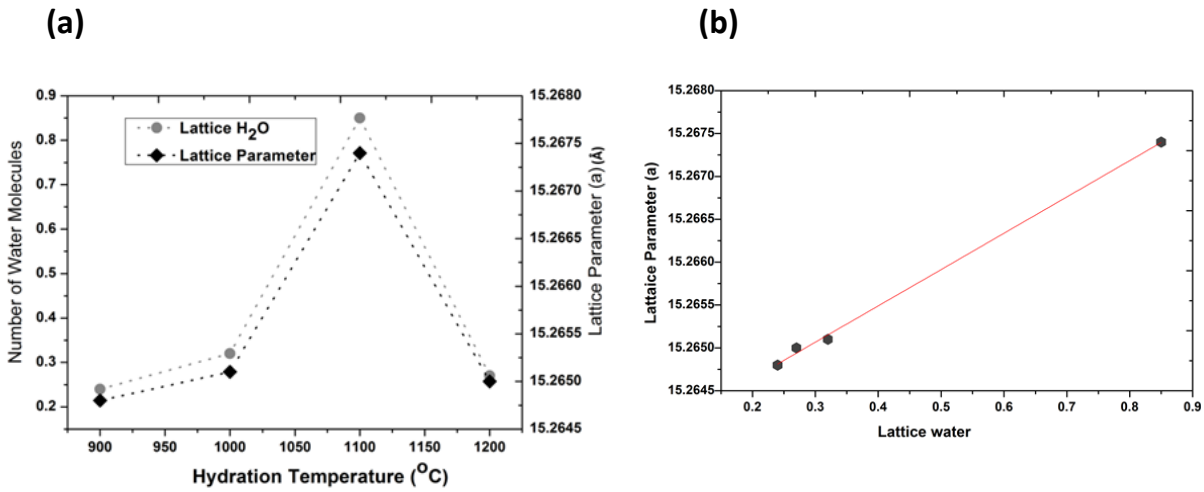

Figure 4-9 **a,** shows a good correlation between the degree of hydration and lattice parameter as a function of hydration temperature which confirms that the hydration influenced structural properties of the material. **b**, corroborates that the relationship between degree of hydration and lattice parameter is a linear one.

The non-hydrated C3A had a crystallite size of 0.920 µm which agrees with the 1µm observed in the SEM micrographs in Figure 4-10a. The particle size increased after the samples were hydrated except the sample hydrated at 1100 ^{o}C whose particle size shrank. The sample hydrated at 1000 ^{o}C has the largest particle size.

Table 4-3 showing influence of water uptake on particle size variation

Sample	2Thetha Angle	FWHM	Crystallite Size (µm)
Non-hydrated CA3	33.161	0.074	0.920
C3A-900 ^{o}C	33.169	0.069	1.790
C3A-1000 ^{o}C	33.168	0.068	2.206
C3A-1100 ^{o}C	33.234	0.081	0.550
C3A-1200 ^{o}C	33.180	0.070	1.508

Thus, like other parameters characterized, the results obtained shows there is correlation between the particle size and the hydration temperature.

There is observable difference in surface morphology between the non-hydrated and hydrated samples in the SEM micrographs as shown in Figure 4-10a-f. All the samples have averagely same particle size of about 1µm and smooth surfaces for catalysis. The observed particle size agrees with the calculated in Table 4-3. The morphology as seen on the micrographs indicates that the hydration occurred carefully and the C3A surface did not show any evidence of agglomeration of particles due to the reaction of C3A with water and formation of calcium aluminate hydrate as is often observed when C3A was hydrated in reasonable water quantity[26].

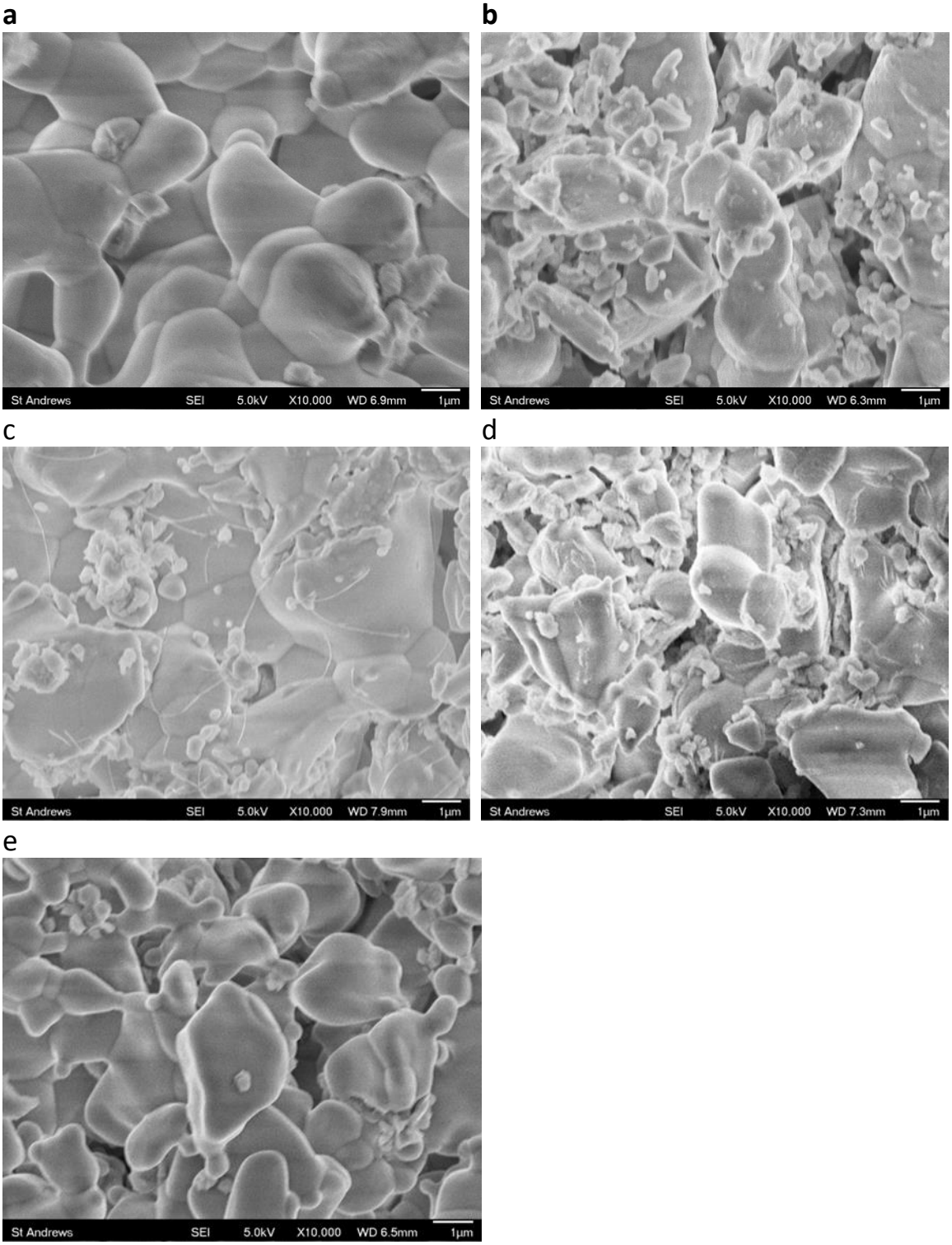

Figure 4-10 SEM micrographs showing the surface morphology of **a**, non-hydrated C3A samples and hydrated C3A **b**, at 900 ^{o}C **c**, at 1000 ^{o}C, **d**, at 1100 ^{o}C and **e**, at 1200 ^{o}C

It is believed that much hydration affects the surface morphology by agglomeration. However, it appears there is formation of tiny phases on the surface of the hydrated samples that are not seen on the non-hydrated C3A which might be due to the

hydroxide products. Furthermore; the samples seems to become denser with the increase in hydration temperature from 900-1200 ^{o}C or from Figure 4-10b-f. The phases on the SEM micrographs of the hydrated samples though not confirmed could be the hydroxide products.

4.2.3 Hydration of C3A at different temperatures and its influence on physicochemical properties

Tricalcium aluminate was hydrated at different temperature and the influence of hydration temperature on the surface area, pore volume and size was investigated and the results are as shown in Table 4-4. Micromeritics Tristar II 3020 was used for Branuer-Emmet-Teller (BET) surface area and Barret-Joyner-Halenda (BJH) pore volume and size determination using nitrogen adsorption/desorption at 77.35K. The surface area and pore size decreased with increase in hydration temperature from 900-1200 ^{o}C.

Table 4-4 physicochemical properties of hydrated tricalcium aluminate

Catalyst System	Hydration Temperature (^{o}C)	Surface Area (m^2g^{-1})	Pore Volume (cm^3g^{-1})	Pore Size (nm)
$Ca_3Al_2O_6$	Non-hydrated	2.0937	0.00128	11.3951
‘’	900	3.3584	0.01367	13.9927
‘’	1000	2.5339	0.01027	13.5463
‘’	1100	2.1239	0.00734	12.3843
‘’	1200	1.5894	0.00395	8.0280

This is attributable to the fact that the materials has taken up water vapour and expands up to 900 ^{o}C leading to high surface area but at higher temperatures from 1000-1200 ^{o}C the amount of surface water uptake gradually decreases. This observation is corroborated in the thermo-gravimetric analysis shown in Figure 4-3. The increase in the pore volume could also be attributed to same reason. This indicates that the hydration temperature has influence on physicochemical properties of the materials which are important parameters in catalysis. It is important to note that C3A 1100 ^{o}C large lattice water uptake and large cell parameter did not translate to a large surface area for it which may likely reduce it activity. Perhaps this is due to the formation of large hydration products due to large water uptake that led to the observed reduced surface area. This further justifies the optimisation of the hydration temperature. Therefore, from this it is likely that the samples hydrated from 1000 ^{o}C

and above may have reasonable surface water and might be more active since in transesterification reaction requires all the species participating in the reaction to be dry[27].

4.2.4. Influence of hydration temperature or degree of hydration on the catalyst activity

Figure 4-11 shows the results of the screening test carried out among the non-hydrated and samples hydrated at different temperatures using biodiesel yield as index for measuring activity. The test was done at 80 ^{o}C with methanol and vegetable oil-methanol ratio of 1:18 for 7 hours. The result indicates that the hydrated samples are active for biodiesel synthesis. This is attributable to the strong basic sites on their surfaces due to formation of hydroxide products from the hydration process as shown by the TGA and TPD results in section 4.2.1.1 and 4.2.1.2 respectively. The samples hydrated at 1000 ^{o}C and 1200 ^{o}C were more active yielding 96% and 92% biodiesel respectively while the sample at hydrated at 900 ^{o}C was the least active which gave only 43% biodiesel yield. The error bar show no much variation when the test was repeated. The non-hydrated C3A yielded little perhaps due to its weak basic surface relatively. Thus the hydration and consequent formation of basic products have enhanced the catalytic behaviour of C3A.

The high catalytic activity of the samples hydrated at 1000 ^{o}C and 1200 ^{o}C is attributable to having the optimum basic site as seen in the TGA and TPD analysis of section 4.2.1.1 and 4.2.1.2 respectively. The poor yield recorded for the 900 ^{o}C hydrated sample despite its strong basic surface as seen in section 4.2.1.2 is attributable to its poor vapour or moisture uptake which might have affects formation of the basic products on its surface. What is also clear is the fact that the strong basic properties of the sample hydrated at 1100 ^{o}C did not translate to best activity which suggests its large lattice water and formation of hydration products influences it performance in the catalysis of transesterification reaction as seen in Figure 4-3. The reaction require all the reactants and catalysts to be dried as water or moisture might lead to emulsion which consumes catalyst and make biodiesel separation difficult. Thus, C3A-1000 ^{o}C and C3A-1200 ^{o}C represents the optimum hydration temperature.

Why C3A takes lot of water at 1100 ^{o}C which lies between the two optimum temperatures (1000 and 1200 ^{o}C) is not yet ascertained perhaps experimental errors.

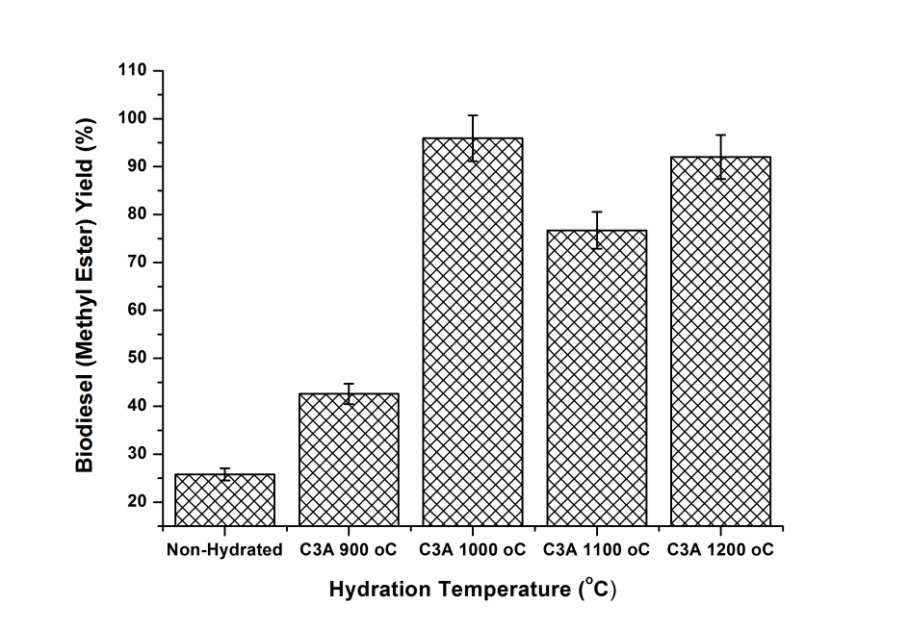

Figure 4-11 Results of screening test showing biodiesel yield as function of catalysts hydration temperature

Generally it is interesting to observe that there is a good correlation between the degree of hydration, lattice parameter and catalyst activity as shown in Figure 4-12. This concludes that, hydration temperature could be tailored to enhance structural properties and surface chemistry of C3A for enhanced biodiesel synthesis.

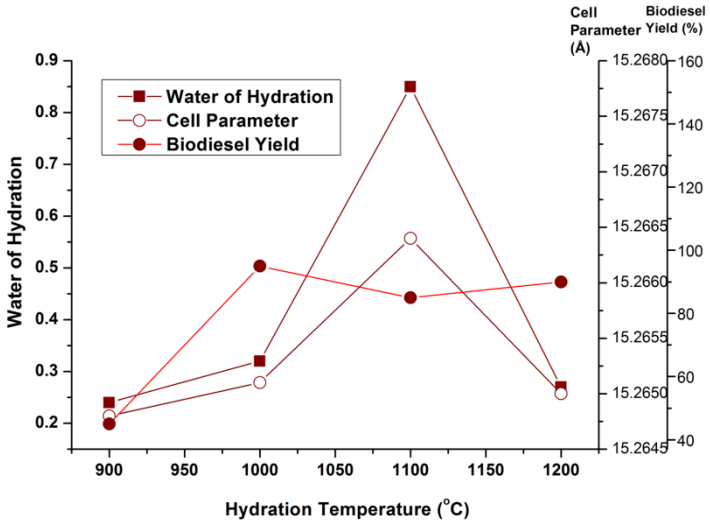

Figure 4-12 shows a close correlation between degree of hydration, lattice parameter and biodiesel yield.

Note that further analysis was based on the sample hydrated at 1000 ^{o}C only as a representative sample which showed the highest performance.

4.2.5 Influence of reaction conditions on the catalyst activity

4.2.5.1 Influence of catalyst amount and vegetable oil-to-methanol ratio

The optimum quantity of catalyst required for the transesterification was investigated using C3A 1000 ^{o}C sample at 80 ^{o}C with 1:18 methanol ratios for seven hours. The catalyst amount was measured in weight percent (wt %) based on the weight of the vegetable oil used for the transesterification reaction. Catalyst amount ranging from 1% to 2.5% was chosen for the study. The results obtained as shown in Figure 4-13b shows that biodiesel yield increased steadily as the quantity of catalyst increases to a maximum at 2% but dropped when the catalyst amount was increased to 2.5%. The decrease in yield at 2.5% might be due to catalyst particles agglomerating with increase in catalyst amount resulting to poor catalyst surface accessibility which led to undesired reactions and consequent decrease in yield.

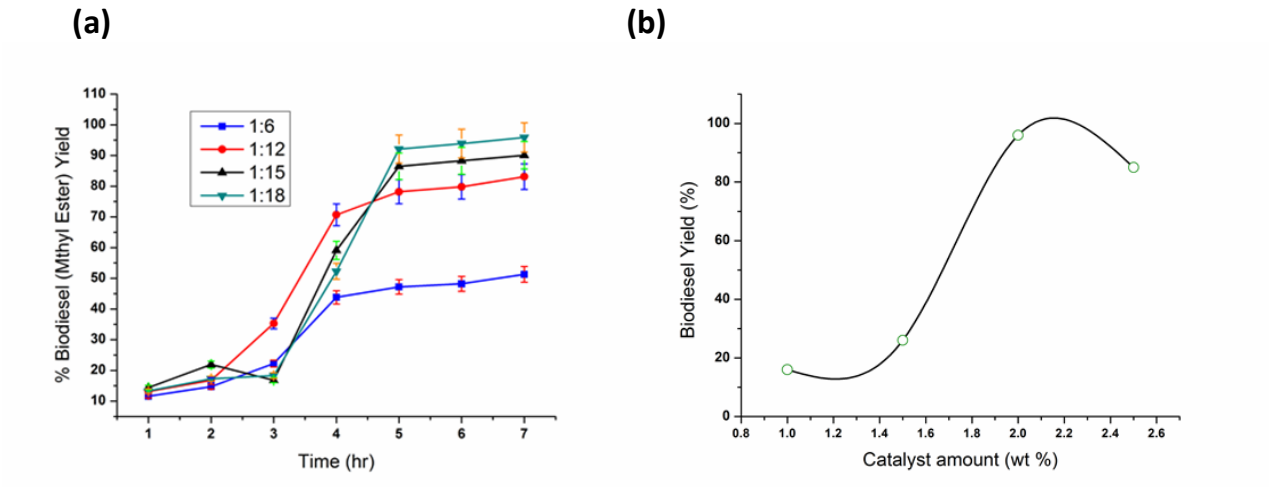

Figure 4-13 Influence of reaction condition: **a,** influence of vegetable oil-to-methanol ratio and **b,** optimization of catalyst amount

The stoichiometric equation for transesterification in Eqn. 2-1 shows that one mole of vegetable oil requires only three moles of methanol for complete transesterification of vegetable oil. In practice, higher methanol ratio is used to keep the equilibrium reaction to the right hence favouring biodiesel yield. Results of the optimization test as depicted in Figure 4-13a shows that vegetable oil-to-methanol ratio of 1:18 is the optimum for hydrated tricalcium aluminate catalyst. This value is reasonable and

attributable to the strong basic site of the hydrated tricalcium alumina surface which also agrees with the fact that strong basic catalysts do not usually require much methanol for complete transesterification. Furthermore, the yield with the other ratios-1:15, 1:12 and 1:6 was 90%, 83% and 51% biodiesel yield respectively which shows that good yield is obtainable even at lower vegetable oil-to-methanol ratio. The progress of the conversion monitored over time as seen in Figure 4-13a shows that conversion was not good within the first 3 hours but soared after three hours and highest conversion was attained within seven hours. The slow progress of the yield within the first three hours is attributable to the immiscibility of the three important components of the reaction mixture (vegetable oil-catalyst-methanol) as limiting factor which gets better over time under vigorous stirring as the liquid phase are immiscible. Because the three components of the reaction mixtures are not miscible with one another there is limited contact for effective reaction to occur. Mixing and agitation improves contact and miscibility over time. Although the highest conversion was obtained after seven hours, significant conversion >50% was obtained in virtually all the cases within 4 hours except 1:6 which gave conversion >40%. More importantly biodiesel yield >80 and >90% was obtained using 1:15 and 1:18 ratio within five hours. These attest to the high activity of these catalysts. The catalytic behaviour and performance observed compares with what Yan et al reported for very active oxides of group II (CaO, MgO, SrO and BaO) in transesterification of rapeseed oil at 64.5 ^{o}C using 18:1 methanol-vegetable oil ratio. Their work also reported that conversion was related to basic strength of the catalyst surface[28].

4.2.5.2 Influence of transesterification reaction temperature

Transesterification reaction was done at different temperatures using 1:18 vegetable oil-to-methanol ratio for seven hours to optimize the reaction temperature. Reaction temperature is an essential factor that influences transesterification reaction and the result is shown in Figure 4-14.

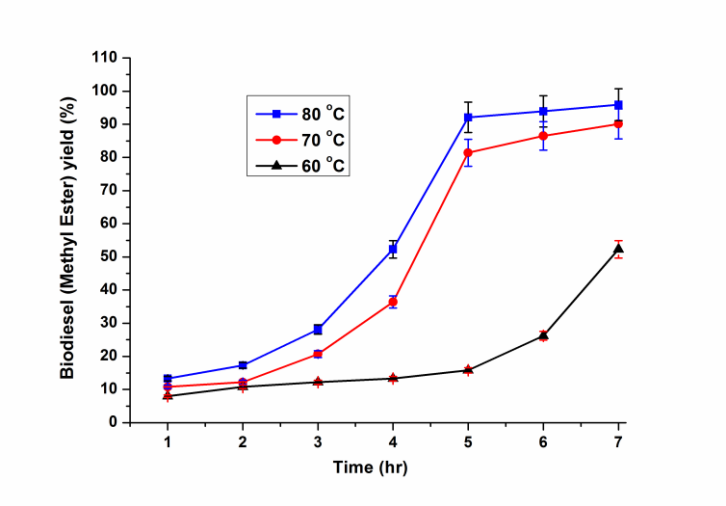

Figure 4-14 showing how biodiesel yield changes under the influence of temperature

The result confirmed that 80 ^{o}C is the optimum temperature for the transesterification reaction using hydrated tricalcium aluminate. Generally, biodiesel yield increased with increase in temperature. Progress of the conversion monitored over time as seen in the Figure also shows similar trend obtained in section 4.2.5.2 with the most active time still falling between 3 and 5 hours. The result indicates that conversion > 80 % is obtainable within five hours at 70 ^{o}C and 80 ^{o}C respectively whilst reasonable or good conversion > 50 % was obtained at 60 ^{o}C after 7 hours. This has further strengthened the good catalytic activity observed or recorded for the strongly basic hydrated tricalcium alumina. Suffices to add that controlled hydration of tricalcium aluminate is capable of enhancing its properties for use as basic catalyst for biodiesel synthesis.

4.3 Alkaline earth and transition metals doping on $Ca_3Al_{2-X}M_xO_{33}$ (M=Mg, Sr and Zn. while X= 0.1, 0.25 and 0.5) and its influence in catalysis of transesterification reaction to biodiesel

In this section, tailoring structural and surface properties of tricalcium aluminate (C3A) by doping its Al-site with strongly basic cations of alkaline-earth metals (Mg and Sr) and transition metal (Zn) to enhance its structural and surface properties as basic catalyst for biodiesel synthesis was explored. The work is also expected to offer some remedy to leaching problems associated with the use of metal oxides such as MgO, SrO and ZnO as catalyst for biodiesel synthesis which despite their good activity deactivate rapidly due to leaching of the active phase.

4.3.1 Thermal stability and basic strength of the catalyst surface

4.3.1.1 Thermal stability

Result of thermo-gravimetric analysis on the pure C3A and metal doped-C3A samples in Figure 4-15 shows one point of significant weight loss as results of dehydration and possible phase transformation. The weight loss which occurred at around 370-450 ^{o}C is attributable to dehydration of the C3A and metal doped-C3A samples as well as possible decomposition of the samples. Absence of weight loss at much lower temperature shows the samples are significantly dried containing little or no surface or loosely held water molecules in the samples compared to what was seen with hydrated samples in the previous section. Because C3A is sensitive to moisture or rapidly react with water, it can absorb moisture when exposed to atmosphere during processing which could impart some level of hydration to it.

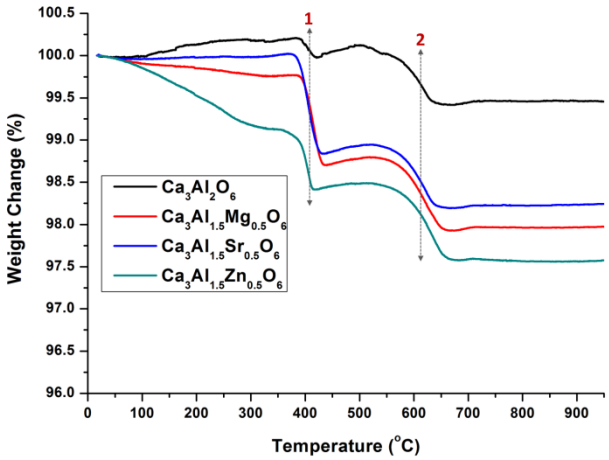

Figure 4-15 weight change in the doped and non- doped C3A samples during thermo-gravimetric analysis

When C3A is heated in a stream of dry air, it dehydrates and possibly decomposes releasing free oxides of the compound i.e. CaO and Al_2O_3. In the case of metal-doped C3A, XO (where X= Mg, Sr and Zn in this case) is added to the oxides released[29]. This explains why the observed weight loss increased with the doped samples compared to that of pure C3A. The Sr-doped seems less stable relatively. Since C3A reacts with water rapidly at room temperature and it is known that its hydration increases when doped with basic metals[16-18] due to their hygroscopic nature, then is apparent the doping has enhanced water uptake as reflected by the trend of the weight loss.

Therefore the weight loss is due to dehydration as well as decomposition which vary with the doping cations. The degree of hydration is related to the formation of basic hydration products and catalytic behaviour as established in section 4.2. Thus this further suggests Sr-doped as the most basic judging by its largest weight loss hence more suitable for the catalysis of transesterification reaction to biodiesel. To further support this observation, the number of water molecule anchored on each molecule of the C3A and metal-doped C3A was calculated and the results are shown in Table 4-5. The results confirm that the Sr-doped is more hydrated ($Ca_3Al_{1.5}Sr_{0.5}O_6.0.2H_2O$) and therefore more basic. The results also reflect high degree of hydration with the metal doped-C3A compared to non-hydrated pure C3A which justifies the aim of doping C3A i.e. to enhance surface and structural properties for maximum biodiesel yield.

Table 4-5 Weight change among the doped samples from thermo-gravimetric analysis

Samples	Number of H_2O molecule/sample
$Ca_3Al_2O_6$	0.03
$Ca_3Al_{1.5}Mg_{0.5}O_6$	0.16
$Ca_3Al_{1.5}Sr_{0.5}O_6$	0.20
$Ca_3Al_{1.5}Zn_{0.5}O_6$	0.11

The second weight loss around 550 to 650 ^oC seems the same with the entire samples and therefore does not reflect their variations and could be due to instrument.

4.3.1.2 Basic strength of the catalyst surface

As explained in section 4.2.1.2, strength of basic site of the doped samples was investigated using CO_2 temperature programmed desorption and the result is shown in Figure 4-16. There is only one distinct CO_2 peak in all the samples which occurred at high temperature attributable to strong basic sites. No corresponding distinct sharp Peak of CO_2 due to weak basic site is observed at low temperatures. This shows that the doped sample surface largely contains strong basic sites. This could be due to the strongly basic alkaline metal dopant ions used. The transition metal Zn-doped samples also showed strong basic surface despite the fact that ZnO may have acidic properties. Even if there are possible basic-acidic sites, it is evident from the TPD test results the basic site are the predominant sites. Compared to pure C3A sample, it is clear the doped samples have their CO_2 at slightly high temperature which suggests stronger

basic sites for the doped-C3A. The result indicates further that among the doped, the Sr-doped C3A has the strongest basic site relatively as its CO_2 peaks desorbs at high temperature. This could influence its catalytic behaviour. It suffices to add that the dopant metals have strengthened the Lewis acid-Bronsted base properties of the doped metal surfaces which could translate to enhanced catalytic basic properties for the transesterification reaction.

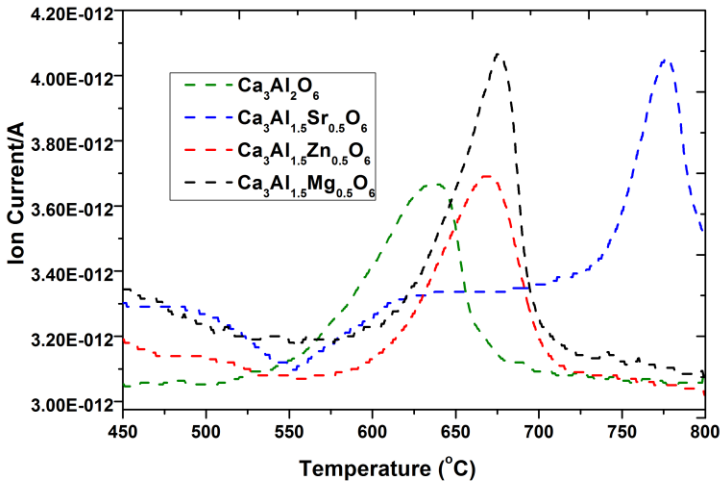

Figure 4-16 The TPD of CO_2 desorption from pure and doped C3A samples monitored as a function of temperature showing comparison of basic site strength between the pure C3A and doped-C3A. There is enhancement of basic strength from the C3A to doped C3A

4.3.2 Crystallographic and micro structure

The X-ray diffraction patterns for the pure tricalcium aluminate sample and those for the Mg, Sr and Zn doped C3A samples are compared in Figure 4-17. All the doped samples have shown the distinct characteristic cubic most intense peak just like the pure C3A at approximately 33.169^{o}. All other major and minor peaks aligned perfectly which suggest high purity, solubilisation and assimilation of the dopants into the C3A lattice structure perhaps due to the very low doping ratio used. If higher dopant ratio was used it would have caused a lot of constrain in the C3A crystal lattice due to replacement of small ion (Al^{3+}) with bigger ones (Mg^{2+}, Sr^{2+} and Zn^{2+}) that would have resulted to formation of secondary phases. So the dopant ratio used in this study is quite suitable.

Furthermore, Magnification of the most intense peaks (4 4 0) as shown in Figure 4-18a revealed a shift to smaller 2theta or bigger d-spacing in the peak position of Sr-doped C3A whilst the Mg-doped and Zn-doped peaks shift to bigger 2theta or smaller d-spacing in relation to the peak position of pure C3A. The shift is attributed to the variation in the ionic size of the dopants as corroborated by the correlation in Figure 4-18b.

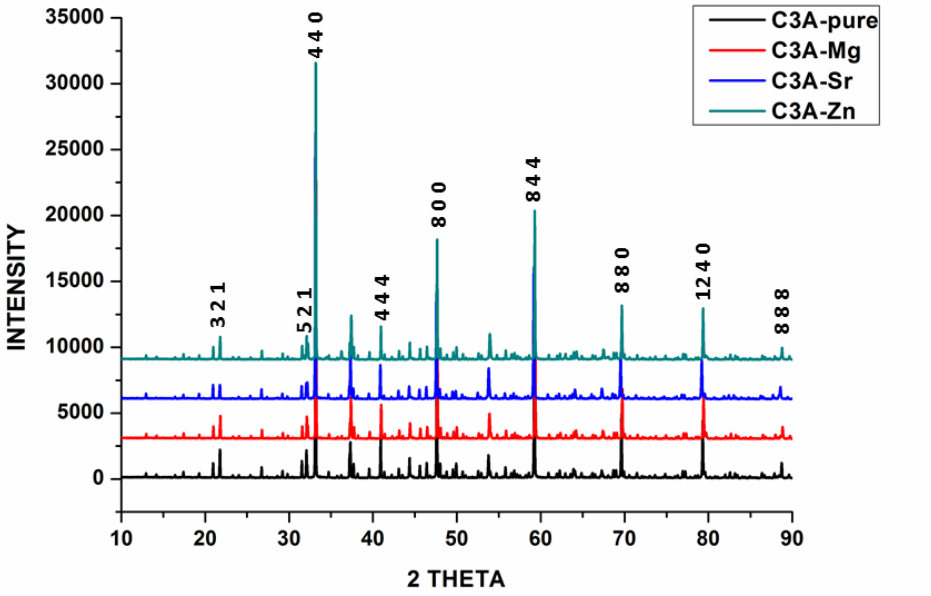

Figure 4-17 Comparison of the XRD patterns of the C3A doped samples with that of pure C3A samples as well as the indexed peaks. The alignment shows no extra peaks due to secondary phase from the dopants ions which suggest high purity due to full solubilisation of the dopants.

The Figure 4-18b also confirms that the doping involved replacement of the smaller Al^{3+} ion with bigger Mg^{2+}, Sr^{2+} and Zn^{2+} ions. The shift further suggests that the substitution was successfully done.

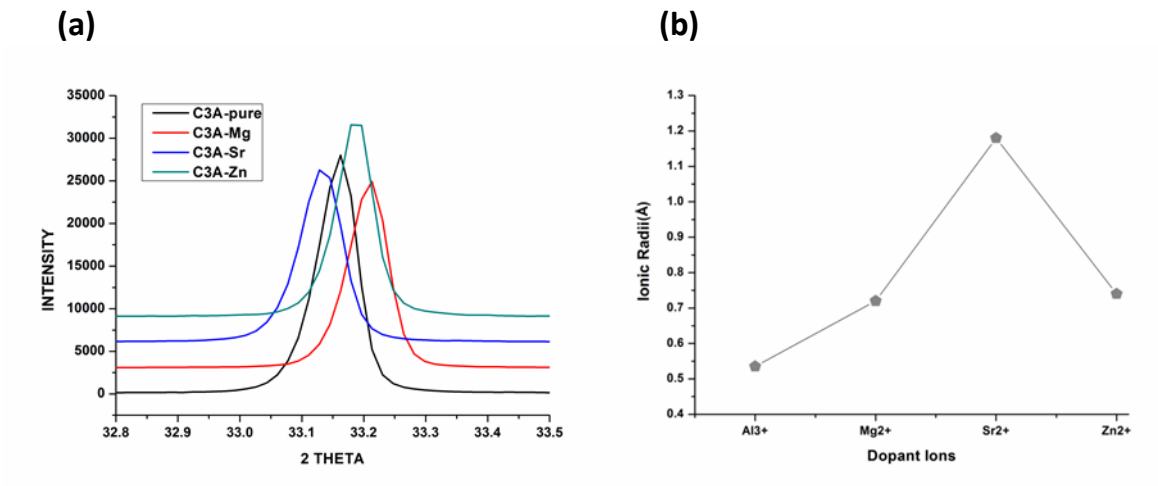

Figure 4-18 Analysis of shift in peaks position and dopants ionic size variations. **a,** shows that the bigger Sr^{2+} shift to smaller 2theta but bigger d-spacing in relation to the peak position of the pure C3A. The peak positions due to Zn^{2+} and Mg^{2+} are at bigger 2theta but smaller d-spacing relatively. The variations clearly reflects the ionic size variations in Figure 4-14b. **b,** variation in dopants ionic size (Shannon[30])

Interestingly, the refinement of the XRD patterns with the STOE WinXpow software with ICSD No.205 has proved them to be cubic with *Pm*3*m* space group. The refinement data in Table 4-6 shows that lattice parameter (a) and cell volume of the representative 0.25% doped sample closely agrees with the 15.263(3) Å and 3555.66 A^3 respectively for C3A from the literature[7].

Table 4-6 Refinement data of the C3A doped samples.

Samples	Lattice Parameter (a)	Cell Volume (A^3)	2thetha zero point
$Ca_3Al_{1.75}Mg_{0.25}O_6$	15.2506(3)	3547.01(11)	0.0049(12)
$Ca_3Al_{1.75}Sr_{0.25}O_6$	15.2798(5)	3567.42(19)	0.0075(20)
$Ca_3Al_{1.75}Zn_{0.25}O_6$	15.2598(3)	3553.44(13)	-0.0056(14)

There is a clear variation in cell parameters and cell volumes among the individual XRD patterns of the C3A-doped samples. Figure 4-19a compares variation in cell parameters among the doped samples to their respective cell volumes. It is clear the two variables show a similar trend. The cell parameter decreased from the host materials to Mg-doped sample and increased at Sr-doped sample and dropped at Zn-doped sample. The cell volume plot against respective samples showed similar variation as well. The variation in cell parameter and cell volume is attributable to the sensitivity of those variables to the variation in ionic size of the individual dopants as

confirmed in Figure 4-19b in a plot of ionic radius and lattice parameter against dopants which reflects a similar trend. These attest to the success of the doping.

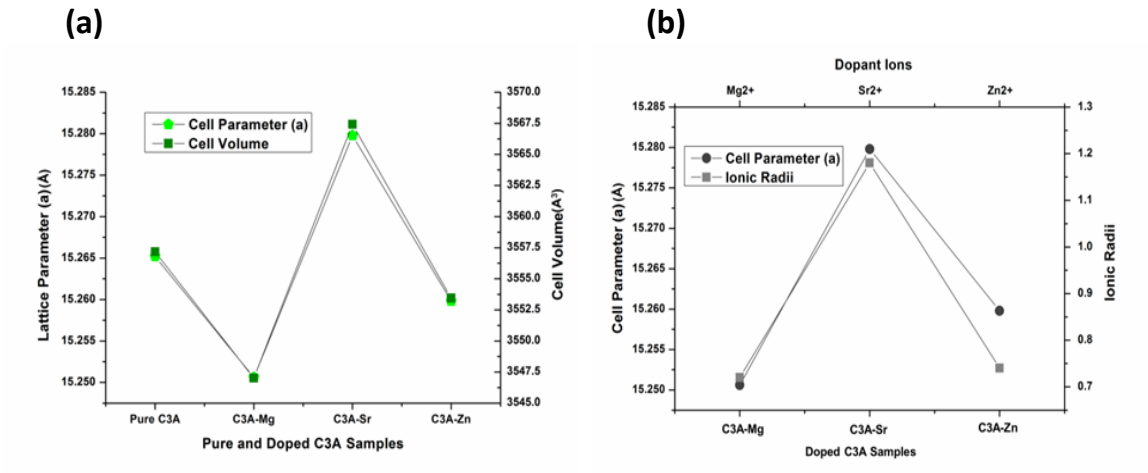

Figure 4-19 comparison between **a**, Lattice parameter and cell volume and **b**, lattice parameter and ionic radius. These shows direct relationship between the cell parameters obtained and the ionic radius of the dopant ions

It is interesting to show there is correlation between the lattice parameter (a) and the degree of hydration or moisture uptake by the samples recorded from TGA analysis of section 4.3.1.1 as shown Figure 4-20. This suggests that surface basic and structural properties can be tailored by doping with suitable metal cations for enhanced biodiesel yield.

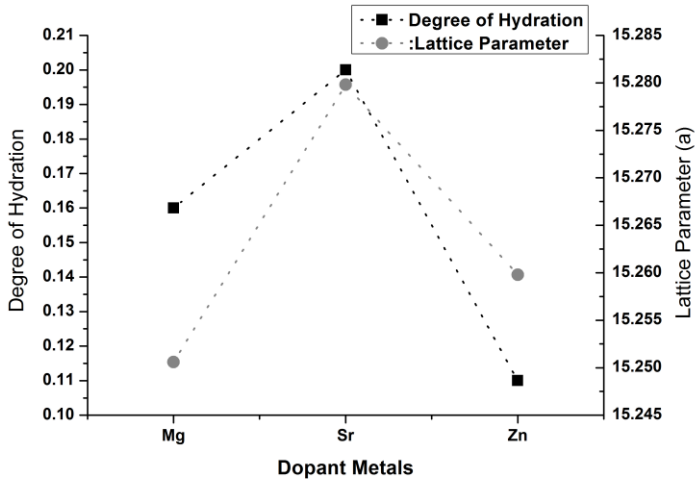

Figure 4-20 Correlation of degree hydration with lattice parameter of the metal-doped C3A

Crystal size analysis was also investigated to further characterize the particle size suitability of the C3A doped samples for catalysis of transesterification reaction to

biodiesel. Table 4-7 give the calculated results obtained from Scherrer's equation using 0.25% doped sample as representative sample.

Table 4-7 influence of dopant ions on particle size

Sample	2Thetha Angle	FWHM	Crystallite Size (µm)
$Ca_3Al_{1.75}Mg_{0.25}O_6$	33.208	0.075	0.841
$Ca_3Al_{1.75}Sr_{0.25}O_6$	33.146	0.083	0.491
$Ca_3Al_{1.75}Zn_{0.25}O_6$	33.178	0.073	1.027

The doped C3A samples had a crystallite size around 1µm which agrees with the 1µm observed in the SEM micrographs in Figure 4-21a. The particle size varies reflecting different dopants used. The Sr-doped sample showed the least particle size which might be of advantage to it in the catalysis. Generally the particle size growth observed is attributable to high calcination temperature used in the sample preparation. Thus, like other parameters characterized, the results obtained shows there is a correlation between the particle size and the dopant ions with Sr-doped having the most suitable particle size.

Micrograph of the doped samples did not show much difference in the microstructure when compared the host C3A sample. All the samples appear to show good, smooth and dense surface area for catalysis as evident in Figure 4-21a-c.

a, Pure C3A

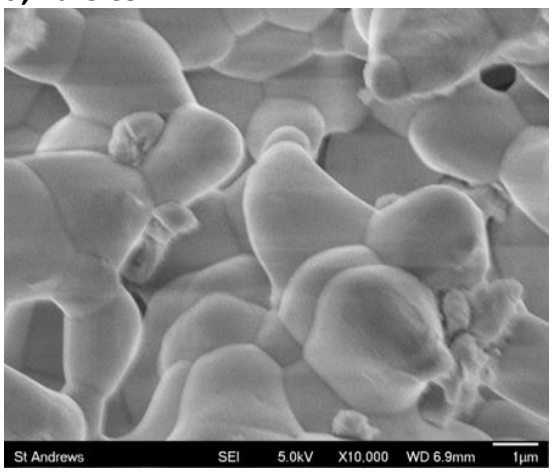

b, C3A-Mg

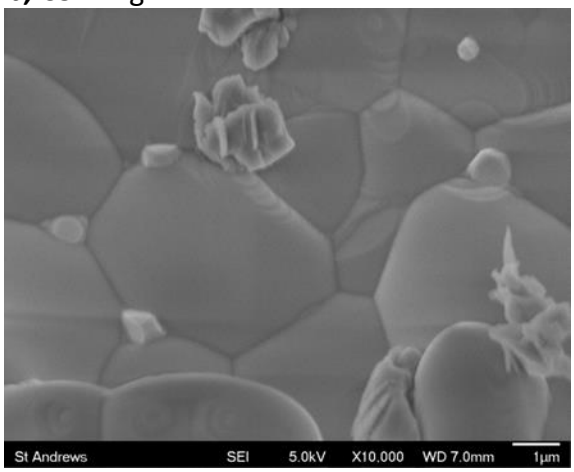

c, C3A-Sr

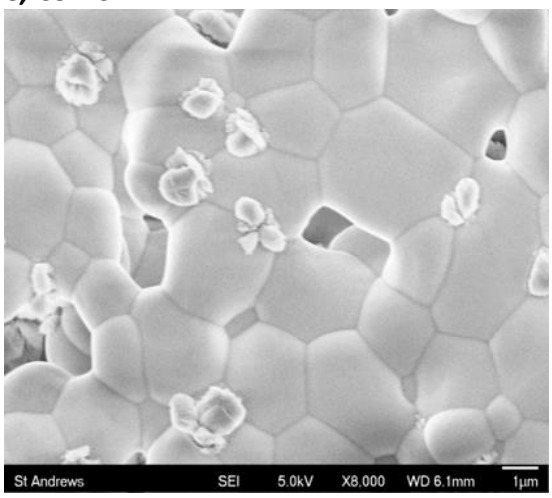

d, C3A-Zn

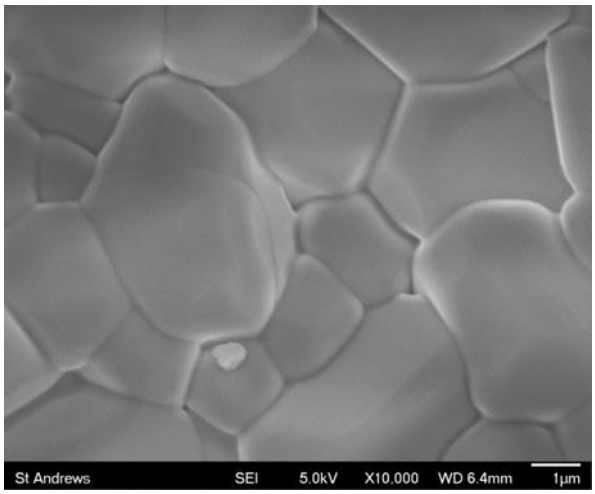

Figure 4-21 SEM micrographs comparing surface morphology of the pure C3A to those of the doped samples

Although they have average particle size of about 1µm, the Sr-doped C3A seems to have smaller particle size relatively. The smaller particle size of the Sr-doped sample corroborates its calculated smaller particle size relatively using Scherrer's equation in Table 4-6 and might favour its catalytic activity for better performance.

4.3.3 Materials physicochemical properties

Table 4-8 shows how surface area of the materials changes with the dopants as well as the doping ratio. The Sr dopant provides better surface area and pore volume and the lowest pore size relatively while the Zn-doped systems showed lowest surface area relatively. Mg-doped showed moderate surface area and pore size. Generally, surface area and pore volume increased as the doping ratio increases among each set of the doped catalyst systems whilst pore size showed the reverse trend. The decrease in the pore volume and increase in pore size as the doping ratio increases is an indication of solubilisation of the dopants into the host tricalcium aluminate lattice structure. Since transesterification reaction of vegetable oil to biodiesel involves long chain triglyceride fatty acids, the potentials of Sr-doped sample such as large pore size in addition to its large surface area relatively are expected to be an advantage to it.

Based on the properties of the materials characterised so far from thermal analysis through crystallography and micro structures up to physicochemical properties such as surface area, it is clear the doping has enhanced structural and surface properties

of C3A. The Sr-doped system has shown the most suitable properties for a catalyst which is likely to translate to good biodiesel yield.

Table 4-8 showing how surface area, pore volume and pore size changes with dopant and doping ratio

Catalyst System	Surface Area (m^2g^{-1})	Pore Volume (cm^3g^{-1})	Pore Size (nm)
$Ca_3Al_{1.9}Mg_{0.1}O_6$	0.7558	0.001806	12.4487
$Ca_3Al_{1.75}Mg_{0.25}O_6$	1.5420	0.005340	13.3427
$Ca_3Al_{1.5}Mg_{0.5}O_6$	7.7374	0.024369	13.8875
$Ca_3Al_{1.9}Sr_{0.1}O_6$	1.7027	0.004770	20.7881
$Ca_3Al_{1.75}Sr_{0.25}O_6$	1.2545	0.004775	15.7160
$Ca_3Al_{1.5}Sr_{0.5}O_6$	1.8233	0.005780	15.6539
$Ca_3Al_{1.9}Zn_{0.1}O_6$	0.8723	0.003093	15.0293
$Ca_3Al_{1.75}Zn_{0.25}O_6$	1.074	0.004112	14.8421
$Ca_3Al_{1.5}Zn_{0.5}O_6$	1.5001	0.004219	9.75620

4.3.4 Influence of dopant concentration on biodiesel yield and optimization of catalyst amount

The Al-site of C3A doped with MgO, SrO and ZnO ions using different doping ratio of 0.1-0.5 mole percent of each metal was meant to enhance its catalytic properties by improving the strength of its basic site due to the poor performance recorded for it (C3A) from the screening test result in section 4.2.4. The diagram in Figure 4-22a shows how each dopant influences biodiesel yield in transesterification reaction of sunflower oil and also how such influence changes with the doping ratio of each dopant. The test was performed at 80 ^oC using 2%wt of the catalyst. Generally, all the catalyst systems are active in biodiesel synthesis. This is due to the possible enhancement of the C3A Lewis acid-Bronsted base properties with the basic metals and suitable surface area as characterization of their properties in the previous sections portrays. On the individual merit of the dopant, the 0.5 mole % systems are more active with Sr-doped catalyst slightly more active yielding 96% biodiesel and 0.5 mole % Zn-doped catalyst had the least yielding 83%. Thus the influence of the dopant on the biodiesel yield follows the order Sr>Mg>Zn. Likewise, the performance of the catalyst based on the doping ratio shows increase with the increase in the doping ratio as seen in Figure 4-22a hence 0.5 mole doping gave the highest biodiesel yield in each series thus: 0.1<0.25<0.5. This corroborates the trend observed in the, SEM, particle

size and TPD analysis above in relation to the basic strength or properties of the samples. Therefore, the performance of the Sr-doped catalyst is attributable to the strength of its basic site as seen in the TPD analysis and good surface area as well as smaller particle size relatively which are all very important parameters to catalysis of transesterification reaction. Although both Mg and Sr belong to same group, Sr occurs after Mg therefore is more basic than Mg since naturally basicity increases down the group.

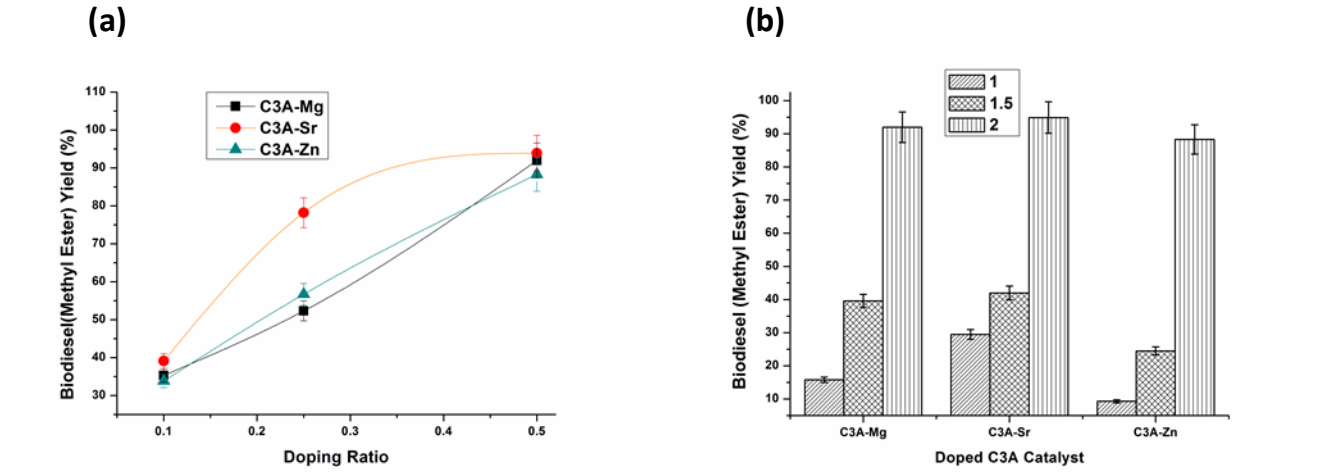

Figure 4-22 Change in biodiesel yield due to the influence of **a,** dopant ratio and **b,** catalyst amount

Zn belongs to the first row transition metal series therefore less basic than the alkaline earth metals. During transesterification reaction, the reaction between the methanol and the catalyst leads to the formation of alkoxide ion which is believed to be what initiate the transesterification reaction. A time this leads to dissolution of the catalyst active phase in the methanol due to formation of products that are soluble in methanol. Consequently, the reaction will be catalysed by both homogeneous and heterogeneous catalysis instead of heterogeneous catalysis only. Therefore methanol kept in contact with the catalyst under same reaction condition yielded no significant biodiesel when used for transesterification reaction. This shows that the dopant metal were not leached to form soluble products with methanol when the catalyst and methanol reacts at the start of the transesterification reaction hence the catalysts are good for reuse or recycling without fear of deactivation due to leaching of active phase. This demonstrates that anchoring or incorporating the active phase in the

crystal lattice as a single phase by way of doping instead composite form by wet impregnation helps to avoid or minimize catalyst deactivation by leaching.

Using the right amount of catalyst is also very important factor in catalysis. Fewer amounts could lead to poor performance due to lack of enough catalyst surfaces to effectively facilitate the conversion process. More so, use of excess might lead to poor performance as well due to lack of accessibility to the active site of the catalyst as a result of agglomeration of catalyst particles. Therefore is essential to optimize the catalyst amount. Optimization of the catalyst amount was investigated and the result is as seen in Figure 4-22b above. The result shows that 2wt% catalyst based on the weight of the vegetable oil used gave the highest yield at 80 ^{o}C using 1:18 vegetable oil-to-methanol ratios in all the sets. The biodiesel yield increases steadily as the catalyst amount increased from 1-2wt% among all the doped catalyst systems. This test also confirms that the Sr-doped catalyst gave the best performance for reason already stated above.

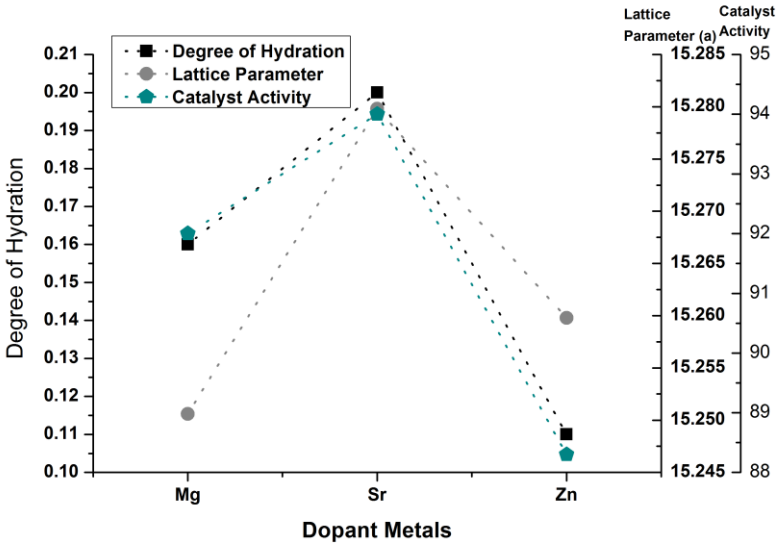

Figure 4-23 Showing correlation between lattice parameter, degree of hydration and catalytic behaviour of the of the metal-doped C3A catalyst systems

What is also interesting from these results is the nice correlation between the amounts of moisture taken by the samples or degree of hydration as calculated in Table 4-5 which is established to be related to the basic surface properties with lattice parameter as well as catalytic activity of the metal-doped C3A as shown in Figure 4-23.

This further confirms that structural and surface properties can be tailored for enhanced properties and biodiesel yield through doping with suitable metal cations. The doping metals enhanced the moisture up take as shown by the TGA investigation which might have resulted to formation of some hydroxide products and stronger basic surface. This also indicates that both doping and hydration or moisture up take affects the structural properties of the materials as well as their catalytic behaviour.

4.3.5 Influence of vegetable oil-to-methanol ratio

From the results of screening test in section 4.3.4 on the metal-doped C3A sample, it is clear tailoring the structural properties by doping has enhanced catalytic behaviour of the material for biodiesel synthesis compared to what was seen in section 4.2.4 with pure C3A. To further investigate the performance of the catalyst in order to establish its robust behaviour, influence of vegetable oil-to-methanol ratio being one of the factors that potentially influences biodiesel yield was explored. The transesterification test was carried out using Sunflower oil at 80 ^{o}C and 2wt % catalyst with methanol. The results of the test as shown in Figure 4-24 indicates that biodiesel yield changes progressively with increase in vegetable oil-methanol ratio. This reaffirms the importance of this factor in transesterification reaction for biodiesel synthesis. Vegetable oil-to-methanol ratio of 1:18 is the optimum ratio for highest conversion.

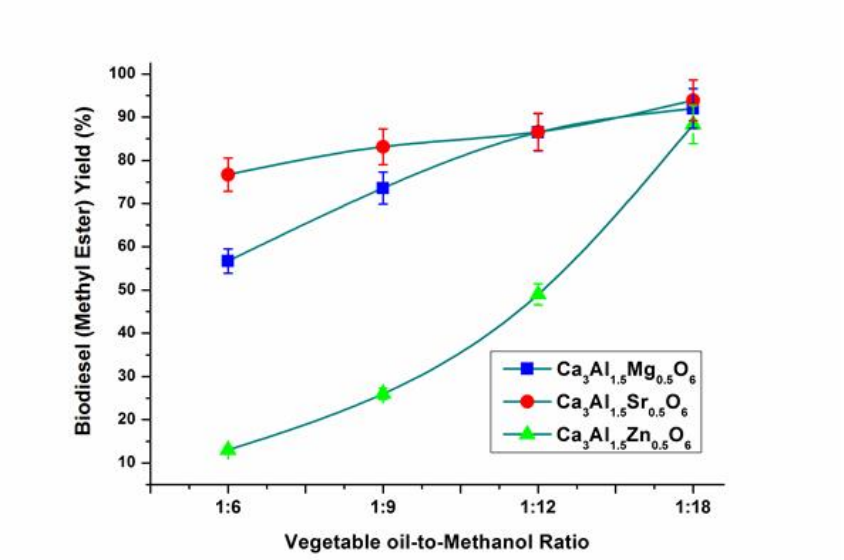

Figure 4-24 Progress in biodiesel yield as a function of vegetable oil-methanol ratio

It is important to observe that although highest conversion was obtained using 1:18 oil-methanol ratio, good biodiesel yield of 87% and 74% was recorded using oil-methanol ratio of 1:9 with Sr-doped and Mg-doped catalysts respectively and Zn-doped catalyst yielded only 26% biodiesel. There was no significant increase in biodiesel yield when oil-methanol ratio increased from 1:9 to 1:12 using the Sr-doped catalyst as depicted in the chart and the increase observed was only 7% as the ratio increased from 1:12 to 1:18 using same catalyst system. In the case of the Mg-doped catalyst, the biodiesel yield increased by 13% and 18% when oil-methanol ratio increased from 1:9 to 1:12 and 1:12 to 1:18 respectively. Zn-doped catalyst showed reasonable increase of 62% increase from 1:9 to 1:18 but showed only increase of 23% from 1:9 to 1:12 respectively. Generally, the result demonstrates the importance of this parameter in transesterification reaction. Therefore, careful choice of vegetable oil-methanol ratio could enhance biodiesel yield. Furthermore, the results show that tailoring the structure of C3A by doping with basic metals is capable of enhancing its structural basic properties for enhanced performance as corroborated by the catalytic behaviour of the doped catalysts in the screening test of section 4.3.4.

4.4 Ion-exchange resins as catalyst for biodiesel production

4.4.1 Introduction

The ion exchange resins have a micro porous polymeric structure commonly made from styrene, polyvinyl benzene monomers with suitable surface area. They also have acidic (sulphonic) or basic (hydroxyl) groups which could provide Bronsted acid or Lewis base surfaces for transesterification of vegetable oil to biodiesel without posing leaching problem. Furthermore, studies revealed that ion exchange resins owe their catalytic properties to their ability to swell thereby making their active sites accessible to reactants[31]. Shibasaki-Kitakawa et al., 2007[32] demonstrated the efficacy of ion exchange resin as catalyst using a continuous bed packed with various ion exchange resins in transesterification of triolein with ethanol. They found that anion exchange resin showed a better reaction rate and conversion than the cation exchange resin. Kim et al, 1998[33] reported high catalytic activity in some micro porous anion exchange resins in transesterification of soybean oil. He also observed that the catalytic activity

of the resin was related to the degree of cross-linking or particle size of the resin. More so, Vicente et al, 1998[34] reported <1% conversion for anionic Amberlyst-A26 and A27 and cationic Amberlyst-A15 although, later Ozbay et al, 2008[35] utilized Amberlyst-A15, 35 and 16 and Dowex HCR-W2 in esterification and obtained a conversion greater >45% with Amberlyst-A15 showing the highest conversion. More recently, Feng et al[31], 2010 demonstrated the use continuous esterification of FFA in a fixed bed using cationic resins as catalyst. The catalyst was active, reusable and yield depends on methanol: oil ratio and reaction temperature among others. Melero et al., 2010[36] reported very low activities (≈35%) for cationic Amberlyst-36 in transesterification of crude palm oil lower than that of modified sulfonic acid functionalised SBA-15. Despite their great potentials as catalyst, not much has been reported on the use of ion exchange resins as catalyst for biodiesel production.

This section explored the catalysis of transesterification reaction of Sunflower oil to biodiesel using Amberlyst-A26 and Amberlyst-36 resins as catalysts. The study was carried out using both traditional and autoclave synthesis methods.

4.4.2 Some physicochemical properties of the resins catalysts

Some physicochemical properties of the ion-exchange resins as shown in Table 4-9 indicates that both the basic Amberlyst-A26 and the acidic Amberlyst-36 have good surface area and particle size for effective catalysis of transesterification reaction. The Amberlyst-36 has slightly larger surface area and smaller particle size relatively whilst the Amberlyst-A26 has much larger pore. Although surface area and particle size are important in catalysis generally, large pores are critical in transesterification reaction involving large triglyceride organic molecules to facilitate reactant contact or collision and also for effective dissemination of the final products.

Table 4-9 physicochemical property of the resins[37]

Catalyst	Physical Form	Chemical Form	Surface area (m^2/g)	Pore Size (mL/g)	Particle Size (mm)
Amberlyst-A26	Beads	OH^-	30	0.30	0.560-0.700
Amberlyst-36	Beads	H^+	33	0.20	0.425

4.4.3 Catalyst screening test for catalytic activity

Different vegetable oil to methanol ratios was used to screen the catalyst using % yield as index for performance or activity of the catalysts in transesterification of Sunflower oil at 60 ^{o}C for five hours. The results obtained are illustrated in Figure 4-25a and b showing how the anion-exchange resin (Amberlyst-A26) and cation-exchange resin (Amberlyst-36) catalytic activity compares.

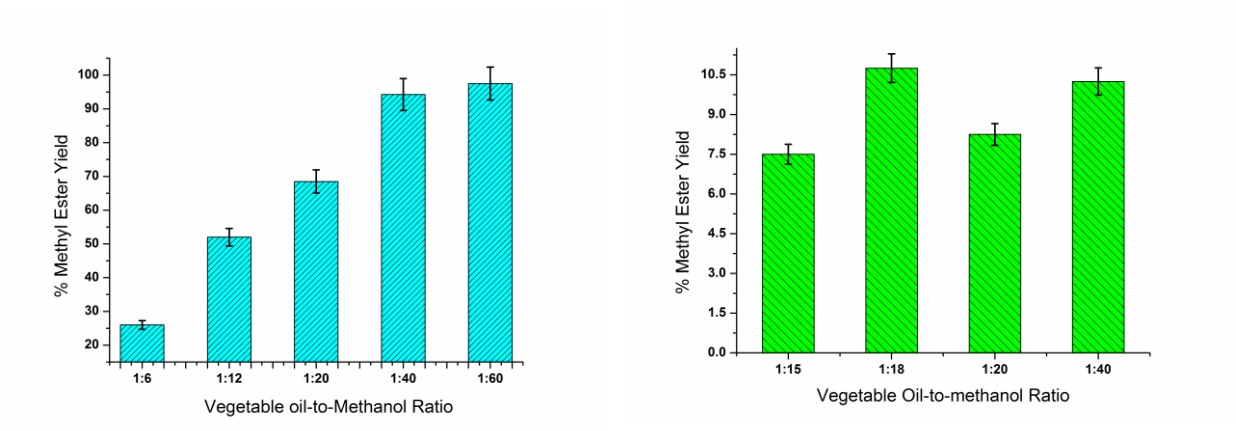

Figure 4-25 Influence of vegetable oil to methanol ratio using **a**, Amberlyst-A26 and **b,** Amberlyst-36

Using the Amberlyst-A26, maximum conversion >90% was obtained with vegetable oil to methanol ratio of 1:60 within five hours while Amberlyst-36 gave only 12 % conversion with vegetable oil to methanol ratio of 1:18 within the same five hours. The yield increased steadily with Amberlst-A26 as the vegetable oil-to-methanol ratio increased to 1:60 while the Amberlyst-36 showed a decrease in yield as the vegetable oil-methanol ratio increased from 1:18 to 1:20. No appreciable change observed when increased to 1:40 which shows the importance of this factor in transesterification. Usually amount greater than the stoichiometric 1:3 is used to move the reaction forward or speed up the rate of methyl ester production. Although cation-exchange resin requires less amount of methanol compared to anion-exchange resin, it is clear that anion-exchange resin is more active. It is interesting to note that even though the highest conversion was obtained with Amberlyst-A26 using vegetable oil-to-methanol ratio of 1:60, very good conversion >50% was obtained using oil-methanol ratio of only 1:12 which is a lot better than 10% yield recorded for Amberlyst-36 at its maximum yield using 1:18. More so, yield was ~70% with 1:20 and 27% using 1:6 with

the same Amberlyst-A26. From these results, there is improvement in the performance of the catalyst compared to what was reported for it as explained in the introductory part of this section[34,35,38]. This shows that even at low vegetable to methanol ratio, the Amberlyst-A26 catalyst is very active and high yield could be obtained. Thus, good performance of Amberlyst-A26 could be attributed to its strong accessible basic site coupled with good physical properties such as large pores and surface area and suitable particle size. Similar observation was made by Feng et al, 2010[31]. More so adsorption strength of the anion resin basic site onto the alcohol is more than what is exerted by the acidic site on the surface of the cation-exchange resin which might have facilitated the robust performance recorded for the Amberlyst-A26[32]. Thus, despite its advantage of having good physical properties such smaller particle size and larger surface area, Amberlyst-36 couldn't do well perhaps due to its weak active site or limited accessibility of triglyceride molecule to those sites as seen in Table 4-9 from its properties.

Subsequent studies on factors that influences biodiesel production such as temperature, catalyst amount as well as reusability was done on the most active and promising catalyst (Amberlyst-A26) only.

4.4.4 Investigation on the influence of reaction condition on the most active Amberlyst-A26 Catalyst

4.4.4.1 Influence of reaction time

Duration of reaction is one of the factors that affect conversion of triglyceride to methyl ester (biodiesel). The relationship between conversion and time was investigated using 1g of the Amberlyst-A26 catalyst per 10g of Sunflower oil, vegetable oil-to-methanol ratio of 1:60 and at 60 ^{o}C. Samples were withdrawn hourly and dissolved in deuterated chloroform ($CDCl_3$) and analysed using ^{1}H NMR.

The results obtained as illustrated in Figure 4-26 show that conversion increases linearly over time and maximum conversion of 99% was obtained after five hours as the optimum reaction time. It is essential to observe that though highest conversion of 99% was obtained in five hours, spectacular yield >60% was obtained within the first one hour and yield >80% within two hours and no much increase was recorded

thereafter and the reaction seemed stabilized. The results illustrates that time has marked effect on the transesterification process and good activity by the catalyst.

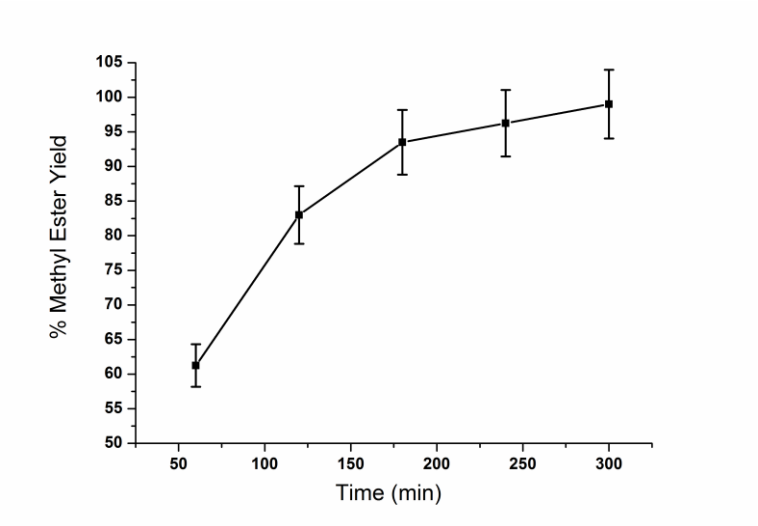

Figure 4-26 Conversion over time in transesterification of sunflower oil catalysed by Amberlyst-A26 catalyst

4.4.4.2 Optimization of catalyst amount

The influence of catalyst amount in the conversion of the Sunflower oil to biodiesel by the anion-exchange resin (Amberlyst-26) was also investigated. Catalyst amount of 0.25-1g (2.5-10 wt%), vegetable oil-methanol ratio of 1:60 at reaction temperature of 60 ^{o}C for five hours was used in the study. The diagram in Figure 4-27 shows that conversion increased with increase in catalyst amount and 10wt% was the best catalyst amount required for maximum triglyceride conversion.

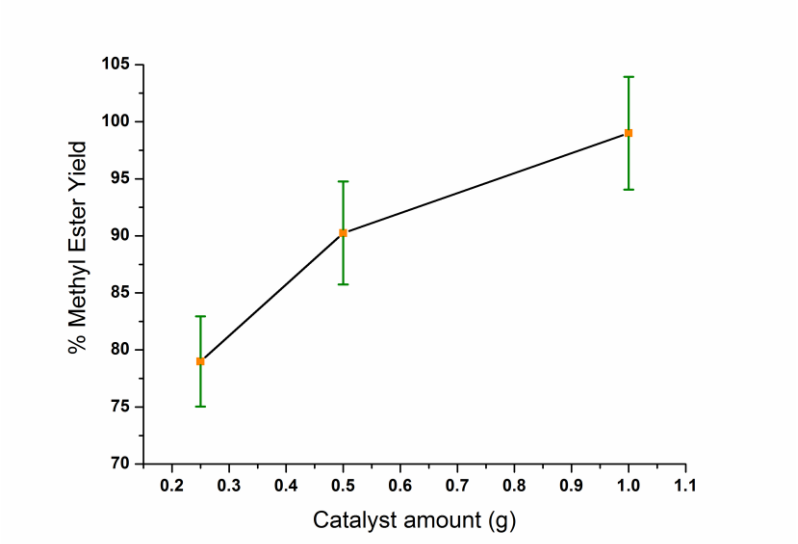

Figure 4-27 Progress in biodiesel yield showing Influence of catalyst amount

As the catalyst amount increased from 2.5-10wt% based on the weight of the vegetable oil used, no drop in conversion was observed because there was no side reactions such as saponification to reduce the yield of methyl esters in the course of the reaction. It is quite interesting that as little as 2.5% (0.25g) gave yield >80% but when the catalyst amount was doubled to 5 wt% (0.5g), the yield increased only by 15% i.e. 95% so also when increased to 10 wt% (1g) the difference was only 4% i.e 99%. This show that remarkable yield is obtainable with as little as 0.25g (2.5 wt%) of the catalyst. Therefore, although highest yield was obtained with 1g equivalent to 10% based on the weight of the vegetable oil (10g) used in the test, 0.25g (2.5%) seems the optimum amount required for maximum yield. Use of excess catalyst amount leads to poor contact and catalyst surface accessibility and therefore no sharp increase in yield was recorded. During transesterification, formation of a vegetable oil-catalyst-methanol immiscible phase (triple phase) is a limiting step which has to be minimised by optimization of catalyst amount and other reaction conditions to enhance miscibility of the reactants and catalyst for maximum biodiesel yield.

4.4.4.3 Transesterification reaction temperature optimization

This study was limited to 60 ^{o}C to guard against catalyst decomposition due to upper temperature limit of 60 ^{o}C of Amberlyst-A26. In Figure 4-28, triglyceride conversion to methyl ester increased with increase in reaction temperature. The optimum temperature for the triglyceride conversion to biodiesel using Amberlyst-A26 catalyst was 55 ^{o}C which gave the maximum conversion >99%. At a low temperature of 40 ^{o}C, conversion was >90% which confirmed high activity, selectivity towards methyl esters and efficiency of the Amberlst-A26 catalyst. This showed that at a very low temperature of 40 ^{o}C good conversion was achieved using Amberlyst-A26 catalyst. Use of low temperature transesterification reduce cost of production and enhance biodiesel synthesis economics. The results obtained are comparable to very active homogeneous catalysts such as KOH, NaOH and there alkoxides in terms of activity and from process integrity perspective[39].

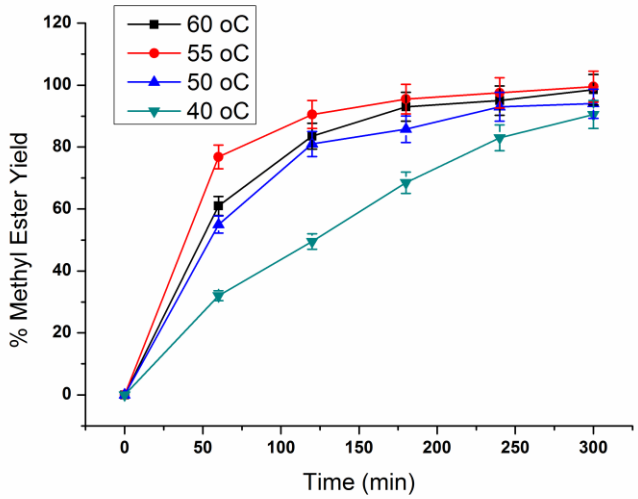

Figure 4-28 Change in biodiesel yield over time as a function of reaction temperature

This test further confirms that bulk of the yield >80% was achieved within the first two hours. Only increase of about 10% was recorded after two hours to five hours of the study which means the yield almost stabilised after the first two hours. As such we could say 2 hours is the optimum time for this reaction using Amberlyst-A26 catalyst to achieve desired results.

4.4.4.4 Catalyst reuse

Figure 4-29 shows the result obtained from repeated use of 1g of the catalyst and 1:60 vegetable oil-to-methanol ratio at 60 ^{o}C. After each run, the catalyst was recovered, washed and reused. It is evident from Figure 4-29 the catalyst activity drops only by 19% of its original activity after reused thirteen times. This is attributable to the fact the catalyst was easy to recover due to its polymeric beads form insoluble in methanol during the reaction. This denotes some sort of high regeneration efficiency, stability, and good activity of the catalyst better than what was obtained using the homogenous catalyst[39,40]

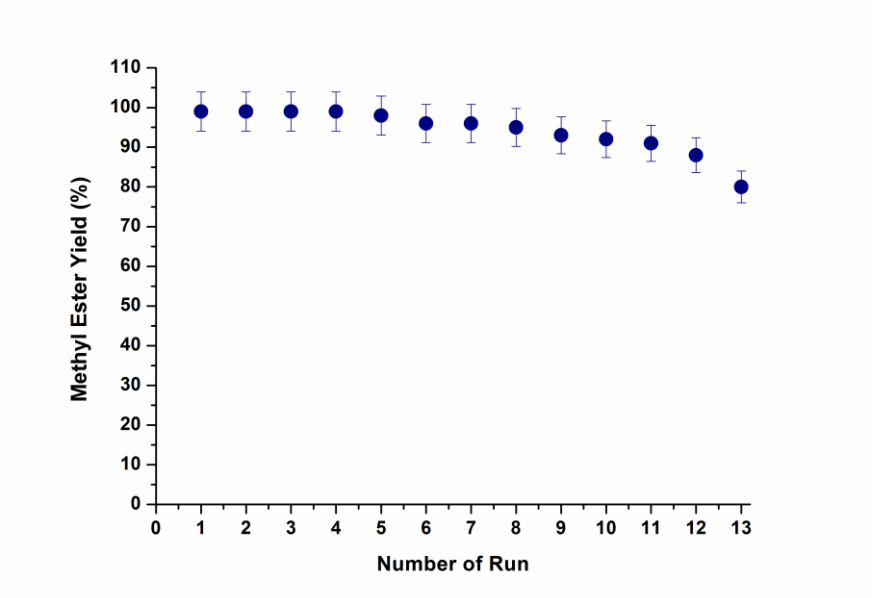

Figure 4-29 Catalyst reusability: Change in biodiesel yield as a function of number of runs

4.4.5 Autoclave synthesis and influence of reaction temperature

Both Amberlyst-A26 and Amberlyst-36 were considered in this study. I took advantage of high pressure to enhance performance of both Amberlyst-36 and Amberlyst-A26 by possibly reducing the vegetable oil-to-methanol ratio. The Influence of reaction temperatures was investigated using 1:18 vegetable oil-to-methanol ratio and 10% (1g) of catalyst based on the weight of the vegetable oil used for 24hrs on both Amberlyst-A26 and Amberlyst-36.

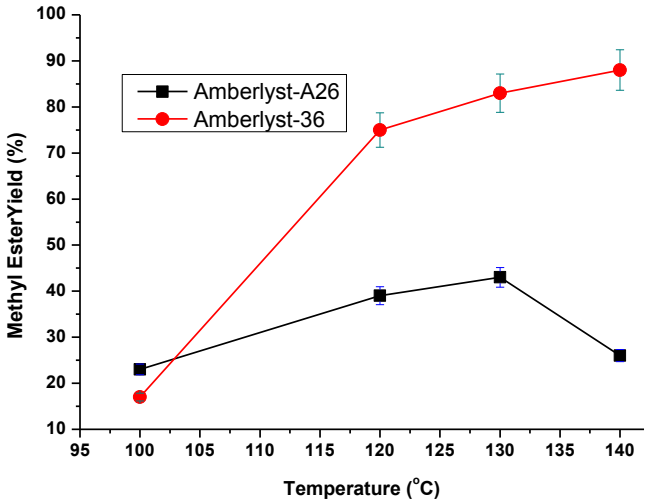

Figure 4-30 Influence of temperature in autoclave synthesis and progress in biodiesel yield over time

Hydrothermal synthesis is usually effective at temperatures above 100 ^{o}C hence the synthesis was performed at high temperature above the upper limit temperature of the Amberlyst-A26 (60 ^{o}C) resin. The results obtained are shown in Figure 4-29. Amberlyst-36 showed a progressive increase in the activity and selectivity with temperature for the methyl ester, whilst Amberlyst-A26 showed a decrease in performance at temperature above 130 ^{o}C.

Consequently, Amberlyst-36 exhibited better tolerance to high temperature and pressure hence gave high activity. In both cases, bulk of the yield was obtained at 120 ^{o}C and not much progress was recorded thereafter. Poor performance of Amberlyst-A26 could be attributed to instability and decomposition of the catalyst observed due to high pressure and temperature. The result shows that although Amberlyst-36 was less active than Amberlyst-A26 in the conventional test, it is more stable and active under severe condition.

4.5 Conclusion

Tricalcium aluminate (C3A) was synthesized successfully and its surface basic properties were enhanced by hydration and doping with some alkaline earth metals and transition metal for utilisation as transesterification reaction catalyst for biodiesel synthesis. Some ion-exchange polymeric resins were also investigated as basic and acidic catalysts for transesterification reaction to biodiesel and compared with the ceramic C3A catalysts.

Hydration of tricalcium aluminate and consequent formation of hydroxide products was found to enhance its surface basic strength. The use of such hydrated tricalcium aluminate for the first time to catalyse transesterification reaction for biodiesel synthesis was achieved. The hydration was carefully controlled and optimised at different temperature successfully. The hydration temperatures of 1000 ^{o}C and 1200 ^{o}C were found to be the optimum hydration temperatures for maximum biodiesel yield >90% using vegetable oil-methanol ratio of 1:18 at 80 ^{o}C within five hours. The robust activity of the catalyst was attributed to enhanced basic properties due to the reaction of C3A with water and subsequent formation basic hydroxides on the catalyst surface during the hydration process at elevated temperature. The hydration temperature of 900 ^{o}C recorded the least biodiesel yield of 43 % attributed to its less

moisture uptake as revealed by the TGA while too much water uptake by the sample hydrated at 1100 ^{o}C is responsible for its drop in performance.

Tricalcium aluminate has also demonstrated some flexibility to doping for enhanced basic properties when doped with alkaline earth metal Mg and Sr and transition metal Zn ions. The dopant ions enhanced the basic properties of the C3A thereby making it more suitable for transesterification reaction catalysis. The doped C3A samples were for the first time used and found to be very effective catalyst for transesterification reaction for biodiesel synthesis. The Sr-doped was found more active than Mg-doped samples and Zn-doped sample was the least active. No evidence of catalyst deactivation due to leaching of the doped active phase was observed in all the samples. Methanol soaked with the catalyst under the same reaction conditions yielded negligible biodiesel in transesterification reaction relatively. These attest to the fact that is a lot better to incorporate active phase into the lattice by doping in a single phase rather than by impregnation in composite form which leads to eroding of the active phase.

Transesterification reaction was successfully catalysed by Ion-exchange resins. Amberlyst-A26 was found to be very active catalyst for transesterification reaction. It showed good activity even at low temperature of 40 ^{o}C and could be repeatedly used without significant change in activity which further support its good activity. Catalytic activity of Amberlyst-36 was enhanced in the autoclave synthesis compared to Amberlyst-A26 whose performance showed decline. The results also showed that Amberlyst-36 is more stable to severe reaction condition than Amberlyst-A26.

References

1. Merlini, M.; Artioli, G.; Cerulli, T.; Cella, F. and Bravo, A. Tricalcium aluminate hydration in additivated systems. A crystallographic study by SR-XRPD. *Cement and Concrete Research* **38**, 477-486 (2008)

2. Manzano, H.; Dolado, J. S. and Ayuela, A. Structural, mechanical and reactivity properties of tricalcium aluminate using first-principles calculations *J. Am. Ceram. Soc.* **92(4)**, 897-902 (2009)

3. Moon, J.; Yoon, S.; Wentzcovitch, R. M.; Clark, S. M. and Monteiro, P. J. M. Elastic properties of tricalcium aluminate from high-pressure experiments and first-principles calculations. *J. Am. Ceram. Soc.* **95(9)**, 2972-2978 (2012)

4. Mishra, R. K.; Fernandez-Carrasco, L.; Flatt, R. J. and Heinz, H. A force field for tricalcium aluminate to characterize surface properties, initial hydration and organically modified interfaces in atomic resolution. *Dalton Trans* **43**, 10602 (2014)

5. Accessed on https://en.wikipedia.org/wiki/Calcium_aluminates

6. Steel, F. A. and Davey, W. P. The crystal structure of tricalcium aluminate *J. Am. Chem. Soc.* **51(8)**, 2283-2293(1929)

7. Mondal, P. and Jeffery, J. W. The crystal structure of tricalcium aluminate, $Ca_3Al_2O_6$ *Acta cryst*. **B31**, 689-697 (1975)

8. Bussem, W. X-rays and cement chemistry *Proc. of int. Symposium on the chemistry of cements* (Ingeniorsyetenskapsakadamien, Stockholm) 146-149 (1938)

9. McMurdie, H. F. Structure of tricalcium aluminate U. S. department of commerce national bureau of standards research paper RP1437 part of *journal of research of the national bureau of standards* **27**, 499-505 (1941)

10. Vagia, E. C. and Lemonidou, A. A. Hydrogen production via steam reforming of bio-oil components over calcium aluminate supported nickel and noble metal catalysts. *Applied Catalysis A: General* **351**, 111-121 (2008)

11. Li, C.; Hirabayashi, D, and Suzuki, K. A Crucial role of O^{2-} and O_2^{2-} on mayenite structure for biomass tar steam reforming over $Ni/Ca_{12}Al_{14}O_{33}$. *Applied Catalysis B: Environment* **88**, 351-360 (2009)

12. Li, C.; Hirabayashi, D, and Suzuki, K. Development of new nickel based catalyst for biomass tar steam reforming producing H_2-rich syngas. *Fuel Processing Technology* **90**, 790-796 (2009)

13. Zhang, Z.; Kong, Z.; Liu, H. and Chen, Y. Mayenite supported perovskite monoliths for catalytic combustion of methyl methacrylate. *Front. Chem. Sci. Eng*. **8**,1, 87-94 (2004)

14. Sharma, M.; Khan, A. A.; Dohhen, K. C.; Christopher, J.; Puri, S. K.; Tuli, D. K. and Sarin, R. A. Heterogeneous catalyst for transesterification of *Argmone Mexicana oil*. *J. Am. Oil Chem. Soc.* **89**, 1545-155 (2012)

15. Wells, L. S. Reaction of water on calcium aluminates *Bureau of standards journal of research,* **1,** 951-1009 (1928)

16. Lee, F. C.; Banda, H. M. and Glasser, F. P. Substitution of sodium, iron and silicon in tricalcium aluminate and the polymorphism of solid solutions *Cem. Concr. Res*. **12**, 237-246 (1982)

17. Stephan, D.; Maleki, H.; Knofel, B.; Hardtl, E. R. Influence of Cr, Ni and Zn on the properties of pure clinker phases: Part II. C_3A and C_4AF *Cem. Concr. Res*. **29**, 651-657 (1999)

18. Stephan, D. and Wistuba, S. Crystal structure refinement and hydration behaviour of doped tricalcium aluminate *Cement and Concrete Research* **36**, 2011-2020 (2006)

19. Pane, I and Hansen, W. Investigation of blended cement hydration by isothermal calorimetry and thermal analysis *Cement and Concrete Research* **35** 1155-1164 (2005)

20. Alarcon-Ruiz, L.; Platret, G.; Massieu, E. and Ehrlacher, A. The use of thermal analysis in assessing the effect of temperature on a cement paste *Cement and Concrete Research* **35**, 609-613 (2005)

21. Levin, E. M. and McMardie, H. F. Phase diagrams for ceramists, 1969 supplement (Figure 2067-4149) *National Bureau of Standards*, The American Ceramic Society Inc. Pg 536 Fig. 4033 (1969)

22. Levin, E. M. and McMardie, H. F. Phase diagrams for ceramists *National Bureau of Standards*, The American Ceramic Society Inc. Pg 544, Fig.1983 (1956

23. Irvine, J. T. S. and West, A. R. $Ca_{12}Al_{14}O_{33}$-A possible high-temperature moisture sensor. *Journal of Applied Electrochemistry* **19**, 410-412 (1989)

24. Hayashi, K. Hirano, M. and Hosono, H. Thermodynamics and kinetics of hydroxide ion formation in $12CaO.7Al_2O_3$ *J. Phys. Chem. B* **109**, 11900-11906 (2005)

25. Cheng, C. K.; Foo, S. Y. and Adesina, A. A. H_2-rich synthesis gas production over Co/Al_2O_3 catalyst via steam reforming of glycerol. *Catalysis Communications* **12**, 292-298 (2010)

26. Taher, M. A. and AL-Sulami, A. I. Scanning electron microscopy studies on tricalcium aluminate hydrate pastes after hydration in presence of inorganic mixtures *J. Mater. Environ. Sci.* **4**(1) 17-22 (2013)

27. Demirbas, A. Biodiesel Production from Vegetable oils via catalytic and non-catalytic supercritical methanol transesterification method. *Progress in Energy and Combustion Science* **3**, 466-487 (2005)

28. Yan, S.; Lu, H. and Liang, B. Supported CaO catalysts used in the transesterification of rapeseed oil for the purpose of biodiesel production. *Energy and Fuels* **22**, 1, 646-651 (2008)

29. Lothenbach, B.; Pelletier-Chaignat, L. and Wnnefeld, F. Stability of the system $CaO-Al_2O_3-H_2O$ *Cement and Concrete Research*, **42,** 1621-1634 (2012)

30. http://abulafia.mt.ic.ac.uk/shannon-/ptable.php

31. Feng, Y.; He, B.; Cao, Y.; Li, J.; Liu, M.; Yan, F. and Liang, X. Biodiesel production using cation-exchange resin as heterogeneous catalyst. *Bioresource Technology* **101**, 1518–1521(2010).

32. Shibasaki-Kitakawa, N.; Honda, H.; Kuribayashi, H.; Toda, T.; Fukumura, T. and Yonemoto, T. Biodiesel production using anionic ion-exchange resin as heterogeneous catalyst. *Bioresource Technology* **98,** 416–421 (2007)

33. Kim, M.; Salley, S. O. and Ng, K. Y. S. Transesterification of glycerides using a heterogeneous resin catalyst combined with a homogeneous catalyst. *Energy and Fuels* **22***,* 3594–3599 (2008**)**

34. Vicente, G.; Coteron, A.; Martinez, M. and Aracil, J. Application of the factorial design experiments and response surface methodology to optimize biodiesel production. *Industrial Crops and Products* **8,** 29–35 (1998)

35. O¨zbay, N.; Oktar, N.; and Tapan, N. A.: Esterification of free fatty acids in waste cooking oils (WCO): Role of ion-exchange resins. Fuel, 2008; 87, 1789–1798

36. Melero, J. A.; Bautista, L. F.; Morales, G.; Iglesias, J. and Sánchez-Vázquez, R. Biodiesel production from crude palm oil using sulfonic acid-modified mesostructured catalysts. *Chemical Engineering Journal* **161**, 323–331 (2010)

37. http://www.sigmaaldrich.com/united-kingdom.html

38. Ilgen, O.; Akin, A. N. and Boz, N. Investigation of biodiesel production from canola oil using Amberlyst-26 as a catalyst. *Turk J Chem* **33**, 289 – 294 (2009)

39. Vicente, G.; Martınez, M. and Aracil, J. Integrated biodiesel production: A comparison of different homogeneous catalysts systems. *Bioresource Technology*. **92**, 297–305 (2004)

40. Lam, M.; Lee, K. T. and Mohamed, A. Homogeneous, heterogeneous and enzymatic catalysis for transesterification of high free fatty acid oil (waste cooking oil) to biodiesel: A review. *Biotechnology Advances* **28**, 500–518 (2010)

NICKEL-BASED CATALYSTS FOR GLYCEROL STEAM REFORMING TO HYDROGEN-RICH GAS FOR UTILISATION IN FUEL CELL

5.0 Nickel based metal oxide supported catalyst: The 'traditional' wet impregnation

5.1 Introduction

Glycerol, a by-product of transesterification reaction has demonstrated great potential for renewable hydrogen generation through fuel processing such as steam reforming for utilisation in fuel cell technology especially the SOFC[1,2]. Ni/γ-Al_2O_3 is a popular and promising catalyst system for steam reforming. Essentially, nickel catalyse C-C, C-H and C-O bond cleavages and selective towards syngas with a resultant formation of large carbonaceous substances on the catalyst surface[3]. Gamma alumina is a good adsorbent used as catalyst support due to its mesoporous nature, ordered sponge-like pore structure, thermal stability and large surface area that could enhance diffusivity of reacting species and resulting products[4]. The major setback in the use of Ni-based catalyst is deactivation due to carbon deposition and sintering at high temperature. The Ni/Al_2O_3 catalyst system is an interesting catalyst for steam reforming of biomass feedstock and well researched[5,6]. Much is still needed to optimize parameters such as catalyst loading, reaction and calcination temperature and how coke formation and types are influenced by those parameters which are the aims of this section.

In this work, steam reforming of pure glycerol using Ni/Al_2O_3 as catalyst was investigated to optimize reaction conditions and to provide a room for comparison with other new nickel-based catalysts developed with enhanced properties based on the use of promoters and alternative supports. Different nickel catalyst loading (5, 10 and 30 wt% based on the weight of support) would be explored. It is also to investigate the catalysis in steam reforming of by-product glycerol. These would provide basis for comparison between oxide-supported metal catalyst prepared by wet impregnation and those from redox lattice reorganisation and redox exsolution phenomena in subsequent chapters especially from the perspective of catalytic activity, catalyst-support interaction and suppression of carbon deposition.

5.2 Glycerol steam reforming over Ni/γ-Al_2O_3 for hydrogen production

5.2.1 Crystallographic studies

The diffraction peak due to NiO and active alumina were observed in the XRD pattern of the samples as shown below in Figure 5-1a. The two most conspicuous peaks at 45.8°, 66.4° and a wider one at 37.3° conforms to γ-Al_2O_3 and their presence at all the calcination temperatures as seen in Figure 5-2 signifies thermal stability of γ-Al_2O_3. Similar pattern was reported by Sanchez[3]. The intensity of the peaks at 45.3°, 77.45° and 79.4° due to NiO increases with increase in nickel loading (The nickel loading is in wt% based on the weight of the alumina support) as seen in Figure 5-1a. The observed increase in peaks intensity as nickel loading increases could be due to lumping together or agglomeration of nickel particles with increase in loading. This is confirmed in the result of crystallite size calculation using Scherrer's equation below in Table 5-1 and 5-2 respectively. The XRD pattern of the original alumina (as taken from the bottle) when compared with fresh alumina (after degassing at 700 °C) showed transformation from aluminium hydroxide phase to active alumina phase in Figure 5-1b though the exact point or temperature at which the transformation occurred is not ascertained. The observed slight decrease in surface area after degassing at 700 °C as seen in Table 5-3 could be attributed to sintering.

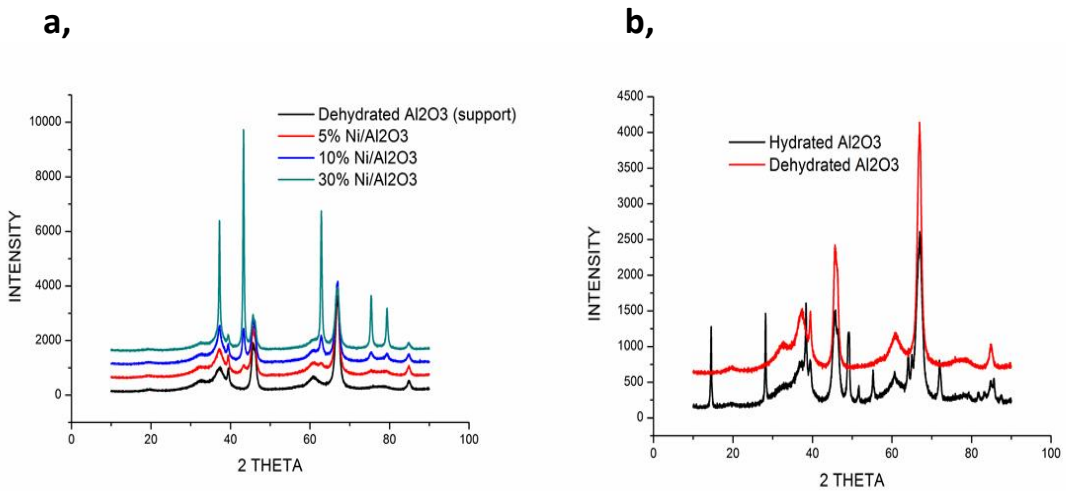

Figure 5-1 **a**, XRD Pattern showing influence of catalyst loading **b**, Transformation of alumina from hydrated hydroxide form to active gamma alumina phase.

The observed increase in intensity of the alumina peak at 37.3° with increased nickel loading from 5-30% showed overlap of NiO peak with alumina peak which depicts

possible formation of the spinel $NiAl_2O_4$ structure. The nickel oxide peaks intensity increased also with increase in temperature of calcination especially from 300-500 ^oC which is indicative of increased particle crystallinity in Figure 5-2. Increase peak intensity is not pronounced amongst samples prepared at 900 – 1000 ^oC. The impact of high temperature is more pronounced in the sample fired at 1000 ^oC as seen in Figure 5-2, where there is increase in the $NiAl_2O_4$ peak intensity at high temperature which shows that its formation is energy dependant.

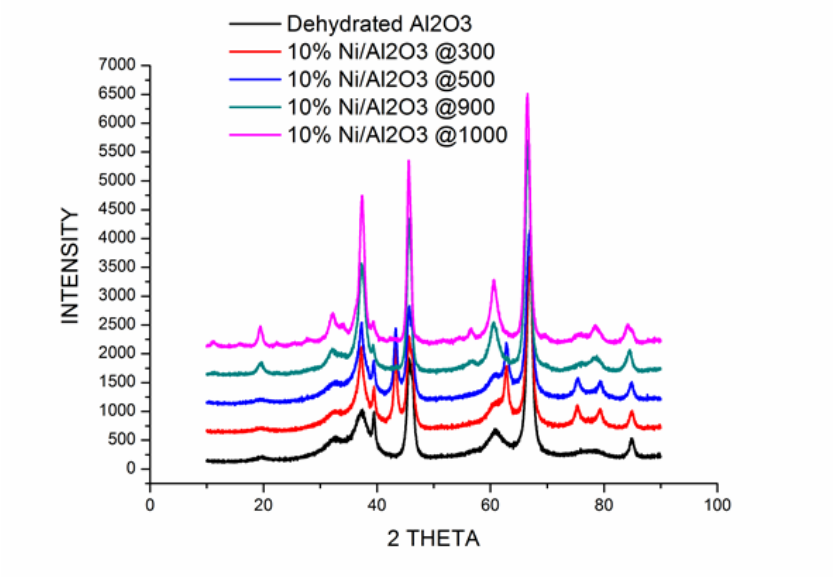

Figure 5-2 XRD Pattern showing influence of calcination temperature

Different calcination temperatures used gave different colours of the Ni/Al_2O_3, at 300 ^oC it was dark grey, 500 ^oC light grey, 900 ^oC light blue and 1000 ^oC deep blue as seen in Figure 5-3. The colour change could be attributed to different oxidation state of nickel in the samples which could also be used as index for extent or strength of metal-support interaction[4]. The NiO peaks at 45^o, 78^o and 80^o are only present at low temperatures i.e. 300-500 ^oC but conspicuously absent at high temperature i.e. 900-1000 ^oC leaving only peaks corresponding to $NiAl_2O_4$. This means the NiO phase transformed to $NiAl_2O_4$ at high temperature which further confirms temperature dependant of the formation of spinel structure.

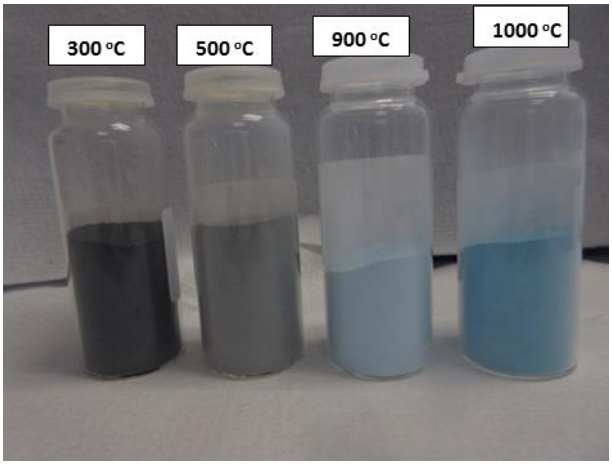

Figure 5-3 Pictures of samples containing same materials but prepared at different Calcination temperatures showing change in colour due the influence of the calcination temperature

Intensity of Al_2O_3 peaks appears at high temperature of 900 ^oC and increased at 1000 ^oC which indicates crystallinity of Al_2O_3 and probable change of phase from amorphous γ-Al_2O_3 to more of crystalline α-Al_2O_3-like material such as θ-Al_2O_3[7]. High nickel loading and calcination temperature seems to have negative influence on the catalyst materials resulting into surface morphological changes such as reduced surface area, possible sintering and phase transformation which are agents of catalyst deactivation.

Crystallite size calculation using Scherrer's equation revealed that particle size increases as nickel loading increase, but decreases with increase in temperature as shown in Table 5-1 and Table 5-2 respectively. This could be attributed to particles agglomerating to form bigger particle as loading increases while at high temperature particle size was expected to increase with increase in calcination temperature due to agglomeration, but instead the peaks get broader resulting in smaller particle size as seen in Table 5-2. What might be responsible for the observed peak broadening is not yet ascertained.

Table 5-1 Influence of catalyst loading on crystallite size

Sample	Calcination Temperature (^oC)	Crystallite Size (nm)
5wt%Ni/Al_2O_3	500	14.5
10wt%Ni/Al_2O_3	500	20.2
30wt%Ni/Al_2O_3	500	45.0

Table 5-2 Influence of calcination temperature on crystallite size

Sample	Calcination Temperature (^{o}C)	Crystallite Size (nm)
10wt%Ni/Al_2O_3	300	29.3
10wt%Ni/Al_2O_3	500	20.2
10wt%Ni/Al_2O_3	900	16.2
10wt%Ni/Al_2O_3	1000	14.9

5.2.2 Materials physicochemical properties and microstructures

Physical and chemical properties such as surface area pore size and volume of the support and catalyst systems were investigated and the results are as shown in Table 5-3. Is clear from the data; dispersion of active component (NiO) on the surface of the dehydrated alumina has further progressively reduced the surface area of the γ-Al_2O_3 support as the loading increases. This indicate active components have occupied certain proportion of the pores of Al_2O_3 support resulting in dispersion of the active phase on the γ-Al_2O_3 as evidenced in the SEM micrograph in Figure 5-4a-d below. Table 5-4 show the influence of calcination temperature where surface area also progressively reduces as the calcination temperature increases from 300-1000 ^{o}C perhaps due to particle size growth and agglomeration at high temperatures.

Table 5-3 Effect of catalyst loading on the surface area

Catalyst	Temperature ^{o}C	BET Surface Area (m^2g^{-1})	Pore volume (cm^3g^{-1})	Pore diameter (nm)
Fresh Al_2O_3	-	76.64	0.31	20.33
Dehydrated Al_2O_3	700	74.46	0.37	25.50
5wt%Ni/Al_2O3	500	49.76	0.38	34.60
10wt%Ni/Al_2O_3	500	48.74	0.39	37.12
30wt%Ni/Al_2O_3	500	42.86	0.45	40.41

Table 5-4 Effect of calcination temperature on the surface Area

Catalyst	Temperature ^{o}C	BET (m^2g^{-1})	Pore volume (cm^3g^{-1})	Pore diameter (nm)
10wt%Ni/Al_2O_3	300	54.23	0.42	33.22
10wt%Ni/Al_2O_3	500	48.78	0.39	37.12
10wt%Ni/Al_2O_3	900	41.62	0.35	39.25
10wt%Ni/Al_2O_3	1000	36.10	0.32	44.67

Both fresh alumina and Ni/Al_2O_3 have pore size in the range of 2 nm-50 nm and type-IV BET adsorption isotherms which depicts mesoporous nature of the materials. The hysteresis is of H1-type which shows regular shape and size cylindrical pore[8].

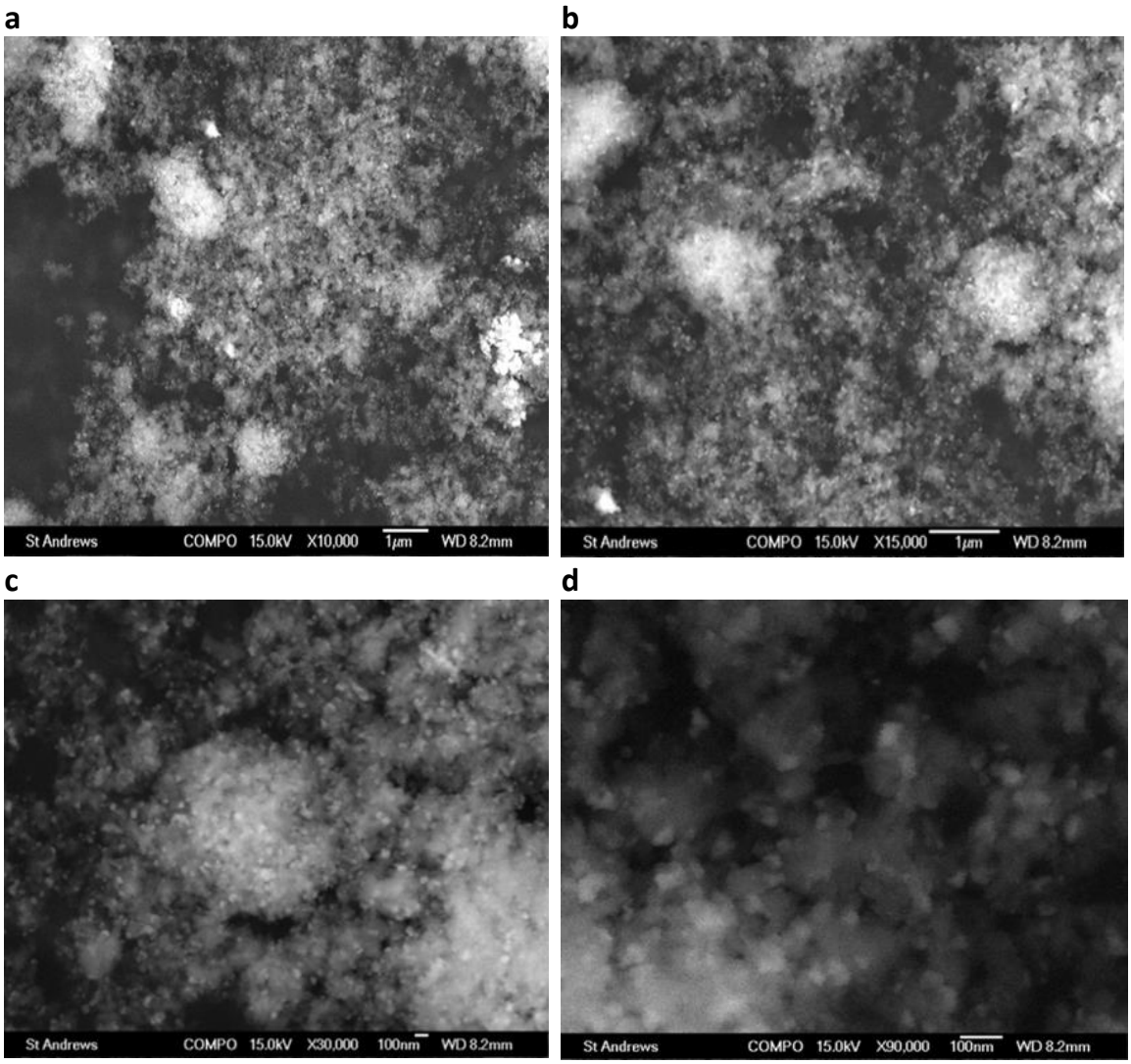

Figure 5-4 SEM micrograph showing nickel particles dispersion on alumina support in different magnifications

The nickel particles are uniformly dispersed on the surface of the γ-Al_2O_3 as evident in the SEM micrographs shown in different magnification above. The particle size calculated using Scherrer's equation as seen in Table 5-1 and 5-2 is also corroborated by the particle size found from the SEM micrograph with the mean particle size of 100 nm.

5.2.3 Catalyst performance evaluation

5.2.3.1 Influence of catalyst loading in glycerol steam reforming

To evaluate the performance of catalysts containing different Ni loadings, reforming tests were carried out at 500 ^{o}C and S/C ratio of 3 using catalysts prepared and calcined at 500 ^{o}C. Different catalyst loadings of 5wt%, 10wt% and 30wt% based on the weight of the support were used for the test for 2 hours using 50mg of the catalyst. The weight hourly space velocity (WHSV) was 28 h^{-1} calculated based on the method in appendix 3. Preliminary tests using an empty tube or calcined alumina (Al_2O_3) under the same reaction conditions gave negligible glycerol conversion. This shows that neither non-catalytic glycerol decomposition nor Al_2O_3 support contributed to the observed performance. The results taken at steady state of the reaction has revealed that catalyst activity seen as amount of products generated and glycerol conversion to gaseous products increased with catalyst loading from 5wt% to 10wt% but decreased at 30wt% as shown in Figure 5-5a. As the catalyst loading increases to 30wt%, the drop in the glycerol conversion could be attributed to reduced surface area and particle size growth due to nickel particles agglomerating which would have reduced active site accessibility, surface reactions and enhanced possible side reactions that could lead to deactivation due to carbon deposition. Therefore 10wt% seems the optimum catalyst loading required for maximum glycerol conversion in this test.

The product distribution shows H_2, CO_2, CO, and CH_4 as the only gaseous products detected during the steam reforming of glycerol at such temperatures; similar products were reported using glycerol[9.] H_2 and CO_2 were the predominant products with lots of CO as well as seen in Figure 5-5a. Comparison is made as seen in Table 5-5 with equilibrium composition based on glycerol decomposition among reactions presumed to be the possible major drivers of the glycerol conversion (see Table 2A-2 and 2A-3 of appendix 2). This is to see if the system was at equilibrium or the observed performance was largely due to glycerol decomposition as provided by Eqn. 2-3 or perhaps other reactions exemplified in Table 2A-3 of appendix 2. There is a variation between the values from the experiment and the equilibrium composition values which signifies the data collected was not an equilibrium composition rather from

reaction controlled region. The amount of hydrogen produced per mole of glycerol for instance shows that not even increasing the nickel content from 10% to 30% has taken the yield closer to the equilibrium. The H_2/CO ratio analysis on the Table also suggests catalytic decomposition due to nickel's support for glycerol C-C cleavages.

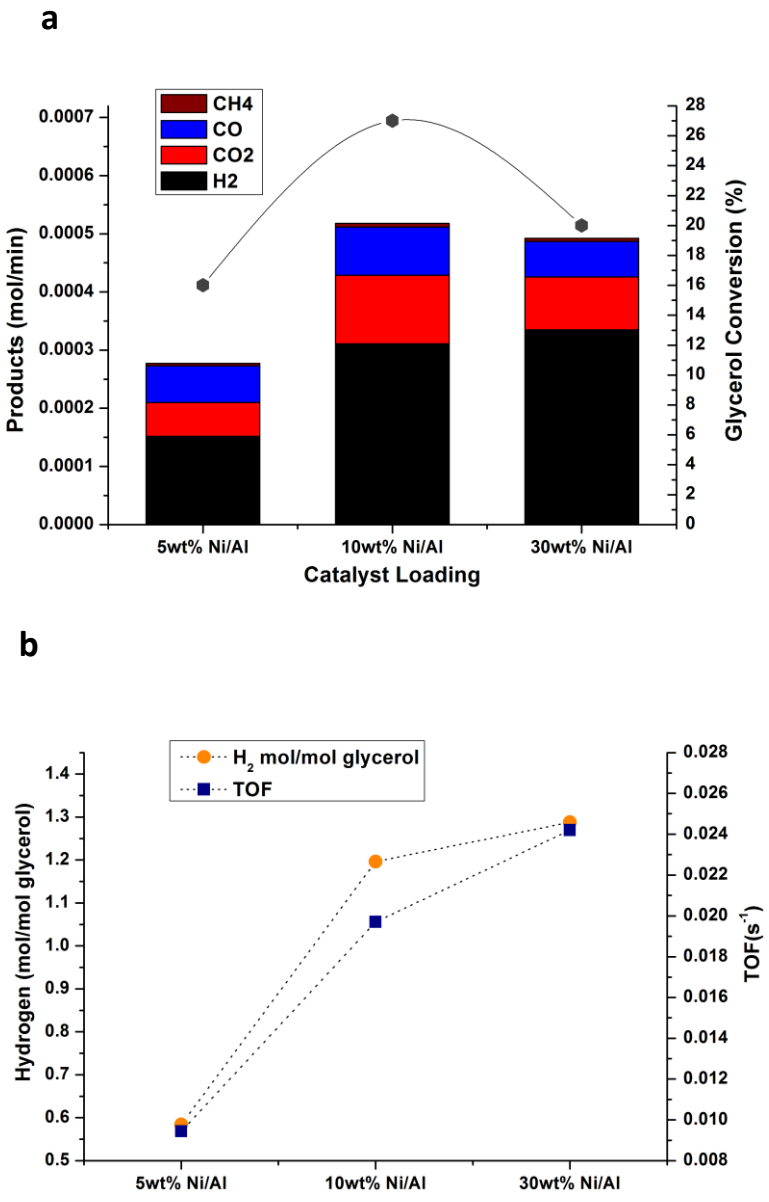

Figure 5-5 **a**, Influence of catalyst loading on catalytic activity for glycerol conversion **b**, Comparison between hydrogen yield and turnover frequency. The test was carried out at 500 ^{o}C, S/C ratio of 3 and glycerol molar flow rate of 8.2 x 10^{-5} moles/min of glycerol and 7.3 x 10^{-4} moles/min of water and WHSV of 28 h^{-1}

That might be responsible for the relatively high CO content. Another possible reaction that would have contributed to the observed performance especially looking at the H_2/CO_2 ratio is water gas shift reaction (WGSR). Analysis based on water

conversion would have helped to confirm that, but water was not measured during the experiment[10]. The ratios further indicate the catalyst is useful for H_2 and syngas production.

The maximum glycerol conversion of 27% was obtained. The conversion was limited by reactions that lead to carbon deposition, little catalyst amount used-0.05g which resulted to thin catalyst bed, short contact time and too much throughput with glycerol passing through unconverted or other unwanted reactions as corroborated by the turnover frequency value of Figure 5-5b. Turnover frequency which expresses the number of molecules that reacted per active site or surface area shows a low value which depicts possible decomposition or rapid deactivation. Unlike glycerol conversion, hydrogen production per mole of glycerol increased with increase in catalyst loading as seen in Figure 5-5b. The hydrogen production was about 30% of the equilibrium composition with 10wt% catalyst loading and increased to 33% with 30wt%[11,12] as seen in Figure 5-6 and compared to equilibrium composition in Table A2-2 of appendix 2. This further shows the catalyst support for rapid decomposition and possibly WGSR. The hydrogen yield was limited by some reactions such as dehydration of glycerol which leads to formation of products such as acrolein or carbonyl compounds (Eqn. 2-4 and 2-5), unconverted glycerol due to short contact time, water production and CH_4 formation.

Table 5-5 Comparison of products from the experiment with equilibrium composition based on glycerol pyrolysis[11,12]

	Temperature (^oC)	Conv.= Conversion (C basis)	H_g= H_2/Glyc. (mole/mole)	H_g/Conv.	H_2/CO	H_2/CO_2
Equilibrium	500	-	4.0	-	10.00	2.00
5wt% Ni/Al_2O_3	500	0.16	0.6	3.75	2.41	2.62
10wt% Ni/Al_2O_3	500	0.27	1.2	4.45	3.73	2.65
30wt% Ni/Al_2O_3	500	0.20	1.3	6.50	5.48	3.69

Comparing other gaseous products with equilibrium composition in Table A2-2 of appendix 2, Figure 5-6 shows all other gases i.e CO, CO_2 and CH_4 are below the equilibrium values. The catalyst loading of 10wt% gave a CO value close to the equilibrium value. This further indicates that the high CO composition as seen in Table 5-5 came from the catalytic glycerol decomposition.

The catalytic behaviour as seen above demonstrates that choosing the right amount of catalyst for the test and suitable catalyst loading could enhance catalytic properties and production of gaseous products such as H_2 and CO through rapid glycerol decomposition and WGSR for fuel cell application.

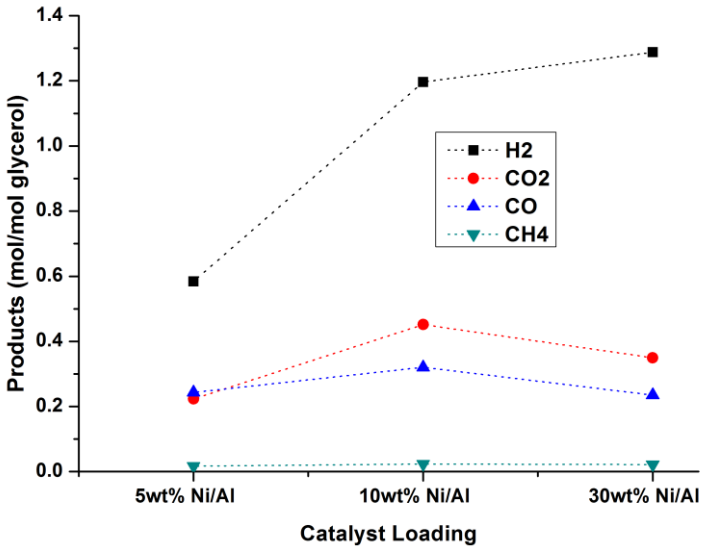

Figure 5-6 products produced per glycerol fed as a function of catalyst loading. The test was performed at 500 ^{o}C, S/C ratio of 3 and glycerol molar flow rate of 8.2 x 10^{-5} moles/min and 7.3 x 10^{-4} moles/min of water and WHSV of 28 h^{-1}

5.2.3.2 Influence of reaction temperatures

The effect of reaction temperature was investigated using 10wt% Ni/Al_2O_3 calcined at 500 ^{o}C which gave the highest conversion of glycerol in the screening test for 2 hours using 50mg of the catalyst. S/C ratio of 3 was used and WHSV of 28 h^{-1} at different reaction temperatures of 500-800 ^{o}C. The graph below in Figure 5-7a shows how glycerol conversion and products in mole per mole of glycerol changed with temperature. Comparing the products with equilibrium composition based on glycerol decomposition as seen in Table 5-6, it is clear the temperature (kinetics) played an important role in the products distribution and yield. This is attributable to glycerol decomposition due to kinetics. The H_2/CO_2 value also suggests possible contributions from other processes such as WGSR.

For instance, At 500 ^{o}C, though the H_2 and CO_2 are high compared to CO which would have suggests WGSR (Eqn. 2-6) comparing that to equilibrium composition (Table 2A-2 of appendix 2), the CO is higher than CO_2 which suggests glycerol decomposition is significant. The H_2 production at 500 ^{o}C was 30% of equilibrium composition largely from rapid catalytic glycerol decomposition attracted at that temperature resulting to also reasonable glycerol conversion. The activity is corroborated by large carbon deposition seen in Figure 5-10 of section 5.2.4.1. The CH_4 yield is best at 500 ^{o}C but decreases with temperature. The high CH_4 at 500 ^{o}C is attributable to reactions such as CO methanation (Eqn. 2-8 to 10) but decomposes at elevated temperature to yield more hydrogen. The H_2 and CO_2 yield drops at 600 ^{o}C while simultaneously CO formation increased. This means as the temperature increases, reverse water gas shift reaction which is slightly endothermic set in and favoured CO formation by utilising CO_2 and H_2 (Eqn.2-6). Reverse WGSR is one of the factors and a limiting reaction preventing H_2 from getting to equilibrium. This analysis compares with what was observed with equilibrium composition simulation of Figure 2-4. The drop in H_2 and CO_2 at 600 ^{o}C could be attributed to reversible self-poisoning deactivation effect which occurs most frequently at 550-600 ^{o}C[13].

Table 5-6 Comparison of experimental data with equilibrium composition based on glycerol decomposition[11,12] showing influence of temperature

	Temperature (^{o}C)	Conv.= Conversion (C basis)	H_g= H_2/Glyc. (mol/mol)	H_g/Conv.	H_2/CO	H_2/CO_2
Equilibrium	500	-	4.00	-	10.00	2.00
Equilibrium	600	-	5.50	-	6.88	2.50
Equilibrium	700	-	6.00	-	6.00	3.00
Equilibrium	800	-	5.80	-	4.83	-
Experimental	500	0.27	1.20	4.45	3.73	2.65
Experimental	600	0.26	1.10	4.30	3.46	2.50
Experimental	700	0.33	1.16	3.52	3.16	1.90
Experimental	800	0.38	1.19	3.13	3.51	1.48

Moreover at high temperatures, the amount of CO_2 produced per mole of glycerol increased as shown in Table 5-6 and Figure 5-7. This suggests possible contribution from endothermic steam reforming (Eqn.2-7 and see Table 2A-3 of appendix 2) and to some extent methane steam reforming (Eqn. 2-11) favoured both by kinetics whilst

CH_4 decreased. The amount of hydrogen produced per mole of glycerol is within the equilibrium composition (Table A2-2 of appendix 2) and did not show appreciable increase with temperature (after 700 ^{o}C). The CO production per mole glycerol increased with temperature to a maximum at 700 ^{o}C but dropped at 800 ^{o}C.

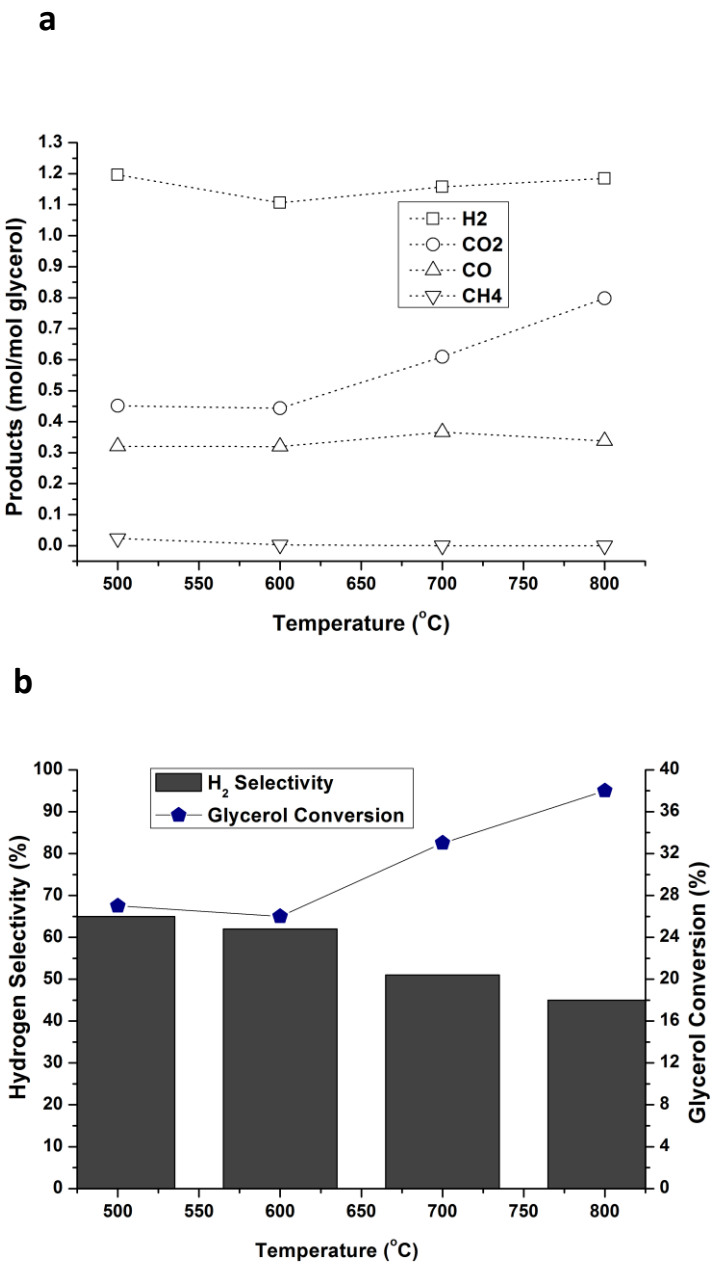

Figure 5-7 **a**, Change in reformates composition as a function of temperature **b**, Comparison between hydrogen selectivity and glycerol conversion and influence of reaction temperature. Both were carried out at 500 ^{o}C, S/C ratio of 3 and glycerol molar flow rate of 8.2 x 10^{-5} moles/min and 7.3 x 10^{-4} moles/min of water and WHSV of 28 h^{-1}

The CO increase from 500–700 ^{o}C further suggest importance of glycerol decomposition to this process and possible indication of catalyst deactivation due to

catalyst particle size growth. The CO, CO_2 and CH_4 amount are reasonable and not at equilibrium[11] at 700-800 ^oC as shown in Figure 5-6a. This shows that kinetics favoured rapid glycerol decomposition facilitated by the nickel content. Suffice to say that rapid glycerol decomposition favoured by kinetics and facilitated by the nickel content of the catalyst significantly favoured production of H_2 and CO. However, despite the favourable kinetic influence, the hydrogen production is limited by reactions such as reverse WSGSR which becomes more active at elevated temperature. Use of low catalyst amount (0.05g) has lowered glycerol conversion to gaseous products. Consequently, right choice of reaction temperature is significant to achieving maximum conversion with high hydrogen yield. Therefore, at suitable reaction temperature (500 and 700 ^oC) coupled with appropriate amount and loading, the catalyst could be useful for syngas production for high temperature fuel cell such as SOFC's utilisation.

Figure 5-7b shows how change in reaction temperature influences H_2 selectivity and how that compares with glycerol conversion at different temperatures. Generally, hydrogen selectivity shows an opposite trend with glycerol conversion in Figure 5-7b - decreased steadily to 800 ^oC and conversely glycerol conversion increased with increase in temperature to 800 ^oC. The reaction temperature of 500 ^oC gave the highest hydrogen selectivity and reasonable glycerol conversion >25%. High reaction temperature seems to generate more carbon containing species and reduce hydrogen selectivity perhaps due to kinetics. This could also be due to decreased surface properties of the catalyst such as reduced surface area and agglomeration of nickel particles. Carbon deposition also decreases with temperature as seen in section 5.2.4.1 which might have favoured glycerol conversion. From the foregoing, it is apparent temperature enhances rapid glycerol decomposition and glycerol conversion but hydrogen production and selectivity hasn't shown much appreciable increase at high temperature. Thus, 500 ^oC and 700 ^oC represent optimum temperature for hydrogen production and selectivity in this work.

Analysis based on carbon balance as shown in Table 5-7 suggest there is carbon loss comparing total mole of carbon IN with total carbon OUT which is attributable to carbon deposition and too much throughput due to the little amount of catalyst used.

It is interesting to note that the carbon loss decreases with temperature which implies carbon deposition decreases with temperature.

Table 5-7 Analysis based on carbon balance

Temperature (oC)	Total carbon **IN** (moles/min)	Total carbon **OUT** (moles/min)	CO **OUT** (moles/ min)	CO_2 **OUT** (moles/min)	CH_4 **OUT** (moles/ min)
500	7.8×10^{-4}	2.1×10^{-4}	8.3×10^{-5}	1.2×10^{-4}	6.1×10^{-6}
600	7.8×10^{-4}	2.0×10^{-4}	8.2×10^{-5}	1.2×10^{-4}	7.5×10^{-7}
700	7.8×10^{-4}	2.6×10^{-4}	9.5×10^{-5}	1.6×10^{-4}	-
800	7.8×10^{-4}	3.0×10^{-4}	8.8×10^{-5}	2.1×10^{-4}	-

5.2.3.3 Relationship between calcination temperature and hydrogen selectivity

Both reaction and calcination temperatures of the catalysts has profound influence on the selectivity of the desired products. Figure 5-8 shows that irrespective of calcination temperature of the catalyst, selectivity for hydrogen decreases with reaction temperature. Though relatively, catalyst calcined at low temperatures had a better selectivity for H_2 than those prepared at high temperatures. Catalyst prepared at 500 ^{o}C for instance showed a steady decrease in hydrogen selectivity through all the reforming temperatures.

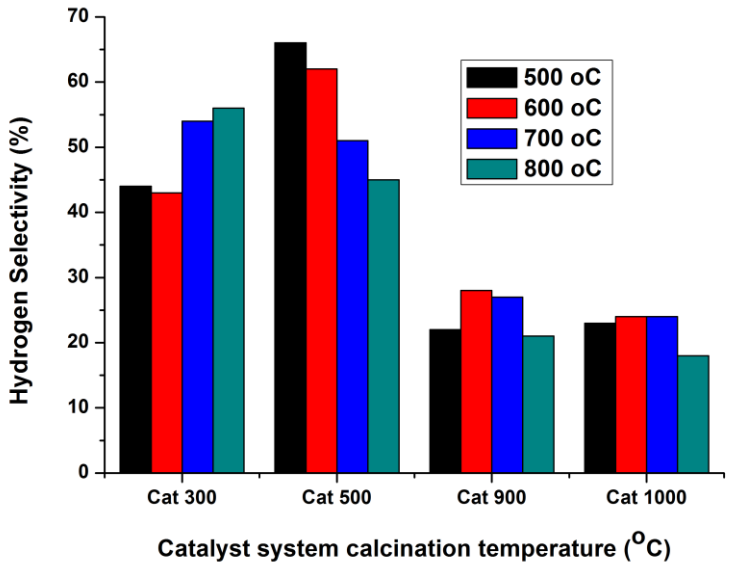

Figure 5-8 influence of calcination and reaction temperature on hydrogen selectivity carried out at temperatures 500-800 ^{o}C, S/C ratio of 3 and glycerol molar flow rate of 8.2×10^{-5} moles/min and 7.3×10^{-4} moles/min of water and WHSV of 28 h^{-1}

Is apparent that H_2 and CO_2 yield was better among the low temperature calcined catalysts, which means they were better for WGS reaction, perhaps due to their better surface area, smaller particle size and good catalyst-support relationship. Thus, hydrogen selectivity was limited by kinetics but favoured at low temperature due to reactions such as WGSR. Relatively, due to sintering and agglomeration or phase transformation, those catalyst prepared at high temperatures-900-1000 ^{o}C favoured reverse water gas shift reaction hence had reduced H_2 and CO_2 and increased CO and CH_4 formation. Generally, H_2 selectivity decreased with both reaction and calcination temperatures except for the catalyst prepared at 300 ^{o}C where hydrogen selectivity increased with reaction temperature. Therefore, suffices to say even though steam reforming and glycerol decomposition are favoured at elevated temperatures, the nagative influence of high temperature operations on the general morphology of the catalysts might have affected the behaviour of the catalyst systems.

5.2.4 The Carbon deposition

The XRD pattern of the used samples in Figure 5-9 shows a peak at 26.2 2θ which is absent in the fresh Ni/Al_2O_3. The peak corresponds to carbon which suggests carbon deposition. Similar diagnosis or interpretation was used by Newnham et al[14.] More so, reduced Ni metal peaks are prominent at 52.1 2θ and 76.6 2θ in the XRD pattern of the used catalyst as a result of reduction of the catalyst before usage as compared to the fresh sample pattern with peaks due to NiO only. During catalysis, deposition of carbonaceous substance on catalyst surface and pores occur which might lead to subsequent catalyst deactivation[14]. Most times, carbon deposition occurs because most catalyst follows the decomposition-gasification route which is known to favour carbon deposition[15]. Temperature programmed oxidation run in parallel with thermo-gravimetric analysis (TPO-TGA) on the used samples showed one or more CO_2 Peaks and weight loss on the TGA due to gasification of carbon on the catalyst surface depending upon the reaction condition, catalyst calcination temperature, composition of the catalyst and many more factors. The CO_2 peaks in the temperature programmed oxidation profile provides points or temperatures at which oxidation of carbon occurs which depends on the nature and location of the coke whilst the TGA

profile shows the extent of carbon deposition hence TPO-TGA is used to characterize the coke deposited[14].

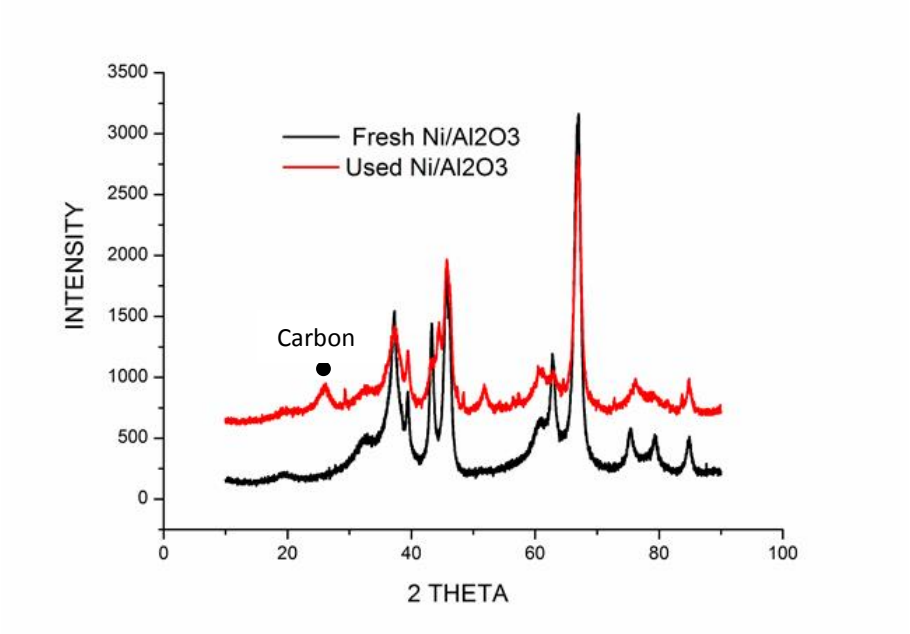

Figure 5-9 Comparison between the XRD pattern of fresh and used catalyst with the used catalyst pattern showing extra peak due to carbon and peaks due to reduced nickel metal

Different types of coke such as graphitic, polymeric, amorphous or bulk carbon are oxidized at different temperatures. The amorphous carbon usually deposited on the catalyst surface are easy to remove therefore oxidises at low temperature, amorphous and graphitic carbon deposited at metal-support interphase oxidises at moderately high temperature while bulk carbon found mainly on the support are more difficult to remove as such oxidises at much high temperature[16-18].

5.2.4.1 Correlation between reaction temperature and coking phenomenon

Figure 5-10 shows the CO_2 and TGA profiles obtained from oxidation of used catalyst calcined at 500 ^{o}C but used at different steam reforming reaction temperatures of 500-800 ^{o}C. It is shown that quantity and type of coke deposited is affected by change in the reaction temperature. At low reaction temperatures-500 and 600 ^{o}C, major CO_2 peak is a medium temperature type found at 500-520 ^{o}C which means bulk of the coke was deposited at metal-support interface and is polymeric or graphitic type. Although small CO_2 peak detected at low temperature show that oxidation of carbon starts at

low temperature. Table 5-8 give the CO_2 peak positions as seen in Figure 5-11. Conversely, high temperature reforming-700-800 ^{o}C was characterized by low, intermediate and high temperature peaks with the dominant peaks at low temperatures which indicate bulk of the catalyst was deposited on the active phase (Ni) and is amorphous type which is usually easy to regenerate the sample by oxidation. The extra peaks at intermediate and high temperature suggests presence of polymeric or graphitic carbon and bulk carbon respectively which are difficult to remove relatively and therefore oxidised at elevated temperatures. This implies that although carbon deposition is hindered at high temperature, they could be associated with the worse kind of coke. Therefore, reaction temperature needs to be tailored to an optimum condition in order to limit carbon deposition or severe kind of coke and to enhance catalyst performance.

The TGA profile showed a decrease in carbon deposition with increase in reforming temperature which proved that carbon deposition is indeed limited by temperature as suggested in Eqn. 2-12-14 by thermodynamics above. The equations show that the reactions leading to carbon deposition are exothermic and therefore favoured at low temperatures and hindered at high temperatures. Thus reforming at high temperatures reduce tendency for catalyst deactivation by carbon deposition.

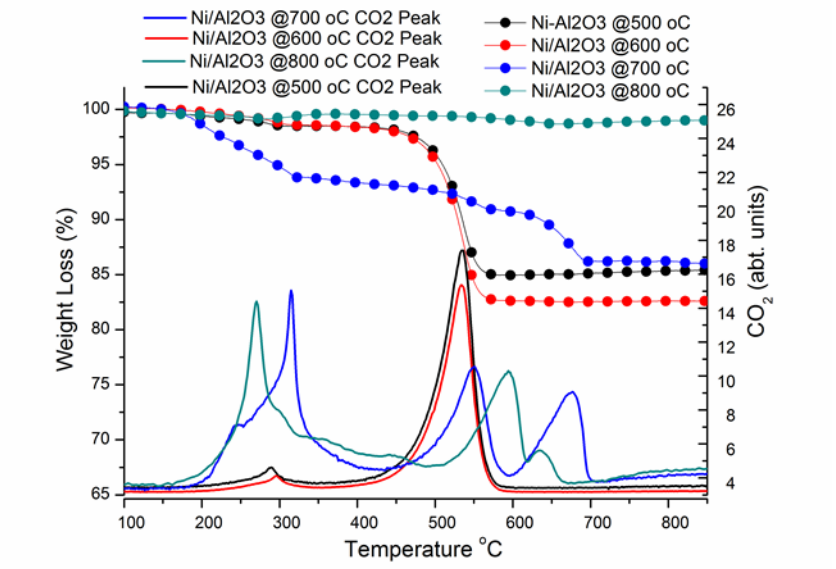

Figure 5-10 Change in weight of the selected used catalyst samples in oxidising atmosphere monitored in parallel with CO_2 as a function of temperature showing extent and type of carbon deposition as a function of temperature.

The high carbon deposition at 500 ^{o}C and 600 ^{o}C is also attributable to large adsorption of glycerol and reforming that occurred at those temperatures which might have left large carbonaceous products relatively from glycerol decomposition on the catalyst surface. Therefore choice of optimum reforming temperatures and good catalyst properties could enhance reformates yield and supression of carbon deposition.

Table 5-8 CO_2 peak position due to influence of reaction temperature

Catalyst	Reaction Temp. ^{o}C	Low Temp Peak	Medium Temp Peak	High Temp Peak
10wt%Ni/Al_2O_3	500	290	540	-
10wt%Ni/Al_2O_3	600	290	540	-
10wt%Ni/Al_2O_3	700	320	550	660
10wt%Ni/Al_2O_3	800	260	580	640

5.2.4.2 Correlation between calcination temperature and coking phenomenon

Figure 5-11 shows how the calcination temperature influences the quantity and type of coke deposited. The catalysts were prepared at different temperatures of 300 ^{o}C, 500 ^{o}C, 900 ^{o}C and 1000 ^{o}C respectively and steam reforming was performed at 500 ^{o}C. The TPO performed on the used catalyst was analysed and the results are as seen in Figure 5-11. Table 5-9 showed that major CO_2 peak among them was a medium temperature type deposited at metal-support interface although lower calcination temperatures catalysts showed some little low temperature peaks. This suggest that the low temperature (300 and 500 ^{o}C) calcined catalysts had a more polymeric and graphitic carbon which are difficult to oxidise and therefore CO_2 peaks due to them occurs at high temperatures. The high temperature (900-1000 ^{o}C) calcined catalysts showed a low temperature CO_2 peaks which suggests deposition of amorphous coke on the active phase which are easy to oxidise. The low temperature catalyst attracts more reaction and cracking of the feedstock due to their higher activity and therefore more likely to have severe coke on their surfaces.

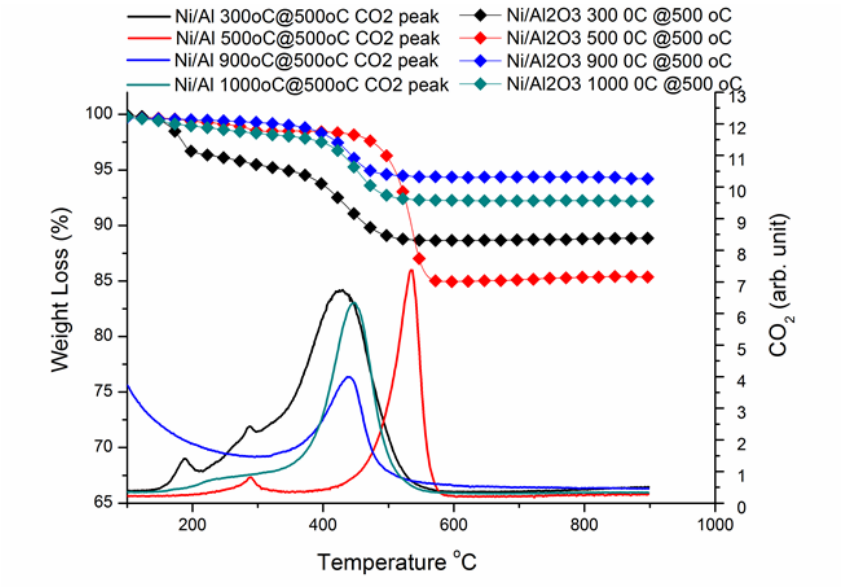

Figure 5-11 Change in weight of the selected used catalyst samples in oxidising atmosphere monitored in parallel with CO_2 as a function of temperature showing extent and type of carbon deposition as a function of temperature.

The lower temperature calcined catalysts have more carbon deposition compared to high temperature catalyst as seen on the TGA profile. This might be due to their large surface area relatively and hence more glycerol adsorption and therefore intense surface reaction. Therefore, catalyst calcination temperature could be controlled and optimised to guard against carbon deposition and to improve on the catalytic performance of the catalyst.

5-9 CO_2 peak positions due to influence of calcination temperature

Catalyst	Calcination Temp. oC	Low Temp. Peak	Medium Temp Peak	High Temp. Peak
10wt%Ni/Al_2O_3	300	280,180	420	-
10wt%Ni/Al_2O_3	500	280	540	-
10wt%Ni/Al_2O_3	900	-	450	-
10wt%Ni/Al_2O_3	1000	-	450	-

5.3 Enhancing structural properties and catalytic performance of Ni/γ-Al_2O_3 catalyst system using promoters and alternative supports

5.3.1 Introduction

The analysis in section 5.2 raises evidently many issues relating to the use Ni/Al_2O_3 catalyst system to catalyse steam reforming of biomass feedstock such as glycerol. The

good cracking potential of the catalyst was marred with carbon deposition, agglomeration and phase transformation leading to poor performance and consequent catalyst deactivation. Therefore there is need for improvement which is the main aim of this section.

Several efforts in most cases, using rare earth metals such as ceria, lanthana and first row transition metals such as Mn, Fe, Co and Zr as promoters to stabilize Ni-based catalyst systems or to enhance catalytic activity and coke suppression were made[19-22]. Despite all efforts, there is still need for enhanced activity, sustained stability and better suppressed or tolerant to coking activity. Furthermore, Ceria-Zirconia mixed oxides are gaining prominence over the years due to their redox potentials, basic and acidic properties, oxygen storage-release capacity and above all their strong catalytic abilities and coke resistance[19,23-24]. Their basic-acidic-redox property particularly enhances their support potentials which make them very useful support and a major driver in a number of reactions such as water gas shift reaction (WGSR) to generate hydrogen[23,24], reforming of hydrocarbons[24-31] and in the three way catalyst (TWC) for conversion of nasty gases from car exhaust[32]. The fundamental issue with the use of Ce-Zr-based catalysts in reforming biofuels is deactivation due to coking, formation of intermediate products and side reactions. These could lead to low performance especially in reactions performed at low temperatures except where they are used with precious metals which are prohibitively expensive[33,34].

Basically, this section sought to enhance the structural properties, catalytic activity and carbon deposition suppression ability of the Ni/Al_2O_3 catalyst system using perovskite and ceria-based materials as promoters and alternative supports respectively.

5.3.2 Use of ceria (CeO_2) and LSCM ($La_{0.75}Sr_{0.25}Cr_{0.5}Mn_{0.5}O_{3-\delta}$) as promoters in Ni/Al_2O_3 catalyst

5.3.2.1 Crystallographic studies

Figure 5-12 shows the XRD pattern of the host catalyst and the promoted catalyst samples. The little projection on the $Ni\text{-}Ce/Al_2O_3$ as peaks at $2\theta = 28.5^o$ and 33.0^o corresponds to the 111, and 200 plane of cubic fluorite structure of ceria[34], other

peaks due to ceria at around 47° and 56° not conspicuous perhaps due to the sharp peaks of alumina and the fact that very little amount of ceria (2% based on the weight of the support) was used. The only peak that is attributable to LSCM on the NI-LSCM/Al_2O_3 catalyst XRD pattern is the one at 2θ = 33.2° which could be due to same reason mentioned above.

Particle size analysis from crystallite size calculation using Scherrer's equation revealed that average particle size of the host catalyst did not change much with the addition of the promoters as seen Table 5-10. The Particle size becomes smaller in the promoted system which is interesting for catalysis with the LSCM promoted system having relatively smaller particle size.

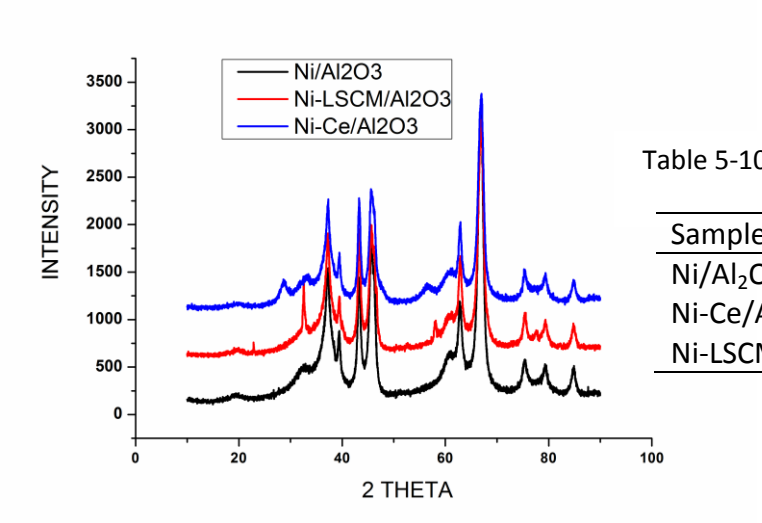

Table 5-10 Crystallite size of the catalysts

Sample	Crystallite Size (nm)
Ni/Al_2O_3	20.02
$Ni\text{-}Ce/Al_2O_3$	19.50
$Ni\text{-}LSCM/Al_2O_3$	19.07

Figure 5-12 XRD Patterns of 10wt% Ni/Al_2O_3 and the promoted catalyst systems

5.3.2.2 Physicochemical properties

Result of surface area analysis shown in Table 5-11 revealed that addition of active component (NiO) on the surface of the dehydrated alumina support has decreased the surface area and pore volume of the γ-Al_2O_3 support. The surface area and pore volume was further decreased with the addition of a perovskite promoter $La_{0.75}Sr_{0.25}Cr_{0.5}Mn_{0.5}O_{3-\delta}$ (LSCM) but increased with addition of ceria as a promoter. In either case, this indicates active components and the promoters have occupied certain proportion of the pores of Al_2O_3 support resulting in their dispersion on the Al_2O_3 support. Such interpretation was supported by the observed increase in pore diameter among the catalyst systems compared to that of the support as evident in Table 5-11.

Table 5-11 Surface area, pore volume and size of the catalysts

Catalyst	Calcination Temperature ^{o}C	BET Surface Area (m^2g^{-1})	Pore volume (cm^3g^{-1})	Pore Size (nm)
γ - Al_2O_3	700	74.46	0.39	25.50
Ni/Al_2O_3	500	48.74	0.37	37.12
Ni-Ce/Al_2O_3	500	51.44	0.36	30.24
Ni-LSCM/Al_2O_3	500	43.68	0.35	39.98

The pore size in all the catalyst systems is in the range of 2nm-50nm and type-IV BET adsorption isotherms which depicts mesoporous nature of the materials and the hysteresis is of H1-type which shows regular shape and size cylindrical pore.

5.3.2.3 Comparing the promoting activities of ceria and LSCM in Ni/Al_2O_3 in relation to glycerol steam reforming

To evaluate the performance of each promoted and non-promoted catalyst systems, screening test was performed at 500 ^{o}C using 0.1g (100mg) catalyst for 2 hours, WHSV of 28 h^{-1}, glycerol solution molar flow rate of 2.60 x 10^{-4} mole/min and at atmospheric pressure. The result obtained at steady state of the reaction is as shown in Figure 5-13a. Product distribution shows that H_2 and CO_2 gases were the predominant gases with hydrogen production in mole per mole of glycerol around 30-36% of the equilibrium composition (see Table 2A-2 of appendix 2) as shown in Figure 5-13b. The high H_2/CO mole ratio suggests glycerol decomposition facilitated by the nickel catalyst as the comparison of the experimental data with equilibrium composition due to glycerol decomposition shows in Table 5-12. The H_2/CO_2 mole ratio of Table 5-12 also indicate possible nickel's support for water-gas-shift reaction which the promoters might have influenced as well. Formation of acrolein and carbonyl species might have reduced the hydrogen yield. Other limiting factors for the H_2 yield are production of water, CH_4 formation and throughput.

Table 5-12 Comparison of experimental data with equilibrium composition based on glycerol decomposition [11,12]

	Temperature (^{o}C)	Conv.= Conversion (C basis)	H_g= H_2/Glyc. (mole/mole)	H_g/Conv.	H_2/CO	H_2/CO_2
Equilibrium	500	-	4.00	-	10.00	2.00
Ni/Al_2O_3	500	0.30	1.20	4.00	4.72	2.37
Ni-LSCM/Al_2O_3	500	0.34	1.38	4.05	4.92	2.27
Ni-Ce/Al_2O_3	500	0.31	1.43	4.61	5.27	2.45

The Ce-promoted catalyst system gave more hydrogen per mole of glycerol while the LSCM-promoted catalyst was more selective towards other gaseous products-CO, CO_2 and CH_4 hence showed higher glycerol conversion as shown in Figure 5-13b.

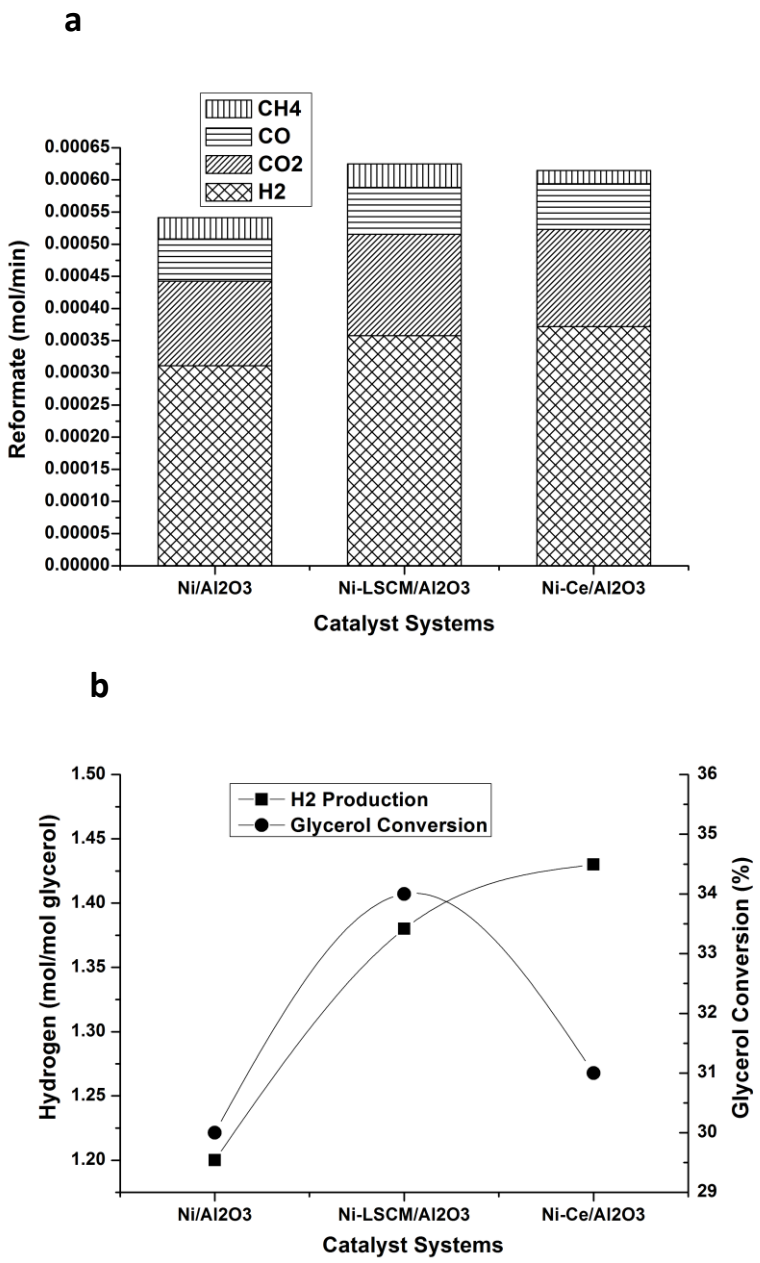

Figure 5-13 Comparison in the catalytic activity of the promoted and non-promoted Ni/Al_2O_3 catalyst system in terms of **a,** product distributions as a function of catalyst systems **b,** change in hydrogen yield and glycerol conversion as a function of catalyst. The test was performed at 500 ^{o}C, S/C ratio of 3 and glycerol molar flow rate of 8.2 x 10^{-5} moles/min and 7.3 x 10^{-4} moles/min of water and WHSV of 28 h^{-1}

The gaseous products CO_2 and CH_4 are within 26-31% and 16-25% of the equilibrium composition respectively across all the catalyst system, perhaps limited by reactions

such as reverse WGS as the CO mole ratio suggests in Table 5-12. The CO is between 63-70% of the equilibrium composition. This is attributable to rapid glycerol decomposition supported by the nickel-based catalyst as corroborated by the H_2/CO mole ratio in Table 5-12. Interestingly, doubling the catalyst amount from 0.05g used previously in section 5.2 to 0.1g in this case has significantly improved the catalyst performance such as glycerol conversion to gaseous products and hydrogen production rate using the Ni/Al_2O_3 catalyst system. This is due to increase in contact time with catalyst bed thickness. Therefore optimizing catalyst amount and choice of promoters could be tailored to enhance catalyst performance.

It is evident in Figure 5-13a and b the catalytic activity of the Ni/Al_2O_3 system was enhanced by the use of promoters. The LSCM-promoted catalyst is slightly more active. Glycerol conversion increased from 30% with non-promoted Ni/Al_2O_3 to 34% with LSCM promoted Ni-LSCM/Al_2O_3 catalyst system as shown in Figure 5-13b. The enhanced performance is attributable to enhanced surface area, particle size as well as reducibility in relation to the amount of reducible nickel particles in the samples as seen in Table 5-11 and 5-10 respectively. Another important factor responsible for the observed improvement is attributable to the stabilizing influence of LSCM on nickel which reduced occurrence of side reaction that could lead to deactivation due to carbon deposition. It could also be due to improved metal-support interaction as seen on the TGA profile. The glycerol conversion was limited by carbon deposition and glycerol passing unconverted perhaps due to much throughput despite doubling the initial catalyst amount of 0.05g used previously to 0.1 mg. Therefore use of promoters such as LSCM and ceria is capable of enhancing catalytic behaviour of Ni/Al_2O_3 catalyst for production of H_2 and syngas provided suitable amount of catalyst is used.

Influence of steam reforming temperature on the product distributions was investigated on the most promising catalyst system Ni-LSCM/Al_2O_3 and the result is as shown in Figure 5-14. The results show that at 500 ^oC, H_2 and CO_2 production was high and simultaneously CO and CH_4 were low. This is due to water-gas-shift reaction (WGSR) which is slightly exothermic (Eqn. 2-6) and known to utilise CO from glycerol pyrolysis in the presence of water to produce H_2 and CO_2. The high CH_4 at low

temperature (500 ^{o}C) is due to methanation but decomposes at higher temperature through slightly endothermic reaction yielding more hydrogen. The decrease of CO_2 and H_2 at 600 ^{o}C suggests reverse water-gas-shift reaction. The product production behaviour corroborates what is observed from the equilibrium composition simulation of Figure 2-4. As the temperature increased to 700 ^{o}C all the gases showed increase and the rise could be due to increased pyrolysis. Thus kinetics favours hydrogen yield at 700 ^{o}C. All the gaseous products H_2, CO_2, CO and CH_4 as the products in mole/mole glycerol shows in Figure 5-14 are within the equilibrium composition at all temperatures (see Table 2A-2 of appendix 2).

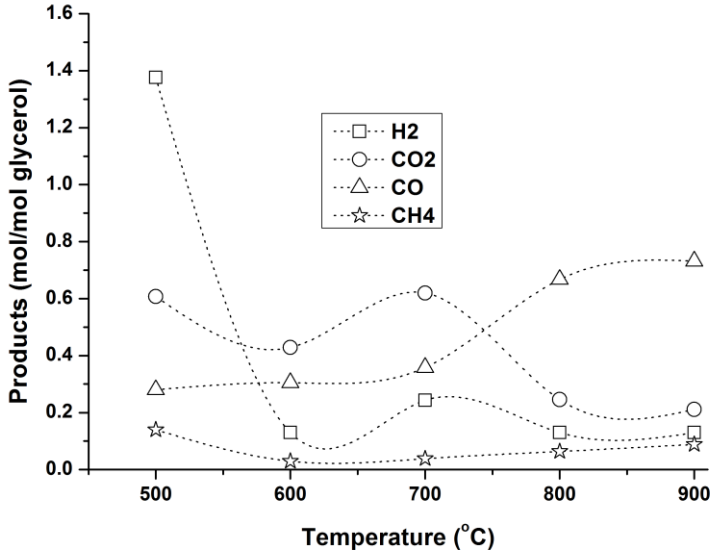

Figure 5-14 Product distribution using Ni-LSCM/Al_2O_3 catalyst as function of temperature (500 – 900 ^{o}C), S/C ratio 3 and glycerol molar flow rate of 8.2 x 10^{-5} moles/min and 7.3 x 10^{-4} moles/min of water and WHSV of 28 h^{-1}

Generally, it is essential to note that hydrogen gets lower with increase in temperature despite the endothermic nature of the glycerol pyrolysis, steam reforming and CH_4 reforming which are all expected to produce more H_2 due to kinetics at high temperatures. This implies that reaction temperature of 500 ^{o}C is the optimum for H_2 generation in this work. The decrease in H_2 production at high temperatures could also be attributed to catalyst deactivation with temperature due to catalyst surface morphology change with temperature leading to carbon deposition. Other factors include formation of compounds such as acrolein through

undesired reactions. Reaction such as reverse WGSR also reduce hydrogen yield especially at elevated temperatures (>500 ^{o}C).

This goes to show that despite enhanced properties due to the use of LSCM as promoter, the catalyst metal-support interaction is still not good enough to fully prevent deactivation by any means perhaps due to the wet impregnation used for the synthesis. It is possible to improve the shelf life of the catalyst by looking at alternative support or method of synthesis. Essentially, high temperature fuel cell such as SOFC would still be able to utilise CO-rich gas as fuel due to its flexibility on fuel choice. Therefore, choice of suitable promoters such as ceria and LSCM and reaction condition such as temperature could be tailored to enhance catalytic properties and performance of Ni/Al_2O_3 catalyst.

5.3.2.4 Correlation between the influence of promoters and carbon deposition in glycerol steam reforming

Figure 5-15 shows the TGA profile and CO_2 peak obtained from temperature programmed oxidation (TPO) of used catalyst from glycerol steam reforming. The TPO of carbon on the catalyst surface was carried out by gradual but steady ramping up of temperature to 900 ^{o}C in oxygen atmosphere during which, carbon oxidises to CO_2 which was captured and monitored on mass spectrometer. The weight loss from the gassified coke was monitored in parallel on the TGA. It is evident from the TGA profile weight loss there was carbon deposition from the steam reforming reactions. The weight loss from the individual catalyst was 26.53%, 20.23% and 15.12% from Ni/Al_2O_3, $Ni\text{-}Ce/Al_2O_3$ and $NI\text{-}LSCM/Al_2O_3$ respectively. There is a smooth correlation between the promoted and non- promoted catalyst systems on the extent of the carbon deposition. The extent of carbon deposition increased in the order $NI\text{-}LSCM/Al_2O_3 < Ni\text{-}Ce/Al_2O_3 < Ni/Al_2O_3$.

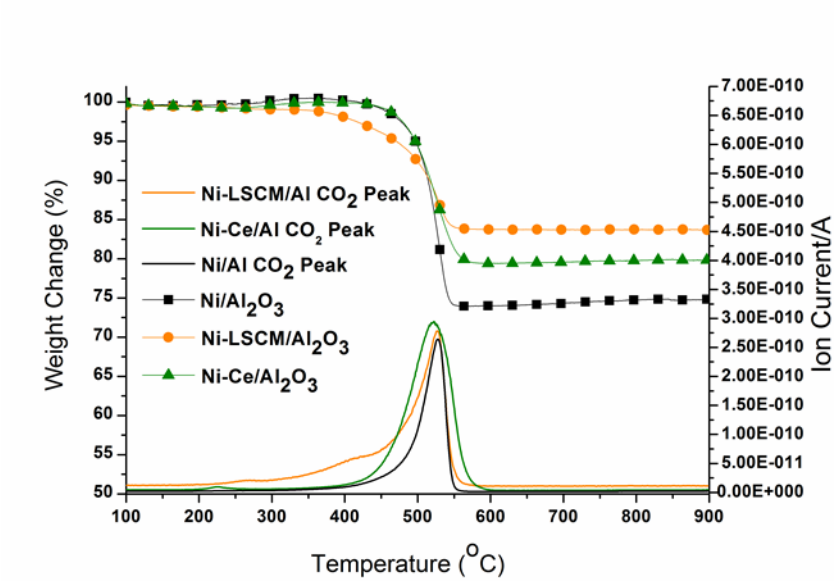

Figure 5-15 Change in weight of the selected used catalyst samples in oxidising atmosphere monitored in parallel with CO_2 as a function of temperature

It is clear that the promoting influence of LSCM and Ceria has reduced the extent of carbon deposition. The LSCM promoter has some stabilizing influence on the nickel particles by reducing its tendency to agglomeration and to promote side reaction that could lead to carbon deposition. Ceria on the other hand possesses the twin influence of acidic-basic and redox properties as well as oxygen-storage-release behaviour which enhances oxidation and gasification of carbonaceous substance on the catalyst surface that helps to prevent coking. On the other hand, the Al_2O_3 support due to its acidic surface, strongly absorb glycerol and dehydrate it leaving behind liquid carbonaceous products which coked the catalyst surface.

The CO_2 profile however showed that the temperature at which bulk of the carbon oxidised from the catalyst surface is the same in all the catalyst systems irrespective of the influence of the promoters. The oxidation temperature of 500-520 ^oC was a medium type which shows amorphous or graphitic carbon deposited at metal-support interface. Based on the foregoing, the promoters have influence on the extent or how much carbon is deposited but did not show any influence on the location and type of carbon deposited.

5.3.3 Alternative support to γ-Al_2O_3 in Ni/γ-Al_2O_3 in glycerol steam reforming

5.3.3.1 Use of zirconia-doped ceria (Ce-Zr) or (ZDC) and samaria-doped ceria (SDC) as alternative support to γ- Al_2O_3 in Ni/Al_2O_3 catalyst in glycerol steam reforming

5.3.3.1.1 Thermo-gravimetric analysis

Results of the TGA on the fresh promoted catalyst systems in air in Figure 5-16a showed no significant weight lost which denotes some stability in the samples. The weight loss between 80 ^oC and 350 ^oC in virtually all the samples is attributed to loss of surface and lattice water respectively. The weight gain in the ceria containing samples Ni-LSCM/Ce-Zr and Ni-LSCM/SDC at 500-650 ^oC is due to oxygen intake by the samples as a result of ceria's oxygen storage-release properties. The Figure 5-16b shows the reducibility of the samples in a hydrogen atmosphere. The gentle weight loss in the ceria containing samples Ni-LSCM/Ce-Zr and Ni-LSCM/SDC profile at around 350-400 ^oC may be attributed to reduction of highly reducible Ni^{2+} to Ni^0 and the weight loss at 400-700 ^oC is attributable to reduction of highly dispersed non-crystalline Ni^{2+} or nickel/ceria into intimate contact or reduction of ceria from Ce^{4+} to Ce^{3+} [34]. Comparing the weight loss due to the influence of each support, it is evident that the proportion of reducible NiO is high in the Ce-Zr and SDC supported catalyst which is attributable to enhanced metal-support interactions. Such enhancement could have a positive impact on catalytic performance of the materials. There is also a slight shift towards low reduction temperature in the order Ni-LSCM/Al_2O_3>Ni-LSCM/SDC>Ni-LSCM/Ce-Zr. The Ni-LSCM/Ce-Zr catalyst system with the lowest reduction temperature has the strongest Ni-support interaction hence less likely to have agglomeration and more tendencies for good catalytic behaviour.

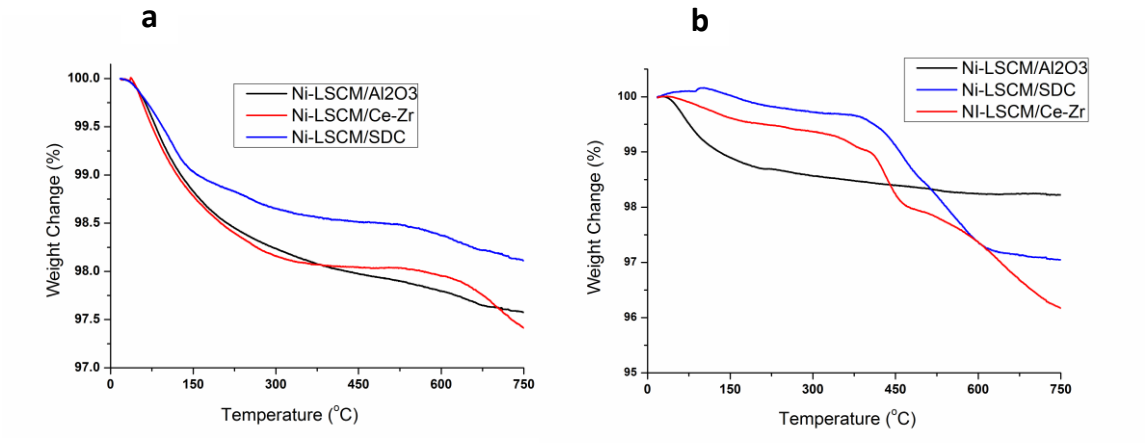

Figure 5-16 TGA showing change in weight of the catalyst system on different support under the influence different atmospheres **a,** Air and **b,** Hydrogen

5.3.3.1.2 Crystallography and microstructure

In Figure 5-17a, the diffraction peaks due to NiO are at 2θ = 37.1, 43.2, 62.7, 75.5 and 79.4°, active γ- Al_2O_3 at 2θ = 45.7 and 66.9° are conspicuous in the Ni-LSCM/Al_2O_3 XRD pattern while peaks due to LSCM are not visible. This is because either it is well dispersed or due to the small quantity (2wt %) used. The XRD pattern due to Ni-LSCM/Ce-Zr and Ni-LSCM/SDC shows peaks at 2θ = 28.5, 33.0, 47.3 and 56.2° corresponding to (111), (200), (220) and (311) plane of the cubic fluorite structure of ceria[34].

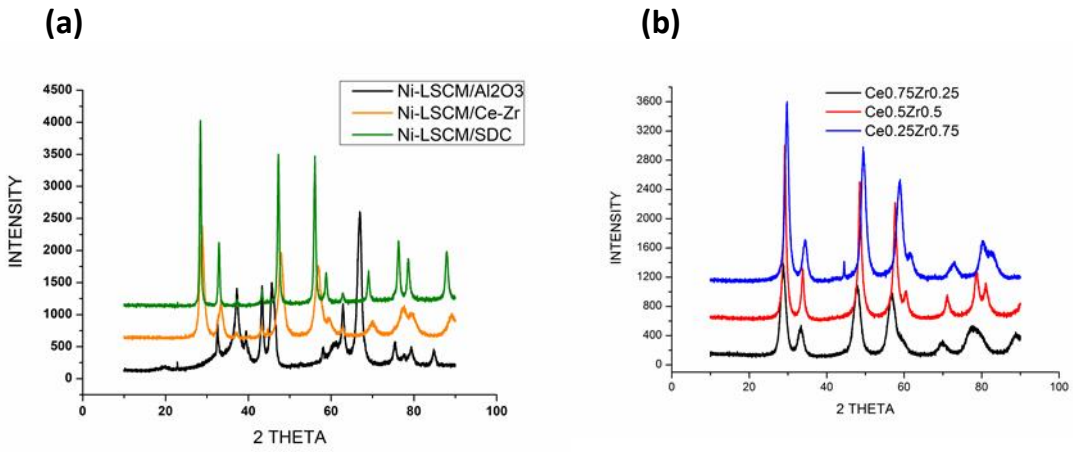

Figure 5-17 **a**, XRD pattern of the promoted catalyst and **b**, XRD pattern of the optimised $Ce_{1-x}Zr_xO_2$ series

The peaks are more intense in the SDC supported materials which indicates the particles are more crystalline. Similar peaks at 2θ = 28.8, 33.3, 47.8 and 56.7^{o} due to ceria are also observed in the XRD pattern of the optimized samples as seen in Figure 5-17b and are in pure phase except $Ce_{0.25}Zr_{0.75}O_2$ which show extra peak at 45^{o} 2θ position probably due to excess doping of the ceria. Particle size analysis showed that the particle size of the catalyst systems followed the order Ni-LSCM/Ce-Zr< Ni-LSCM/Al_2O_3> Ni-LSCM/SDC as supported by the intensity of peaks in the XRD patterns.

The TEM images of the Ce-Zr support in Figure 5-18a Show the sponge-like and hexagonal pore arrangement which also depicts the mesoporous nature of the material.

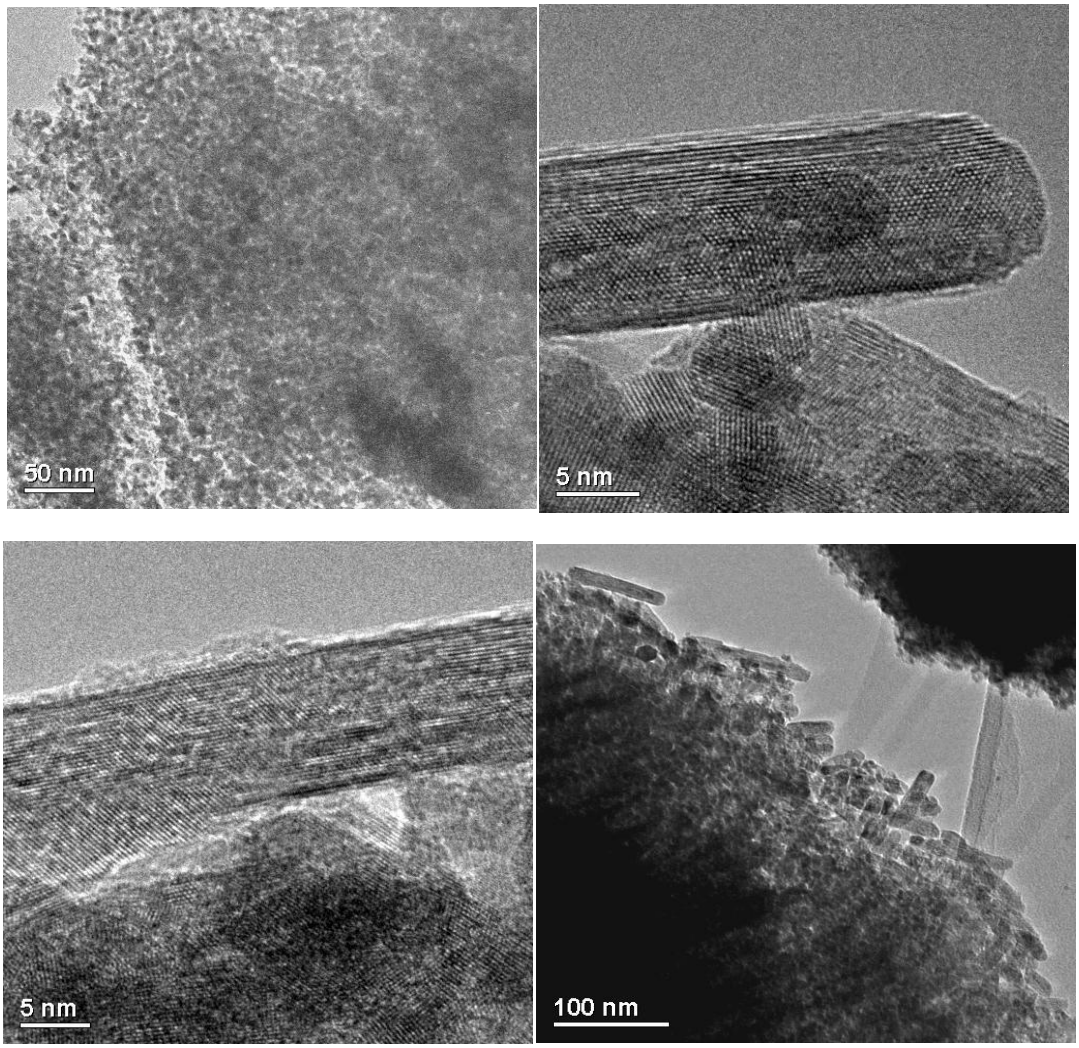

Figure 5-18 TEM images of the $Ce_{0.75}Zr_{0.25}O_2$support showing the sponge-like structures typical of mesoporous materials and interconnected pore channels

Figure 5-18b, c and d indicates formation of nanofibers of interconnected pore channels with regular pore size of approximately 5nm as confirmed in the BET test results in Table 5-14 and pore size distribution in Figure 5-20a. This also reaffirms preservation of the mesoporous structure after the surfactant was removed, perhaps due to the formation of rigid Ce-O-Ce framework during synthesis.

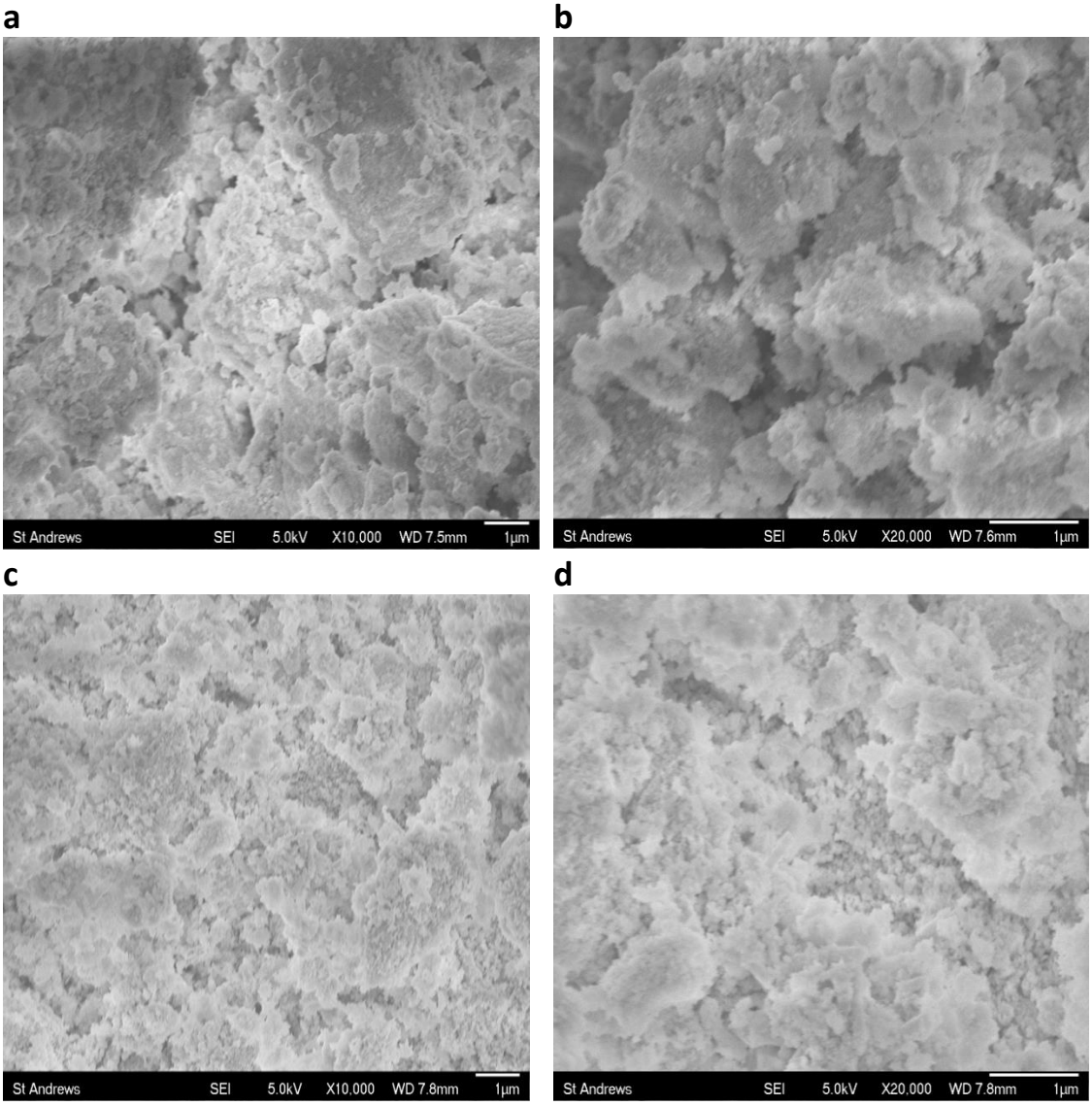

Figure 5-19 SEM micrograph showing surface morphology of the a,b, Ni-LSCM/Ce-Zr Catalyst and c,d, Ni-LSCM/SDC catalyst system

The SEM micrograph of the Ni-LSCM/Ce-Zr is shown in Figure 5-19a and b and those of Ni-LSCM/SDC are shown in Figure 5-19c and d respectively in different magnification. There are evidence of nickel catalyst particles dispersion on the support surface though not very much visible as seen in the case of Ni/Al_2O_3 catalyst system perhaps

obscured by the supports. Although each catalysts system has shown a peculiar surface morphology, what is common to all the catalysts from the SEM micrograph is their average particle size of about 1μm.

5.3.3.1.3 Physicochemical properties

As observed previously with other catalysts prepared by wet impregnation, Table 5-13 shows that the surface area of the supports and its pore volume decreased after impregnation of the nickel catalyst and the LSCM promoter on their surfaces. This denotes dispersion of the active catalyst on the support which results in increased surface area of the catalyst and possible improvement on their catalytic behaviour. The pore size among all the samples is in the range of 2-50nm which indicates the mesoporous nature of the materials. The $Ce_{0.75}Zr_{0.25}O_2$ support showed high surface area relatively while the $Ce_{0.8}Sm_{0.2}O_2$ showed the lowest surface area among the supports. It is interesting to note that the $Ce_{0.75}Zr_{0.25}O_2$ support showed a lot of decrease in surface area after impregnation more than what was observed with the other supports. This implies perhaps $Ce_{0.75}Zr_{0.25}O_2$ support might likely offer better support advantage to the nickel catalyst hence may show better catalytic behaviour in steam reforming of glycerol.

The $Ce_{1-x}Zr_xO_2$ series was synthesized as described in section 3 and their surface area was optimised to maximize activity as shown in Table 5-14. Low temperature calcination synthesis (400 ^oC) was used to preserve the ceria-mediated capacity for CO oxidation in ceria supported metals[25] as corroborated by TGA in Figure 5-16. The doping was limited between 25-75% and sample with 25% Zr i.e $Ce_{0.75}Zr_{0.25}O_2$ gave the highest surface area and therefore used in these studies.

Table 5-13 Physicochemical properties of the support and the impregnated catalyst

Catalyst	Surface Area (m^2g^{-1})	Pore Volume (cm^3g^{-1})	Pore Diameter (nm)
γ-Al_2O_3	74.46	0.37	25.50
$Ce_{0.75}Zr_{0.25}O_2$	126.25	0.18	5.46
$Ce_{0.8}Sm_{0.2}O_2$	31.85	0.18	20.86
Ni-LSCM/Al_2O_3	43.68	0.36	39.90
Ni-LSCM/ $Ce_{0.75}Zr_{0.25}O_2$	63.28	0.23	05.80
Ni-LSCM/$Ce_{0.8}Sm_{0.2}O_2$	29.25	0.16	18.48

Table 5-14 Surface area, pore size and volume of $Ce_{x-1}Zr_xO_2$ series

Catalyst	BET (m^2g^{-1})	Pore volume (cm^3g^{-1})	Pore diameter (nm)
$Ce_{0.75}Zr_{0.25}O_2$	126.25	0.188436	5.15040
$Ce_{0.5}Zr_{0.5}O_2$	89.63	0.181421	5.25350
$Ce_{0.25}Zr_{0.75}O_2$	95.27	0.158477	5.66930

Their pore sizes are within the range of 2-50nm as seen in Table 5-14 and Figure 5-20a respectively which indicates they are mesoporous materials as corroborated also by their type-IV BET adsorption isotherms and H1-type hysteresis loop in Figure 5-20b which shows regular shape and size cylindrical pore.

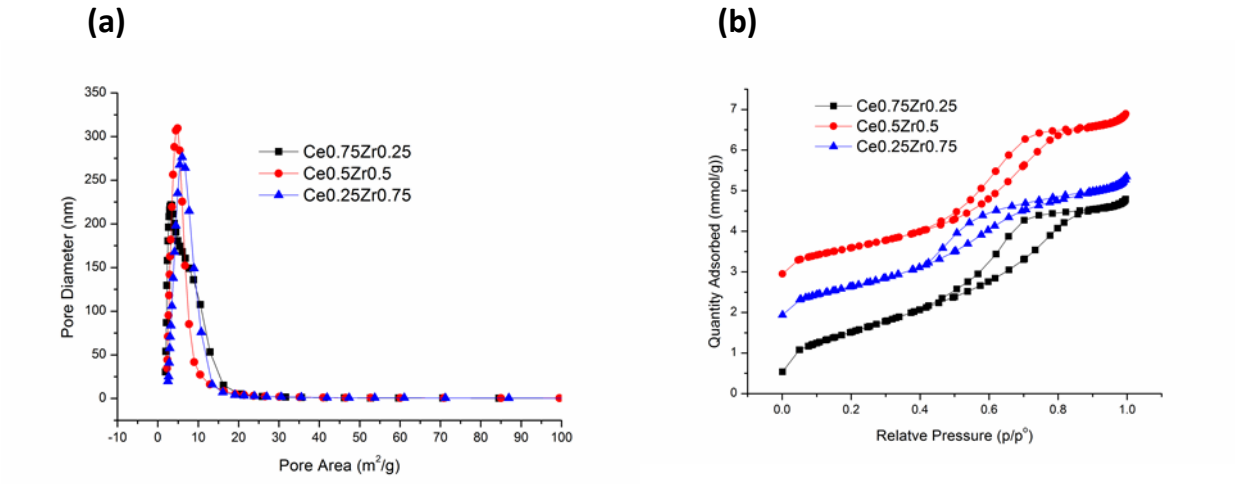

Figure 5-20 physicochemical properties of the $Ce_{1-x}Zr_xO_2$ series support showing **a**, pore size distribution and **b,** hysteresis loops

5.3.3.1.4 Catalyst performance evaluation in glycerol steam reforming

The catalyst performance evaluation to investigate the influence of support was carried out at 500 ^oC using 0.1g of the catalyst at atmospheric pressure, 0.019 ml/min feed flow rate and steam-to-carbon ratio of 3. The WHSV was 28 h^{-1} throughout the duration of the test. The ceria-based supports $Ce_{0.75}Zr_{0.25}O_2$ (Ce-Zr) and $Sm_{0.2}Ce_{0.8}O_2$ (SDC) were investigated as possible alternative supports to Al_2O_3. The result taken at steady state of the reaction as seen in Figure 5-21a and b shows H_2, CO, CO_2 and CH_4 as the only products in the gas stream with H_2 and CO_2 as the predominant gases with all the catalyst systems. This observation is also supported by the analysis of Table 5-15. The H_2 and CO_2 predominance suggest catalyst's possible support for water-gas-shift reaction due to nickel in all the samples as corroborated by the high H_2/CO_2 mole

ratios in Table 5-15. Comparison of the equilibrium composition due to glycerol decomposition based on Eqn. 2-3(see Table 2A-3 of appendix 2) as shown in Table 5-15 with experimental data indicates the amount of hydrogen produced per mole of glycerol is within the equilibrium values. The high H_2/CO mole ratio in Table 5-15 shows that rapid glycerol catalytic decomposition has contributed to the observed performance. The Ce-Zr supported catalyst gave more H_2, CO_2 and CH_4 but less CO relatively, in contrast, both SDC supported and Al_2O_3 supported catalyst systems gave more CO than the Ce-Zr supported catalyst as Figure 5-21a shows. The Ce-Zr supported catalyst is more active while the SDC supported catalyst is the least as the product distribution suggests in Figure 5-21a. Hydrogen production in mole/mole glycerol and glycerol conversion also followed same trend as seen in Figure 5-21b.

Table 5-15 Comparison of experimental data with equilibrium composition based on glycerol decomposition [11,12]

	Temperature (^oC)	Conv.= Conversion (C basis)	H_g= H_2/Glyc. (mole/mole)	H_g/Conv.	H_2/CO	H_2/CO_2
Equilibrium	500	-	4.00	-	10.00	2.00
Ni-LSCM/Al_2O_3	500	0.34	1.38	4.06	4.92	2.27
Ni-LSCM/Ce-Zr	500	0.35	1.50	4.29	6.28	2.19
Ni-LSCM/SDC	500	0.25	1.18	4.72	4.65	2.89

Though the Ce-Zr supported LSCM-promoted catalysts show a better glycerol conversion (35.2%) relatively compared to the Al_2O_3 supported LSCM-promoted catalyst (34.4%), the result signifies that both are good support for the reforming of glycerol pyrolysis products. However, what is not clear is the fact that the SDC supported catalyst despite its good reducibility and enhanced metal-support interaction observed in the TGA analysis which was better than that of Al_2O_3 supported catalyst, the performance was better with the Al_2O_3 supported catalyst. Perhaps this might be connected with better surface area and smaller particle size of the Al_2O_3 supported catalyst system as seen in Table 5-13 and Figure 5-19 respectively. Interestingly, the H_2/CO mole ratio in Table 5-15 suggests that all the catalyst systems are quite useful for hydrogen and syngas production.

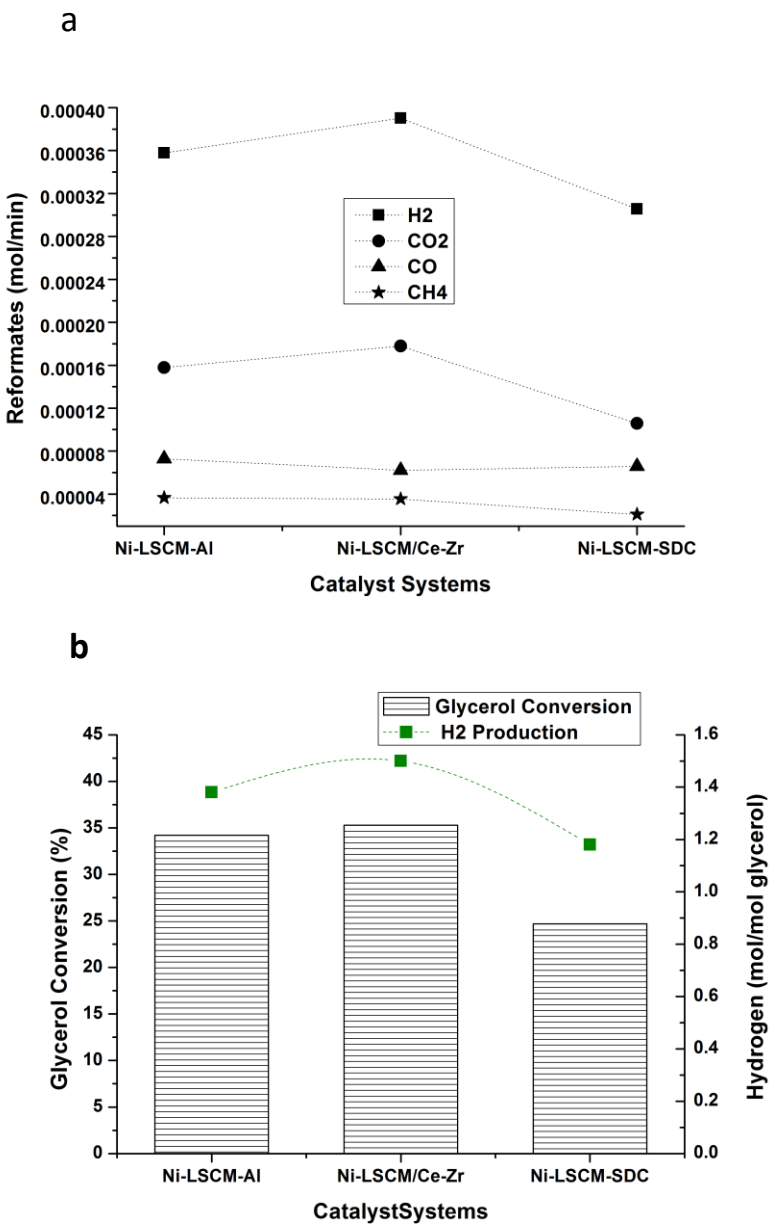

Figure 5-21 catalytic behaviour of the catalyst **a,** gaseous product distribution as a function of catalyst and **b**, comparison of glycerol conversion to hydrogen yield as a function of catalyst. The test was performed at 500 ^{o}C, S/C ratio of 3 and glycerol molar flow rate of 8.2 x 10^{-5} moles/min and 7.3 x 10^{-4} moles/min of water and WHSV of 28 h^{-1}

Figure 5-21b which compares amount of hydrogen produced per mole of glycerol shows that the Ce-Zr supported catalyst gave the highest hydrogen per mole of glycerol of 1.5 equivalents to 38% of the equilibrium composition (4.0) at that temperature. The trend in hydrogen production could be attributed to ceria's support for water gas shift reaction resulting to relatively high concentration of H_2 and CO_2 as demonstrated in many experiments[25,26,32]. The general enhanced performance of the Ce-Zr catalyst compared to the Al_2O_3 supported catalyst is due to its large surface

area, smaller particle size and enhanced metal-support interaction much better than was recorded for other catalysts. Similar behaviour of Ce-Zr as a support was reported in many studies[13,26].

The Ce-Zr's combined influence of its acidic-basic and redox properties has also contributed to its improved catalytic performance. The combined promoting behaviour of LSCM and that of the alternative support not only significantly improved the performance of the catalyst Ni-LSCM/Ce-Zr but suppressed carbon deposition drastically as seen in section 5.3.3.5. This was attributed to Mn tendency to enhance the oxygen storage capacity as well as oxygen mobility on the surface of Ce-Zr for effective oxidation[29]. Other gaseous products CO_2, CH_4 and CO were less than the equilibrium composition. The CO which was between 60-70% of the equilibrium composition (Table A2-2 of appendix 2), suggests there was rapid decomposition of glycerol influenced by the nickel-based catalysts surface in addition to reforming of glycerol. Therefore proper choice of support enhances glycerol conversion with high hydrogen yield. The Ce-Zr and SDC supports have shown robust catalytic behaviour as alternative support to Al_2O_3. The low amount of catalyst used (0.1g) has resulted to low glycerol conversion due to low contact time. Therefore using reasonable amount (2-5g) would increase catalyst bed thickness and contact time which could maximize glycerol conversion to gaseous products.

5.3.3.1.5 Correlation between the influence of support and carbon deposition

The carbon deposition phenomenon among the supported catalysts as shown in Figure 5-22 below shows evidence of carbon deposition in all the catalyst investigated. It is interesting to know that despite the trend in performance observed among the supported catalyst, SDC supported catalyst has shown better resistant to carbon deposition than the Al_2O_3 supported catalyst. The carbon deposition suppression followed the order Ni-LSCM/Ce-Zr> Ni-LSCM/SDC> Ni-LSCM/Al_2O_3 as reflected by the TGA profiles in Figure 5-22. The ceria-based supports proved better in preventing carbon deposition due to their oxygen storage-release properties which helps in oxidation and gasification of carbon from the catalyst surface. Generally the carbon

deposition from the TGA profile was highest with the Al_2O_3 supported catalyst recording 15% whilst 7% and 3% was recorded for SDC and Ce-Zr supported catalysts respectively. The alternative ceria-based supports (SDC and Ce-Zr) showed a remarkable improvement on the Al_2O_3 supported catalyst performance in suppression of carbon deposition.

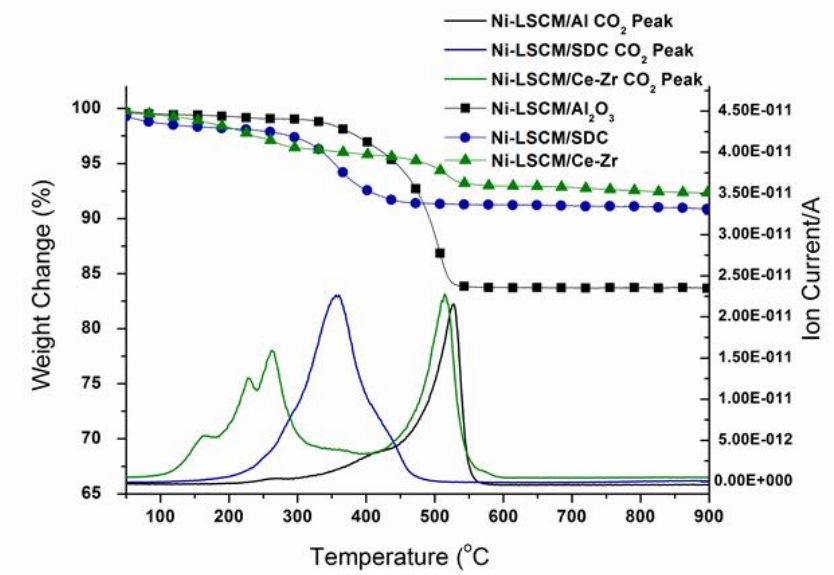

Figure 5-22 Change in weight due to oxidation of carbon from the surface of the used catalyst surfaces in oxidising atmosphere monitored in parallel with CO_2 as a function of temperature showing the extent of carbon deposition and type of carbon from the temperature at which bulk of the carbon oxidised.

The CO_2 profile indicates the temperature at which bulk of the carbon was oxidised during the temperature programmed oxidation. It is evident from the CO_2 profile that bulk of the carbon was oxidised at different temperatures in each of the catalyst systems. While both Al_2O_3 and Ce-Zr supported catalyst showed a major peak at 500 ^oC, the Ce-Zr supported catalyst showed another major peak at lower temperature of 250 ^oC. The SDC supported catalyst showed only one distinct major CO_2 peak at low temperature of 350 ^oC. The low temperature CO_2 peaks due to Ce-Zr and SDC corresponds to amorphous carbon deposited on the metal surface which are very easy to remove therefore oxidised at low temperature. The medium temperature CO_2 peak is usually due to polymeric or graphitic carbon deposited at the metal-support interphase which is more difficult to remove relatively and therefore oxidised at higher temperature. The ceria-based supports had more easy carbon compared to complex graphitic carbon associated with Al_2O_3-based support. It is interesting to note

that the low temperature CO_2 peak due to Ce-Zr supported catalyst occur at lower temperature than that of SDC supported catalyst which further suggests robust behaviour of the Ce-Zr supported catalyst. The carbon suppression capabilities of the ceria-based supports is attributable to their acidic-basic properties, redox potential and oxygen storage and release properties which is known to reduce carbon deposition as explained above in section 5.4.2.5. Despite the influence of LSCM promoter on the acidic surface of the Al_2O_3 which seemed to have reduced its tendency to dehydrate glycerol which could result in carbon deposition, the other supports seemed to do better. It is interesting to note that unlike the use of promoters which had influence on the extent of carbon deposition only and showed no influence on the nature of type of carbon and its location, the supports investigated have shown influence on the extent, location and type of carbon deposited.

Subsequent investigations will be on the new promising catalyst Ni-LSCM/Ce-Zr only.

5.4 The New Ni-$La_{0.75}Sr_{0.25}Cr_{0.5}Mn_{0.5}O_{3-\delta}$/$Ce_{0.75}Zr_{0.25}O_2$ (Ni-LSCM/Ce-Zr) catalyst system

5.4.1 Correlation between reforming temperature and catalyst performance

Influence of reaction temperature on the products distribution, hydrogen production as well as glycerol conversion was explored from low to moderate temperatures-300-600 ^oC using the more promising Ni-LSCM/Ce-Zr catalyst system. The S/C ratio of 3:1 using pure glycerol was used and WHSV of 28 h^{-1} and glycerol solution molar flow rate of 2.60 x 10^{-4} moles/min. Hydrogen production in mole/mole glycerol and glycerol conversion in Figure 5-23a shows similar trend with the amount of reformate generated in Figure 5-23b i.e. increased with reaction temperature. Though there was a drop at 800 ^oC, the results shows that those processes were favoured by kinetics. Unlike Ni/Al_2O_3 catalyst system that gets deactivated rapidly at low temperature due to coking, Ni-LSCM/Ce-Zr gave reasonable conversion ≥15% at temperature as low as 400 ^oC. This is attributable to combined influence of LSCM and Ce-Zr and strong Ni-support interaction which decrease dehydration and increase possible decomposition of glycerol and coke resistance. The H_2/CO_2 mole ratio in Table 5-16 suggests that the

steady rise in H_2 and CO_2 profile could be attributed to the endothermic nature of glycerol pyrolysis and to water-gas-shift reaction which both increase with increase in temperature to 500 ^oC as shown in Eqn. 2-3 and Eqn. 2-6 respectively. The little rise in CH_4 could be attributed to slight methanation reaction (Eqn. 2-8 to 10). Looking at the H_2/CO_2 mole ratio of Table 5-16, Water gas shift reaction which is slightly exothermic and strive well at temperatures up to 500 ^oC could be the real contributing factor to the steady rise in H_2 and CO_2 and less probably methane reforming or dehydrogenation especially at low temperatures as shown by Eqn. 2-5 and Table 2A-3 of appendix 2 and as also proved by thermodynamic evaluation[11]. Similar trend was reported for H_2 in glycerol steam reforming over Ni/Al_2O_3 by Wu et al 2013[35].

Table 5-16 hydrogen to CO_2 and CO ratio as a function of reforming temperature

Temperature (^oC)	H_2/CO_2	H_2/CO
300	11.8	0.28
400	3.43	2.66
500	2.19	6.28
600	3.29	3.70

The hydrogen produced per glycerol fed generally increased with temperature due to kinetic influence. The hydrogen yield was within 1.5-38% of the equilibrium composition (Table A2-2 appendix 2) across the temperature range studied. This suggests as the temperature increases, the system produces more hydrogen. Conversely, the Ni/Al_2O_3 systems strongly absorbs glycerol to its surface and dehydrate it due to its acidic surface which might have led to formation of ethylene and propylene or carbonyl compounds and thus offers weak corresponding coke resistance and consequent deactivation and low conversion at low temperatures[15]. The hydrogen production though favoured by kinetics is limited by reactions such as reverse WGSR and formation of acrolein or carbonyl compounds especially at lower temperatures as corroborated by the H_2/CO ratio in Table 5-16. Unwanted reactions especially at low temperatures such as dehydration (Eqn. 2-4) would have also reduced the hydrogen yield. Glycerol passing through unconverted is also another contributor.

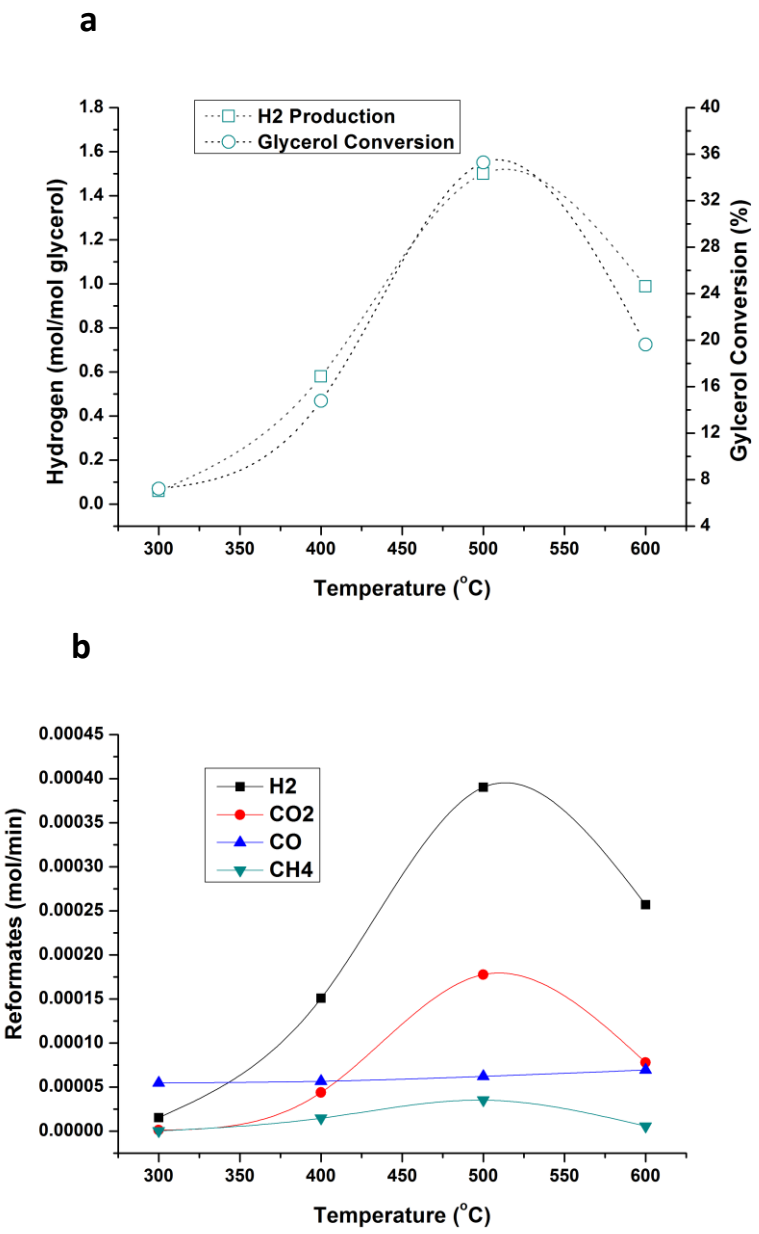

Figure 5-23 Influence of reforming temperature was investigated at different temperatures (300-600 °C), S/C ratio of 3 and glycerol molar flow rate of 8.2 x 10^{-5} moles/min and 7.3 x 10^{-4} moles/min of water and WHSV of 28 h^{-1} **a,** Influence of temperature on hydrogen yield and glycerol conversion **b,** Change in reformate composition with temperature

The calculated CO/CO_2 ratio lower value at 500 °C in Table 5-17 corroborates the WGS reaction at that temperature as well generating lots of H_2 and CO_2[36]. The relatively high values of CO/CO_2 at lower temperatures confirms occurrence of some unwanted reactions at those temperatures and consequent low performance relatively.[34] Therefore 500 °C represents the optimized temperature for high hydrogen yield and glycerol conversion in this work. The drop in the activity at 600 °C could be attributed

to reversible self-poisoning deactivation which usually occurs at 600-650 ^{o}C as similarly reported by Breen et al, 2002[13] or coking activities.

Table 5-17 Molar ratio of CO to CO_2 in steam reforming of glycerol on the Ni-LSCM/Ce-Zr catalyst system at different temperatures in pure glycerol and 3:1 S/C ratio

Temperature (^{o}C)	CO/CO_2 (mol. %)
300	4191
400	129
500	35
600	89

Looking at the carbon balance shown in Table 5-18 as a function of temperature, it is clear low temperatures glycerol steam reforming such as 300 and 400 ^{o}C are associated with lots of carbon loss as results of carbon deposition which gets better with temperature. Consequently, temperature of 500 ^{o}C represents best condition with this catalyst system. These further suggest optimization of reaction condition such as temperature is important to maximize yield and reduce carbon loss.

Table 5-18 Analysis based on carbon balance as function of temperature

Temp.(^{o}C)	Total carbon **IN** (moles/min)	Total carbon **OUT** (moles/min)	CO **OUT** (moles/ min)	CO_2 **OUT** (moles/ min)	CH_4 **OUT** (moles/ min)
300	7.8×10^{-4}	5.7×10^{-5}	5.5×10^{-5}	1.3×10^{-6}	2.4×10^{-7}
400	7.8×10^{-4}	1.2×10^{-4}	5.7×10^{-5}	4.4×10^{-5}	1.5×10^{-5}
500	7.8×10^{-4}	3.0×10^{-4}	6.2×10^{-5}	1.8×10^{-4}	3.5×10^{-5}
600	7.8×10^{-4}	1.6×10^{-4}	7.8×10^{-5}	8.0×10^{-5}	5.7×10^{-6}

5.4.2 Influence of steam-to-carbon ratio (S/C), glycerol type and stability of the catalysts

The influence of S/C ratio in steam reforming of glycerol using the Ni-LSCM/$Ce_{0.75}Zr_{0.25}O_2$ catalyst at the optimised temperature of 500 ^{o}C and S/C ratio of 3:1 and 1:1 using both pure and by-product glycerol was investigated and the results obtained are shown in Figure 5-24. The glycerol solution molar flow rate of 2.60×10^{-4} mol/min (0.019 ml/min) was used for S/C ratio of 3 and 1.36×10^{-4} mol/ min (0.01 ml/min) for S/C ratio 1 to keep the amount of glycerol fed into the reactor constant. The WHSV was 28 h^{-1} in the case of S/C ratio 3 and 15 h^{-1} for S/C 1 calculated based on

the method shown in appendix 3. The results as shown in Figure 5-24 revealed that S/C ratio has significant influence on the steam reforming. Using S/C ratio below the stoichiometric amount has reduced hydrogen production per mole of glycerol and glycerol conversion. This means water favours forward reaction of WGSR leading to more hydrogen production. Despite impurities such as unconverted vegetable oil, biodiesel, residual catalyst, intermediate products and probably methanol in the by-product glycerol which would have reduced performance, the conversion and amount of hydrogen produced per mole of glycerol is as good as using pure glycerol. The results using by-product glycerol compares favourably with what Kamonsuangkasem et al[37] reported using different grades of glycerol looking at the reaction condition and catalyst amount used in this work. These show that optimising the water dilution is essential to strike a balance between maximization of hydrogen production rate and glycerol conversion with the negative influence of much dilution on the methane production rate as explained above especially where CH_4 production is important.

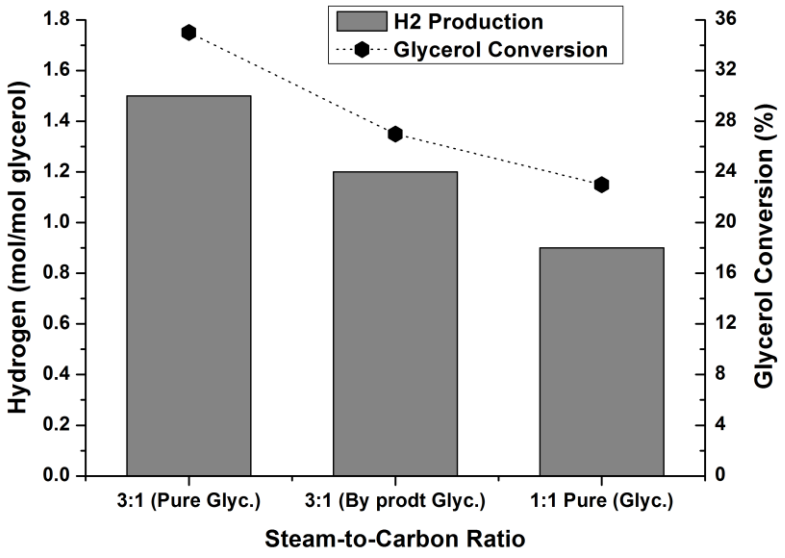

Figure 5-24 Comparison between hydrogen production and glycerol conversion in relation to influence of S/C ratio and glycerol type in a test performed at 500 ^{o}C, S/C ratio of 1-3 at 1.36 x 10^{-4} - 2.60 x 10^{-4} glycerol solution molar flow rate and WHSV of 15-28 h^{-1}

The most striking difference among the catalysts was observed in the stability test. Change in amount of hydrogen produced per mole of glycerol over time in Figure 5-25 show that non-promoted Ni/Al_2O_3 catalyst gets deactivated rapidly after prolonged 9

hour test. Perhaps due to coking which is known to cause active site poisoning and pore blockage reducing surface area, hydrogen yield and general activity of the catalyst. It was only relatively stable within the four hours of the test, then rapidly deactivated thereafter. With the LSCM promoted and Ce-Zr supported catalysts, the deactivation was slow. The hydrogen yield loss with the Ni-LSCM/Al_2O_3 and Ni-LSCM/Ce-Zr catalysts was approximately 6% and 4% respectively after 9 hours while Ni/Al_2O_3 recorded 86% loss in hydrogen yield. The LSCM and Ce-Zr has significantly influenced hydrogen production per mole of glycerol and stability of nickel in Ni-LSCM/Al_2O_3 and Ni-LSCM/Ce-Zr catalyst systems. One mechanism through which such could happen is by hindering re-oxidation of Ni in such reaction condition[34]. The superiority observed with Ni-LSCM/Ce-Zr could be due to combined influence of LSCM and Ce-Zr as explained in section 5.3.3.4 above.

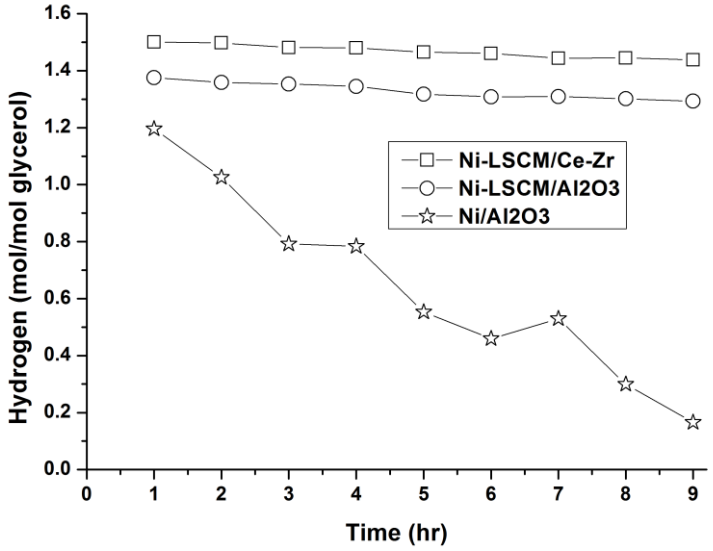

Figure 5-25 Change in hydrogen yield over time at 500 ^{o}C, S/C ratio of 3 and glycerol molar flow rate of 8.2 x 10^{-5} moles/min and 7.3 x 10^{-4} moles/min of water and WHSV of 28 h^{-1}

Thus water dilution of feedstock such as glycerol is capable of enhancing catalytic behaviour for maximum hydrogen and syngas production via steam reforming of pure and by-product glycerol. More so, by-product glycerol phase directly from biodiesel synthesis seen as a waste is as useful as pure glycerol and could be harnessed for production of hydrogen and syngas for fuel cell application. Proper choice of support enhances catalyst stability for sustained generation of hydrogen and syngas.

5.4.3 Comparing carbon deposition phenomenon to the influence of S/C ratio and glycerol type

Figure 5-26a shows CO_2 peaks and TGA profile of the catalyst systems tested at 500 ^oC reaction temperatures in oxygen atmosphere. The used catalyst systems TPO profile in this case are overplayed to clearly show the influence of support and promoter on the Ni/Al_2O_3 catalyst ability to suppress carbon deposition at the same time. In all the samples, the major CO_2 peak occurs at approximately 550 ^oC indicating that bulk of the coke was polymeric or graphitic deposited at the interface between the active phase and support. Interestingly, Ni-LSCM/Ce-Zr catalyst system showed two distinct CO_2 peak depicting two types of carbon species on the catalyst surface. The CO_2 peak at low temperature indicates oxidation of amorphous carbon deposited on the metal surface. This means it has a mixture of polymeric or graphitic and amorphous carbon. This confirms that the coke type and properties depend upon the type of substrate used as support and its involvement in the reaction cycle.

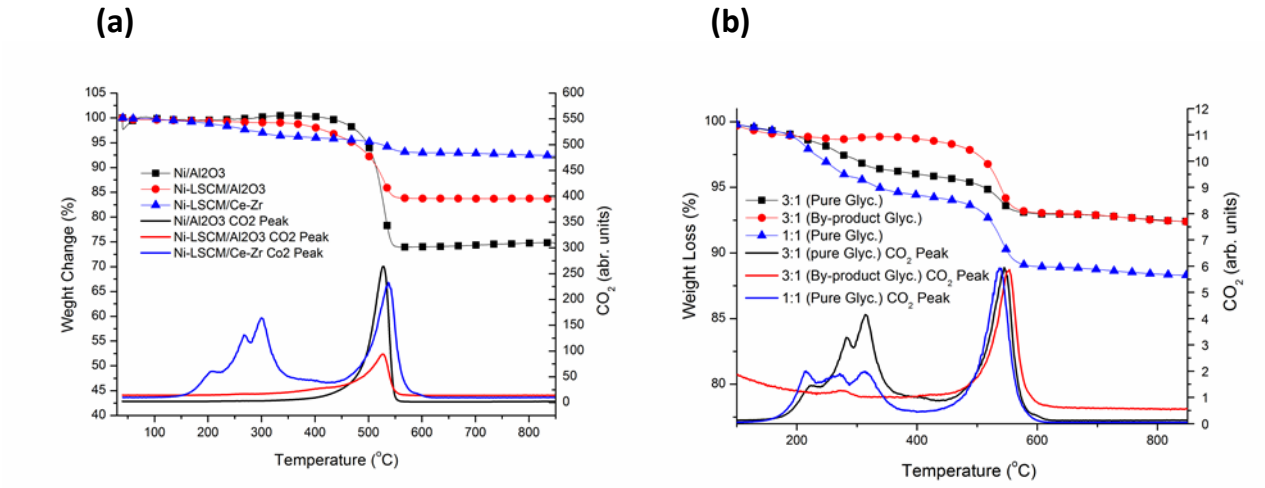

Figure 5-26 **a,** Change in weight due to carbon oxidation of the selected used catalyst samples in oxidising atmosphere monitored in parallel with CO_2 as a function of temperature **b,** Change in weight due to carbon oxidation of the selected used catalyst samples in oxidising atmosphere monitored in parallel with CO_2 as a function of temperature showing influence of S/C ratio and glycerol type

The extent of carbon deposition reduces due to the stabilizing influence of LSCM and Ce-Zr support from 26.53% in Ni/Al_2O_3 to 15.12% and 2% in Ni-$LSCM/Al_2O_3$ and Ni-LSCM/Ce-Zr respectively. The carbon suppression therefore followed the order Ni/Al_2O_3<Ni-$LSCM/Al_2O_3$<Ni-LSCM/Ce-Zr. It is evident the supports have profound

influence on the carbon deposition. Figure 5-26b shows the influence of S/C ratio and glycerol type on the carbon deposition with the Ni-LSCM/Ce-Zr catalyst only. It is obvious that the major carbon dioxide peak is a medium temperature type irrespective of the S/C ratio used. It is also clear from the chart that using stoichiometric S/C ratio of 3:1, there was another CO_2 peak at low temperature using either pure or by-product glycerol which indicates formation of amorphous carbon in addition to polymeric or graphitic carbon. But in comparison to S/C ratio of 1:1, only the CO_2 peak at medium temperature due to graphitic carbon was obtained. Therefore lots of more severe carbon occurred when steam-to-carbon ratio below the stoichiometric amount (1:1) was used due to probable formation of intermediates and by-products which signifies the influence of water in suppressing carbon deposition. This observation was corroborated in the TGA profile of the same Figure 5-26b which shows significant increase in carbon deposition when S/C ratio less than the stoichiometric value were used. This attest to the robust behaviour of the catalyst system suggesting that just like pure glycerol, by-product glycerol phase directly from biodiesel synthesis could also achieve similar results with the new Ni-LSCM/Ce-Zr catalyst system.

5.5 Conclusion

Ni-based catalysts prepared by wet impregnation were investigated in steam reforming of pure and by-product glycerol to produce hydrogen-rich gas for utilization in fuel cell. Influence of catalyst loading, reaction and calcination temperature, promoters, supports and carbon deposition in glycerol steam reforming were explored.

Reaction and calcination temperatures, catalyst loading and steam-to-carbon ratio had profound influence on glycerol conversion, hydrogen production per mole of glycerol and suppression of carbon deposition on Ni/Al_2O_3 catalyst system. Water-gas-shift reaction strives well at low temperature favouring H_2 yield and was at its best at 500 ^oC which was the optimum reaction and calcination temperature in this work. Higher reaction temperature (>500 ^oC) led to deactivation by agglomeration while lower temperature led to deactivation by carbon deposition as further supported by

analysis based on carbon balance. High calcination temperature >900 ^{o}C affects the structural properties of the catalyst material due to phase transformation to spinel ($NiAl_2O_4$) which resulted to low performance and consequent catalyst deactivation. Structural properties and catalytic behaviour of Ni/γ-Al_2O_3 was enhanced using LSCM and Ceria as promoters. The LSCM promoter has a stabilizing influence on the nickel metal by improving metal-support interaction, glycerol conversion, and hydrogen yield. It also reduced catalyst deactivation by agglomeration and carbon deposition. The Ceria-based supports; samarium-doped ceria (SDC) and Zirconia-doped ceria (Ce-Zr) have greatly enhanced structural properties and the general catalytic performance of Ni/Al_2O_3. For the first time, a new catalyst Ni-$La_{0.75}Sr_{0.25}Cr_{0.5}Mn_{0.5}O_{3-\delta}$/$Ce_{0.75}Zr_{0.25}O_2$ (Ni-LSCM/Ce-Zr) has demonstrated great potential for steam reforming of pure and by-product glycerol even at low temperatures and almost hindered carbon deposition completely. The catalyst showed better surface area, suitable particle size, catalyst reducibility and enhanced metal-support interaction compared to Ni/Al_2O_3 catalyst system. This implies that despite limitations of wet impregnation, enhanced catalytic performance could be achieved if the structural properties of catalyst system are tailored through proper choice of promoter and support.

Generally, low catalyst amount (0.1g) was used for the catalytic tests which gave short contact time with lots of glycerol passing unconverted and consequent low glycerol conversion. Therefore use of reasonable quantity of 2-5g would enhance conversion significantly.

References

1. Balat, H. and Kırtay, E. Hydrogen from biomass – present scenario and future prospects. *International Journal of Hydrogen Energy* **35**, 7416–7426 (2010)

2. Kırtay, E. Recent advances in production of hydrogen from biomass. *Energy Conversion and Management* **52**, 1778–1789 (2011)

3. Sanchez, E. A. and Comelli, R. A. Hydrogen by glycerol steam reforming on a nickel–alumina catalyst: Deactivation processes and regeneration. *International Journal of Hydrogen Energy* **37**, 1474 - 4746 (2012)

4. Kim, Y.; Kim, P.; Kim, C. and Yi, J. A novel method for synthesis of a Ni/Al_2O_3 catalyst with a mesoporous structure using stearic acid salts. *J. Mater. Chem.* **13**, 2353–2358 (2003)

5. Seo, Y.; Jung, Y.; Yoon, W.; Jang, I. and Lee, T. The effect of Ni content on a highly active $Ni\text{-}Al_2O_3$ catalyst prepared by the homogeneous precipitation method. *Int. j. of hydrogen energy* **36,** 94-102 (2011)

6. Fiuza, R. D.; Da Silva, M. A. and Boaventura, J. S. Development of Fe-Ni/YSZ-GDC electrocatalyst for application of SOFC anodes: XRD and TPR characterization and evaluation in the ethanol steam reforming reaction. *Int.j.of hydrogen energy* **35** 11216-11228 (2010)

7. Rerego, C. and Villa, P. Chapter 3 Catalyst preparation methods. *Catalysis Today* **34**, 281–305 (1997)

8. Leofanti, G.; Padovan, M.; Tozzola, G. and Venturelli, B. Surface area and pore texture of catalysts *Catalysis Today* **41,** 207-219 (1998)

9. Buffoni, I. N.; Pompeo, F.; Santori, G. F. and Nichio, N. N. Nickel catalysts applied in steam reforming of glycerol for hydrogen production. *Catalysis Communications* **10** 1656–1660 (2009)

10. Md Zin, R.; Ross, A. B.; Jones, J. M. and Dupont, V. Hydrogen from ethanol reforming with aqueous fraction of pine pyrolysis oil with and without chemical looping *Bioresource Technology* **176**, 257-266 (2015)

11. Adhikari, S.; Fernando, S.; Gwaltney, R. S.; To, S. D. F.; Bricka, R. M.; Steele, P. H and Haryanto, A. A Thermodynamic analysis of hydrogen production by steam reforming of glycerol. *Int. j. Hydrogen Energy* **32**(14), 2875-80 (2007)

12. Dieuzeide, M. L. and Amadeo, N. Thermodynamic analysis of glycerol steam reforming *Chem. Eng. Technol.* **33**, 1, 89–96 (2010)

13. Newnham, J.; Mantri, K.; Amin, M. H.; Tardio, J. and Bhargava, S. K. Highly stable active Ni-mesoporous alumina catalysts for dry reforming of methane.*int.j. of hydrogen energy* **37**,1454-1464(2012)

14. Breen, J. P.; Burch, R. and Coleman, H. M. Metal-catalysed steam reforming of ethanol in the production of hydrogen for fuel cell applications. *Applied Catalysis B: Environmental.* **39** 65–74 (2002)

15. Paweewan, B.; Barrie, P. J. and Gladden, L. F. Coking and deactivation during *n*-hexane cracking in ultra stable zeolite Y. *Applied Catalysis A: General* **185** 259–268 (1999)

16. Mawdsley, J. R. and Krause, T. R. Rare earth-first-row transition metal perovskites as catalysts for the autothermal reforming of hydrocarbon fuels to generate hydrogen. *Applied Catalysis A: General* **334** 311–320 (2008)

17. Martı´n, N.; Viniegra, M.; Lima, E. and Espinosa, G. Coke characterization on Pt/Al2O3—β-zeolite reforming catalysts, *Ind. Eng. Chem. Res*. **43** 1206–1210 (2004)

18. Hilaire, S.; Wanga, X.; Luoa, T.; Gorte, R. J.; Wagner, J. A comparative study of water-gas-shift reaction over ceria supported metallic catalysts. Applied Catalysis A: General **215** 271–278 (2001)

19. Therdthianwong, S.; Siangchin, C. and Therdthianwong, A. Improvement of coke resistance of Ni/Al_2O_3 catalyst in CH_4/CO_2 reforming by ZrO_2 addition. *Fuel Processing Technology.* **89,** 160 – 168 (2008)

20. Profeti, L. P. R.; Ticianelli, E. A. and Assaf, E. M. Production of hydrogen via steam reforming of biofuels on $Ni/CeO_2–Al_2O_3$ catalysts promoted by noble metals. *International journal of hydrogen energy* **34** 5049– 5060 (2009)

21. Ebshish, A.; Yaakob, Z.; Narayanan, B.; Bshish, A. and Daud, W. R. W. The Activity of Ni-based catalysts on steam reforming of glycerol for hydrogen production. *International Journal of Integrated Engineering* **3**(1) 5-8 (2011)

22. Buffoni, I. N.; Pompeo, F.; Santori, G. F. and Nichio, N. N. Nickel catalysts applied in steam reforming of glycerol for hydrogen production. *Catalysis Communications* **10** 1656–1660 (2009)

23. Bezen, M. C. I.; Breitkopf, C.; Kolli, N. E. I.; Krafft, J. Louis, C. and Lercher, J. A. Selective modification of the acid–base properties of ceria by supported Au. *Chem. Eur. J.* **17** 7095 – 7104 (2011).

24. Aneggi, E.; Boaro, M.; de Leitenburg, C.; Dolcetti, G. and Trovarelli, A. Insights into the redox properties of ceria-based oxides and their implications in catalysis. *Journal of Alloys and Compounds* **408–412** 1096–1102 (2006)

25. Bunluesin, T.; Gorte, R. J. and Graham, G. W. Studies of the water-gas-shift reaction on ceria-supported Pt, Pd, and Rh: Implications for oxygen-storage properties. *Applied Catalysis B: Environmental* **15,** 107-l 14 (1998)

26. Gorte, R. J. and Zhao, S. Studies of the water-gas-shift reaction with ceria-supported precious metals. *Catalysis Today* **104,** 18–24 (2005)

27. Łamacz, A.; Pawlyta, M.; Dobrzański, L. A. and Krztoń, A. Characterization of the structure features of $CeZrO_2$ and $Ni/CeZrO_2$ catalysts for tar gasification with steam. *Archives of Materials Science and Engineering* **48**(2) 89-96 (2011).

28. Breen, J. P.; Burch, R.; Coleman, H. M. Metal-catalysed steam reforming of ethanol in the production of hydrogen for fuel cell applications. *Applied Catalysis B: Environmental* **39,** 65–74 (2002).

29. Bampenrat, A.; Meeyoo, V.; Kitiyanan, B.; Rangsunvigit, P. and Rirksomboon, T. Naphthalene steam reforming over Mn-doped CeO_2–ZrO_2 supported nickel catalysts. *Applied Catalysis A: General* **373** 154–159 (2010).

30. Gould, B. D.; Tadd, A. R. and Schwank, J. W. Nickel-catalysed autothermal reforming of jet fuel surrogates: *n*-dodecane, tetralin, and their mixture. *Journal of Power Sources* **164,** 344–350 (2007).

31. Łamacz, A.; Krzton, A. and Djega-Mariadassou, G. Steam reforming of model gasification tars compounds on nickel based ceria-zirconia catalysts. *Catalysis Today* 1**76,** 347– 351(2011)

32. Trovarelli, A.; Boaro, M.; Rocchini, E.; Leitenburg, C. and Dolcetti, G. Some recent developments in the characterization of ceria-based catalysts. *Journal of Alloys and Compounds* **323–324,** 584–591 (2001)

33. Sundari, R. and Vaidya, P. D. Reaction kinetics of glycerol steam reforming using a Ru/Al_2O_3 catalyst. *Energy Fuels* **26,** 4195−4204 (2012)

34. Profeti, L. P. R.; Ticianelli, E. A. and Assaf, E. M. Production of hydrogen via steam reforming of biofuels on Ni/CeO_2–Al_2O_3 catalysts promoted by noble metals. *International journal of hydrogen energy* **34,** 5049– 5060 (2009)

35. Wu, G.; Zhang, C.; Li, S.; Han, Z.; Wang, T.; Ma, X. and Gong, J. Hydrogen production via glycerol steam reforming over Ni/Al_2O_3: Influence of nickel precursors. *ACS Sustainable Chem. Eng*. **1,** 1052−1062 (2013)

36. Kauppi, E. I.; Kaila, R. K.; Linnekoski, J. A.; Krause, A. O. I. and Veringa Niemela, M. K. Temperature-programmed oxidation of coked noble metal catalysts after autothermal reforming of n-hexadecane*. international journal of hydrogen energy* **35**, 7756-7767 (2010)

37. Kamonsuangkasem, K.; Therdthianwong, S. and Therdthianwong, A.: Hydrogen production via oxidative steam reforming of biodiesel by-products over Ni/CeO_2-ZrO_2/Al_2O_3 catalyst. *International Conference on Chemistry and Chemical Process*. **10,** 107-113 (2011)

6.0 Nickel-based metal oxide supported catalyst: The redox lattice reorganisation and redox exsolution phenomenon

6.1 Introduction

The use of promoters and alternative supports has evidently yielded some improvements in the structural and catalytic behaviour of nickel-based catalyst such as Ni/Al_2O_3 especially coke suppression, metal-support interaction and overall catalytic performance. However, there is no doubt much still need to be done. For instance, synthesis of metal oxide supported metal particle catalysts which constitute bulk of the catalysts used in steam reforming is largely done by metal impregnation/deposition or assembling techniques[1-3]. The 'traditional' wet impregnation is time consuming, costly and difficult to control particle size, growth and distribution. It also offers only weak interaction between the active phase metal particles and support resulting to agglomeration, instability and deactivation at times even where a promoter was used, hence offers poor catalytic properties[4,5]. Alternatively, metal catalysts such as nickel nano particles could be exposed to the surface from the bulk itself and supported on 'inert' oxide surface by means of thermal treatment in reducing atmosphere as seen with exsolution phenomenon depicted in Figure 6-1. That has shown some promising properties such as control over particle size, growth, distribution and strong metal catalyst-support interaction. Hence is seen as improvement to the traditional trend in development of supported metal catalysts using wet impregnation[6,7].

In this work, it is demonstrated using redox lattice reorganisation phenomenon in spinel for the first time that metal catalyst particles could grow out of the support itself and firmly anchored on the spinel oxide support leaving behind elaborate macro porous channels. This provides good surface area, strong metal-support interaction and reduce tendency for catalyst deactivation by agglomeration and offers effective coking suppression and control over particle size and growth hence efficient catalytic behaviour. Unlike wet impregnation, it also reduces catalyst processing time. To further investigate this new phenomenon, nickel nano particles were also grown out of the bulk using the redox exsolution phenomenon seen as a sister phenomenon to

redox lattice reorganisation and use of defect chemistry to enhance surface redox exsolution of B-site catalyst particles and possibly redox rearrangement.

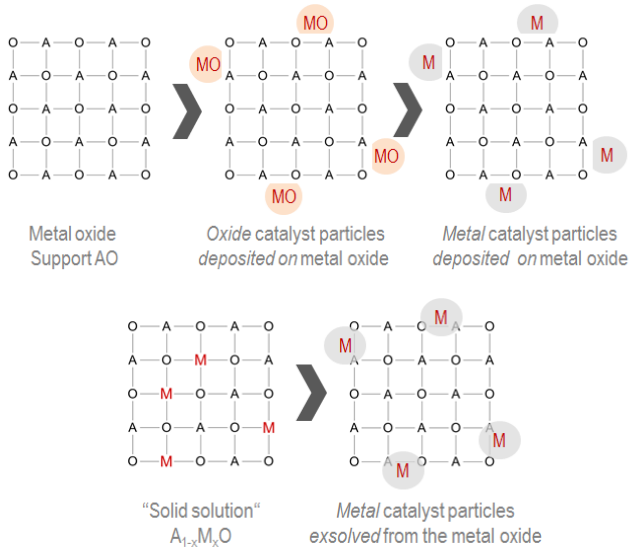

Figure 6-1 Comparative illustration of the steps required to decorate an oxide support AO with catalyst particles M through wet impregnation or in situ redox exsolution. a,chemical impregnation and thermal treatment steps followed by a reducion to produce the metal particles M on the outer surface of the support AO. b, in situ redox exsolution M is incorporated in its cation form in the crystal lattice of AO and exsolved in one step, upon reduction[5,6].

Perovskite oxides (ABO_3) and spinel oxide (AB_2O_4) are at the centre of this research due to their robust properties and flexibility to doping for enhanced properties[5,8]. Perovskite for instance have intrinsic ability to stretch their bond angles or tilt to accommodate doping as a response to steric constrain from the dopant cation. They could also alter covalent interaction between the cations and anions in the lattice, though a times doping could lead to formation of ordered structure[5,6]. Perovskites generally owe their good catalytic properties to good micro structures, ionic and electronic conductivity, existence of oxygen ion vacancies and their mobility in the lattice and defect chemistry[5,8,9]. Doping on either A or B site could enhance structural and catalytic properties as well as ionic and electronic behaviour of the materials. Defects could be introduced into their structures through redox processes or doping with a lower valence cation on either A or B site which also significantly enhances structural and catalytic properties. Defect and non-stoichiometric formulations such as $A_{1-\alpha}BO_3$ and $ABO_{3-\gamma}$ known as deficient perovskite or $A_{1+\alpha}BO_3$ and $ABO_{1+\gamma}$ known as excess perovskite with contrasting properties have been studied[5,6]. Due to the relative

stability of the B-site site, it rarely exhibits such non-stoichiometric tendencies. Deficiencies on either A or O sites creates defects whose advantage could be harnessed for catalysis as would be seen in the subsequent studies in the following sections. Furthermore, morphology of both spinel and Perovskite microstructures could be modified for enhanced properties upon reduction in a H_2-rich environment at suitable temperature (800-1000 ^{o}C ±). On reduction abstraction of oxide ions leads oxygen non-stoichiometry and occurrence of vacancies which enhances mobility of oxide ions that is known to facilitate oxidation and reduce coking during catalysis [5,6,8].

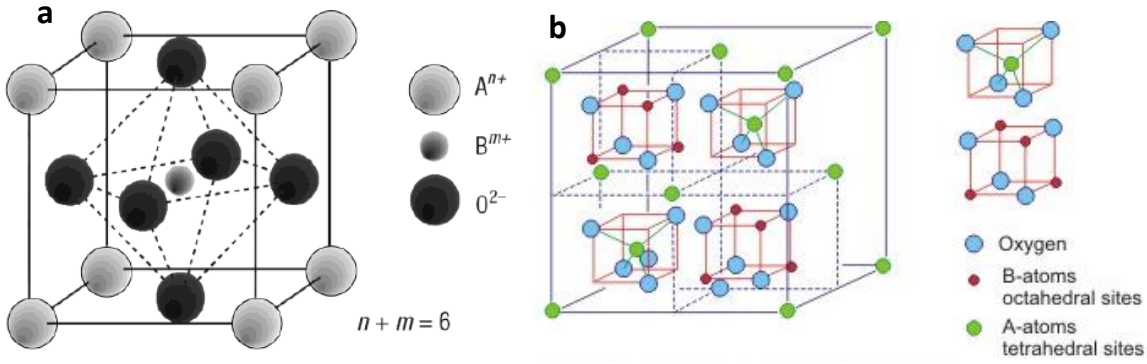

Figure 6-2 the unit cell for **a**, perovskite and **b**, spinel[10,11]

In the Perovskite ABO_3 type unit cell, the larger size but lower valency 'A' cation occupies the 6-folded coordinated corners while the 'B' cation with higher valency and smaller size occupies the centre with the 12-fold coordination as seen in Figure 6-2a. The oxygen atoms are usually attracted around the smaller high charged 'B' cation at the centre. The overall total charge on the perovskite is +6. In the case of spinel, the structure is a bit more complicated having both tetrahedral and octahedral coordinated voids as in Figure 6-2b. It has a partial occupancy where the A^{2+} ion occupies 1/8 of the tetrahedral coordinated sites and the B^{3+} ion occupies ½ of the octahedral coordinated sites and a total of 32 oxygen atoms arranged in a face-centred cubic lattice[10,11].

To the best of my knowledge not much work is reported on the use of such exsolved materials as catalyst in steam reforming of liquid feedstock such as glycerol where more severe coking is expected which is one of the aims of this work. In the light of the above, in this work, the use of chromium-rich spinel and highly doped chromite-

based perovskites oxides as catalyst and support for nickel-based catalyst using redox lattice reorganisation and redox exsolution phenomena respectively in glycerol steam reforming (GSR) will be explored. Influences of first row transition metal (Mn, Fe, Co and Ni) doping especially on the B-site, catalyst reduction and reaction conditions on the lattice structure, microstructure and catalytic properties in relation to glycerol steam reforming (GSR) will be investigated. Relationship between lattice defects, dopant cations and redox exsolution in some titanate perovskite in relation to glycerol steam reforming will be looked at. An attempt will also be made to compare with the Ni/Al_2O_3 catalyst system from wet impregnation investigated in the previous sections.

6.2 Chromium-rich spinel and spinel oxide-supported metal particle catalysts from redox lattice reorganisation for glycerol steam reforming

The work presented in this section on the spinel was done in collaboration with my colleague in the group Elena Stefan and her contributions for material processing and characterization are hereby acknowledged. The catalysis was done by me.

6.2.1 Crystal and micro structure of the catalyst systems

Crystallographic data of the host $MnFeCrO_4$ and the $MnNi_xFe_{1-x}CrO_4$ (x = 0.3, 0.5) series shown in Figure 6-3 and 6-4a-b confirms pure single cubic phase spinel was synthesized. The $MnFeCrO_4$ host material as tested under reducing atmosphere showed an extra peak due to MnO and metallic Fe which increased with the reduction time[12]. Rietveld refinement of the XRD patterns revealed characteristic $Fd\bar{3}m$ (No 227) cubic crystal structure for the spinel with origin at *3-m* and the A, B, and O site positions corresponding to 8a (¼, ¼, ¼), 16d (½, ½, ½) and 32e (u, u, u), respectively. The cell parameter slightly increased in the nickel substituted materials compared to the host materials as seen from the Rietveld refinement data in Table 6-1 and 6-2 respectively. This is attributable to the sensitivity of the cell parameter towards the dopant cation. In the case of the reduced spinel, Rietveld refinement was performed with a minimum of three phases (e.g. spinel, MnO and Fe/Ni metals/alloys). MnO was refined in the space group *Fm3-m* (No 225) and atomic positions 4a (0, 0, 0) and 4b (½, ½, ½) for Mn and O, respectively. Fe was refined in the space group *Im3-m* (No 229) and atomic position 2a (0, 0, 0), Ni in the space group *Fm3-m* (No 225) and atomic

position 4a (0, 0, 0) and Fe-Ni alloys were considered in the space group *Fm3-m* (No 225) and atomic position 4a (0, 0, 0).

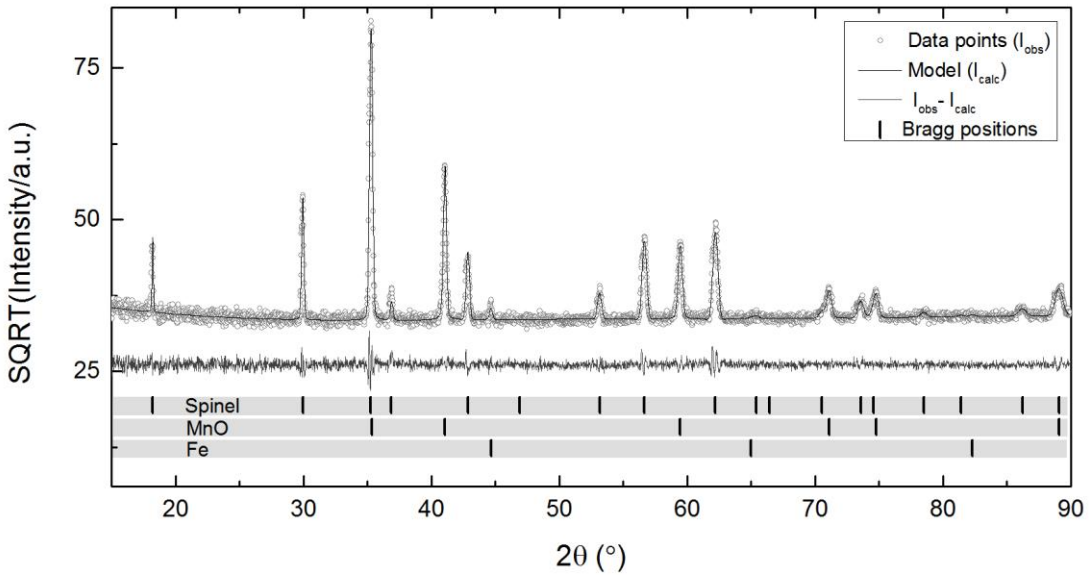

Figure 6-3 Rietveld refinement of MnFeCrO4 reduced at 1200 °C for 1 hour under vacuum with observed data represented as grey dots, calculated profile with black line and difference profile with dark grey line. Corresponding Bragg positions are indicated for each of the identified and refined phases. Rp = 2.40 %, Rwp = 3.18 %, Rexp = 3.00 %, $\chi 2 = 1.12$[12]

Table 6-1 Parameters resulted from refinement of reduced $MnFeCrO_4$ XRD pattern

Parameter	Spinel matrix	MnO	Fe
A	8.4339	4.3966	2.8709
U	0.2616	-	-
V	599.92	84.985	23.662

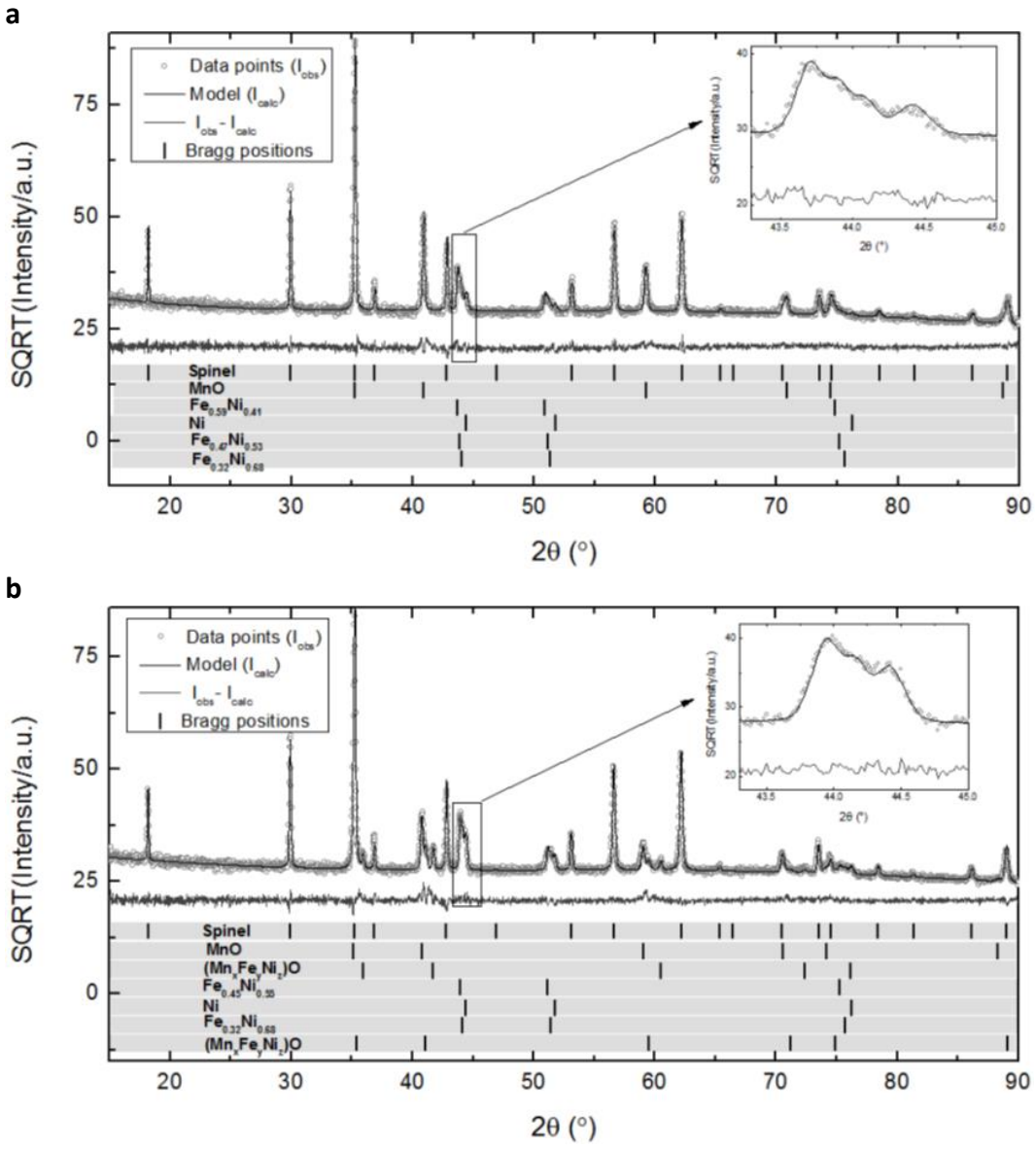

Figure 6-4 Rietveld refinement of the $MnNi_{0.3}Fe_{0.7}CrO_4$ and $MnNi_{0.5}Fe_{0.5}CrO_4$ sintered at 1000°C and reduced in TORVAC furnace at 1200°C for 1.5h at a pressure of 0.2 bar 5%H2/Ar. a, Refinement plot of $MnNi_{0.3}Fe_{0.7}CrO_4$. Rp = 2.64 %,Rwp = 3.41 %, Rexp = 3.33 %, χ2 = 1.05. b, Refinement plot of $MnNi_{0.5}Fe_{0.5}CrO_4$. Rp = 2.64 %, Rwp = 3.61 %, Rexp = 3.46 %, χ2 = 1.09. Observed data are represented with grey dots, calculated profile with black line and difference profile with dark grey line. Corresponding Bragg positions are indicated for each of the identified and refined phases

Among the $MnNi_xFe_{1-x}CrO_4$ (x = 0.3, 0.5) spinel series, the unit cell parameter (*a*) was found to vary linearly with Ni^{2+} substitution (*x*) following Vegard's law and thus implying that Ni^{2+} was successfully solubilised in the $MnFeCrO_4$ lattice as illustrated in Figure 5-5. An attempt was made to synthesize the x = 1 member of the series, but NiO was observed as secondary phase alongside a majority spinel phase with lattice

parameter corresponding to x ≈ 0.56 Ni which can probably be regarded as an upper solubility limit.

Table 6-2 Parameters resulted from refinement of reduced $MnNi_{0.3}Fe_{0.7}CrO_4$ and $MnNi_{0.5}Fe_{0.5}CrO_4$ XRD

Parameter $MnFe_{0.7}Ni_{0.7}CrO_4$	Spinel Matrix	MnO	Ni	$Fe_{0.6}Ni_{0.4}$	$Fe_{0.47}Ni_{0.53}$	$Fe_{0.32}Ni_{0.68}$	
a (Å)	8.4376	4.4090	3.5300	3.5850	3.5700	3.5550	
u (Å)	0.2622						
v ($Å^3$)	600.70	7085.71	43.99	46.08	45.5	44.93	
$MnFe_{0.5}Ni_{0.5}CrO_4$	Spinel Matrix	MnO	Ni	$Fe_{0.6}Ni_{0.4}$	$Fe_{0.47}Ni_{0.53}$	$Fe_{0.32}Ni_{0.68}$	
a (Å)	8.4388	4.4220	4.3247	4.3900	3.5300	3.5665	3.5500
u (Å)	0.2605						
v ($Å^3$)	600.96	86.47	80.88	84.60	43.99	45.37	44.74

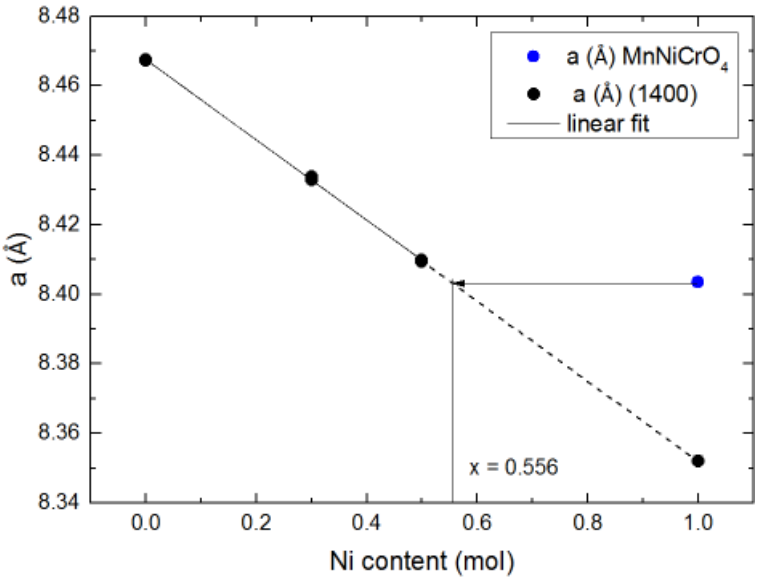

Figure 6-5 Variation of the unit cell parameter a, with the Ni content in $MnNi_xFe_{1-x}CrO_4$ (x = 0.3, 0.5) spinel series

Figures 6-6, 6-7 and 6-8 respectively shows the influence of reduction temperature on the microstructure of the host $MnFeCrO_4$ and nickel substituted $MnNi_xFe_{1-x}CrO_4$ (x = 0.3, 0.5) series spinel. In Figure 6-6, the $MnFeCrO_4$ material undergoes a dramatic redox lattice reorganisation after reduction as a result of the reducible Fe streaming out of the partially reducible bulk material and settled on the surface as micron-size Fe metal particles as confirmed in Figure 6-9 by EDX thereby creating an elaborate interconnected macro-channels of the partially reduced perhaps single crystalline Mn-

Cr nano porous cages in the grain as supported by Eqn. 6-1 and 6-2. The manner this phase segregation occurred and its crystalline-like nature could render it very useful for many future applications.

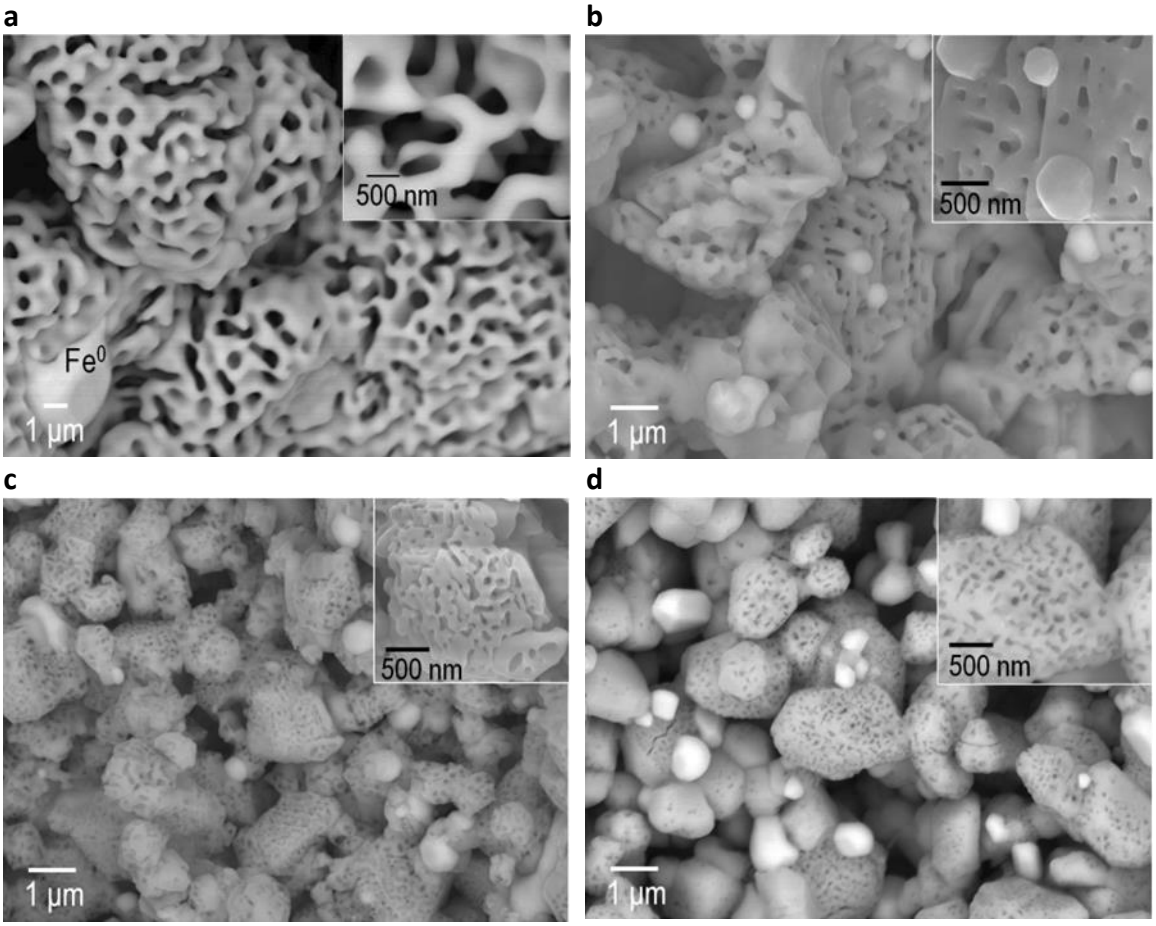

Figure 6-6 The microstructure of spinels $MnFeCrO_4$ sintered at 1400 °C for 12 hours, in air and reduced for 1 hour, under vacuum at , **a** 1200 °C, **b**, 1100 °C, **c**, 1000 °C and **d** 900 °C °C showing changes in the porosity and population of the exsoluted particles with temperature

It is believed that the influence of reduction temperature on the mobility as well as size, distribution and frequency of the reducible Fe chemical species across the bulk material to the surface is behind this remarkable structural change. The size of the channels for instance get smaller with decrease in reduction temperature and that of the reduced Fe metal on the surface gets bigger as the reduction temperature decreases. These basically suggests that, control over reduction temperature offers advantage for particle size, distribution and frequency and general morphology of the material to be tailored for effective catalytic activity. This is very much unlike what

happens with the traditional wet impregnation. What is spectacular with these materials is despite the significant redox reorganisation, the materials are able to retain their physical integrity as seen in the micrograph and corroborated by the surface area analysis in Table 6-3.

The microstructure of the nickel substituted $MnNi_xFe_{1-x}CrO_4$ (x = 0.3, 0.5) series spinel as seen in Figure 6-7 and 8 also showed similar remarkable particle growth on the surface due to redox lattice reorganisation. In this case, the metal nanoparticle dispersion and population increased compared to what was observed in the host and they are perhaps predominantly Ni and some Fe and possible Ni-Fe alloy. This morphology will certainly offer a huge and better advantage in catalysis than what we have seen in the previous sections. Although the macro channels are not visible in this case compared to what was observed in Figure 6-6 for $MnFeCrO_4$, it is believed that the two phenomena are the same. Etching of the nickel substituted spinel with HNO_3 acid has revealed the micro channels as seen in Figure 6-10 and supported by Eqn. 6-3 below. What might be responsible for the observed difference is believed to be the mobility of the individual reduced metal across from the bulk to the surface which is believed to be very slow in the case of reduced nickel (Ni) metal as compared to what was observed for reduced iron (Fe) metal particles. What is also observable is the influence of the reduction temperature on the nickel particle size, growth and frequency or population as seen in Figure 6-7 and 6-8 respectively which decreased as the reduction temperature increases. Therefore, reduction temperature seems the major driver in the behaviour of these materials.

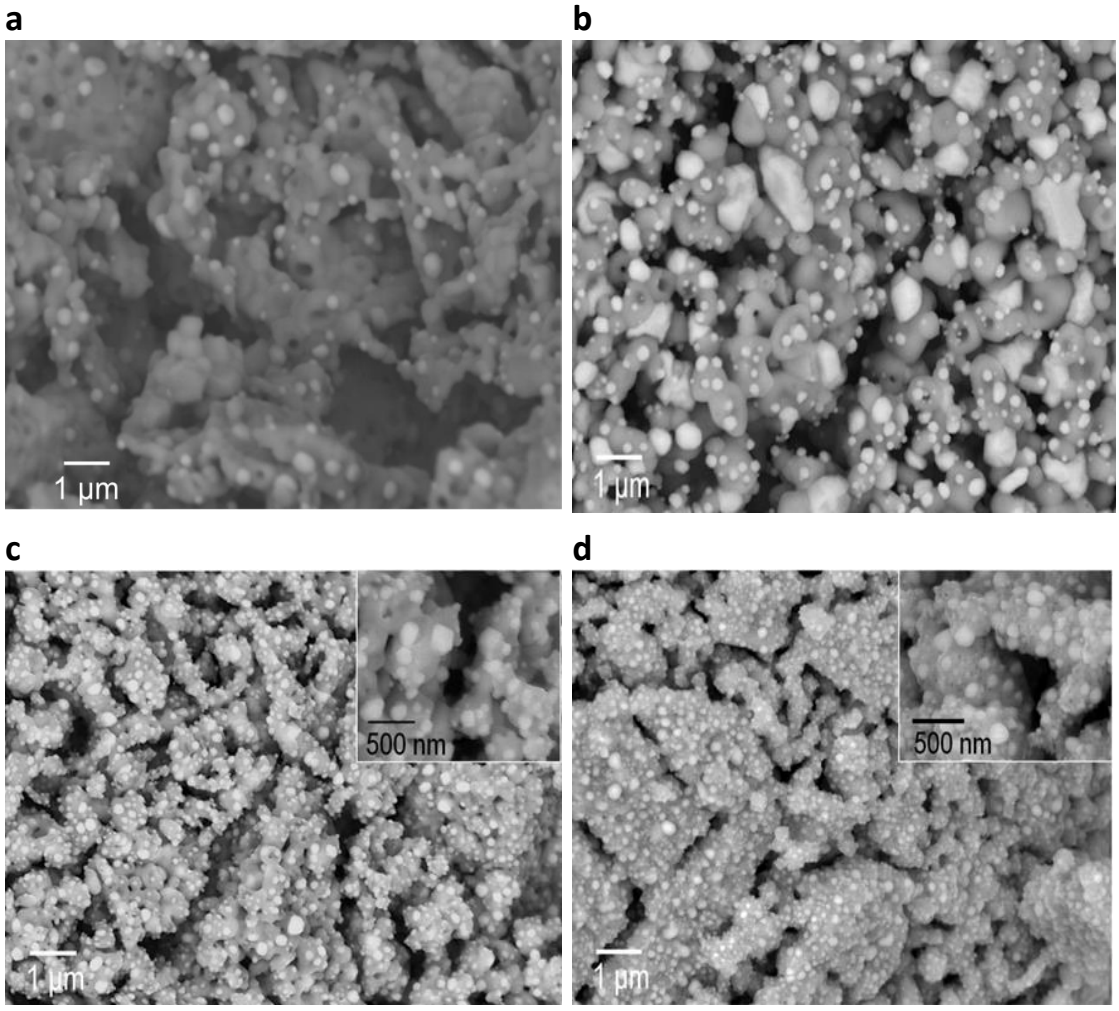

Figure 6-7 Micrographs of $MnNi_{0.3}Fe_{0.7}CrO_4$ sintered at 1000 °C and reduced in TORVAC furnace for 1.5 h at a pressure of 0.2 bar 5%H_2/Ar at, **a** 1200 °C, **b** 1100 ^{o}C, **c** 1000 ^{o}C and **d** 900 ^{o}C showing particle size and population distribution as a function of reduction temperature. the micrograph were taken in backscattering mode

Detailed micro struture of the micro channels as presented in Figure 6-9C shows how complicated the channels due redox lattice reorganisation phenomena are. What is clear from the Figure is the interconnected nature of the channels which might be good for catalysis. Figure 6-9d shows in a qunеched sample the reduced metallic phase streaming out of the main grains or bulk perhaps triggered by the spinel decompsition during reduction as supported by Eqn 6-2 below. That results to formation of nano metal particles on the surface which then creates or leaves behind the nano-channels. Freezing the high temperature microstructure no doubt gave an insight to undestanding the mechanism of this redox reorganisation phenomenon.

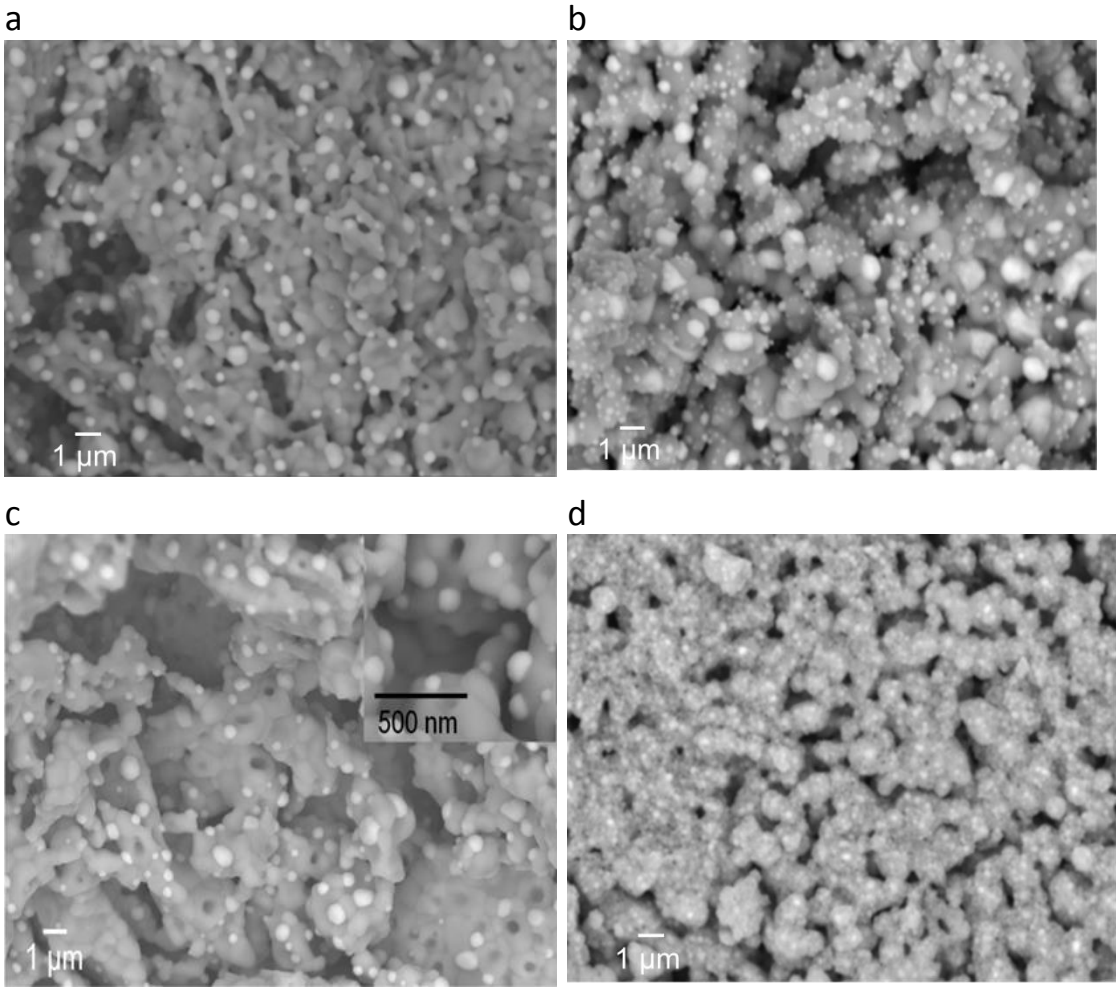

Figure 6-8 Micrographs of $MnNi_{0.5}Fe_{0.5}CrO_4$ sintered at 1000 °C and reduced in TORVAC furnace for 1.5 h at a pressure of 0.2 bar 5%H2/Ar at, **a** 1200 °C, **b** 1100 ^{o}C, **c** 1000 ^{o}C and **d** 900 ^{o}C showing particle size and population distribution as a function of reduction temperature. The micrographs were taken in backscattering mode

Although the real mechanism is not yet ascertained, it suffices to add that under the redox condition, only the reducible ions species such as Fe and Ni in this case that were reduced only instead of the whole bulk or host spinel. The bulk or host after the expulsion of the reduced metal particle is left partially reduced. As such, with the expulsion of the reduced chemical specie to the surface, the lattice undergoes reorganisation leading to the creation of the nano porous channels of the Mn-Cr grain left behind as supported possibly by Eqn. 6-1, 6-2 and 6-3 thus:

$MnX_2CrO_4 + 2H_2 \rightarrow MnCrO_2 + 2H_2O + X_2$ (X = Fe and Ni) Eqn. 6-1

$2MnX_2CrO_4 + 6H_2 \rightarrow MnO + MnCr_2O + 6H_2O + 2X_2$ (X = Fe and Ni) Eqn. 6-2

$MnX_2CrO_4 + 2HNO_3 \rightarrow MnCrO_4 + X_2(NO_3)_2 + H_2\uparrow$ (X = Fe and Ni) Eqn. 6-3

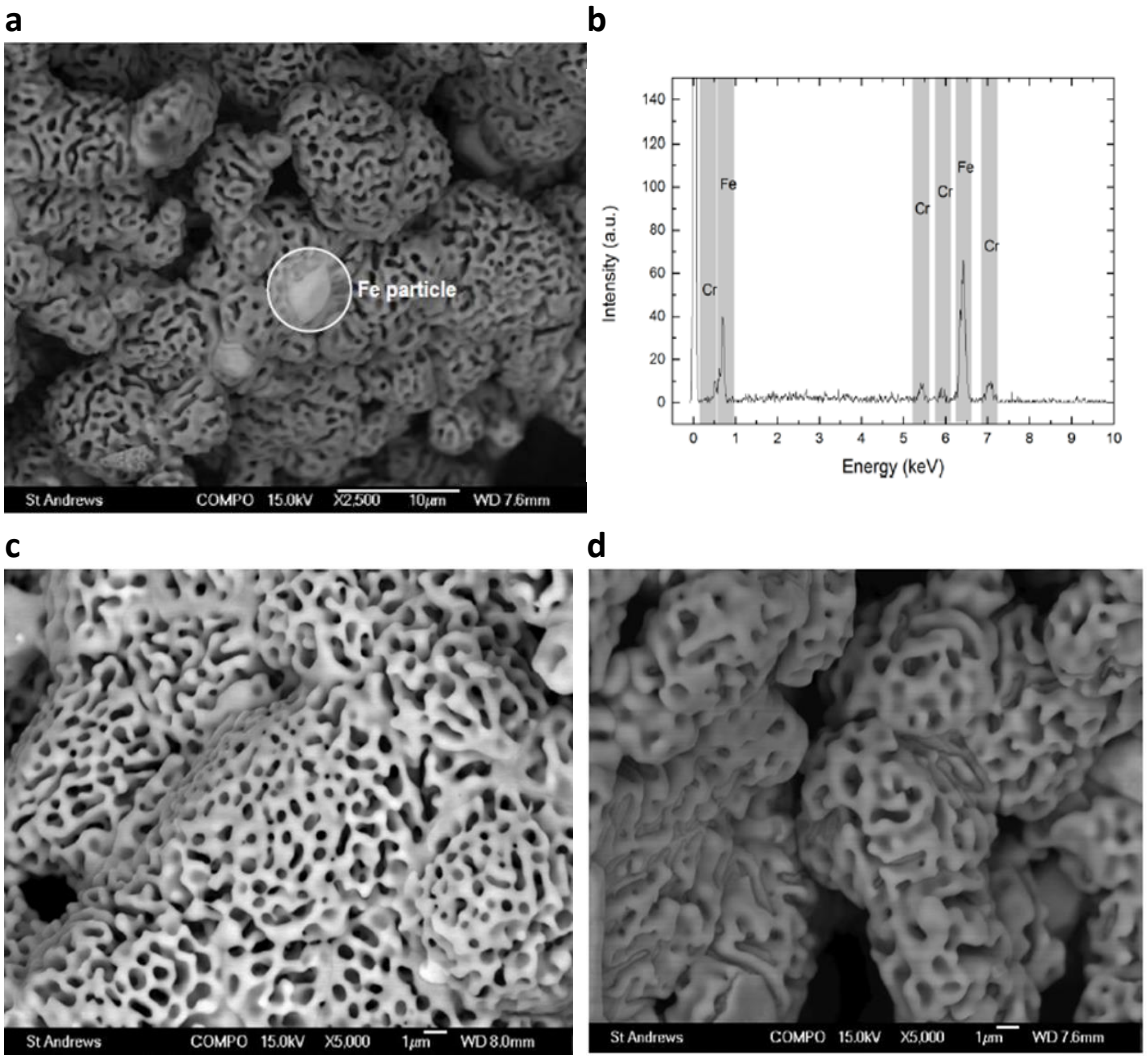

Figure 6-9 Microstructure of $MnFeCrO_4$ reduced at 1200 °C for 1 hour under vacuum. **a,** overview of the microstructure and highlight of an Fe particle. **b,** EDX spectrum on the area highlighted in a. **c,** detail of the pores. **d,** detail of a quenched sample showing what appears to be the metallic phase streaming out of the main grains to form the nano-channels

Consequently, with redox lattice reorganisation in spinel, metal particles can be produced in situ from spinel even when they are part of complex layered/supported microstructures, provided that the adjacent phases tolerate well the influence of the reduction. The phenomenon allows scaling of important properties such as particle size and frequency by mere playing with reduction temperatures as demonstrated in Figure 6-6, 6-7 and 6-8.

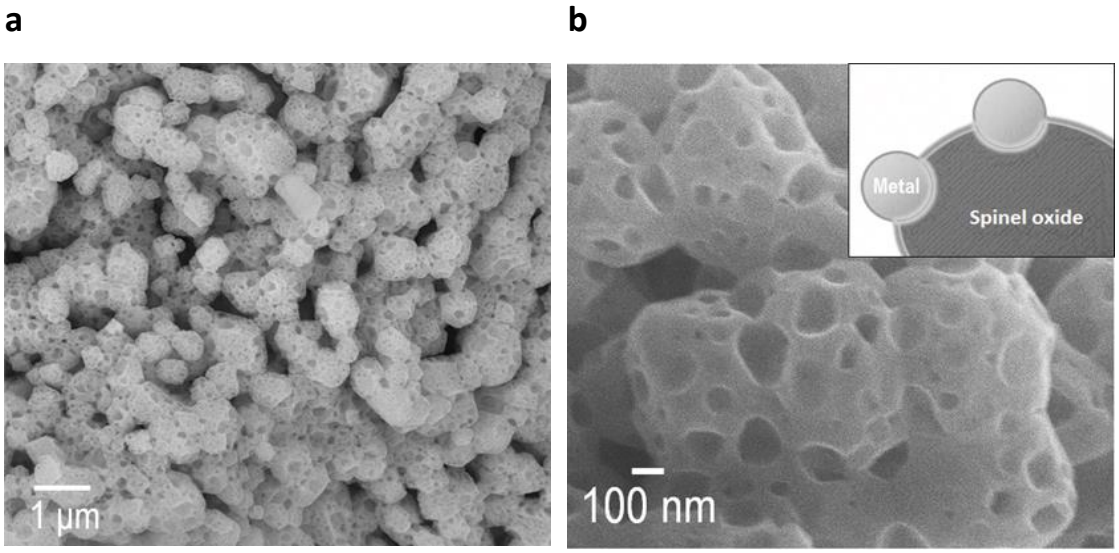

Figure 6-10a-b Micrograph of $MnNi_{0.3}Fe_{0.7}CrO_4$ revealing similar micro channels observed in $MnFeCrO_4$ after etching in HNO_3 acid. This confirms that both are product of the same redox lattice reorganisation

Contrary to what occurs in the traditional wet impregnation where metal catalysts superficially interact with the oxide support, in redox lattice reorganisation the metal catalyst grow out of the support itself and firmly anchored on the spinel oxide as corroborated by the etching in Figure 6-10. This provides elaborate surface area, strong metal-support interaction and therefore reduce tendency for catalyst deactivation by agglomeration and offers effective coking suppression and efficient catalytic behaviour.

6.2.2 Physicochemical properties

The spinel materials $MnFeCrO_4$ and the nickel substituted $MnFe_{1-x}Ni_xCrO_4$, (x = 0.3, 0.5) series synthesized by the combustion method and reduced at different temperatures in 5%H_2 in TOVAC at 0.1-0.2 bar or 2-5 x 10^{-2} mbar pressure were analysed for surface area, pore size and pore volume, the result is as shown in Table 6-3. The result reveals that reduction temperature plays an important role in determining the overall physicochemical properties of the materials which is an important parameter that shapes the catalytic behaviour.

Table 6-3 Surface area, pore volume and pore size

Sample	Reduction temperature (^oC)	BET surface area (m^2g^{-1})
$MnFeCrO_4$	900	2.5482
$MnFeCrO_4$	1000	1.9234
$MnFeCrO_4$	1200	1.6562
$MnFeCrO_4$ (milled)	1200	5.3470
$MnFe_{0.7}Ni_{0.3}CrO_4$	900	2.9339
$MnFe_{0.7}Ni_{0.3}CrO_4$	1000	3.0128
$MnFe_{0.7}Ni_{0.3}CrO_4$	1200	1.2249
$MnFe_{0.5}Ni_{0.5}CrO_4$	900	7.1840
$MnFe_{0.5}Ni_{0.5}CrO_4$	1000	1.9782
$MnFe_{0.5}Ni_{0.5}CrO_4$	12000	1.2508

The reduction temperature has shown influence on the surface area of both $MnFeCrO_4$ spinel and its nickel-substituted derivatives. Generally, surface area decreases with increase in reduction temperature attributable to exposed particle (Fe and Ni) growth with temperature. This denotes that surface area could be tailored by choice of suitable reduction temperature for effective catalytic behaviour. Increasing concentration of nickel from 0.3 to 0.5 mole % seemed to have reduced the surface area of the nickel substituted materials. This is attributable to the surface blockage as the nickel content increases as corroborated in Figure 6-11 showing how the pore volume decreased with increase in the concentration of nickel.

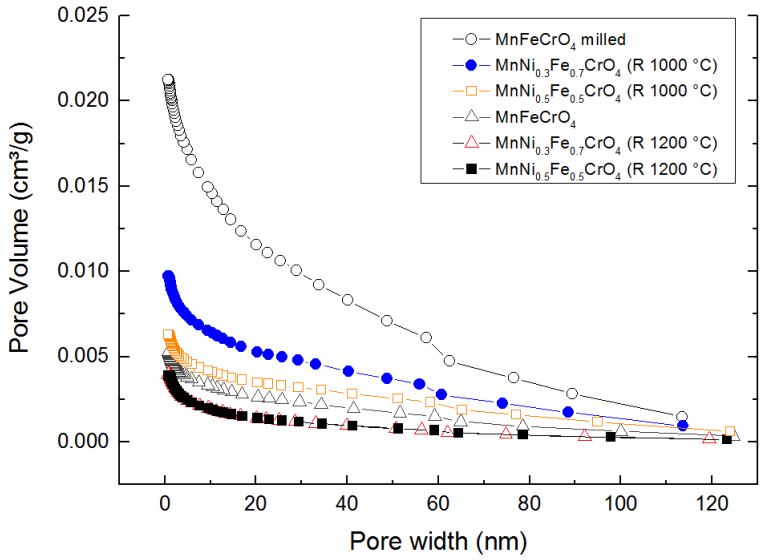

Figure 6-11 Pore volume distribution of catalysts

It is also clear that change in reduction temperature can influence the pore volume as was observed on the surface area. Particle size distribution as seen in Figure 6-12 shows an average particle size of approximately 60 nm across all the samples. Influence of temperature on particle size distribution is clear in the same Figure 6-12. Comparing the Ni-containing samples, the 1200 ^{o}C reduced samples had bigger particle compared to the 1000 ^{o}C. With the non-nickel containing systems, the milled $MnFeCrO_4$ had the smallest particle size compared to the hand ground original sample. All these are due to particle size growth with temperature and concentration of the constituent metals.

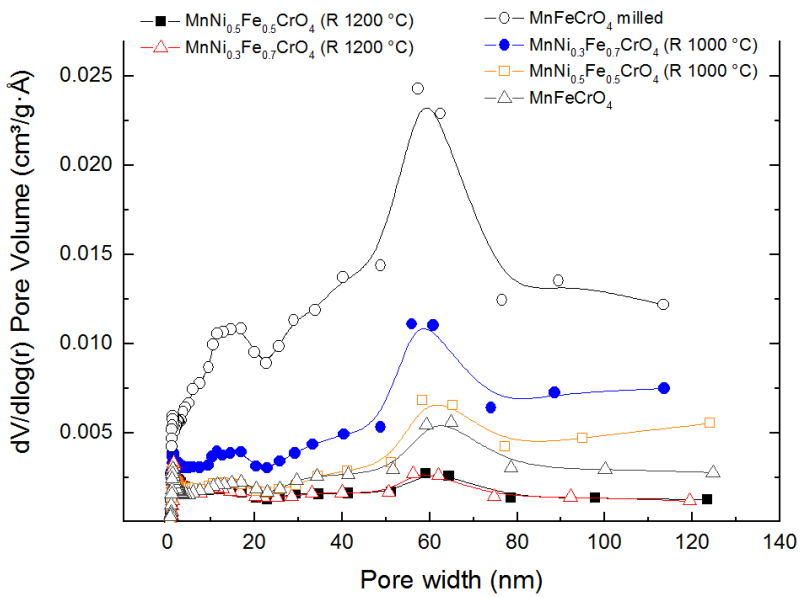

Figure 6-12 Pore size distribution of catalysts

6.2.3 Catalytic behaviour in relation to glycerol steam reforming (GSR)

The Catalyst testing was performed with the pre reduced spinel catalysts at 700 ^{o}C using both pure glycerol and by-product glycerol and steam-to-carbon ratio of 3:1 at atmospheric pressure to screen the catalysts. The feedstock solution molar flow rate of 2.60 x 10^{-4} moles/min for 2 hours from a syringe pump was applied and weight hourly space velocity of 28 h^{-1}. Figure 6-13 shows moles of the reformate gases produced per mole of glycerol fed to the reactor against the respective catalyst systems. It is evident that the catalysts were active in reforming the glycerol decomposition products to syngas-H_2 and CO as well as CO_2 and CH_4. This could be attributed to good surface morphology of the catalyst such as surface area, micro

pores and channels as seen in the SEM micrographs. The product distribution profile of Figure 6-13 shows H_2, CO and CO_2 constituted the main gaseous products as corroborated by the ratios in Table 6-4.

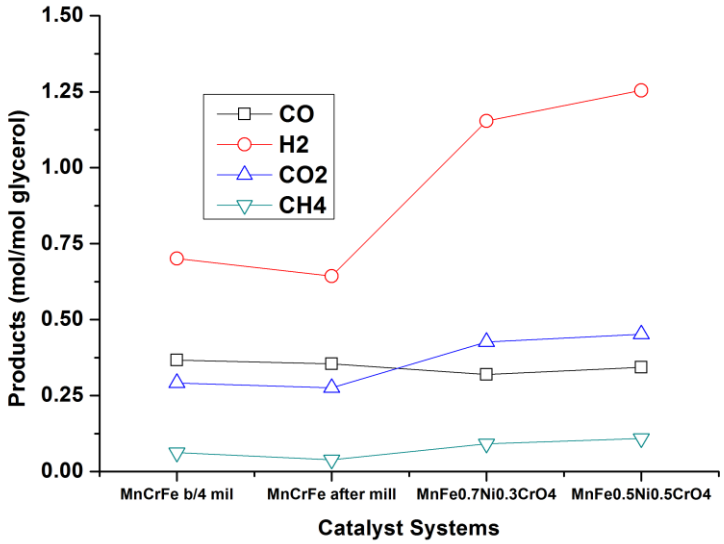

Figure 6-13 gaseous products in mole per mole of glycerol injected to the reforming system against the respective catalyst systems. The test was at 700 ^{o}C, S/C ratio of 3 and glycerol molar flow rate of 8.2 x 10^{-5} moles/min and 7.3 x 10^{-4} moles/min of water and WHSV of 28 h^{-1}

The $MnFeCrO_4$ CO composition in Figure 6-13 as supported by its high H_2/CO ratios and CO selectivity in Table 6-5 suggests its supports for syngas production via reverse WGSR and methane reforming. Glycerol decomposition at such temperature would have also contributed to the CO production. Unlike what was observed with the $MnFeCrO_4$, the modified $MnFe_{1-x}Ni_xCrO_4$ series gave more of H_2, CO_2 and CH_4 as seen in Figure 6-13 and as also shown by the high H_2/CO_2 in Table 6-4 and low CO selectivity in Table 6-5. This implies the nickel incorporation into the lattice of the host $MnFeCrO_4$ catalyst has enhanced its properties to support and favour water gas shifts and methanation reactions which are known to produce H_2 and CO_2 (Eqn. 2-6) and CH_4 (2-8 to 2-10) respectively. Comparison of the H_2/CO_2 and H_2/CO ratios as well as amount of hydrogen produced per mole of hydrogen with equilibrium composition due to glycerol decomposition as provided by Eqn. 2-3 in Table 6-4 also indicates possible contribution from glycerol decomposition among some major derivers of the

conversion as seen in Table 2A-3 of appendix 2. The H_2 produced in mole per mole of glycerol as shown in Figure 6-13 was between 0.64-1.25 mol/mol glycerol which was within 11-22% of the equilibrium composition (see Table 2A-2 of appendix 2). The hydrogen yield was limited by reactions such as reverse water gas shift reaction. This is evidenced by the high CO with all regardless of the catalyst system which is within 32-37% of the equilibrium composition.

Table 6-4 Comparison of products from the experiment with equilibrium composition based on glycerol pyrolysis

	Temperature (^oC)	Conv.= Conversion (C basis)	H_g= H_2/Glyc. (mol/mol)	H_g/Conv.	H_2/CO	H_2/CO_2
Equilibrium	700	-	6.0	-	6.00	3.00
$MnFeCrO_4$ b/4 mill	700	0.24	0.70	2.92	1.92	2.41
$MnFeCrO_4$ after mill	700	0.22	0.64	2.90	1.82	2.34
$MnFe_{0.7}Ni_{0.3}CrO_4$	700	0.28	1.15	4.12	3.61	2.70
$MnFe_{0.5}Ni_{0.5}CrO_4$	700	0.30	1.25	4.17	3.66	2.78

Activity of the catalysts was also expressed as moles of the reformate gases per min and glycerol conversion to gaseous product in % plotted against the respective catalyst systems as illustrated in Figure 6-14a. The $MnFeCrO_4$ catalyst was tested both as hand ground using agate mortar and pestle as well as milled powder using planetary ball miller to enhance surface area. The activity chart as shown in Figure 6-14a indicates that catalyst activity dropped after milling the powder hence did not improve the performance of the catalyst. Either the milling has changed the surface morphology of the catalyst resulting to the reduced activity observed or the activity depended on other parameters such as particle size or catalyst particle interface with the oxide support which the milling did not enhanced. The nickel modified $MnFeCrO_4$ was also screened for activity in the same manner as shown in the same Figure 6-14a. The comparison showed increased activity with the Ni modified catalyst because both Fe and Ni promote C-C and C-H bond cleavages[10]. The glycerol conversion has risen to 30% with the nickel substituted $MnNi_xFe_{1-x}CrO_4$ (x = 0.3, 0.5) series spinel reduced at 1200 ^oC as also corroborated by their COx selectivity in Table 6-5. Throughput due to the little amount catalyst (0.05g) used and small bed thickness resulted to glycerol passing unconverted which might have limited the glycerol conversion. Ideally, COx

selectivity represent the sum of CO_2 and CO reformate in mole divided by the number of moles of feed stock (glycerol) fed to the reactor which indicates the extent of reforming. If the value is one it means reforming is full. The closer the value is to one, the better the catalyst[9].

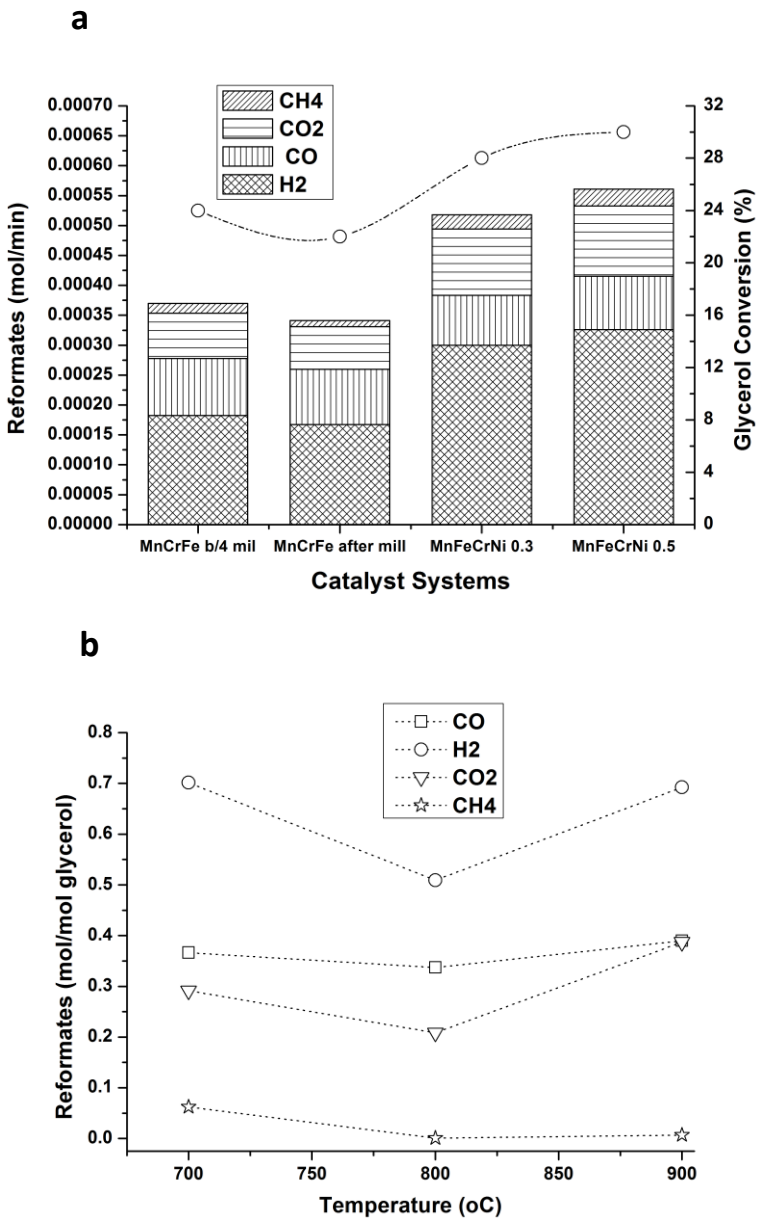

Figure 6-14 Catalysts performance test carried out at different temperatures of 700-900 ^{o}C, S/C ratio of 3 and glycerol molar flow rate of 8.2 x 10^{-5} moles/min and 7.3 x 10^{-4} moles/min of water and WHSV of 28 h^{-1} : **a,** shows amount of gas produced in comparison with the glycerol conversion to gaseous products and **b,** products distribution as a function of temperature over the host $MnFeCrO_4$ catalyst.

Therefore the extent of reforming was higher among the nickel substituted $MnNi_xFe_{1-x}CrO_4$ (x = 0.3, 0.5) series spinel. The COx selectivity analysis was considered in this test

because the test was performed at high temperature. At low temperature, CH_4 formation could be very important in the determination of extent of reforming since it is a major product.

The influence of reforming temperature was also investigated on the host $MnFeCrO_4$ catalyst to investigate how catalyst activity and product distribution changes with temperature. The results obtained as shown in Figure 6-14b show that reformate production rate increased with temperature. Although there was a slight drop at 800 ^oC, no sign of catalyst deactivation from the gaseous composition at all temperatures. The H_2, CO and CO_2 gases were higher at all temperatures and glycerol conversion also increased with temperature as shown in the Figure and corroborated by the activity analysis in Table 6-6. Therefore gaseous products formation rate and glycerol conversion were favoured by kinetics. Hydrogen Selectivity decreased with temperature but that of CO increased to 800 ^oC and decreased to 900 ^oC as seen in Table 6-6. This could be due to strongly endothermic nature of glycerol pyrolysis (Eqn. 2-3) and reverse water gas shift reaction (Eqn. 2-6). Interestingly, methane formation rate decreased with temperature which suggests possible methane reforming.

Table 6-5 CO, COx and H_2 selectivity recorded for each catalyst

Catalyst	H_2 Selectivity (%)	CO Selectivity (%)	COx Selectivity (%)
$MnFeCrO_4$ b/4 mill	42	51	0.24
$MnFeCrO_4$ after mill	41	53	0.20
$MnFe_{0.7}Ni_{0.3}CrO_4$	59	38	0.24
$MnFe_{0.5}Ni_{0.5}CrO_4$	60	38	0.30

The high H_2/CO_2 ratio which is near equilibrium in Table 6-4 especially the nickel substituted $MnNi_xFe_{1-x}CrO_4$ (x = 0.3, 0.5) series spinel suggest water gas shift reaction being slightly exothermic might be responsible for the performance observed at 700 ^oC but drops when temperature increased to 800 ^oC. Hydrogen selectivity increased from 42% in $MnFeCrO_4$ to 60% with the nickel substituted $MnNi_xFe_{1-x}CrO_4$ (x = 0.3, 0.5) series spinel because of the combined effect of Ni on WGSR as well as glycerol pyrolysis due to effect of temperature as seen in Table 6-6. Generally, all the catalysts are particularly highly selective for CO which could be attributed to mobility of the oxygen ion in the lattice as enhanced by the lattice reorganisation and their ability to effect oxidation of the pyrolysis products. $MnFeCrO_4$ was relatively more selective for

CO compared to the Ni modified system hence tends to support more of RWGSR to generate more CO while the later supports WGSR giving more CO_2 and less CO. Consequently, oxidation of glycerol decomposition could be made more effective for H_2 and syngas production by tailoring structural properties of spinel through lattice reorganisation and transition metal doping. Therefore these materials could be useful for hydrogen and syngas production.

Table 6-6 Selectivity for CO, COx and H_2 on $MnFeCrO_4$ (b/4 mill) catalyst as a function of temperatures

Temperatures (%)	H_2 Selectivity (%)	CO Selectivity (%)	Glycerol Conversion (%)	COx Selectivity (%)
700	42	51	24	0.24
800	40	62	18	0.20
900	38	50	26	0.30

6.2.4 Redox lattice reorganisation, reduction temperature and its influence on the catalyst in relation to glycerol steam reforming

Relationship between catalytic activities and morphological changes due to variation in reduction temperature used for the processing of the catalyst systems was explored. The test was done at 700 ^oC, steam to carbon ratio of 3 and glycerol solution molar flow rate of 2.60 x 10^{-4} mol/min and WHSV of 28 h^{-1}. Both the $MnFeCrO_4$ catalyst and the nickel substituted $MnNi_xFe_{1-x}CrO_4$ (x = 0.3, 0.5) series spinel reduced at different temperatures had exhibited varying surface morphology and degree of redox lattice reorganisation as seen in the micrograph of Figure 6-6, 6-7 and 6-8. For instance, particle size, population and distribution, channels complexity and intensity all varied linearly with the reduction temperature. All these variations are expected to show varying influences on the catalytic behaviour of these materials. Result of steam reforming of pure glycerol on all the catalyst systems using 50 mg of the catalysts at 700 ^oC for 2 hours was analysed both as amount of reformate produced in mol/min in comparison with glycerol conversion and as reformates produced in mole per mole of glycerol as shown in Figure 6-15a and b respectively. Figure 6-15a shows the amount of products generated in mole/min in comparison with glycerol conversion. The $MnFeCrO_4$ series showed increase in catalytic activity in terms of amount of reformate produced in mol/min and glycerol conversion (%) to gaseous products with increase in reduction temperature as seen by the reduced $MnFeCrO_4$ catalyst series labelled **A**, **B**

and **C** in the chart reduced at 900 ^{o}C, 1000 ^{o}C and 1200 ^{o}C respectively. This is in tandem with the behaviour of the catalyst as seen in the SEM micrograph of Figure 6-8.

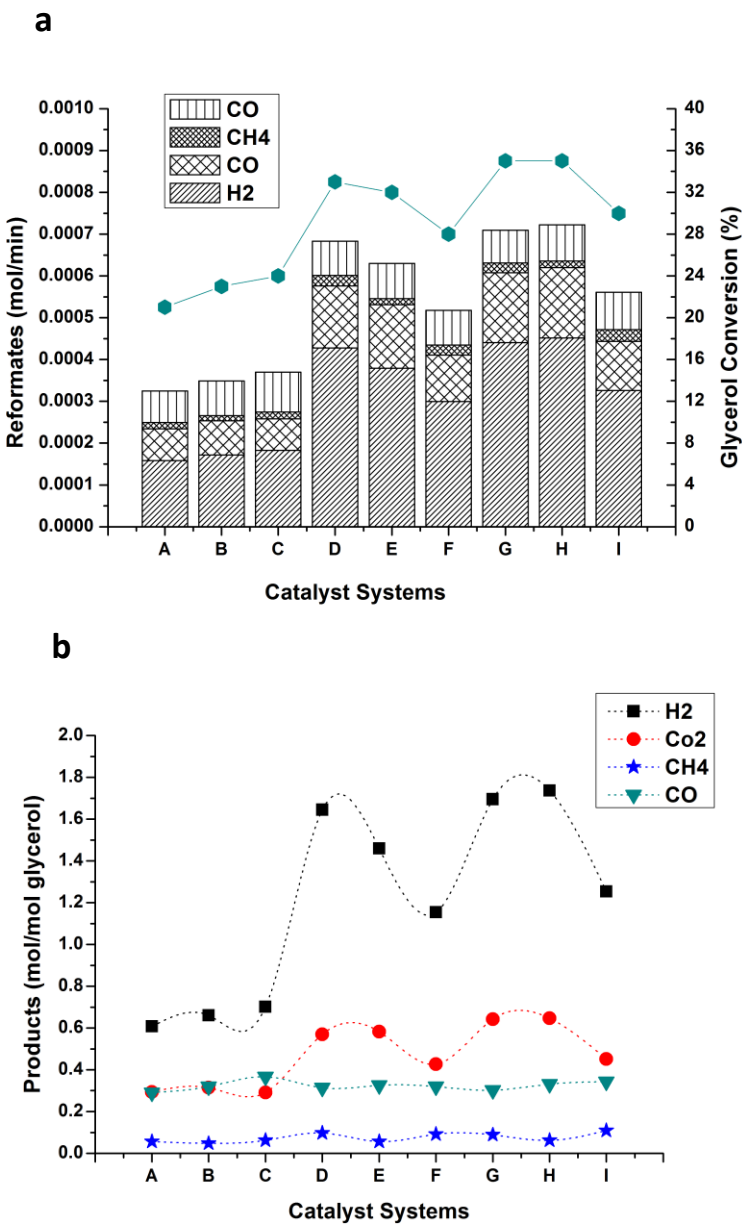

Figure 6-15 **a,** Catalytic activity in terms of reformate generated and glycerol conversion to gaseous products of the catalyst systems **A, B** and **C** are $MnFeCrO_4$ catalysts reduced at 900 ^{o}C, 1000 ^{o}C and 1200 ^{o}C respectively, **D, E** and **F** are $MnFe_{0.7}Ni_{0.3}CrO_4$ series reduced at 900 ^{o}C, 1000 ^{o}C and 1200 ^{o}C respectively, **G, H** and **I** are $MnFe_{0.5}Ni_{0.5}CrO_4$ series reduced at 900 ^{o}C, 1000 ^{o}C and 1200 ^{o}C respectively. **b,** reformates produced in mole per mole of glycerol. The performance test was carried out at temperatures of 700 ^{o}C, S/C ratio of 3 and glycerol molar flow rate of 8.2 x 10^{-5} moles/min and 7.3 x 10^{-4} moles/min of water and WHSV of 28 h^{-1}

The channels intensity and complexity due to redox rearrangement becomes more elaborate with increase in reduction temperature.

The nickel substituted $MnNi_xFe_{1-x}CrO_4$ (x = 0.3, 0.5) on the other hand showed a reverse trend with the catalyst activity decreasing with increase in reduction temperature as depicted by $MnFe_{0.7}Ni_{0.3}CrO_4$ series in **D, E** and **F** catalyst reduced at 900 ^oC, 1000 ^oC and 1200 ^oC respectively and $MnFe_{0.5}Ni_{0.5}CrO_4$ series as **G, H** and **I** also reduced at 900 ^oC, 1000 ^oC and 1200 ^oC respectively as shown in Figure 6-15a. This is attributable to the decrease in particle size and increase in the particle population and surface area observed in the SEM micrograph of Figure 6-7 and 6-8 and Table 6-3 respectively as the redox lattice reorganisation temperature decreases. The $MnFe_{0.5}Ni_{0.5}CrO_4$ (**H**) reduced at 1000 ^oC showed the best catalytic activity relatively.

Figure 6-15b which shows the reformate production in mole per mole of glycerol also indicates that the catalysts are active towards production of H_2, CO_2, CO and CH_4 with H_2, CO_2 and CH_4 relatively higher among the nickel substituted catalyst while the $MnFeCrO_4$ produced more CO. H_2 increased with reduction temperature among the $MnFeCrO_4$ series but decreased with reduction temperature with the nickel substituted $MnNi_xFe_{1-x}CrO_4$ (x = 0.3, 0.5) spinel series. The gas compositions are within the equilibrium composition (see Table 2A-2 of appendix 2). H_2 for instance is between 10-29 % of the equilibrium composition while CO was 29-37% of the equilibrium composition across all the catalyst systems.

H_2, CO and COx selectivity also showed similar trend among all the catalyst. Table 6-7 compares H_2 selectivity, CO selectivity and COx Selectivity as a function of reduction temperatures respectively. In all cases, H_2, CO and COx selectivity increased with increase in redox rearrangement reduction temperature with $MnFeCrO_4$ catalyst systems but showed a reversed trend among the nickel substituted $MnNi_xFe_{1-x}CrO_4$ (x = 0.3, 0.5) spinel. What is interesting is that H_2 selectivity for instance increased from 42% with $MnFeCrO_4$ catalyst reduced at 1200 ^oC to 72% with $MnFe_{0.7}Ni_{0.3}CrO_4$ catalyst reduced at 900 ^oC. Even more interesting, H_2 Selectivity has risen from ~59% with the nickel substituted $MnNi_xFe_{1-x}CrO_4$ (x = 0.3, 0.5) spinel reduced at 1200 ^oC to 72% with $MnFe_{0.7}Ni_{0.3}CrO_4$ and $MnFe_{0.5}Ni_{0.5}CrO_4$ reduced at 900 ^oC respectively. The COx Selectivity has risen from 0.20 with $MnFeCrO_4$ to 0.33 with the $MnNi_xFe_{1-x}CrO_4$ (x = 0.3, 0.5) spinel reduced at lower temperatures which is indicative of enhanced steam reforming. This shows relationship between the reduction temperature and the

catalytic behaviour of spinel catalyst as it does on the redox lattice reorganisation. Hydrogen produced per mole of glycerol is within 10-12% of the equilibrium composition among the host $MnFeCrO_4$ catalyst systems and 24-29% among the nickel substituted $MnNi_xFe_{1-x}CrO_4$ (x = 0.3, 0.5) spinel series. The CO composition is between 29 and 37% of the equilibrium composition with $MnFeCrO_4$ and 30-35% with $MnNixFe_{1-x}CrO_4$ (x = 0.3, 0.5) spinel series.

Table 6-7 Catalytic performance of the catalysts as a function of reduction temperature

Catalyst System	Reduction Temperature (^oC)	H_2 Selectivity (%)	CO Selectivity (%)	COx Selectivity
$MnFeCrO_4$	900	41	45	0.20
$MnFeCrO_4$	1000	42	47	0.21
$MnFeCrO_4$	1200	42	51	0.23
$MnFe_{0.7}Ni_{0.3}CrO_4$	900	72	32	0.30
$MnFe_{0.7}Ni_{0.3}CrO_4$	1000	65	34	0.30
$MnFe_{0.7}Ni_{0.3}CrO_4$	1200	59	38	0.25
$MnFe_{0.5}Ni_{0.5}CrO_4$	900	70	29	0.32
$MnFe_{0.5}Ni_{0.5}CrO_4$	1000	72	32	0.33
$MnFe_{0.5}Ni_{0.5}CrO_4$	1200	60	38	0.27

To further establish the robust behaviour of the catalyst systems due to redox lattice reorganisation, some selected catalysts were subjected to steam reforming using by-product glycerol phase as collected from biodiesel synthesis. The biodiesel synthesis was carried out using KOH as catalyst, Sunflower and methanol as the reactants. Because no post synthesis treatment was administered on the by-product glycerol, it may therefore contains some impurities such as KOH catalyst, residual methanol, unconverted sunflower oil and conversion intermediate products such as mono-glyceride and di-glyceride. TGA analysis on the by-product glycerol confirmed trace of KOH as TGA residue. The steam reforming was investigated at 700 ^oC, at atmospheric pressure, steam-to-carbon ratio of 3 and 50 mg catalyst. Glycerol solution molar flow rate of 2.60 x 10^{-4} mol/min was administered and WHSV of 28 h^{-1}. The result obtained is as shown in Table 6-8. The $MnFeCrO_4$ reduced at 1200 ^oC gave the highest performance among the host materials while the $MnFe_{0.5}Ni_{0.5}CrO_4$ catalyst recorded best performance both among the nickel substituted $MnNi_xFe_{1-x}CrO_4$ (x = 0.3, 0.5) spinel and overall using pure glycerol in the previous analysis, these materials are therefore used for this test. It is clear from the results in Table 6-8 all the catalysts

have shown catalytic activity during the steam reforming despite the impurities which were expected to deactivate catalyst due to severe cooking and slow or decrease performance. This stressed further the robust behaviour of these catalyst systems.

Table 6-8 Catalytic performance of the catalysts using by-product glycerol

Catalyst	Reduction temperature (^oC)	H_2 selectivity (%)	Glycerol conversion (%)	COx selectivity
$MnFeCrO_4$	1200	30	22	0.22
$MnFe_{0.5}Ni_{0.5}CrO_4$	900	87	31	0.29
$MnFe_{0.5}Ni_{0.5}CrO_4$	1000	67	30	0.28
$MnFe_{0.5}Ni_{0.5}CrO_4$	1200	56	27	0.26

It is interesting to note that despite the impurities highlighted above, conversion ≥30% was achieved with nickel substituted catalyst systems and conversion >20% with the $MnFeCrO_4$. Hydrogen selectivity also dropped only slightly compared to what we noticed using pure glycerol. The COx selectivity corroborates all these observations which are indicative of reforming activity from these catalysts. It is essential to say the basic properties of the residual KOH transesterification catalyst may have contributed to the performance of the catalysts.

Analysis based on carbon balance as shown in Table 6-9 has further strengthened the robust behaviour of these catalyst systems and reaffirms the importance of choice of reduction temperature.

Table 6-9 Carbon loss as a function of reduction temperature

Catalyst System	Reduction Temp. (^oC)	Total C **IN** (moles/min)	Total C **OUT** (moles/min)	CO **OUT** (moles/min)	CO_2 **OUT** (moles/min)	CH_4 **OUT** (moles/min)
$MnFeCrO_4$	1200	7.8×10^{-4}	2.0×10^{-4}	9.6×10^{-5}	7.6×10^{-5}	1.6×10^{-5}
$MnFe_{0.5}Ni_{0.5}CrO_4$	900	7.8×10^{-4}	2.7×10^{-4}	8.0×10^{-5}	1.7×10^{-4}	2.3×10^{-5}
$MnFe_{0.5}Ni_{0.5}CrO_4$	1000	7.8×10^{-4}	2.7×10^{-4}	7.8×10^{-5}	1.7×10^{-4}	1.7×10^{-5}
$MnFe_{0.5}Ni_{0.5}CrO_4$	1200	7.8×10^{-4}	2.4×10^{-4}	8.9×10^{-5}	1.2×10^{-4}	2.9×10^{-5}

The nickel based catalyst shows reduced carbon loss due to their enhanced performance relatively. More so, the carbon loss increased with reduction temperature among the nickel-based catalysts. Therefore just as the catalyst performance evaluation revealed, 1000 ^oC represents the best reduction temperature.

Looking at the trend of the performance suffices it to say that redox temperature had a significant influence on the catalytic behaviour of the catalysts as it does on microstructure. Therefore, through careful control of reduction temperature, redox lattice reorganisation and surface morphology catalytic behaviour can be tailored to achieve enhanced results. It is important to note also that by-product glycerol seen as a waste at the moment is an intense energy commodity very much comparable to pure glycerol and could be harnessed to provide the much desired renewable fuel for fuel cell application. From the performance recorded with 0.05g for the catalyst test in above, use of reasonable quantity (2-5g) could drive the conversion to 100%.

6.2.5 Time on stream (TOS) and stability testing

Changes with time on stream in the activity of the catalysts were investigated by monitoring glycerol conversion and hydrogen produced in mol/mol glycerol over time to check the resistant of the catalysts to deactivation by carbon deposition due to prolonged running. The testing was done at constant temperature of 700 ^{o}C at atmospheric pressure, steam-to-carbon ratio of 3:1 and WHSV of 28 h^{-1} using pure glycerol and the result is as shown in Figure 6-16. It is clear from the result that $MnFeCrO_4$ and $MnFe_{0.5}Ni_{0.5}CrO_4$ used as representative catalysts incurred only a mild deactivation of ~ 9-15% of glycerol conversion and 13-14% of hydrogen yield for the 32 hours used for the test. This observation is as well corroborated by temperature programmed oxidation performed on the used catalysts in Figure 6-17. Relatively, the nickel substituted catalysts suffered more lost over time which is attributed to the intense glycerol decomposition and catalyst activity it attracted due to nickel content.

Notwithstanding, the result shows that, the nickel substituted catalyst was not much affected by the nickel's high affinity for C-C, C-H and C-O breakage which could lead to severe coke deposition and possibly subsequent catalyst deactivation. Comparing this to what we have seen using nickel oxide-supported catalyst prepared by wet impregnation in section 5.4.2, it is obvious there is a huge difference in stability.

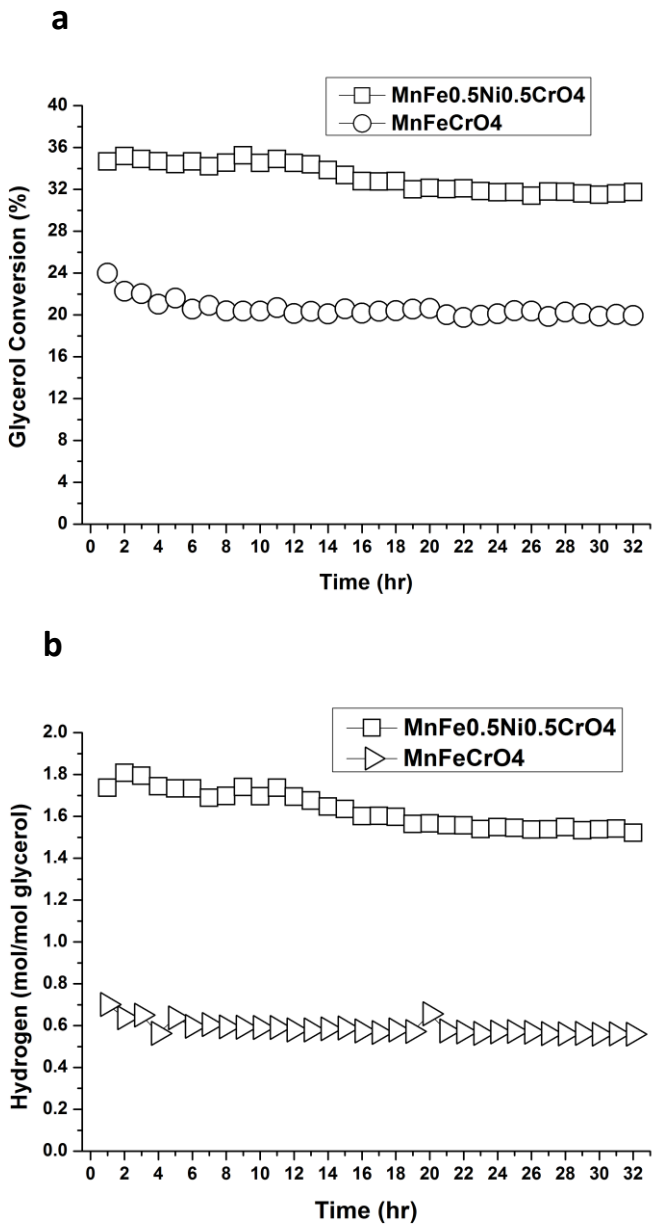

Figure 6-16 Times on stream test showing **a,** glycerol conversion and **b,** mole hydrogen produced per mole glycerol overtime which reflects stability and resistance of the materials to some agents of deactivation over time. The test was carried out at temperatures of 700^{o}C, S/C ratio of and glycerol molar flow rate of 8.2 x 10^{-5} moles/min and 7.3 x 10^{-4} moles/min of water and WHSV of 28 h^{-1}

The Ni/Al_2O_3 deactivated rapidly after few hours of test, the relative stability obtained due to the influence of promoter and alternative support was not comparable to what we observed with the spinel either. This is attributable to the morphology of the spinel catalyst due to lattice reorganisation which gave enhanced metal-support interaction and improved reducibility of the nickel particles. Consequently, these enhanced not only catalytic behaviour but also suppressed carbon deposition. Because of poor

metal-support interactions with the wet impregnated catalyst, carbon fibre grows easily at the metal-support interface and rapidly deactivates catalysts[10]. Therefore catalyst stability and performance was enhanced by lattice reorganisation and careful choice of reduction temperature compared to catalysts prepared by wet impregnation.

6.2.6 Coking phenomenon with the spinel oxide and spinel oxide-supported nickel particle catalysts in glycerol steam reforming

Figure 6-17a and b shows the result from temperature programmed oxidation investigated on the spent $MnFeCrO_4$ and the nickel substituted $MnNi_xFe_{1-x}CrO_4$ (x = 0.3, 0.5) spinel series as representative catalysts all reduced at 1200 ^oC and used in steam reforming of both pure glycerol and by-product glycerol respectively at 700 ^oC and steam-to-carbon ratio of 3:1. The thermo-gravimetric profile weight change in Figure 6-17a and b shows the extent of carbon deposition while the CO_2 peak indicates the temperature at which bulk of the carbon oxidised which depends on the nature of the carbon and its location. It is evident from the weight change in Figure 6-17a there was some mild carbon deposition during the catalytic activity using pure glycerol. The nickel substituted $MnNi_xFe_{1-x}CrO_4$ (x = 0.3, 0.5) spinel series catalysts showed more coking activity compared to the $MnFeCrO_4$ catalyst, this was quite in order and expected. The nickel-based catalyst attracted more surface catalyst activity due to nickel's propensity for cracking of hydrocarbon hence had more tendencies to coking. Generally the weight change was ~3% in the nickel substituted $MnNi_xFe_{1-x}CrO_4$ (x = 0.3, 0.5) spinel series catalysts which indicates very high coking suppression. Interestingly, with $MnFeCrO_4$ coking was almost hindered.

The CO_2 peak shows that bulk of the carbon deposited by the nickel substituted $MnNi_xFe_{1-x}CrO_4$ (x = 0.3, 0.5) spinel series catalysts was oxidised partly at low temperature and partly at intermediate temperature as depicted by their distinct CO_2 peaks. The low temperature peak is due to amorphous carbon on the catalyst or metal surface which is easy to remove hence oxidised at low temperature.

a

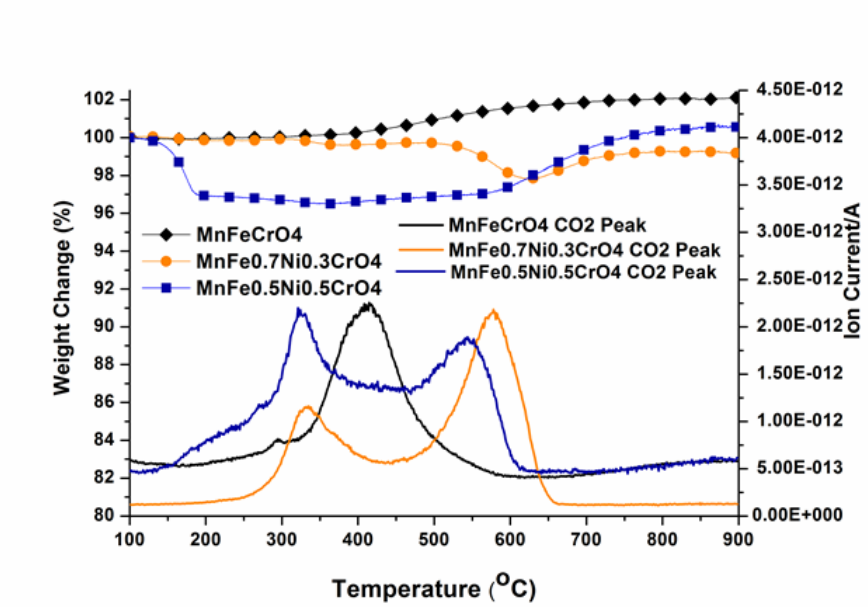

b

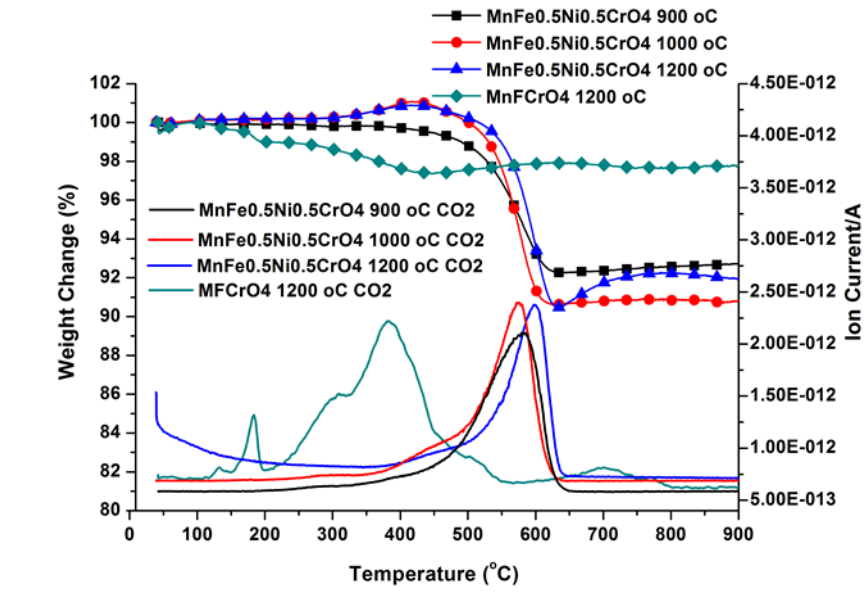

Figure 6-17 Weight change of selected samples in oxidising atmosphere monitored in parallel with the released CO_2 as a function of temperature showing the extent of carbon deposition and type of coke formed **a,** with some selected representative samples all reduced at 1200 °C after steam reforming with pure glycerol **b,** with best performing catalyst- $MnFeCrO_4$ reduced at 1200 °C and $MnFe_{0.5}Ni_{0.5}CrO_4$ reduced at 1000 °C using by-product glycerol. The chart also shows the influence of reduction temperature on the coke formation using the $MnFe_{0.5}Ni_{0.5}CrO_4$ catalyst system reduced at 900, 1000 and 1200 °C respectively.

The other CO_2 peak at intermediate temperature correspond to polymeric or graphitic carbon deposited at metal-support interphase which are more severe and difficult to remove so oxidised at higher temperature compared to the amorphous type. The

$MnFeCrO_4$ showed only one distinct CO_2 peak at low temperature due to amorphous carbon deposited on the metal surface. This reflects robust suppression of carbon deposition by the host $MnFeCrO_4$ catalyst. The nickel substituted $MnNi_xFe_{1-x}CrO_4$ (x = 0.3, 0.5) spinel series catalysts mild carbon deposition is also a good sign.

To further investigate the resistant of the catalyst systems to coking; some of the catalysts were further put to test in steam reforming using the contaminated impure by-product glycerol which is more prone to show coking activity. The results of the TPO on the used catalysts is shown in Figure 6-17b. It is evident from the weight loss on the TGA profile, the coking activity has increased with the by-product glycerol. Interestingly, the $MnFeCrO_4$ catalyst had only a mild coking from the slight weight loss recorded for it despite the impurities of the by-product glycerol. This attests to the coking resistant of the catalyst. The nickel substituted catalysts showed more tendencies to coking relatively. There is a correlation between the amount of coke deposited and the reduction temperature. The weight loss was 7.45%, 10.45% and 10.35% for the $MnFe_{0.5}Ni_{0.5}CrO_4$ catalyst reduced at 900 ^oC, 1000 ^oC and 1200 ^oC respectively. The relatively highest carbon deposition recorded for $MnFe_{0.5}Ni_{0.5}CrO_4$ reduced at 1000 ^oC is attributable to its high performance due to its strong attraction for glycerol and reforming activity on its surface. The CO_2 peak for the $MnFeCrO_4$ also occurred at low temperature of about 400 ^oC just like using the pure glycerol plus a little shoulder at much lower temperature of about 180 ^oC which suggests amorphous carbon deposited on the catalyst surface. But the CO_2 peaks due the $MnFe_{0.5}Ni_{0.5}CrO_4$ catalysts all occurred at medium temperature of about 600 ^oC which depicts polymeric or graphitic carbon deposited at metal-support interphase. Therefore more serious graphitic carbon is associated with the nickel containing catalysts compared to the amorphous type of the host non-nickel containing catalysts.

What is interesting from the foregoing is that, the scanty coking activity with the $MnFeCrO_4$ irrespective of using either pure or by-product glycerol was easy-to-remove amorphous coke which can be regenerated by oxidation and does not deactivate catalyst. The nickel substituted catalyst showed combination of both easy-to-remove amorphous and the more severe graphitic carbon which is also a lot good and can be partly regenerated by oxidation compared to Ni/Al_2O_3 which showed even bulk carbon

deposition at much higher temperature as seen in previous sections which is difficult to remove and therefore make catalyst regeneration by oxidation almost impossible.

6.2.7 Comparison between the oxide-supported metal catalysts prepared by wet impregnation and oxide-supported metal catalyst prepared by redox lattice reorganisation

Catalytic activity of the chromium-rich spinel catalysts prepared by redox reorganisation/rearrangement as seen above in steam reforming of pure glycerol at 700 ^{o}C at atmospheric pressure and S/C ratio of 3:1 is compared with that of 10% Ni/Al_2O_3 catalyst prepared by the traditional wet impregnation with high surface area γ-Al_2O_3 (48 m^2/g) and also used in steam reforming under same reaction condition. Hydrogen Selectivity and production per mole of glycerol is compared as shown in Figure 6-18a-b. It is clear from this plot that the nickel substituted redox reorganised/rearranged catalysts have superior activity in terms of hydrogen production per mole of glycerol and selectivity compared to the much higher surface area Ni/Al_2O_3 system. The nickel substituted $MnNi_xFe_{1-x}CrO_4$ (x = 0.3, 0.5) spinel reduced at 1200 ^{o}C have shown a better performance than the 10wt% Ni/Al_2O_3 as evident in Figure 6-18. The hydrogen production did not show much increase with the increase in the compositional nickel content. In contrast, the $MnFeCrO_4$ without nickel yielded little hydrogen. This strengthened the observation that nickel plays important role in hydrogen generation through reactions such as water-gas-shift reaction. This means while nickel substituted species supported WGSR for H_2 and CO_2; the $MnFeCrO_4$ enhanced the reverse water-gas-shift reaction as supported by their highest CO content relatively. Both enhanced glycerol decomposition due to their Fe and Ni contents. Hydrogen selectivity also followed similar trend.

Another important area of comparison is in the ability of the catalyst materials to suppress carbon deposition which was investigated by subjecting the used catalyst to temperature programmed oxidation in oxidising environment. The weight change monitored in parallel with the released CO_2 as a function of temperature give a profile that helps to understand extent of carbon deposition and temperature at which bulk of the carbon oxidised hence is used to characterize carbon deposition as shown in

Figure 6-18b. The CO_2 profile suggests there were some carbon deposition activities on the catalyst systems as supported by the weight loss in the TGA profile.

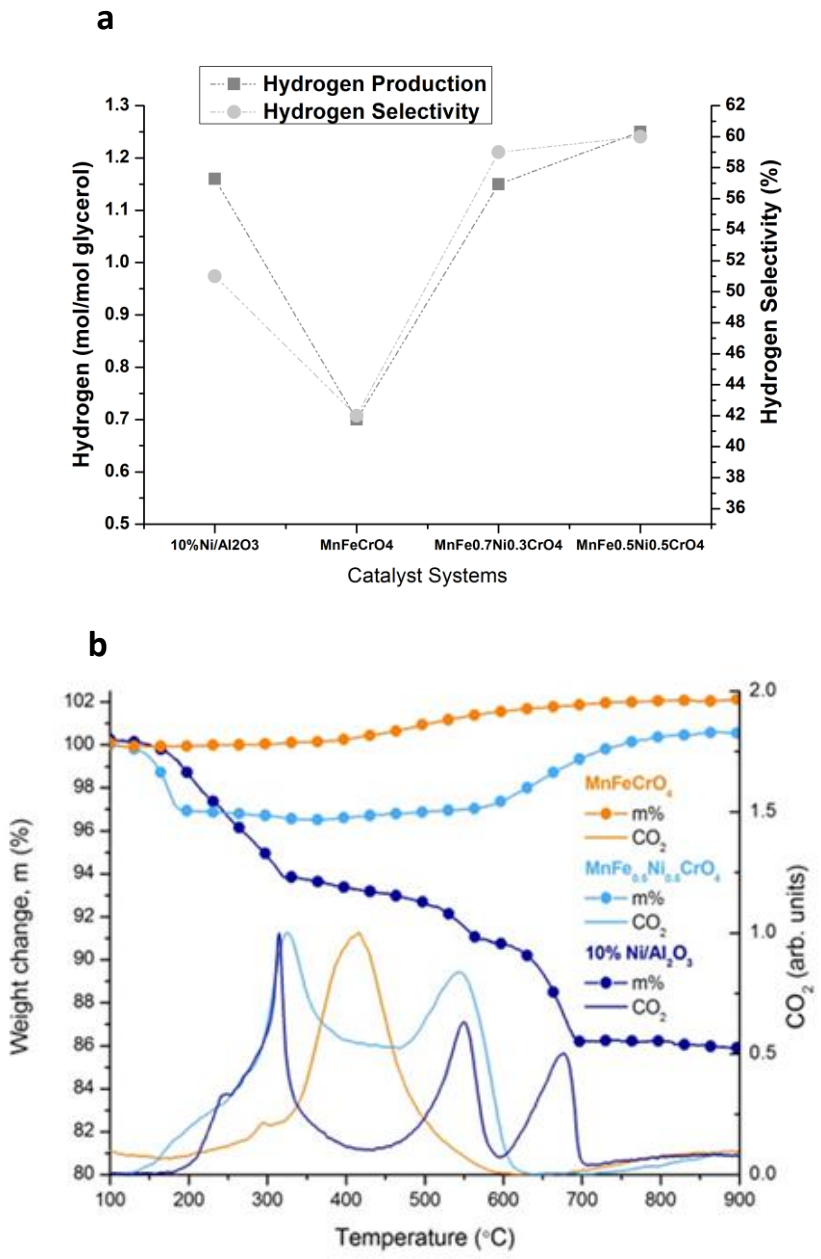

Figure 6-18 Catalysts prepared through exsolution display superior hydrogen production per mole glycerol and stability as compared to deposited ones. **a,** hydrogen production per mole glycerol and selectivity. **b,** weight change of selected samples in oxidising atmosphere monitored in parallel with the released CO_2 as a function of temperature. The test was carried out at temperatures of 700 ^{o}C, S/C ratio of 3 and glycerol molar flow rate of 8.2 x 10^{-5} moles/min and 7.3 x 10^{-4} moles/min of water and WHSV of 28 h^{-1}

The 10wt% Ni/Al_2O_3 system showed a considerable weight loss (~14%) across the investigated temperature range, indicative of significant carbon deposition. The

weight loss profile is closely reflected by the CO_2 release profile, both indicating that there are three main temperature regions where the carbon on these samples was removed. Typically this is indicative of three types of carbon with increasingly higher resilience towards oxidation, deposited at the metal centres (~300 °C), at the metal-oxide interface (~550 °C) and on the support (~675 °C) as explained in the previous chapter. Obviously, the Ni/Al_2O_3 system contained significant quantities of each of these carbon types. This probably explains the lower activity and conversion observed for this catalyst and highlights again that deposited Ni catalysts are prone to coking and thus severe deactivation, especially on prolonged running. The weight gain observed with $MnFeCrO_4$ and $MnNi_{0.5}Fe_{0.5}CrO_4$ especially at temperature >650 ^oC is due to reoxidation of the transition metal-based catalysts.

By contrast, the system $MnNi_{0.5}Fe_{0.5}CrO_4$ with lattice reorganisation-mediated metal particles (primarily Ni, Fe-Ni alloys) only shows two carbon peaks, but only the low temperature carbon has a noticeable weight loss component associated to it (~3%) although this is still not up to half of the analogue quantity for Ni/Al_2O_3. This suggests that even if limited coking does occur on these catalysts, it can be removed easily through a mild oxidation at ~300 °C. Interestingly, the Fe-exclusive catalysts system, $MnFeCrO_4$ displayed no weight loss, indicative of very limited carbon deposition. It is reasonable to assume at this stage that this is related probably to a synergistic effect of alloying (Fe-Ni) and also to the unique particle genesis and subsequent strong interaction with the oxide support due to redox lattice reorganisation.

6.3 B-Site metal doping in chromite based perovskite catalyst with Mn, Fe, Co and Ni and redox exsolution in glycerol steam reforming

6.3.1 The $La_{0.75}Sr_{0.25}Cr_{0.5}X_{0.5}O_{3-\delta}$ (X=Mn, Fe and Co) catalyst systems

Chromite-based perovskites have been found to be very promising materials as interconnect and anode materials in SOFCs and as catalyst for methane reforming [13-15]. Incorporating transition metals in the B-site of $La_{1-x}Sr_xCr_{y-1}M_yO_{3\pm\delta}$ (where M = Fe, Mn, Co Ni and Cu) has been reported to have potential for improving its catalytic properties in methane reforming[15]. High concentration doping (50%) of chromium with transition metals such as manganese on the B-site as in Lanthanum strontium chromium manganese oxide ($La_{0.75}Sr_{0.25}Cr_{0.5}Mn_{0.5}O_{3\pm\delta}$ - LSCM) was particularly

reported to enhance catalytic activity coke suppression and stability in fuel environment[16]. Manganese was substituted for iron (Fe) in $La_{0.75}Sr_{0.25}Cr_{0.5}Fe_{0.5}O_{3\pm\delta}$ (LSCF) using same doping strategy also enhanced conductivity and was also found active in methane reforming though not as good as LSCM in coke suppression[17]. Not much is reported to the best of my knowledge on the use of such catalysts and high doping strategy in reforming of liquid fuel such as glycerol where more severe coking is expected.

In the same context, an attempt would be made in this section to synthesize and investigate the influence of some selected substituted elements on the structural and catalytic properties of a highly doped (50%) B-site chromium-based $La_{0.75}Sr_{0.25}Cr_{0.5}X_{0.5}$ $O_{3\pm\delta}$ (X=Mn, Fe and Co) Perovskites catalyst in glycerol steam reforming. Attempt would also be made to modify such catalyst systems by way of impregnation with nickel into the lattice structure of the pre-reacted both A-site and B-site stoichiometric $La_{0.75}Sr_{0.25}Cr_{0.5}X_{0.5}$ $O_{3\pm\delta}$ (X=Mn, Fe and Co) Perovskites catalysts by reaction with nickel nitrate solution and subsequent redox exsolution of Ni nano particles supported on the 'inert' oxide surface of the materials. Influence of such modification on the structural and catalytic properties, exsolution phenomenon as well as coke suppression or tolerance behaviour in relation to glycerol steam reforming will be explored.

6.3.1.1 Thermo-gravimetric analysis

Thermal stability as well as reducibility of the metal substituted catalysts and the Ni-support interaction in the nickel impregnated catalyst were investigated under air (oxidation) and H_2 (reduction) or redox cycles using TGA and the results is as illustrated in Figure 6-19a-c. The first segment as indicated by the dotted lines represents oxidation of the samples in air and second reduction in 5% hydrogen both at heating and cooling ramp rate of 3^{o}/min to 900 ^{o}C. In Figure 6-19a, the first segment which represents oxidation in air, all catalyst host materials (i.e. LSCM, LSCF and LSCC) shows no weight loss or gain which indicates all the materials are very stable thermally in air. The gentle weight loss from 400 ^{o}C to 480 ^{o}C in the 2nd segment indicates weight loss due to reduction and the extent of which could be attributed to the reducibility and

stability of the materials in the hydrogen environment. The Mn substituted catalyst get reduced at higher temperature while the Co substituted was reduced at lowest temperature relatively and the Fe substituted comes in-between the two. Therefore, Mn substituted catalyst (LSCM) is more stable in reducing environment while the Co substituted catalyst (LSCC) is more reducible. This is consistent with what Mawdsley and Krause, 2008 reported for Co-containing perovskite[9]. Although, the weight loss is minimal (2.7%) in LSCC and almost negligible (0.5-1%) in LSCM and LSCF respectively, this might cause a change in the symmetry of the structure of the materials as reported by Tao and Irvine, 2004[16],[17] in the case of LSCF and LSCM respectively.

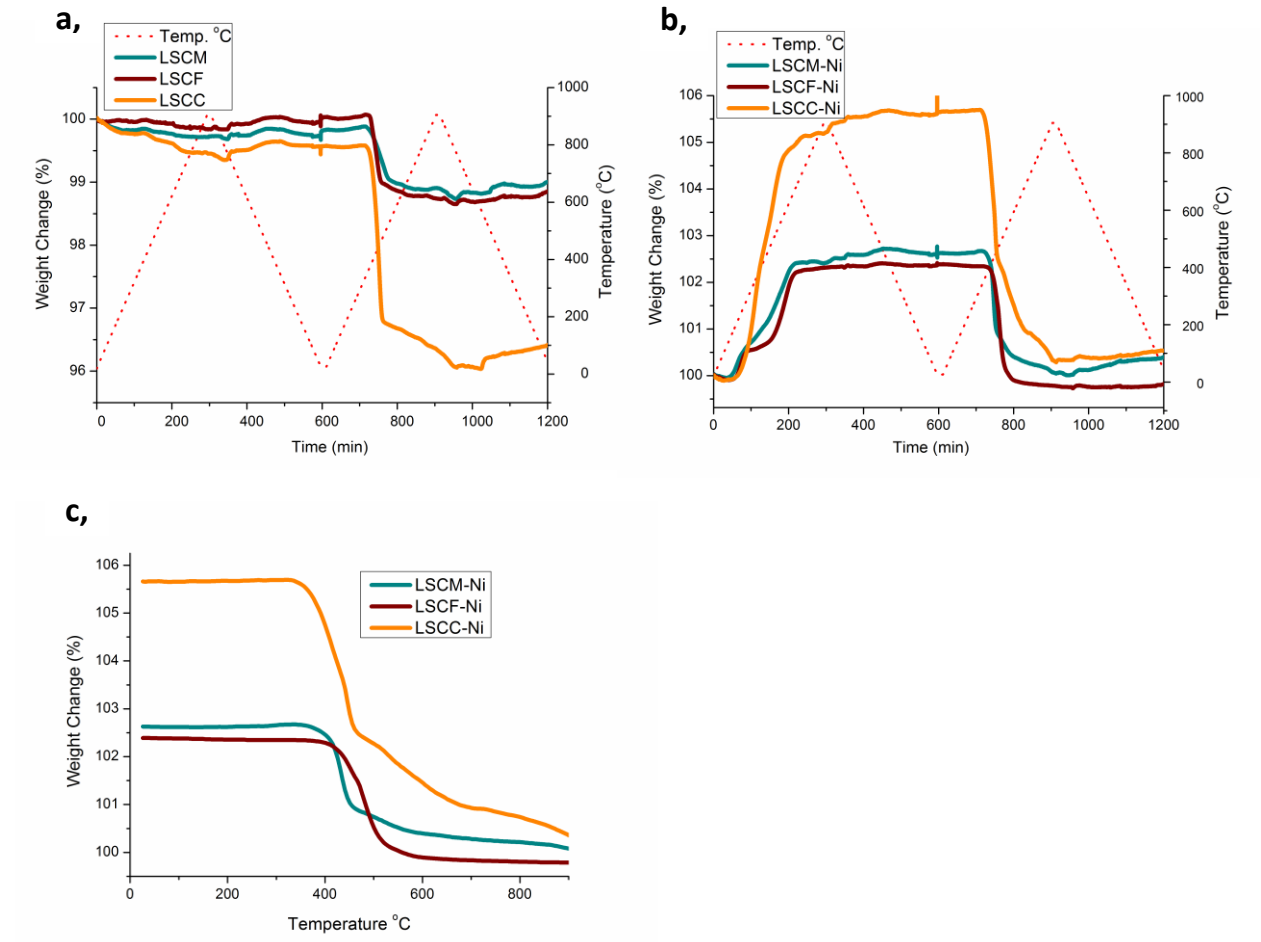

Figure 6-19 Thermo gravimetric Analysis of **a,** metal substituted catalyst and **b,** reduced Ni-impregnated catalysts respectively showing stability in air and then in hydrogen environments as denoted by the dotted line while **c,** shows how the host materials influences the reducibility of the nickel-containing catalyst

Figure 6-19b shows the air-hydrogen TGA of the Ni-impregnated catalyst materials. The sharp weight gain in the 1st segment (air oxidation) is due to oxygen intake by the

highly reduced samples which shows that nickel-impregnated Co substituted catalyst (LSCC-Ni) lost more oxygen during reduction followed by nickel-impregnated Fe substituted (LSCF-Ni) and the Mn substituted (LSCM-Ni) catalysts respectively. The order is same for weight loss observed in the 2nd segment (hydrogen reduction) cycle. This further confirms the high stability of the Mn and Fe substituted materials as compared to the Co substituted. The sharp weight loss at 400 to 480 ^{o}C in Figure 6-19b compared to that of the parent materials (Figure 6-19a) containing no nickel is attributable to reduction of Ni^{2+} to Ni^{0}. More so, the reduction temperature decrease in the order Mn<Fe<Co as represented in Figure 6-19c which is different from what was observed in Figure 6-19a in the case of the host materials. This suggests that the change is due to nickel impregnation. Therefore nickel-impregnated Mn substituted catalyst (LSCM-Ni) with the lowest reduction temperature (400-450 ^{o}C) contains more easily reducible Ni and has better nickel-support interaction. Thus the nickel particles in that system are more likely to be very stable with fewer tendencies for agglomeration and catalytically more active. The reduction temperature is lower than what is observed in Ni-based catalyst prepared using the 'traditional' wet impregnation as seen above in previous sections. This indicates that the nickel particles are more crystalline and dispersed with strong metal-support interaction when prepared using exsolution than wet impregnation. They are likely to resist agglomeration and coking which are the main agents of catalyst deactivation. This corroborates the observation made from the microstructure studies concerning the influence of the host materials on support-catalyst interaction. Thus, it suffices to say that tailoring the support structure or host materials by careful choice of dopant ions could enhance structural stability and overall catalyst behaviour.

6.3.1.2 Crystallographic and micro structures

The XRD pattern for the samples was collected to investigate the phase purity of the materials at room temperature. All the compositions are in single phase before and after the nickel impregnation as shown in Figure 6-20a and b respectively. The peaks at $2\theta = 44.47^{o}$ in Figure 6-20b may be assign to crystal plane of NiO and because no other peak was observed due to NiO explains well dispersion of the nickel in the

samples. This observation corroborates the observed surface area increase with the nickel containing samples notably after reduction as seen in Table 6-12. The different dopants used vary in ionic size and shape hence could influence symmetry and cell parameter of the overall structure differently.

Rietveld refinement of the Mn substituted (LSCM) was done as rhombohedra with *R-3C* space group[17] and Fe substituted (LSCF) was refined as orthorhombic with *R-3C* space group[16]. It is therefore possible the Co substituted (LSCC) may exhibit either structures since all have the same charge and substituted in the same B-site. However, splitting or non-splitting or broadening of the main perovskite peaks which usually have all even miller indices (eee) is used to characterize the symmetry of perovskite materials[5,6].

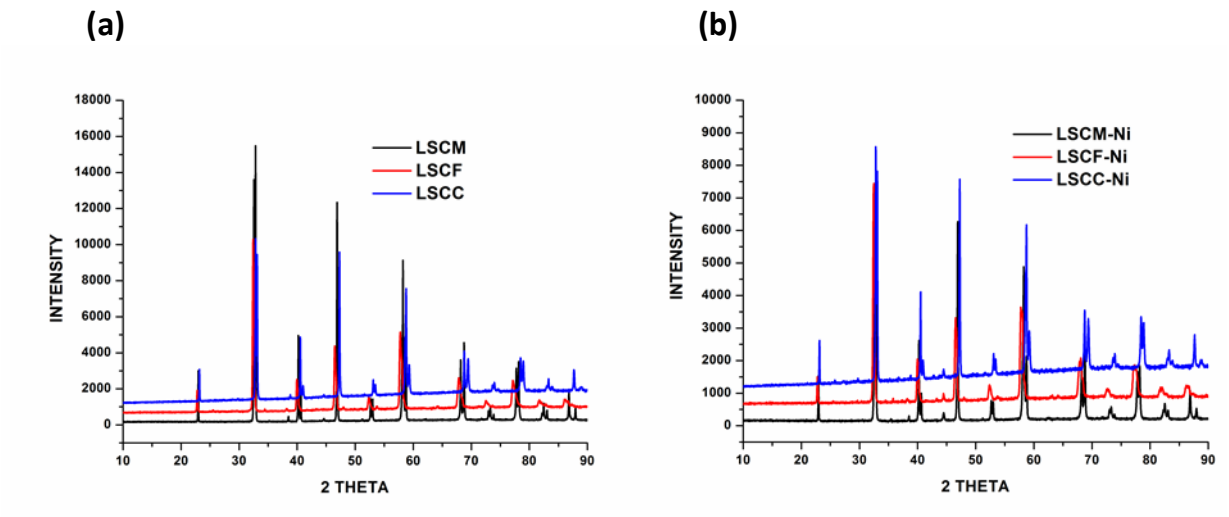

Figure 6-20 XRD Pattern of **a,** $La_{0.75}Sr_{0.25}Cr_{0.5}X_{0.5}$ $O_{3\pm\delta}$ and **b,** Ni-impregnated Catalysts showing the perovskite peaks and phase purity of the materials before and after nickel impregnation. The pattern also reflects shift in peak positions due to different dopant ions used

Splitting of both h00 and hhh peaks such as 004 and 444 suggest an orthorhombic distortion while splitting of only hhh and not h00 suggests rhombohedra distortion. Whilst tetragonal distortion represents reverse of orthorhombic, in the case of monoclinic, all the hhh, hh0 and h00 peaks are split. Tilting from ideal perovskite structure occurs due to size mismatch from the different dopants used or electronic effects with resultant lowering of symmetry. The magnitude of such octahedral tilting could be in-phase symbolised as (+) or out-of-phase (-) superscripts and it could occur

along any of the axes xyz denoted as a, b and c. Where no tilting occurs it is denoted by 0. Note that where the magnitude of tilting is the same in two or in all directions same notation is repeated such as $a^-a^-c^+$ indicating there is equal magnitude of out-of-phase tilting along both x and y axis but in-phase tilting along z-axis[5,6].

Indexing the XRD peaks of the samples on double cells shows that hhh peaks of LSCM and LSCC (i.e. 4 4 4) are split while those of h00 (4 0 0) are not which suggests rhombohedra structure. The LSCF structure had both hhh and h00 peaks splits which conforms to the orthorhombic structure. Rietveld refinement of the samples as shown in Figure 6-21 to Figure 6-23 fits the proposed structures. Both LSCM and LSCC were found to exhibits the rhombohedra structure with space group *R -3 C* whilst LSCF orthorhombic with *P b n m* space group. The crystal structures attached to the Figures also reflects the mode and extent of octahedral tilting caused by the different symmetry or space group exhibited by the samples as a result of the different dopant ions used. The cell parameters are summarized in Table 6-10. The variation observed in cell parameters is attributable to difference in ionic size of the different metal dopants used while influence due to charge could be minimal since all have same ionic charge. The dependency of cell parameters or lattice symmetry on the ionic size of the dopant was clearly evidenced in the XRD pattern of Figure 6-20a by the slight shift towards smaller 2θ or bigger d-spacing from Mn^{3+} in case of Fe^{3+} and to bigger 2θ or smaller d-spacing for Co^{3+} doped chromite due to decrease in the ionic size from Mn^{3+} through Fe^{3+} to Co^{3+}. The shift also confirms that the substitution was successfully achieved.

The sensitivity of the cell parameters to dopant and solubilisation of the dopant was further confirmed in Figure 6-24 where similar profile was obtained when primitive cell parameter (a_p) and ionic radius plotted against dopant metal ion were compared. The fact that the profiles look alike reaffirms the sensitivity of the structure or lattice parameter to the size of the dopant ions and also confirms solubilisation of the dopant ions. Interestingly, the chart also revealed the possible oxidation state and coordination number of the dopant ions in the systems. The ionic radius that matches the primitive lattice parameter (a_P) was those of Mn^{4+}. Fe^{3+} and Co^{4+} all with coordination number of VI[18]. This is attributable to the fact the host Cr ion exhibits

variable oxidation states and the deficiency or defect created by the dopant ions which allows for charge flexibility or variation in oxidation state.

$La_{0.75}Sr_{0.25}Cr_{0.5}Mn_{0.5}O_{3-\delta}$ (LSCM)			
R-3C **($a^-a^-a^-$)**	Projection along XYZ axes	Projection along y axis	Projection along z axis

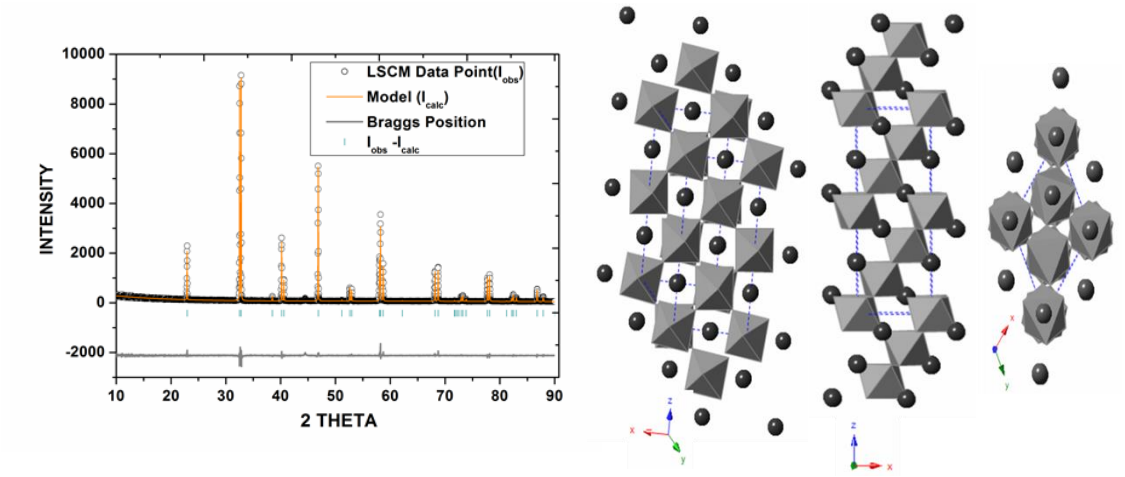

Figure 6-21 Rietveld refinement data showing the structural fitting of the XRD pattern of the sample to the proposed *R-3C* space group and rhombohedra structure. The structural model by the right shows the extent of out-of-phase tilting equal in magnitude along all the axis (x,y and Z) as the notation ($a^-a^-a^-$) suggests

$La_{0.75}Sr_{0.25}Cr_0Fe_{0.5}O_{3-\delta}$ (LSCF)			
Pbnm **($a^-a^-a^+$)**	Projection along XYZ axes	Projection along y axis	Projection along z axis

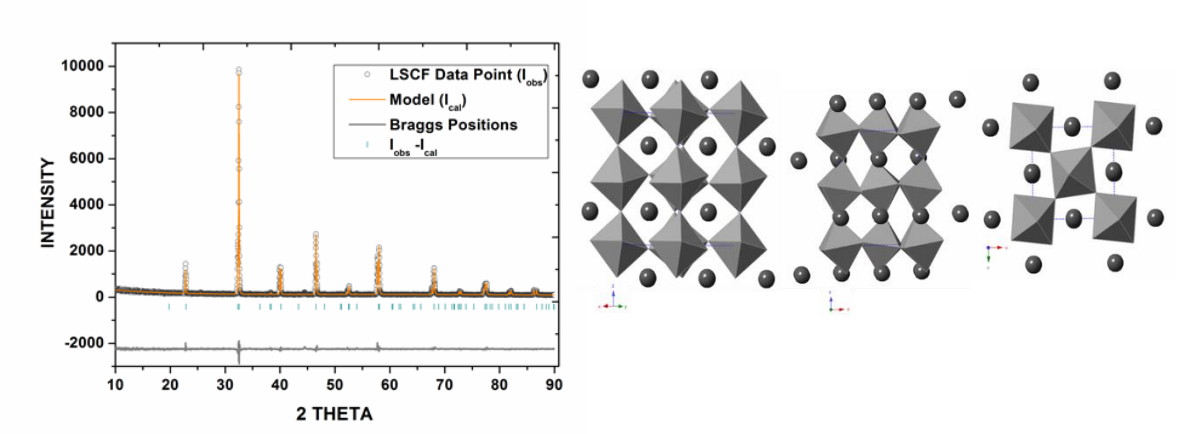

Figure 6-22 Rietveld refinement showing structural fitting of the XRD pattern of the sample to the proposed *Pbnm* space group and orthorhombic structure. The structural model by the right shows the extent of out-of-phase tilting of equal magnitude along x and y axis with in-phase tilting along z axis as the notation ($a^-a^-a^+$) suggests

$La_{0.75}Sr_{0.25}Cr_{0.5}Co_{0.5}O_{3-\delta}$ (LSCC)			
R-3C **($a^-a^-a^-$)**	Projection along XYZ axes	Projection along y axis	Projection along z axis

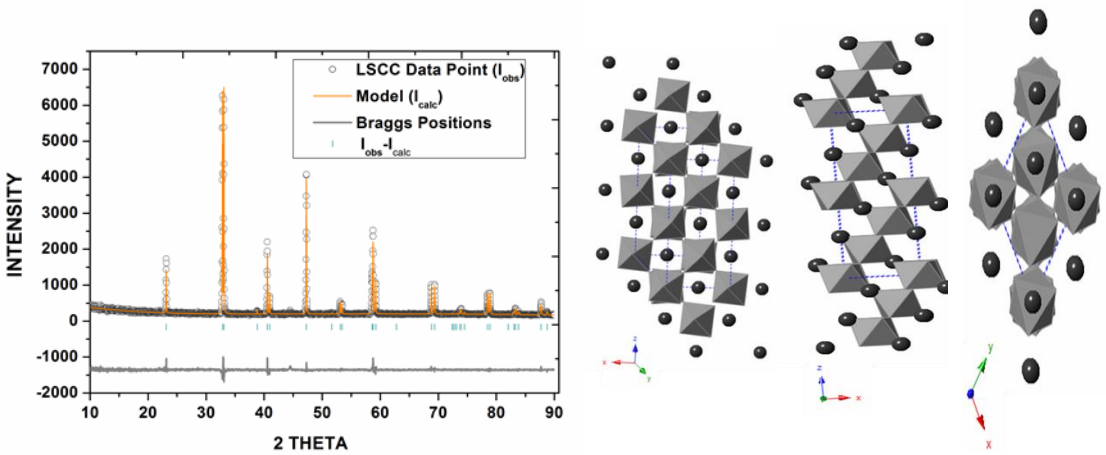

Figure 6-23 Rietveld refinement data showing structural fitting of the XRD pattern of the sample to the proposed *R-3C* space group and rhombohedra structure. The structural model by the right shows the extent of out-of-phase tilting equal in magnitude along all the axis (x,y and z) as the notation ($a^-a^-a^-$) suggests

Therefore cell volume plotted against the respective dopant metals in Figure 6-24b was expected to decrease linearly as you move from Mn^{4+} through Fe^{3+} to Co^{4+} but does not as a result of different symmetry exhibited by the substituted samples. These influences of the dopant metals on the symmetry, cell volumes and cell parameters are expected to influence surface reactions phenomenon and hence could manifest in the catalytic behaviour of the materials.

Table 6-10 Rietveld refinement data for the $La_{0.75}Sr_{0.25}Cr_{0.5}X_{0.5}$ $O_{3\pm\delta}$ (X= Mn. Fe and Co) before nickel impregnation

Catalyst	Space Group	Lattice Parameter (Å)	Cell Volume (Å)	Refinement Fit Parameter
LSCM	*R-3C*	a=5.499 b=5.499 c= 13.318	348.813	R_p= 6.73, R_{wp}=9.35 R_{exp}= 7.92, X^2=1.39
LSCF	*Pbnm*	a=5.496 b=5.534 c= 7.772	236.394	R_p= 6.14, R_{wp}=7.97 R_{exp}= 7.44, X^2=1.15
LSCC	*R-3C*	a=5.453 b=5.453 c= 13.217	340.348	R_p= 4.99, R_{wp}=6.67 R_{exp}= 6.15 X^2=1.18

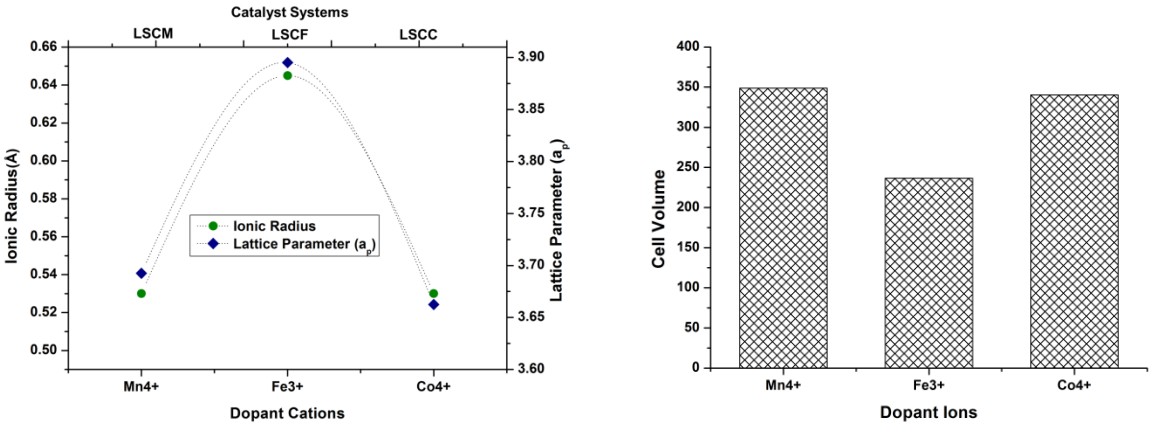

Figure: 6-24 **a,** Comparing influence of ionic radius[18] of the metal dopant ions on Cell Parameters for the $La_{0.75}Sr_{0.25}Cr_{0.5}X_{0.5}O_{3\pm\delta}$ (X= Mn. Fe and Co) perovskite series, it also reflects the actual coordination number and charge of the dopant metal ions and **b,** compares influence of metal dopant ion on cell volume for the same $La_{0.75}Sr_{0.25}Cr_{0.5}X_{0.5}O_{3\pm\delta}$ (X= Mn, Fe and Co) perovskite series

The nickel impregnation did affect the phase purity or symmetry of the host materials as seen in their XRD patterns in Figure-6-20b. Except that, after the Nickel impregnation the cell parameters changed reflecting the space group and different doping cations as summarised in Table 6-11 below. The changes are attributable to the host material support-nickel metal catalyst interaction the extent of which manifests in the observed changes in the lattice parameters. Thus the relationship between the host and nickel catalyst (support-catalyst interaction) is expected to influence the catalytic behaviour of the host materials as much as it does on the microstructures. The refinement fit parameter R_p and R_{wp} for LSCF-Ni are above 10 % which reflects poor fitting behaviour relatively compared to the catalyst systems with less than 10%.

Table 6-11: Rietveld refinement data of the metal substituted catalyst after nickel impregnation

Catalyst	Space Group	Lattice Parameter (Å)	Cell Volume (Å)	Refinement Fit Parameter
LSCM-Ni	*R-3C*	a=5.494 b=5.494 c= 13.317	348.145	R_p= 7.23, R_{wp} =9.57 R_{exp}= 6.57, X^2 = 2.13
LSCF-Ni	*Pbnm*	a=5.494 b=5.536 c= 7.778	236.571	R_p= 11.9, R_{wp} =17.2 R_{exp}= 5.73, X^2 =9.04
LSCC-Ni	*R-3C*	a=5.457 b=5.457 c= 13.216	340.850	R_p= 4.73, R_{wp} =6.45 R_{exp}= 4.66, X^2 =1.92

The microstructure of the three parent samples without the nickel as seen in Figure 6-25a-c are the same except that the particle looks smaller in the LSCF and bigger in the LSCC while the LSCM has moderate sized uniform particles relatively.

a, LSCM

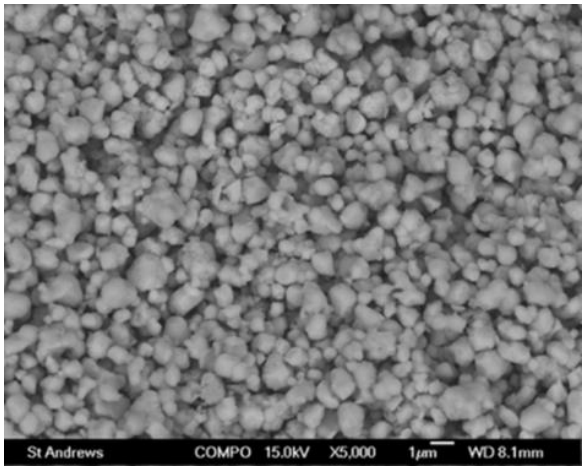

b, LSCF

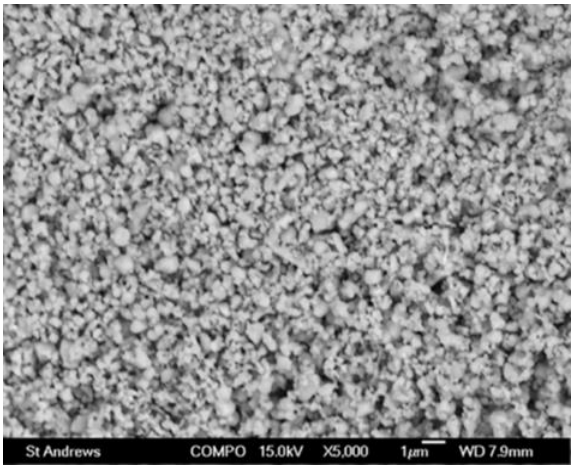

c, LSCC

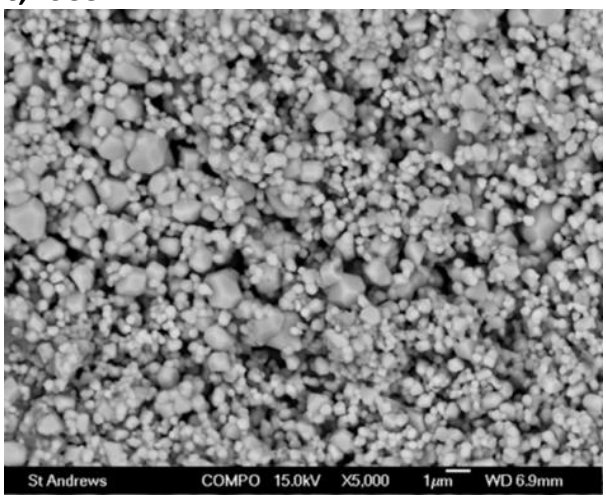

Figure 6-25 Microstructures of the Mn, Fe and Co substituted catalysts before nickel impregnation or reduction a, LSCM, b LSCF and c LSCC collected using the back scatter mode

Detailed micrograph of the materials in bigger magnification in Figure 6-26a-c shows a smooth surface area good for catalysis with average particle size of about 100 nm. Impregnation of nickel into the chromite parent materials and exsoluted in reducing atmosphere has modified the morphology of the catalysts. Figure 6-27a-c shows nickel nano particles exsoluted and supported on oxide surface. This morphology enhanced the surface area as shown in Table 6-12b and could be seen as an index for good

catalytic behaviour. The exsolution is more effective in the Mn substituted catalyst, moderate in Co whilst Fe substituted was poorly exsoluted. Thus, the extent of the phenomenon followed the order Mn>Co>Fe as seen in Figure 6-27a-c below.

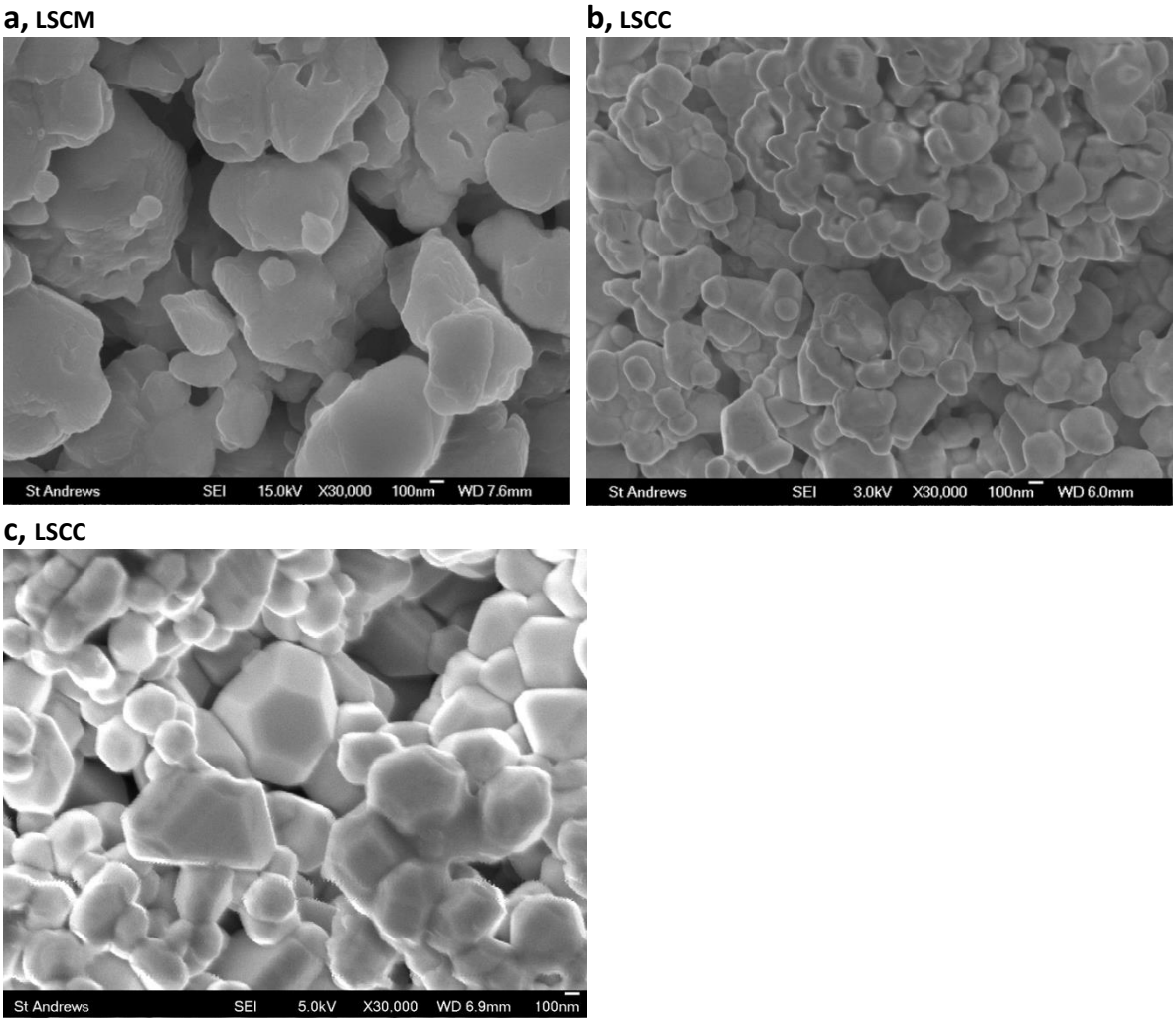

Figure 6-26 Microstructures of the Mn, Fe and Co substituted catalysts before nickel impregnation or reduction **a,** LSCM, **b** LSCF and **c** LSCC

Thus exsolution behaviour observed with the Mn and Co substituted catalyst is attributed to many factors such as the oxygen non-stoichiometry or oxygen vacancies that are known to exist in some Mn, Co and Fe substituted perovskites[19,20]. Ability to incorporate and release nickel upon reduction, reducibility of the materials, versatility to compensate charge and coordination from different dopant ions used which could lead to defect among many others[6]. Such vacancies were found to be more profound in Co substituted materials than in Mn substituted in a different studies[21]. The addition of Cr and perhaps doping strategy in our case seems to have reversed that

order. The vacancies are now seems to be more readily in the Mn than in Co substituted systems and the Fe substituted has the least as evidenced by the trend of extent of exsolution exhibited by the substituted materials as observed in Figure 6-27a-c below.

a, LSCM

b, LSCF

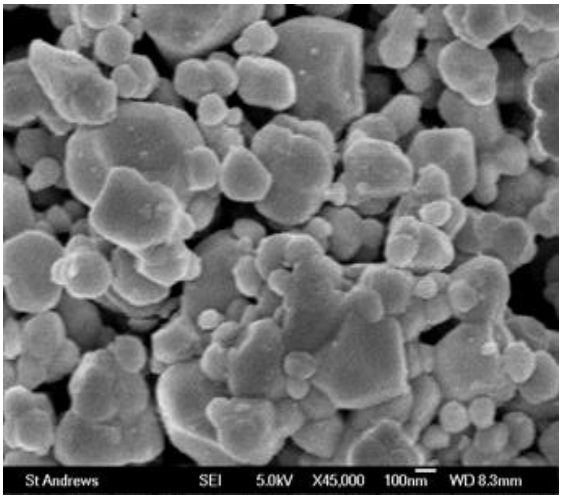

c, LSCC

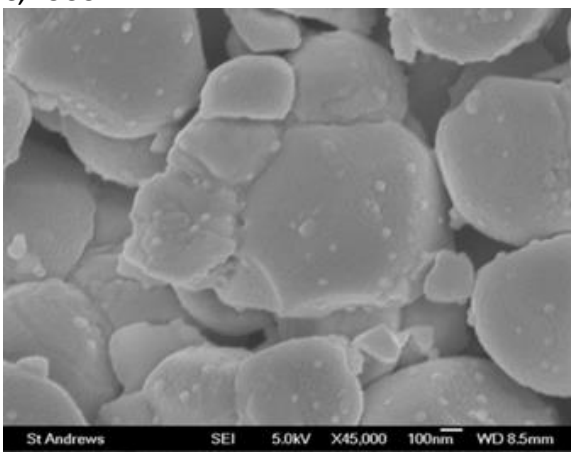

Figure 6-27a-c: Microstructures of the Ni-impregnated Mn, Fe and Co substituted catalysts after reduction showing extent of exsolution phenomenon amongst the metal substituted catalysts

6.3.1.3 Physicochemical properties

The surface area of the transition metal substituted catalysts as well as the nickel impregnated catalysts before and after reduction prepared by combustion synthesis was investigated and the results are as shown in Table 6-12a and b. The results show

that impregnation of nickel into the pre reacted materials has reduced their surface area which was enhanced after reduction.

Table 6-12 Physicochemical properties of the **a**, metal substituted host catalyst system and that of **b,** Ni-impregnated catalyst before and after reduction

Catalyst	Surface Area (m^2g^{-1})
LSCM	3.10
LSCF	3.46
LSCC	3.18

Catalyst	Surface Area (m^2g^{-1}) Before Reduction	Surface Area (m^2g^{-1}) After Reduction
LSCM-Ni	2.5396	4.3850
LSCF-Ni	2.7172	5.0612
LSCC-Ni	2.5352	4.8922

The decrease in the surface area due to nickel impregnation resembles what is observed when nickel particles were deposited on oxide support by wet impregnation[22]. The decrease is as a result of the nickel particles occupying the oxides pore and channels of the host support materials resulting in reduced surface area of the support. That also reflects the extent of the nickel incorporation and solubilisation into the lattice structure of the perovskite. The exsoluted nickel particles well dispersed on the surface of the oxide support as seen in Figure 6-27 might be responsible for the observed increase in surface area after reduction which is indicative of good catalytic properties although the catalyst with the best exsolution (LSCM-Ni) showed the least surface area.

6.3.1.4 Influence of metal dopants on the catalytic behaviour of $La_{0.75}Sr_{0.25}Cr_{0.5}X_{0.5}O_{3\pm\delta}$ (X=Mn, Fe and Co) catalyst series

The results of the screening test on the Mn, Fe and Co substituted catalyst systems known as LSCM, LSCF and LSCC in Figure 6-28 shows that all the catalysts were active in steam reforming of glycerol under the test condition with the Fe substituted slightly more active. The test was carried out at 700 ^{o}C, S/C ratio of 3:1 at atmospheric pressure. The molar glycerol-water solution flow rate was 1.36 x 10^{-4} moles/min with S/C ratio of 1 and 2.60 x 10^{-4} mole/min with S/C ratio of 3 respectively. The moles of products generated per mole of glycerol fed to the reactor plotted against respective catalyst systems indicate how the products distribute among the catalysts systems. It is clear the Fe substituted catalyst is slightly more active. This observation is

corroborated by the activity chart in Figure 2-29a where mol/min of the products is compared with the glycerol conversion. The products distribution shows that all the catalyst systems are particularly more selective for CO compared to CO_2 as supported by the H_2/CO_2 and H_2/CO mole ratios in Table 6-13.

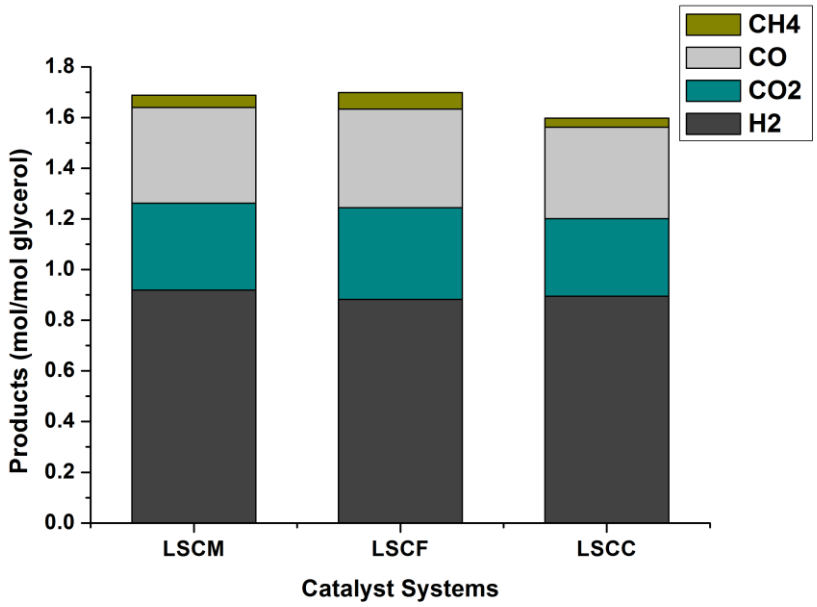

Figure 6-28 gaseous products in mole per mole of glycerol injected to the reforming system against the respective catalyst systems. The test was performed at 700 ^{o}C, S/C ratio of 3 and glycerol solution containing 8.2 x 10^{-5} moles of glycerol and 7.3 x 10^{-4} moles of water and WHSV of 28 h^{-1}

The ratios confirm more CO as compared to CO_2. The Fe substituted catalyst gave the lowest CO but more CH_4 relatively. These suggest that although generally all the catalysts are not good for water-gas-shift reaction (WGSR), the Fe substituted is the worst relatively. Because of their tendency for CO and H_2 production, the catalyst systems are good for syngas production favoured via reactions such as reverse WGSR. The kinetic influence due to high temperature at which the screening test was carried out suggests that contribution of glycerol decomposition to the observed CO production cannot be ignored. Comparison of hydrogen produced per mole of glycerol, H_2/CO and H_2/CO_2 mole ratios with equilibrium composition due to glycerol decomposition (Eqn. 2-3) in Table 6-13 suggests a possible contribution from that reaction. The glycerol conversion was perhaps limited by glycerol passing through unconverted due to much throughput.

On the individual merit of the dopants, the Mn substituted catalyst gave the highest hydrogen yield followed by Co and Fe substituted gave the least. This further agrees with what Mawdsley and Krause, 2008 reported on $LaCoO_3$[9]. The hydrogen produced per mole of glycerol as seen in Figure 6-28 is around 15 % of the equilibrium composition (see Table 2A-2 of appendix 2). Other gaseous products are also within the equilibrium composition. CO which is one of the dominants products is within 36-39 % of the equilibrium composition. The hydrogen production was limited by reaction that produces acrolein, carbonyl compounds and unconverted glycerol perhaps due to throughput.

Table 6-13 Comparison of products from the experiment with equilibrium composition based on glycerol pyrolysis

	Temperature (^oC)	Conv.= Conversion (C basis)	H_g= H_2/Glyc. (mol/mol)	H_g/Conv.	H_2/CO	H_2/CO_2
Equilibrium	700	-	6.0	-	6.00	3.00
LSCM	700	0.26	0.92	3.54	2.43	2.67
LSCF	700	0.27	0.88	3.26	2.26	2.43
LSCC	700	0.25	0.90	3.60	2.48	2.92

The activity was further confirmed as illustrated in Figure 6-29b for glycerol conversion to gaseous products using both pure and by-product glycerol and steam-to-carbon ratio of 3 and 1. It is evident glycerol conversion to gaseous products decreased when steam-to-carbon ratio less than the stoichiometric amount (1:1) was used (Figure 6-29b) and by-product glycerol. The catalysts showed good activity using by-product glycerol despites its impurities. The glycerol conversion dropped by 3 % with LSCM for instance using by-product glycerol compared to pure glycerol. The LSCM's surface morphology relatively as evident in the SEM micrograph of Figure 6-25a-c and Figure 6-26a-c might be responsible for its slightly higher activity except using pure glycerol. Figure 6-30a and b compares the influence of steam-to-carbon ratio and glycerol type on CO selectivity and H_2 production per mole of glycerol been the major products.

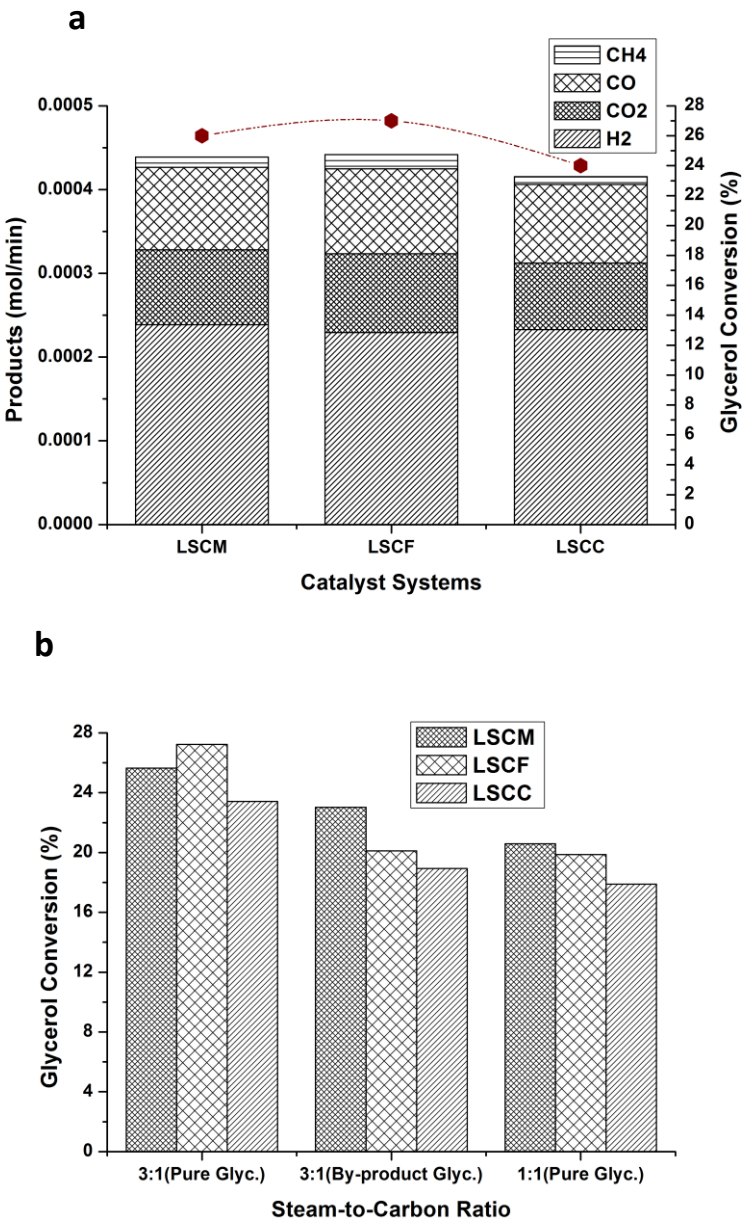

Figure 6-29: **a,** Relationship between catalysts product distribution and glycerol conversion among the metal substituted catalysts and **b,** comparison on the influence of steam-to-carbon ratio among the substituted metal catalysts. The test was performed at 700 ^{o}C, S/C ratio of 3 and glycerol molar flow rate of 8.2 x 10^{-5} moles/min and 7.3 x 10^{-4} moles/min of water and WHSV of 28 h^{-1}

Reducing water content below the stoichiometric ratio tends to favour production of carbon containing species (Figure 6-30a) as illustrated by the CO selectivity chart. In contrast, more hydrogen was produced with high water content (Figure 6-30b). This is attributable to the fact that water supports forward reaction of WGSR leading to more H_2 and CO_2 production[23] and as shown by Eqn. 2-6.

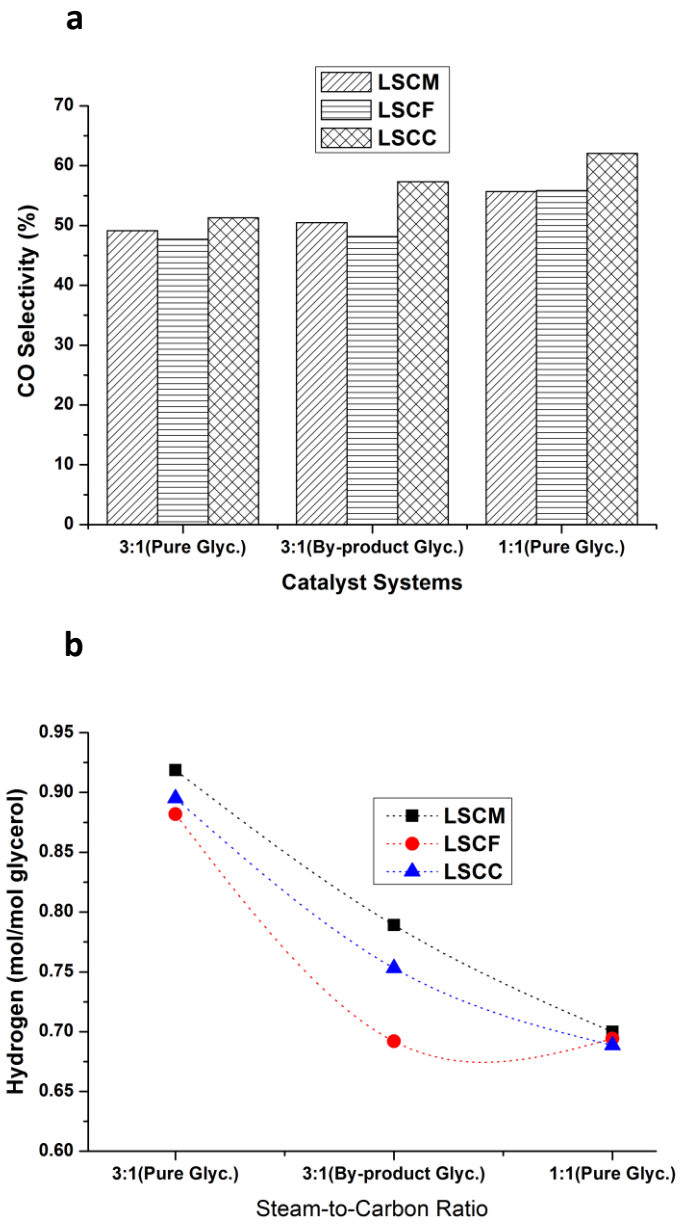

Figure 6-30a and b Comparison on the influences of glycerol type and steam-to-carbon ratio on CO selectivity and H_2 per of mole glycerol respectively amongst the metal substituted catalysts. The test was performed at 700 ^{o}C, S/C ratio of 3 and glycerol molar flow rate of 8.2 x 10^{-5} moles/min and 7.3 x 10^{-4} moles/min of water and WHSV of 28 h^{-1} for S/C ratio 3 and glycerol solution containing 8.2 x 10^{-5} moles of glycerol and 2.4 x 10^{-4} moles of water and S/C ratio of 1

It suffices to add that although water supports forward reaction of WGSR leading to more H_2 and CO_2 in the system, too much water could affect methanation reaction that could lead to low CH_4 yield especially at low temperatures. The reaction produces water therefore addition of water will favour backwards reaction forming H_2, CO or CO_2 (Eqn.2-8 to 2-10). The low CO selectivity of LSCF as compared to LSCM or LSCC in Figure 6-30a might be due to LSCF more CH_4 production than the LSCM and LSCC and

also limited by WGSR. Therefore, Fine tuning structural properties through B-site doping with transition metals and optimization of reaction condition such as S/C ratio and reaction temperature are capable of enhancing glycerol conversion and production of hydrogen and syngas. The test also strengthened the earlier observation from the previous sections that by-product glycerol is an intense energy feedstock that could be harnessed to provide renewable hydrogen or hydrogen-rich gas for the development of fuel cell technology.

6.3.1.5 Modification of the $La_{0.75}Sr_{0.25}Cr_{0.5}X_{0.5}O_{3\pm\delta}$ (X=Mn, Fe and Co) catalyst series by nickel impregnation

The nickel impregnated catalysts were screened at 700 ^{o}C using S/C ratio of 3 and glycerol-water molar flow rate of 2.60 x 10^{-4} moles/min and WHSV of 28 h^{-1}. Product distribution, glycerol conversion and hydrogen production per mole of glycerol has changed significantly with the impregnation of nickel into the lattice structure of the substituted chromite based catalysts and subsequent exsolution of Ni nano particles in reducing environment supported on the oxide support surface of the materials. The amount of products produced per mole of glycerol as shown in Figure 6-31a shows that LSCM-Ni was more catalytically active while LSCF-Ni was the least active. Though, in terms of glycerol conversion to gaseous products, the LSCF-Ni was more active perhaps due to its high CO composition. The LSCM-Ni and LSCC-Ni gave more H_2 and CO_2 than the LSCF-Ni so also CH_4 production was slightly highest with LSCM-Ni and LSCC-Ni than in LSCF-Ni which is contrary to what was observed with the parent materials (Figure 6-28 and 29a). The trend of activity showed a similar pattern in mol/min of products plotted against the respective catalyst systems as seen in Figure 6-32a. The H_2/CO_2 and H_2/CO products ratio analysis in Table 6-14 attests to this. The ratio shows that the catalyst produced more H_2 and CO_2 than CO against what was recorded for the parent materials. Comparison with equilibrium composition due to glycerol decomposition (Eqn. 2-3) of hydrogen produced per mole of glycerol, H_2/CO_2 and H_2/CO ratios as seen in Table 6-14 suggests non-equilibrium composition with regards to Eqn. 2-3. Though, the H_2/CO ratio in Table 6-14 indicates contribution of catalytic glycerol decomposition to the observed performance. The impregnated

nickel has tendency to facilitate the decomposition process due its propensity for C-C and C-H bond cleavages leading to generation of more syngas.

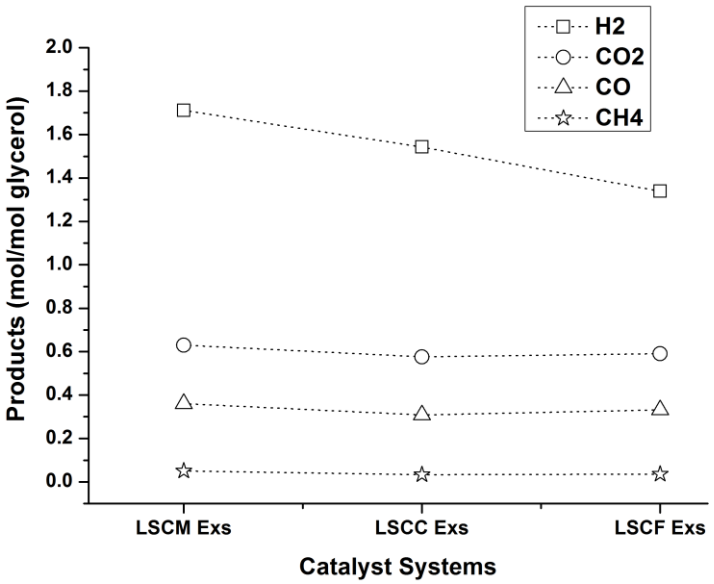

Figure 6-31 products distribution in mole per mole of glycerol injected to the reforming system against the respective catalyst systems. The test was performed at 700 ^{o}C, S/C ratio of 3 and glycerol molar flow rate of 8.2 x 10^{-5} moles/min and 7.3 x 10^{-4} moles/min of water of water and WHSV of 28 h^{-1}

The enhanced activity is attributable to nickel which is known to facilitate WGSR and methanation reactions producing more hydrogen[1]. The exsolution was better with the Mn and Co substituted catalysts having more nickel exposed to the surface. This led to enhanced surface morphology as seen in Table 6-12. Hence they tends to favour hydrogen production per mole of glycerol through reactions such as WGSR than Fe substituted whose nickel particles were perhaps more in the bulk than in the surface. The exposed nickel particles in LSCM-Ni and LSCC-Ni had a better nickel-support interaction as shown by TGA investigations in Figure 6-19c as such are also more likely to adsorb the glycerol feedstock to their surface hence more prone to high activity.

Table 6-14 Comparison of products from the experiment with equilibrium composition based on glycerol pyrolysis

	Temperature (^{o}C)	Conv.= Conversion (C basis)	H_g= H_2/Glyc. (mol/mol)	H_g/Conv.	H_2/CO	H_2/CO_2
Equilibrium	700	-	6.0	-	6.00	3.00
LSCM-Ni	700	0.35	1.71	4.89	4.75	2.72
LSCF-Ni	700	0.32	1.34	4.20	4.04	2.27
LSCC-Ni	700	0.31	1.54	4.96	5.01	2.68

The amount of hydrogen produced per mole glycerol increased from 15 % of the equilibrium composition with the host chromite catalysts to between 23-29 % with the nickel impregnated catalysts. The CO produced per mole glycerol has reduced from 36-39 % of the equilibrium composition with the host chromite to 31-36 % of the equilibrium composition as seen in Figure 6-31 and 32a respectively. These further attests to the change in the material's properties in enhancing syngas production via reverse WGSR to H_2 and CO_2 production via WGSR respectively.

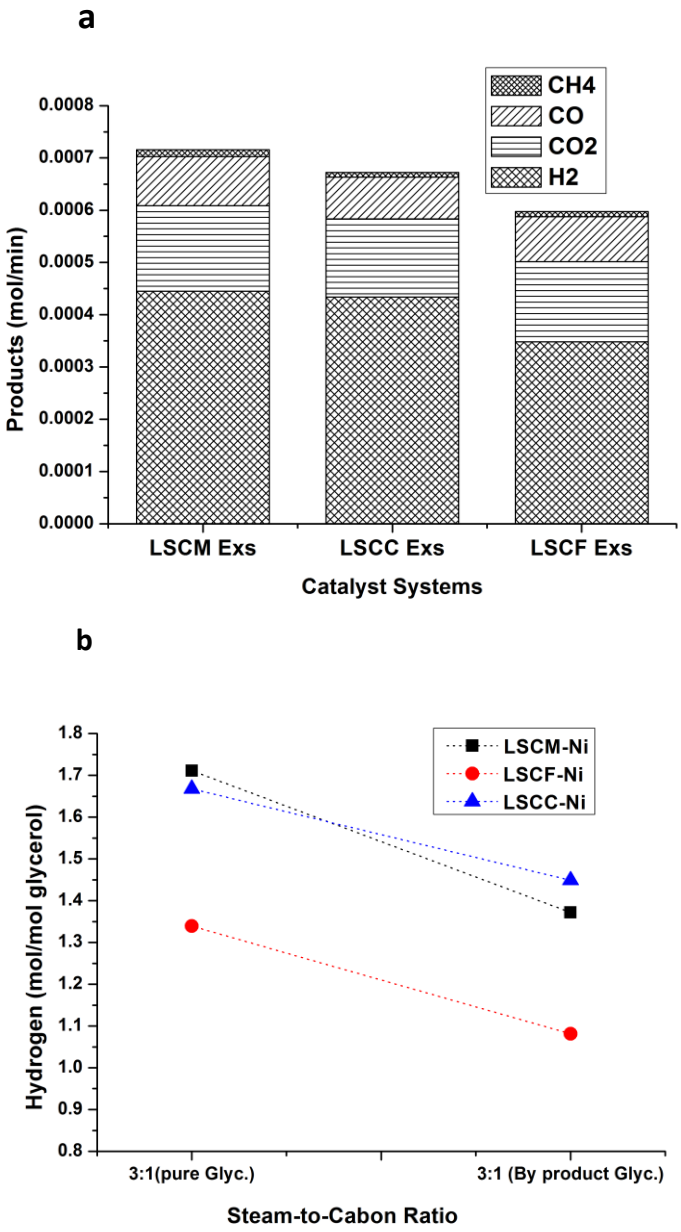

Figure 6-32: **a,** Influence of Ni-impregnation on product distribution among the metal substituted catalysts and **b,** influence of glycerol type on H_2 selectivity among the substituted metal catalyst. The test was performed at 700 ^{o}C, S/C ratio of 3 and glycerol molar flow rate of 8.2 x 10^{-5} moles/min and 7.3 x 10^{-4} moles/min of water and WHSV of 28 h^{-1}

Despite impurities in by-product glycerol such as unconverted vegetable oil, non-separated biodiesel, methanol and catalyst (KOH) residue; the nickel impregnated catalysts showed a reasonable hydrogen production per mole of glycerol using by-product glycerol as seen in Figure 32b. Suffices it to say in addition to robust behaviour of the catalysts, the biodiesel production catalyst residue such as KOH in the by-product glycerol as confirmed by TGA might have increased the basicity of the catalyst thereby favouring forward reaction of the WGSR[24]. Remarkably, the parent catalysts are not good for WGSR but Ni impregnation and exsolution has enhanced their tendency to support WGSR and improve hydrogen production significantly.

Further analysis revealed that carbon loss as a results of carbon deposition during the catalyst test reduces in the order LSCM-Ni<LSCF-Ni<LSCC-Ni as confirmed through carbon balance analysis as shown in Table 6-15.

Table 6-15 Influence of metal dopant substitution on carbon loss

Catalyst System	Reaction Temp.(^{o}C)	Total C **IN** (moles/min)	Total C **OUT** (moles/min)	CO **OUT** (moles/min)	CO_2 **OUT** (moles/min)	CH_4 **OUT** (moles/min)
LSCM-Ni	700	7.8×10^{-4}	2.7×10^{-4}	9.4×10^{-5}	1.7×10^{-4}	1.3×10^{-5}
LSCF-Ni	700	7.8×10^{-4}	2.5×10^{-4}	8.6×10^{-5}	1.6×10^{-4}	9.4×10^{-6}
LSCC-Ni	700	7.8×10^{-4}	2.4×10^{-4}	8.0×10^{-5}	1.5×10^{-4}	8.6×10^{-6}

6.3.1.6 Time on stream (TOS) and stability testing

The change in the activity of the catalysts over time on stream was investigated by monitoring glycerol conversion and hydrogen production per mole glycerol over time for 24 hrs at constant temperature of 700 ^{o}C at atmospheric pressure and steam-to-carbon ratio of 3:1 using pure glycerol as well as WHSV of 28 h^{-1}. The results are shown in Figure 6-33a and b for metal substituted catalysts. It is clear that all the catalysts suffered only mild decrease in glycerol conversion and hydrogen production as a result of deactivation perhaps due to unconverted glycerol, throughout the 24 hr test. This further strengthened the observation made above concerning the robust behaviour of the catalyst systems. Among the metal substituted catalysts, the Mn and Fe substituted catalyst were the most stable with only about 7 % activity loss or deactivation each while the Co had 8 % activity loss/deactivation.

The metal substituted catalyst systems also showed a steady hydrogen production streams over time as shown in Figure 6-33b. The LSCM and LSCF recorded a decrease of 15 % of hydrogen production over 24 hours while LSCC recorded 30 % loss in hydrogen production. The LSCC's loss of performance occurred largely within the initial 2 hrs and seems to have stabilised thereafter. Generally, the LSCM and LSCF are more stable.

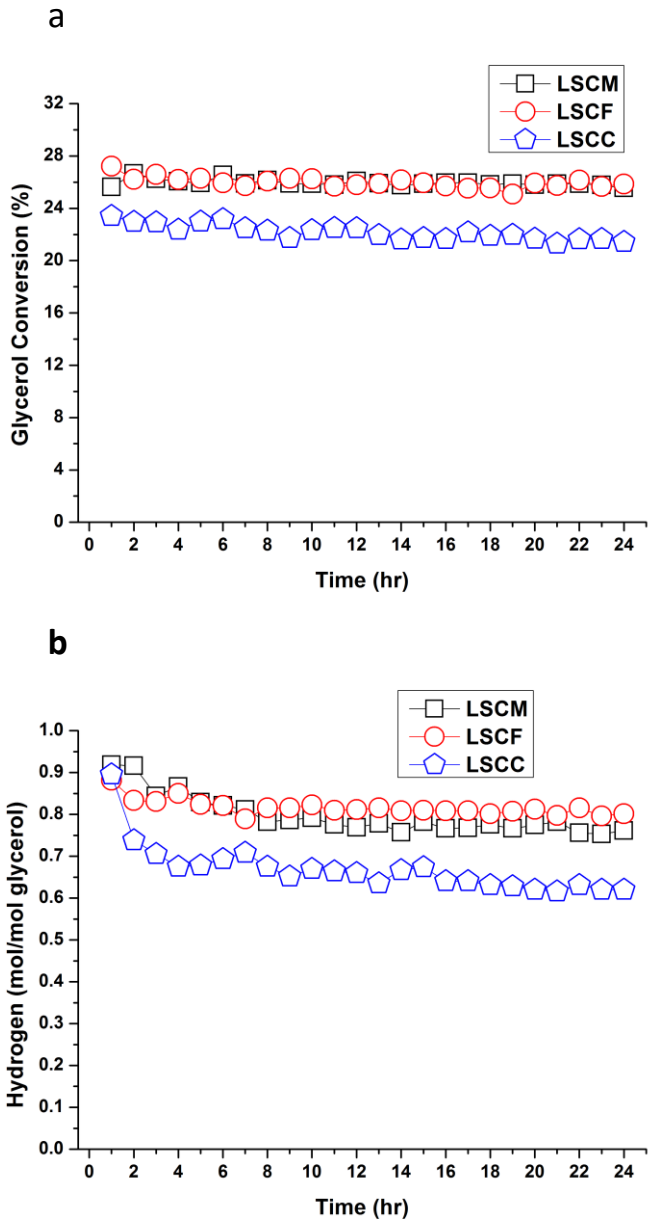

Figure 6-33: Time on stream changes in the activity of the catalyst showing how glycerol conversion and hydrogen production per mole of glycerol for the metal substituted catalysts changes over time and stability of the catalysts. The test was performed at 700 ^{o}C, S/C ratio of 3 and glycerol molar flow rate of 8.2 x 10^{-5} moles/min and 7.3 x 10^{-4} moles/min of water and WHSV of 28 h^{-1}

With the Ni-impregnated catalysts, despite Ni propensity for C-C, C-H and C-O bond breakage which could lead to deactivation due to carbon deposition, the results shown in Figure 6-34 indicates that those catalysts were not severely deactivated. LSCM-Ni and LSCC-Ni catalyst systems are the most stable.

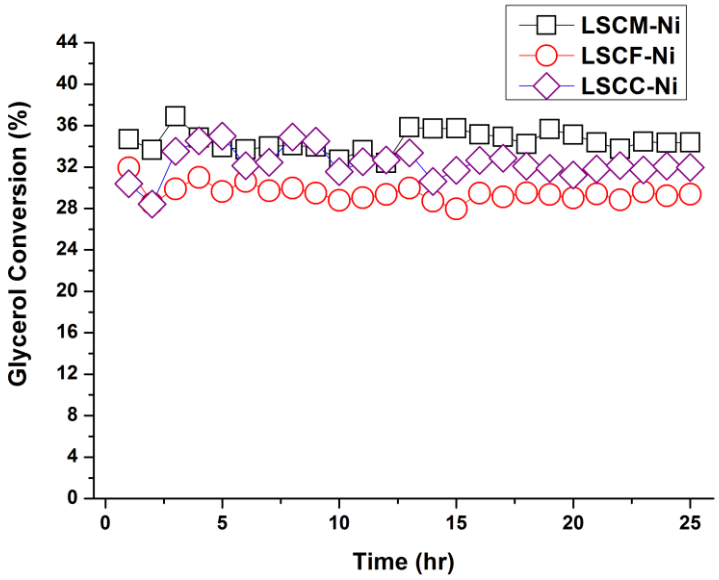

Figure 6-34 Time on stream changes in the activity of the catalyst showing how glycerol conversion changes over time and stability of the nickel substituted catalysts. The test was performed at 700 ^{o}C, S/C ratio of 3 and glycerol molar flow rate of 8.2 x 10^{-5} moles/min and 7.3 x 10^{-4} moles/min of water and WHSV of 28 h^{-1}

The LSCM-Ni incurred about 3% loss of performance followed by LSCC-Ni 10% and LSCF-Ni 13% respectively. Generally the Ni-containing catalysts are the most active and most deactivated therefore less stable. This is because nickel impregnated catalyst systems to attract many reactions and reforming of the decomposition products to their surfaces hence are more susceptible to carbon deposition.

Therefore, the nickel impregnation enhanced hydrogen production without compromising the stability of the catalyst systems.

6.3.1.7 Coke tolerance of $La_{0.75}Sr_{0.25}Cr_{0.5}X_{0.5}O_{3-\delta}$ (X=Mn, Fe and Co) catalyst series and the modified nickel-impregnated derivatives

Steam reforming of feedstock such as glycerol is always followed by deposition of carbonaceous substance on the catalyst surface and pores leading to subsequent catalyst deactivation. This happens because catalyst follows the decomposition-gasification route which is known to favour carbon deposition. With the help of

temperature programmed oxidation, such carbonaceous residues could be characterised. Figure 6-35a-d reflects how the different dopant used in the host chromite-based catalysts and nickel-impregnated catalysts influenced the carbon deposition phenomenon in different reaction conditions. The catalyst test was carried out at 700 ^{o}C at atmospheric pressure. It is evident from Figure 6-35a TGA profile that all the catalyst have remarkably suppressed or almost hindered carbon deposition in steam reforming using pure glycerol but with a slight weight loss due to carbon deposition using by-product glycerol in Figure 6-35b. This is a remarkable improvement compared to what we have seen in previous sections using catalyst from wet impregnation. The weight change is a little more noticeable when steam to carbon ratio less than the stoichiometric amount (1:1) was used as presented in Figure 6-35c. In Figure 6-35c, the Co substituted catalyst had the highest weight loss (around 2%) while the Mn substituted had the least. The increased weight loss observed in Figure 6-35c due to low dilution (S/C 1:1) of glycerol feedstock was expected due to the role of water in oxidation and gasification of carbonaceous species and WGSR[25]. But what is more interesting in the result is that the weight change is less than 2% in all the three scenarios (Figure 6-35a-c) which shows how robust and strong the catalyst systems were in suppressing carbon deposition. Since the extent of the coking suppression among the substituted dopants in the catalyst systems was in the order Mn>Fe>Co, it could be attributed to the oxygen vacancies and non-stoichiometry which allows mobility of oxygen within the lattice for effective oxidation of carbon-containing products. The trend of the carbon suppression is also not unusual since the extent of the oxygen vacancies among the individual dopants follows same order.

Looking at the CO_2 profile in Figure 6-35a and b which indicates the temperature at which bulk of the carbon oxidises, it is clear that carbon oxidation temperatures are same irrespective of whether pure or by-product glycerol was used. This is in agreement with what was observed in section 5.4.3 above using nickel impregnated catalysts. In other words feedstock purity does not affect the nature of the carbon deposited in this case. But is obvious that steam-to-carbon ratio influences the nature of carbon deposited as seen in Figure 6-35c.

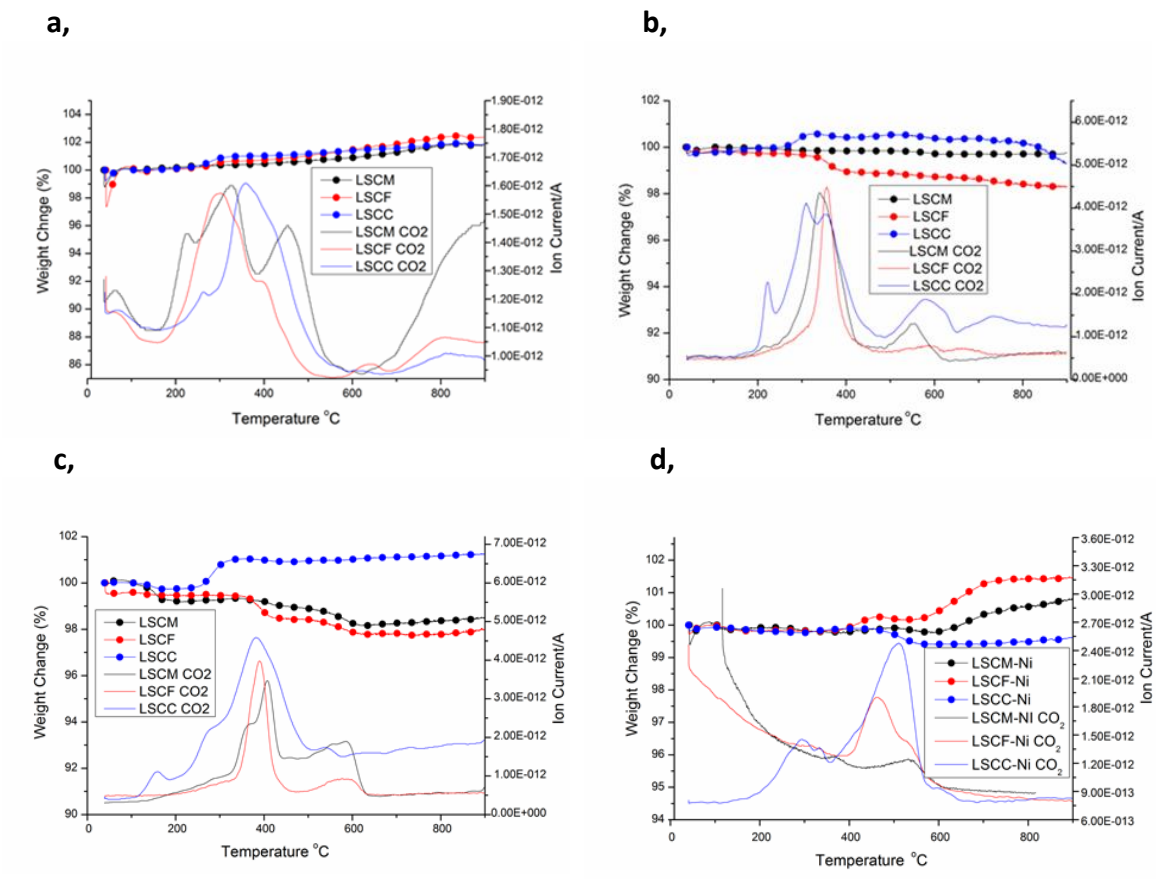

Figure 6-35a-d: Change in weight due to oxidation of carbon from surface of the metal substituted and Ni-impregnated used catalyst samples in oxidising atmosphere monitored in parallel with CO_2 release as a function of temperature. **a,** in pure glycerol (1:3 S/C ratio), **b,** in by-product glycerol (1:3 S/C ratio), **c,** pure glycerol (1:1 S/C ratio) and **d,** Ni-impregnated catalysts on pure glycerol (1:3 S/C ratio)

This is evident where a higher carbon oxidation temperature was found when steam-to-carbon ratio lower than the stoichiometric value was used. Essentially, the carbon oxidation temperature is low (280-350 ^{o}C) using either pure or by-product glycerol which means the carbon is an easy-to-oxidise amorphous carbon deposited on the metal catalyst surface. The carbon becomes polymeric or graphitic which are more difficult to oxidize (400-450 ^{o}C) when the water ratio was lowered. This is a direct reflection of sensitivity of water in oxidation of carbon and WGSR which are known to suppress carbon deposition. It is interesting that impregnation of nickel did not affect the catalyst robust behaviour and ability to suppress carbon deposition as reflected in Figure 6-35d despite the fact that nickel enhances C-C, C-H and C-O scission reactions that are likely to cause severe coking. The highest weight change due to carbon is just about 0.5% in nickel-impregnated Co substituted catalyst using pure glycerol which

indicates strong carbon suppression. It is exciting that carbon oxidation temperature has moved further to high temperature of 450-550 ^{o}C above what was observed in the three scenarios above containing no nickel. This indicates the carbon residues are more graphitic with the nickel containing samples deposited at metal-support interphase. This is typical of nickel containing samples though the oxidation temperature is slightly less than what was observed with the nickel–based catalysts prepared by wet impregnation. This further attests to the enhanced metal-support interaction observed with the exsolved materials compared to those from wet impregnation.

6.4 Lattice defect-constituent-dopant-mediated redox exsolution of oxide-supported nickel nano particles and its influence in glycerol steam reforming

Titanates are very popular materials used as support in catalysis due to their thermal stability and redox properties [5,26]. After the inspirational work by Nishihata et al[27] and Tanaka et al[28] on the intelligent, self-regenerating catalyst, it is important to say the concept of exsolution phenomenon has now been revolutionised by the recent achievements. Irvine et el[6] have demonstrated that B-site exsolution could be achieved preferentially on the outer surface rather than in the bulk and even on the hard-to-reduce cations by tailoring and control of defect chemistry in an A-site deficient precious metal-free titanate-based perovskite. This has in no small measure paved the way for the design of the much desired efficient and cost effective catalysts with robust catalytic properties. This has changed the understanding that exsolution could only be achieved in an A-site stoichiometric perovskite and could only be found preferentially in the bulk rather than on the outer surface and the use of costly precious metals.

In this work, some new non-stoichiometric formulations $(LaM)_{1-\alpha}(ZNi)_xTi_{1-x}O_{3\pm\delta}$ (where M= Ca, Sr, and Ce and Z= Fe, Co and Cr while α was limited to 10-25%) tailored to be A-site deficient involving first-row transition metals were synthesized. The metals doped onto the B-site of an A-site deficient nickel-based titanate perovskite were investigated for the exsolution phenomenon and catalytic behaviour. Varying A-site deficiencies and their influence on the exsolution of B-site cations and catalytic

behaviour in relation to glycerol steam reforming (GSR) were explored. The tolerance and defect accommodation limit of perovskite is also being stretched a little further in one formulation with 25% A-site deficiency which might take the versatility of the perovskite structure a notch higher.

6.4.1 Redox stability of the nickel-based A-site deficient samples by thermo-gravimetric investigation

Thermo-gravimetric analysis of the A-site deficient nickel-based titanates was carried out to understand their thermal and redox stability in both air and hydrogen atmosphere. The result of the test is shown in Figure 6-36a and b. The Figure 6-36a shows the TGA profile of the as prepared samples before reduction in air and hydrogen respectively. The TGA profile has two segments as denoted by the dotted temperature profile. The first segment represents oxidation in air and the second segment is for reduction in hydrogen atmosphere. All the samples as seen in Figure 6-36a are thermally stable in air atmosphere as no evidence of weight gain or loss was observed. In the second segment (reduction in hydrogen), $La_{0.7}Ce_{0.1}Fe_{0.3}Ni_{0.1}Ti_{0.6}O_{3\pm\delta}$ catalyst shows a weight loss of about 1.36% (0.5 mg) in the hydrogen atmosphere. There is also a slight weight loss due to $La_{0.6}Ce_{0.05}Sr_{0.1}Ni_{0.1}Ti_{0.9}O_{3\pm\delta}$. The Co containing sample also showed a slight weight loss of about 0.7% (0.29 mg). It is interesting that all the samples that showed weight loss contain ceria. These weight losses are therefore attributed to oxygen storage-release properties of ceria as no evidence of segregation or decomposition of the A-site deficient perovskite was observed in the XRD pattern of the reduced samples in Figure 6-39.

Figure 6-36b shows the TGA profile of the pre-reduced samples in air and hydrogen respectively. There is a weight gain by same ceria-containing samples in air which is attributable to gain of oxygen by the highly reduced samples. Similar trend of weight loss due to oxygen loss during reduction is evident in the second segment of the TGA profile. The $La_{0.7}Ce_{0.1}Fe_{0.3}Ni_{0.1}Ti_{0.6}O_{3\pm\delta}$ (LCeFeNT) shows a distinct profile in both segments due to its large weight gain of about 2.87% (1.33 mg) and 2.01% (0.72 mg) weight loss. Similarly, $La_{0.7}Ce_{0.1}Co_{0.3}Ni_{0.1}Ti_{0.6}O_{3\pm\delta}$ showed a weight loss of 1.39% (0.64 mg) and gain of 2.60 % (1.19 mg). This might be due to ceria's oxygen storage-release

capacity as corroborated by relatively higher weight gain shown by samples containing ceria compared to non-ceria containing sample.

a,

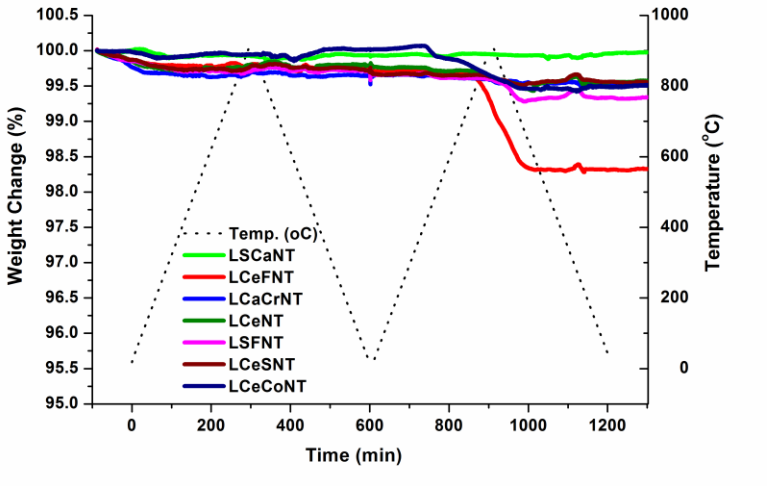

b,

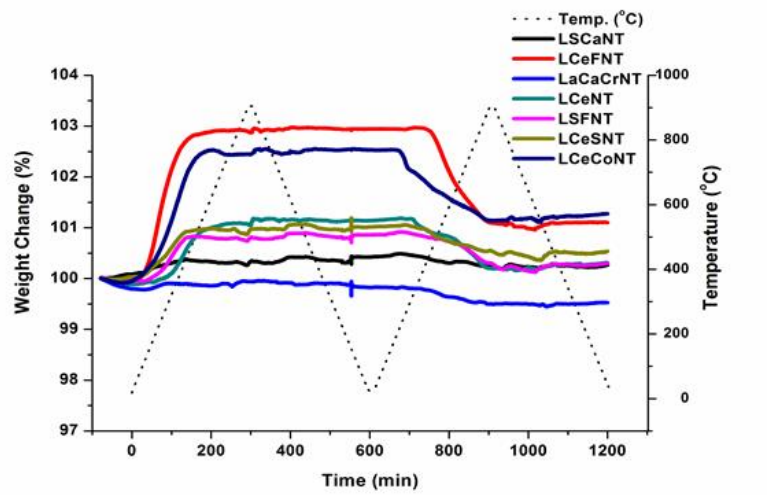

Figure 6-36 Thermo-gravimetric analysis showing redox stability of the samples in air and hydrogen **a,** TGA of the samples before reduction. The first segment as denoted by the dotted line is oxidation in air and the second segment is reduction in hydrogen **b,** TGA of the pre-reduced samples, first in air then in hydrogen as denoted by the dotted line. Generally the ceria containing samples show larger weight change due to ceria's oxygen storage-release properties.

To further strengthened this assertion, it is clear from the TGA profile, amongst the samples doped with ceria, the $La_{0.6}Ce_{0.05}Sr_{0.1}Ni_{0.1}Ti_{0.9}O_{3\pm\delta}$ (LCeSNT) has the lowest amount of ceria (5%) compared to 10% in others therefore showed the lowest weight gain and loss. It is very clear from the XRD pattern of the reduced samples, these weight changes do not translate into segregation or decomposition of those samples

in hydrogen atmosphere but rather to oxygen storage-release properties of ceria. This attests to the structural integrity of these materials. The oxygen storage-release property is an important property that could facilitate or enhance oxidation of glycerol decomposition carbonaceous products on the catalyst surface which would significantly reduce carbon deposition and improve concentration of the desired products.

The weight loss which also partly depicts the reducibility of the nickel-based materials is higher among those that have shown excellent exsolution of metal particles on their surfaces. This implies enhanced metal particle-support interaction and hence higher population of reducible nickel particles.

It is interesting to note the $La_{0.4}Sr_{0.2}Ca_{0.3}Ni_{0.1}Ti_{0.9}O_{3\pm\delta}$ (LSCaNT) and the chromia-doped $La_{0.8}Ca_{0.1}Cr_{0.2}Ni_{0.2}Ti_{0.6}O_{3\pm\delta}$ (LCaCrNT) has demonstrated excellent stability in both atmospheres as evidenced by their straight line-like profile both as prepared and pre-reduced samples. This behaviour might be useful for application as anode materials in SOFC. It will be quite interesting also to see what might be there catalytic behaviour especially suppression of carbon deposition. The behaviour of the chromia-doped sample is not a surprise because chromia-doped samples are known for their high redox stability [16,17]. It is obvious that the constituent dopant metals such as ceria, calcium and strontium influences acidic-basic properties, nickel-support interaction and reducibility of the nickel catalyst in those systems. It is also clear that generally, the titanium oxide-supported nickel particles has a better metal support interaction compared to what was observed with the wet impregnated system and is expected to have same influence on the reducibility of the nickel particles for effective catalytic behaviour as corroborated by the SEM micrograph in Figure 6-45a-f. It is also interesting to note that apart from the dopant influence, A-site deficiency of the samples might have facilitated the oxygen-release-storage properties of the samples due to the defect structure created by the deficiency.

6.4.2 Crystallographic structures

Although stoichiometric structures are the most stable for perovskites, they are highly versatile and flexible when it comes to doping and accommodation of defects. Remarkably, nickel-based titanates with some selected dopants and varying A-site deficiency were successfully synthesized and found to be in single and pure phases as reflected by their XRD patterns displayed in Figure 6-37. Because all the dopant ions used possesses an overall charge less than that of the host titanium ion (Ti^{4+}), the charge difference is compensated by the creation of oxygen valences. As such, the $La_{0.6}Ce_{0.05}Sr_{0.1}Ni_{0.1}Ti_{0.9}O_{3-\delta}$ perovskite was successfully synthesized with 25% (α=0.25) A-site deficiency against the maximum tolerable limit of 20% (α=0.20) A-site deficiency and oxygen vacancies known for $SrTiO_3$-based Perovskites. Interestingly this new material shows a wonderful exsolution of nickel particles dispersed uniformly on its surface as seen in Figure 6-45f. The $La_{0.8}Ce_{0.1}Ni_{0.4}Ti_{0.6}O_{3-\delta}$ perovskite shows many peaks as seen in the XRD pattern compared to other formulations. Indexing of the pattern shows that all the peaks or reflections are due to perovskites as shown in Figure 6-38 below.

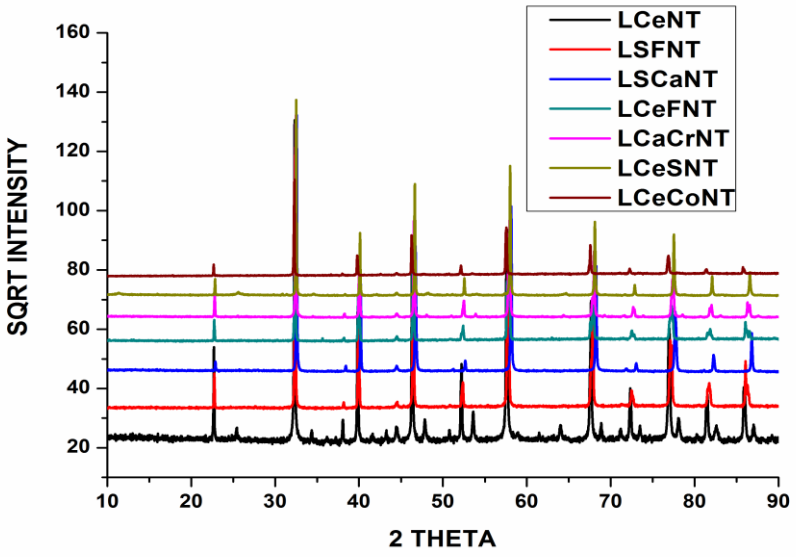

Figure 6-37 The XRD patterns of the synthesized A-site deficient nickel-based titanate perovskites prior to reduction

The Shift in the 2θ position observed in the overlaid patterns is attributable to the size disparity of the dopant ions used and variable structural symmetries exhibited by the samples as confirmed by the refinement data below in Table 6-16.

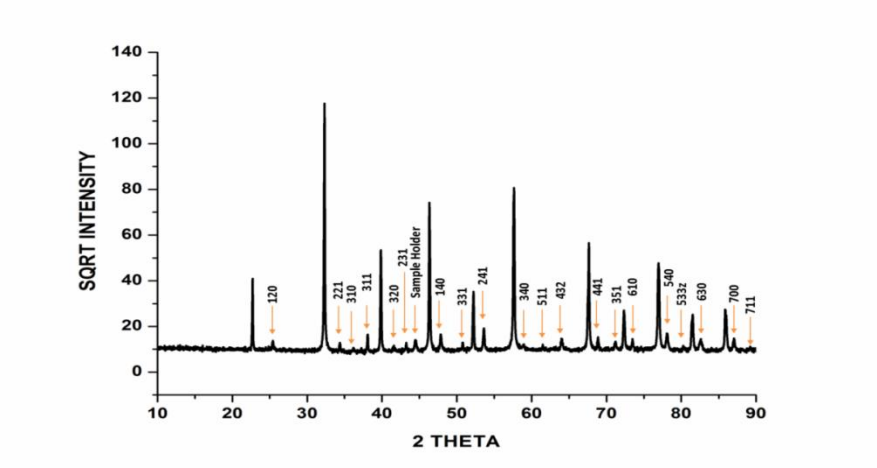

Figure 6-38 showing the XRD Pattern of $La_{0.8}Ce_{0.1}Ni_{0.4}Ti_{0.6}O_{3\pm\delta}$ before reduction showing that all the peaks are due to perovskite structure

The XRD patterns of the reduced samples in Figure 6-39 show that all the samples were quite stable in hydrogen atmosphere and were able to maintain their integrity and perovskite structure after intense reduction for 30 hours at 900 ^{o}C. The reduced samples XRD patterns compared to that of the original samples have some of their minor perovskite peaks disappeared and the splitting of the peaks is also less. This observation is more noticeable with the $La_{0.8}Ce_{0.1}Ni_{0.4}Ti_{0.6}O_{3\pm\delta}$ perovskite which shows less amount of peaks in Figure 6-39 compared to what was observed before reduction in Figure 6-37 above. Comparison of its XRD patterns before and after reduction as shown in Figure 6-40 shows that virtually all the minor perovskite peaks disappeared after reduction and generally, the intensity of the other peaks become smaller. This indicates the reduced materials have moved to high symmetry. There is also a shift to smaller 2θ angles by the reduced sample due to increase in d-spacing as a result of increase in volume of the unit cell. The increase is attributable to the transformation of the smaller Ti^{+4} ions to bigger Ti^{3+} due to electron intake under the influence of reducing atmosphere.

.

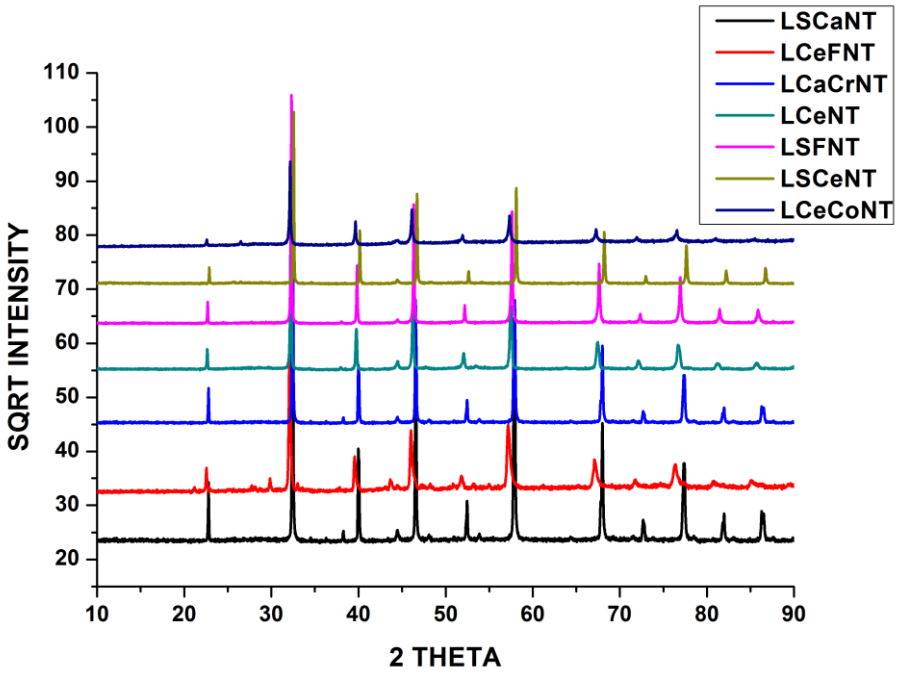

Figure 6-39 XRD pattern of the reduced samples showing them maintain their perovskite structure with no evidence of decomposition or disintegration after reduction for 30 hours

Rietveld refinement of the XRD patterns of the as prepared samples before reduction was carried out and they were found to exhibit different symmetry and space groups as shown in Table 6-16. The lattice parameter 'a' and the cell volume varies reflecting the different dopant and level of defect among them. The refinement was not complete or successful with $La_{0.7}Ce_{0.1}Fe_{0.3}Ni_{0.1}Ti_{0.6}O_{3\pm\delta}$ sample due to the complexity of its structure. After several attempts, the entire space groups proposed for it failed to fit it accurately. The peaks show multiple split that is very uncommon as seen in Figure 6-41.

Table 6-16 Rietveld refinement data of the nickel-based A-site deficient titanates

Catalyst	Space group	Cell Parameter	Cell Volume	Refinement fit parameter
$La_{0.4}Sr_{0.2}Ca_{0.3}Ni_{0.1}Ti_{0.9}O_{3-\delta}$	*I 4 / m c m*	a= 5.4894 b= 5.4894 c= 7.7729	234.22	R_p=8.53, R_{wp}= 10.6, R_{Exp}=11.43, X^2=0.661
$La_{0.7}Ce_{0.1}Fe_{0.3}Ni_{0.1}Ti_{0.6}O_{3-\delta}$	-	-	-	-
$La_{0.8}Ca_{0.1}Cr_{0.2}Ni_{0.2}Ti_{0.6}O_{3-\delta}$	*P b n m*	a= 5.5246 b= 5.0547 c= 7.7836	236.746	R_p=7.24, R_{wp}= 9.69, R_{Exp}=10.93, X^2=0.787
$La_{0.8}Ce_{0.1}Ni_{0.4}Ti_{0.6}O_{3-\delta}$	*P b n m*	a= 5.5452 b= 5.5329	239.992	R_p=6.82, R_{wp}= 9.54, R_{Exp}=12.14,

		c= 7.8221		X^2=0.619
$La_{0.5}Sr_{0.4}Fe_{0.1}Ni_{0.1}Ti_{0.8}O_{3-\delta}$	*I 2/a*	a= 7.8009 b= 5.5387 c= 5.5188	238.454	R_p=11.1, R_{wp}= 15.3, R_{Exp}=10.45, X^2=2.13
$La_{0.6}Ce_{0.05}Sr_{0.1}Ni_{0.1}Ti_{0.9}O_{3-\delta}$	*I 4 / m c m*	a= 5. 5025 b= 5.5025 c= 7.7820	235.622	R_p=10.2, R_{wp}= 13.8, R_{Exp}=7.92, X^2=3.05
$La_{0.7}Ce_{0.1}Co_{0.3}Ni_{0.1}Ti_{0.6}O_{3-\delta}$	*I 2/a*	a= 7.8459 b= 5.5408 c= 5.4007	240.543	R_p=7.24, R_{wp}= 9.54, R_{Exp}=8.54, X^2=1.25

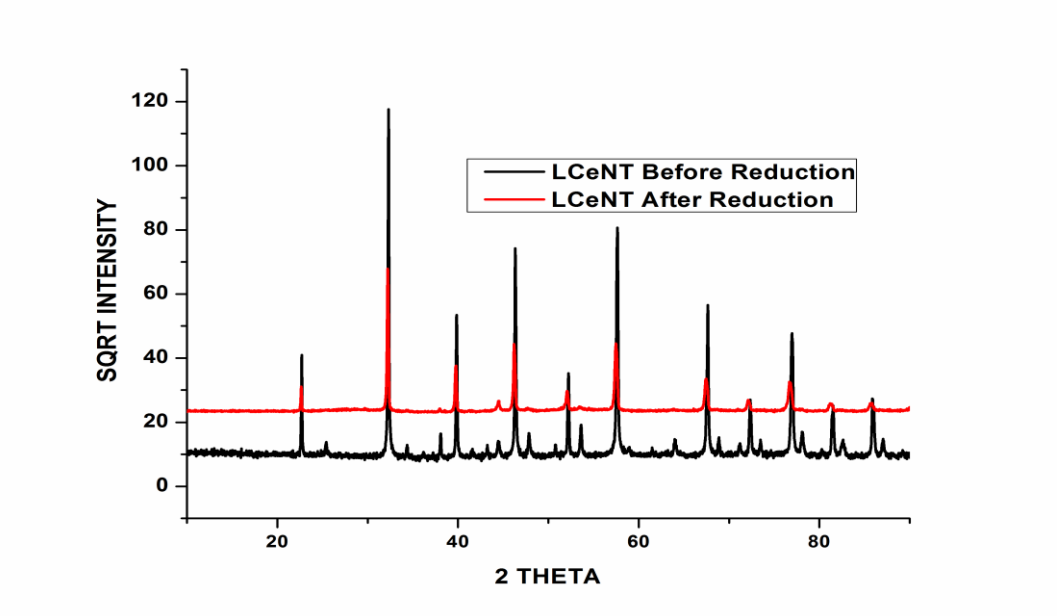

Figure 6-40 Comparing the XRD pattern of $La_{0.8}Ce_{0.1}Ni_{0.4}Ti_{0.6}O_{3\pm\delta}$ before and after reduction showing a slight shift to smaller 2θ angle and peaks disappearance after reduction due to change of symmetry

That was attributed to a possible formation of two perovskites supper imposed in one another and therefore might inform the reason as to why a particular model did not fit it. Generally, the ceria containing samples show slightly a bigger cell volume and cell parameters than the non-ceria-containing samples.

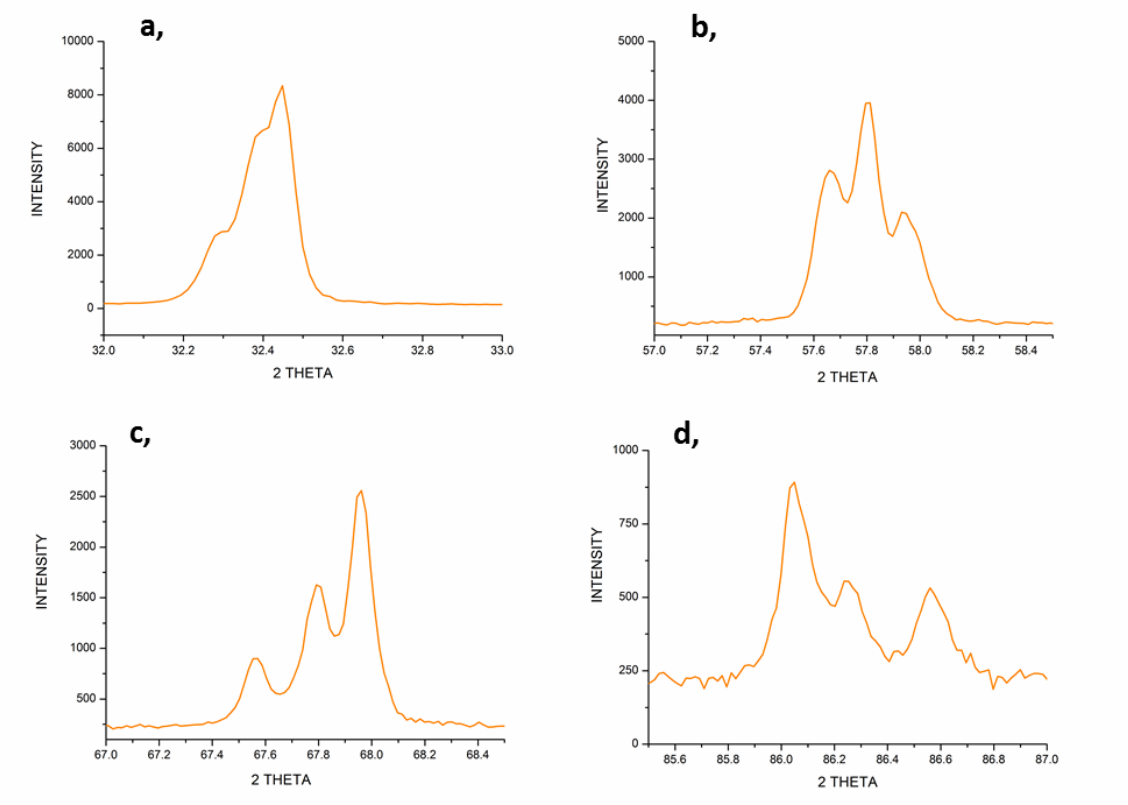

Figure 6-41 Showing peaks with multiple split from the $La_{0.7}Ce_{0.1}Fe_{0.3}Ni_{0.1}Ti_{0.6}O_{3\pm\delta}$ catalyst. The split peaks corresponds to the following hkl values **a,** 220 **b,** 422 **c,** 440 and **d,** 444 respectively

The materials fits all the structural models proposed and octahedral distortions expected from the respective space groups as shown in Figure 6-42 to Figure 6-44 though some have shown refinement fit parameter slightly above 10% as shown in Table 6-16. It is interesting to note that despite their varying defects and dopant cations, some share similarities in their symmetry and distortions. $La_{0.4}Sr_{0.2}Ca_{0.3}Ni_{0.1}Ti_{0.9}O_{3-\delta}$ and $La_{0.6}Ce_{0.05}Sr_{0.1}Ni_{0.1}Ti_{0.9}O_{3-\delta}$ for instance have exhibited the same symmetry and space group *of I4/mc*m despite having Ca and 10% deficiency in the former and Ce doping metals and 25% deficiency in the latter as shown in Figure 6-42a and b.

(a) $La_{0.4}Sr_{0.2}Ca_{0.3}Ni_{0.1}Ti_{0.9}O_{3-\delta}$ *I 4 / mcm* ($a^0a^0c^-$)	Projection along xyz axes	Projection along y axis	Projection along z axis

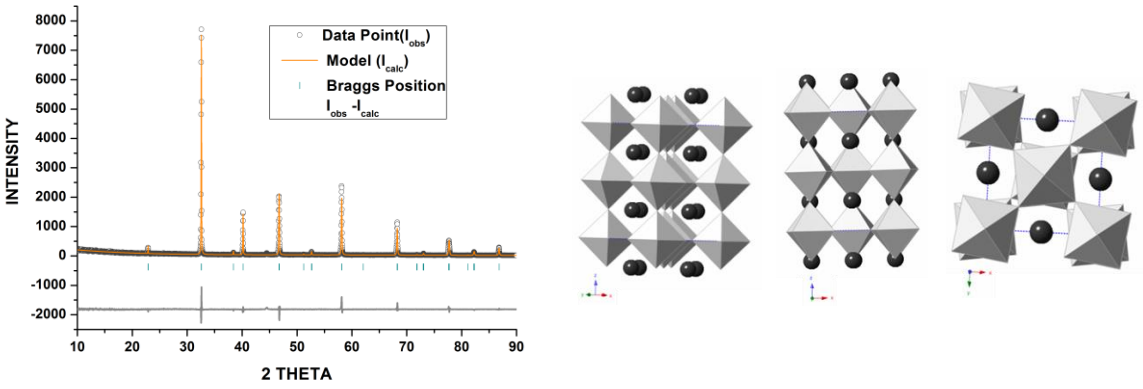

(b) $La_{0.6}Ce_{0.05}Sr_{0.1}Ni_{0.1}Ti_{0.9}O_{3-\delta}$ *I 4 / mcm* ($a^0a^0c^-$)	Projection along xyz axes	Projection along y axis	Projection along z axis

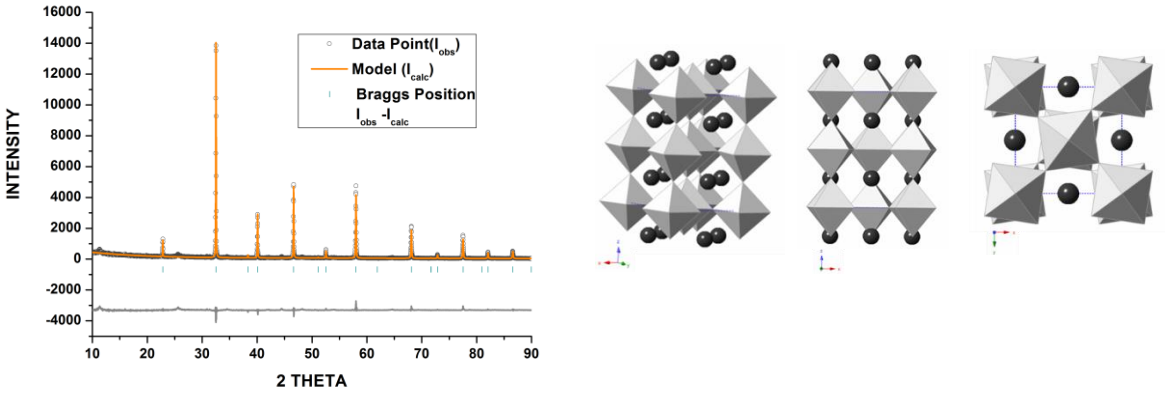

Figure 6-42 showing the fitting of the proposed tetragonal model with the XRD pattern of the materials and the projection of the structure showing out-of-phase tilting along z=axis as the *I4/mcm* space group suggests **a,** in $La_{0.4}Sr_{0.2}Ca_{0.3}Ni_{0.1}Ti_{0.9}O_{3-\delta}$ and **b,** in $La_{0.6}Ce_{0.05}Sr_{0.1}Ni_{0.1}Ti_{0.9}O_{3-\delta}$

Likewise the formulations $La_{0.8}Ca_{0.1}Cr_{0.2}Ni_{0.2}Ti_{0.6}O_{3-\delta}$ and $La_{0.8}Ce_{0.1}Ni_{0.4}Ti_{0.6}O_{3-\delta}$, despite their differences in the A-site dopants, these catalyst systems both shows a good fit with the proposed *P b n m* space group. As the space group suggests and shown in the structural model in Figure 6-43a and b, there is lots of distortions along the entire axis i.e. out-of-phase tilting along the x and y and in-phase tilt along the z axis.

(a)$La_{0.8}Ca_{0.1}Cr_{0.2}Ni_{0.2}Ti_{0.6}O_{3-\delta}$ ***P b n m*** ($a^- a^- c^+$)	Projection along xyz axes	Projection along y axis	Projection along z axis

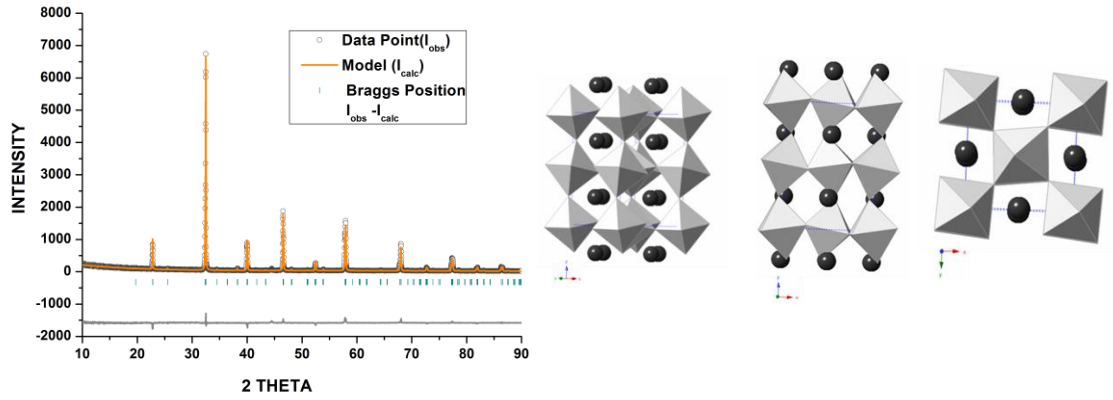

(b) $La_{0.8}Ce_{0.1}Ni_{0.4}Ti_{0.6}O_{3-\delta}$ ***P b n m*** ($a^- a^- c^+$)	Projection along xyz axes	Projection along y axis	Projection along z axis

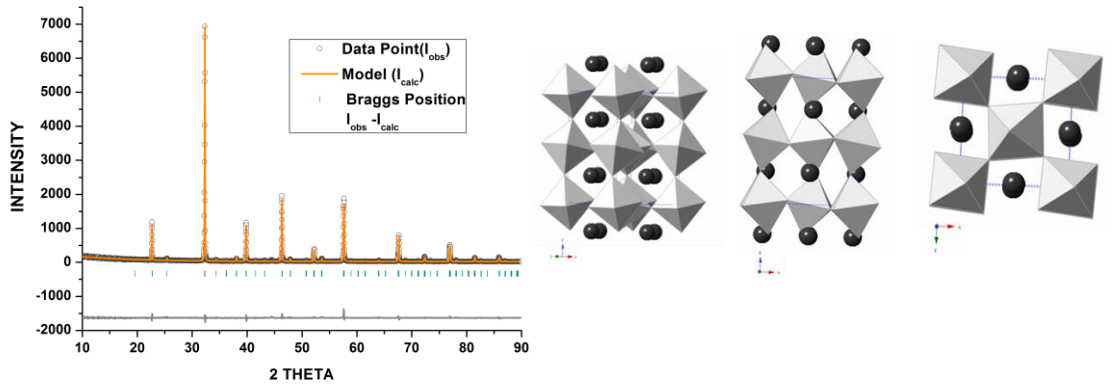

Figure 6-43 showing the fitting of the proposed model with the XRD pattern of the materials and the projection of the structure showing out-of-phase tilting along x and y axis and in-phase tilting along z=axis as the *Pbnm* space group suggests in **a,** $La_{0.8}Ca_{0.1}Cr_{0.2}Ni_{0.2}Ti_{0.6}O_{3-\delta}$ and **b,** in $La_{0.8}Ce_{0.1}Ni_{0.4}Ti_{0.6}O_{3-\delta}$

The catalyst systems $La_{0.5}Sr_{0.4}Fe_{0.1}Ni_{0.1}Ti_{0.8}O_{3-\delta}$ and $La_{0.7}Ce_{0.1}Co_{0.3}Ni_{0.1}Ti_{0.6}O_{3-\delta}$ both conforms to the structure of the space group I 2 / a as seen Figure 6-44a and b respectively. There is significant distortions and out-of-phase tilting along x and y axis and in-phase tilting along z axis as a result of the variations of the dopants ions with respect to that of the host La^{3+} ion.

(a) $La_{0.5}Sr_{0.4}Fe_{0.1}Ni_{0.1}Ti_{0.8}O_{3-\delta}$ *I2 / a* ($a^- a^- c^-$)	Projection along xyz axes	Projection along y axis	Projection along z axis

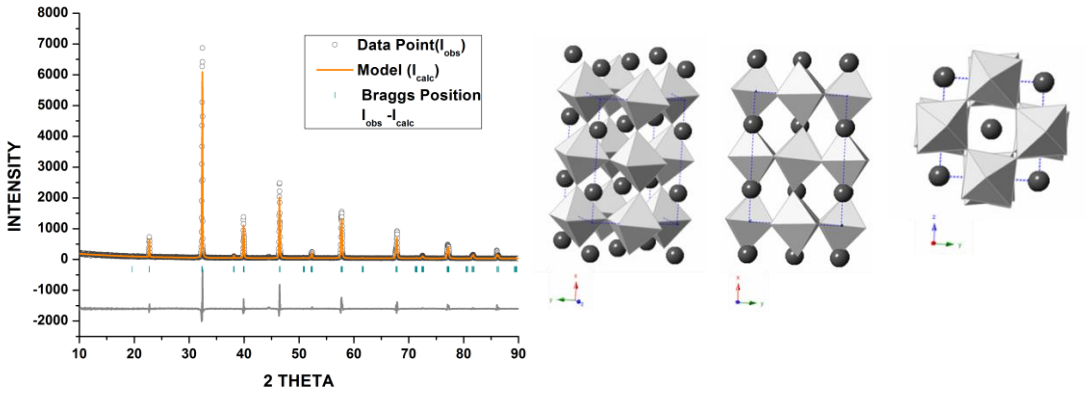

(b)$La_{0.7}Ce_{0.1}Co_{0.3}Ni_{0.1}Ti_{0.6}O_{3-\delta}$ *I2 / a* ($a^- a^- c^-$)	Projection along xyz axes	Projection along y axis	Projection along z axis

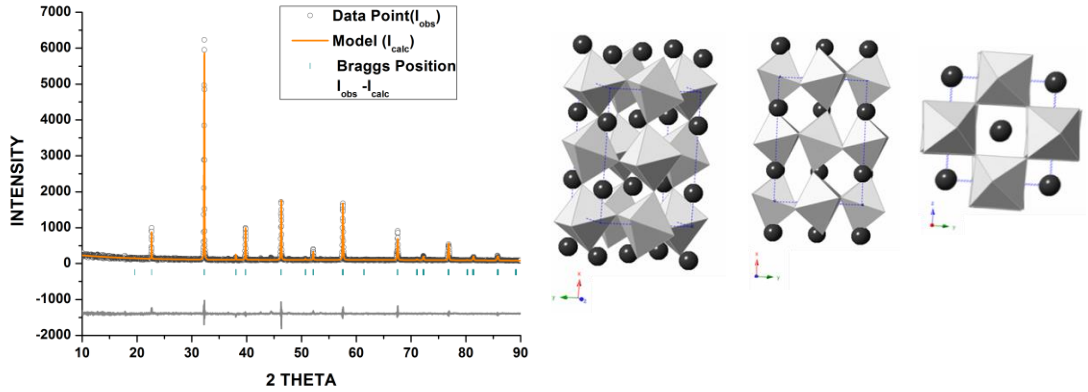

Figure 6-44 showing the fitting of the proposed model with the XRD pattern of the materials and the projection of the structure showing out-of-phase tilting along all the axes axis as the *I2/a* space group suggests in a, $La_{0.5}Sr_{0.4}Fe_{0.1}Ni_{0.1}Ti_{0.8}O_{3-\delta}$ and b, in $La_{0.7}Ce_{0.1}Co_{0.3}Ni_{0.1}Ti_{0.6}O_{3-\delta}$

6.4.3 Physicochemical properties and microstructure

Results of investigation of the surface area of some solid state synthesized nickel-based titanates are shown in Table 6-17. The materials were synthesised at 1430 ^oC and reduced in 5%H_2 at 900 ^oC for 30 hours in a tube furnace. It is clear from the results the surface area of most materials increased after reduction except $La_{0.8}Ce_{0.1}Ni_{0.4}Ti_{0.6}O_{3\pm\delta}$ whose surface area decreased after reduction. This could be attributed to the change in morphology and surface properties after reduction as corroborated by the SEM micrographs in Figure 6-45. The reduction process resulted in nickel particle exposed to the surface and dispersed uniformly across the surface due to exsolution with consequent increase in surface area although the change in

surface area in some samples did not reflect the extent of the observed exsolution in them. In other words the surface area is small in some samples that have shown good exsolution while the surface area is better in some samples that are poorly exsoluted. The ceria-doped samples showed lower surface area compared to those without ceria perhaps due to sintering as results of ceria's low thermal stability. There is no significant direct and consistent correlation observed between the surface area of the materials and the defect due to A-site deficiency. Nevertheless, it is observable that materials or catalyst systems with lower A-site deficiency showed a better surface area compared to those with the higher A-site deficiency relatively.

Table 6-17 Surface area of the samples before and after reduction

Catalyst	Abbreviation	A-Site Deficiency (%)	BET (mg/m^2)	
			Before Reduction	After Reduction
$La_{0.4}Sr_{0.2}Ca_{0.3}Ni_{0.1}Ti_{0.9}O_{3\pm\delta}$	LSCaNT	10	2.8642	8.8172
$La_{0.7}Ce_{0.1}Fe_{0.3}Ni_{0.1}Ti_{0.6}O_{3\pm\delta}$	LCeFNT	20	0.3778	2.6509
$La_{0.8}Ca_{0.1}Cr_{0.2}Ni_{0.2}Ti_{0.6}O_{3\pm\delta}$	LCaCrNT	10	1.9556	4.1757
$La_{0.8}Ce_{0.1}Ni_{0.4}Ti_{0.6}O_{3\pm\delta}$	LCeNT	10	1.3742	1.0886
$La_{0.5}Sr_{0.4}Fe_{0.1}Ni_{0.1}Ti_{0.8}O_{3\pm\delta}$	LSFNT	10	0.660	1.4800
$La_{0.6}Ce_{0.05}Sr_{0.1}Ni_{0.1}Ti_{0.9}O_{3\pm\delta}$	LCeSrNT	25	0.9366	1.0136
$La_{0.7}Ce_{0.1}Co_{0.3}Ni_{0.1}Ti_{0.6}O_{3\pm\delta}$	LCeCoNT	20	1.2671	1.8234

Figure 6-45a-f shows the SEM micrograph of the exsolved materials showing the surface of the materials covered by uniformly distributed oxide-supported metal nano particles grown from the parent perovskite. The dispersed particles are largely nickel with perhaps some possible Ni-Fe or Ni-Co alloys due to exsolution phenomenon. The average size of these particles is about 1µm as seen in the micrograph. It is believed that the surface particles arise due to migration of oxygen ion from the bulk to the surface in response to non-stoichiometry created by abstraction of surface oxygen during the reduction process. Consequently, such instability is balanced by expulsion from the non-defective B-site onto the surface and supported on the titania oxide[6]. The fact that most of the materials have the expelled particles largely on the outer surface rather than in the bulk is likely to be of good advantage to catalysis. Looking at the individual materials it is obvious they respond differently to the reduction process and the B-site exsolution phenomenon. Although such behaviour was related to

defect due to A-site deficiency, it is clear the chemical constituent dopant or metal ions in them also plays an important role. Comparing $La_{0.4}Sr_{0.2}Ca_{0.3}Ni_{0.1}Ti_{0.9}O_{3\pm\delta}$ and $La_{0.6}Ce_{0.05}Sr_{0.1}Ni_{0.1}Ti_{0.9}O_{3\pm\delta}$ for instance, the $La_{0.6}Ce_{0.05}Sr_{0.1}Ni_{0.1}Ti_{0.9}O_{3\pm\delta}$ catalyst system with 25% A-site deficiency was better excluded than the former with only 10% A-site deficiency. Furthermore, the contribution due to the ceria cannot be ignored as corroborated by other samples with such similarity in the formulations. Similarly, $La_{0.7}Ce_{0.1}Fe_{0.3}Ni_{0.1}Ti_{0.6}O_{3\pm\delta}$ and $La_{0.5}Sr_{0.4}Fe_{0.1}Ni_{0.1}Ti_{0.8}O_{3\pm\delta}$ also showed same behaviour due to the combine influences of A-site deficiency and constituent dopant. More so, it is more than a coincidence that all the four samples containing ceria (a, d, f and g) have shown excellent exsolution and uniform dispersion of B-site cations compared to non- ceria containing materials (b, c and e) that were poorly exsoluted. Therefore, A-site deficiency and constituent dopant could be tailored to transform surface morphology for effective metal particle exsolution and distribution for efficient catalyst activity or behaviour. Furthermore, the $La_{0.6}Ce_{0.05}Sr_{0.1}Ni_{0.1}Ti_{0.9}O_{3\pm\delta}$ with the 25% A-site deficiency, apart from exhibiting excellent exsolution behaviour, the TGA analysis of the sample before and after reduction as seen in Figure 6-36 has confirmed the relative redox stability of this sample as no evidence of possible decomposition or rather segregation was noticed on the TGA profile. The observation is corroborated by the XRD pattern of the sample after reduction as seen in Figure 6-39 below. This is against the consequent decomposition or segregation of the constituent atom that happens when the limit of deficiency or excess is exceeded. This goes to show that the deficiency or excess could be stretched without affecting the structural integrity of the sample provided the right constituent dopants tolerant of that situation are selected. Although the reason for the relative stability in this case is not yet fully ascertained, it might have been enhanced perhaps by the combined influence of ceria and strontium dopants.

a, $La_{0.8}Ce_{0.1}Ni_{0.4}Ti_{0.6}O_{3\pm\delta}$

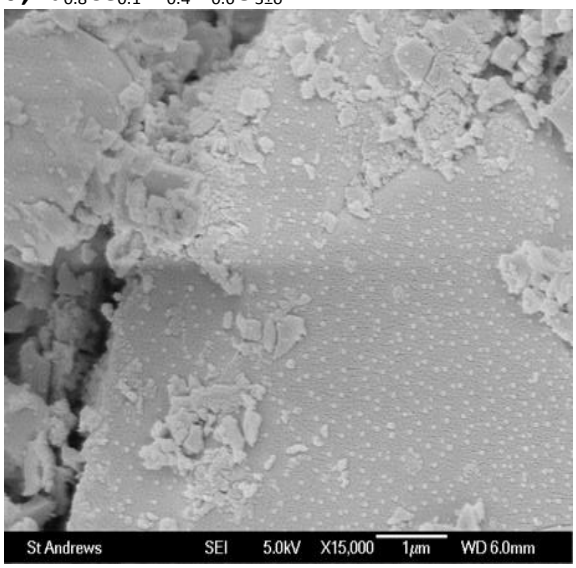

b, $La_{0.5}Sr_{0.4}Fe_{0.1}Ni_{0.1}Ti_{0.8}O_{3\pm\delta}$

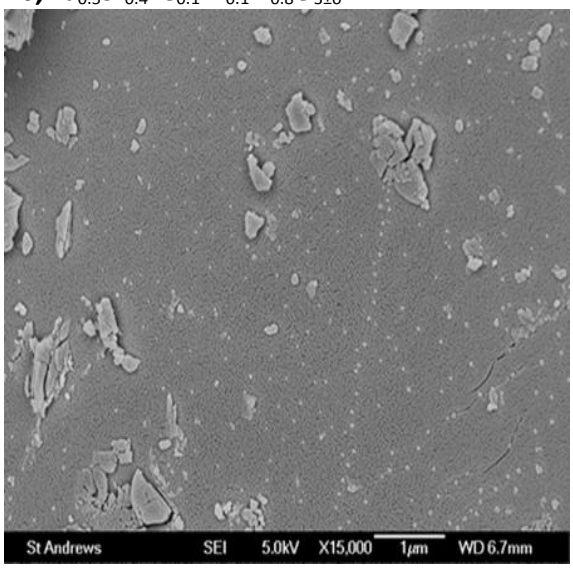

c, $La_{0.4}Sr_{0.2}Ca_{0.3}Ni_{0.1}Ti_{0.9}O_{3\pm\delta}$,

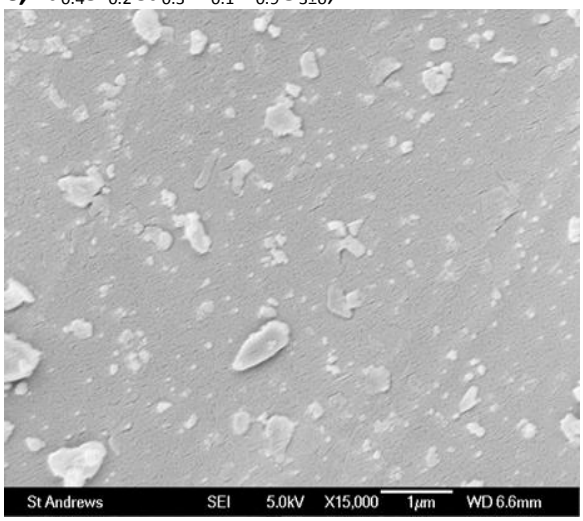

d, $La_{0.7}Ce_{0.1}Fe_{0.3}Ni_{0.1}Ti_{0.6}O_{3\pm\delta}$

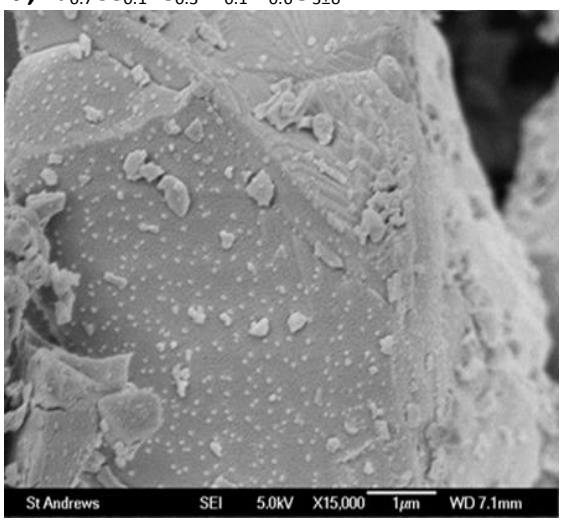

e, $La_{0.8}Ca_{0.1}Cr_{0.2}Ni_{0.2}Ti_{0.6}O_{3\pm\delta}$

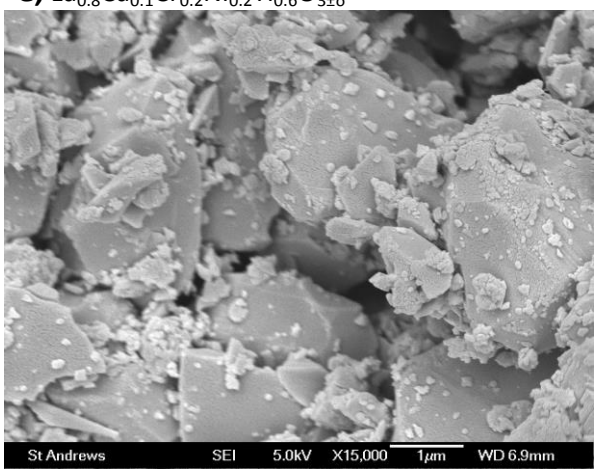

f, $La_{0.6}Ce_{0.05}Sr_{0.1}Ni_{0.1}Ti_{0.9}O_{3\pm\delta}$

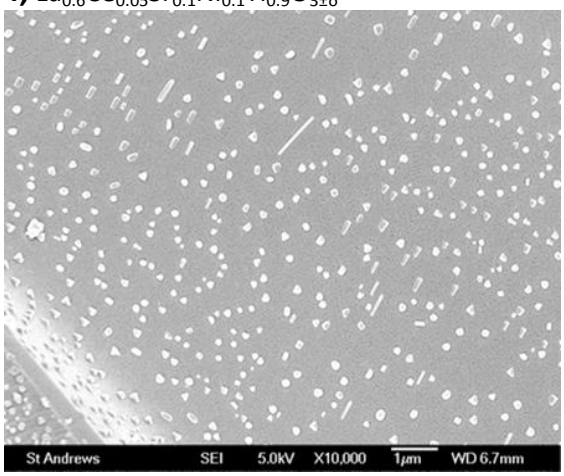

g, $La_{0.7}Ce_{0.1}Co_{0.3}Ni_{0.1}Ti_{0.6}O_{3\pm\delta}$

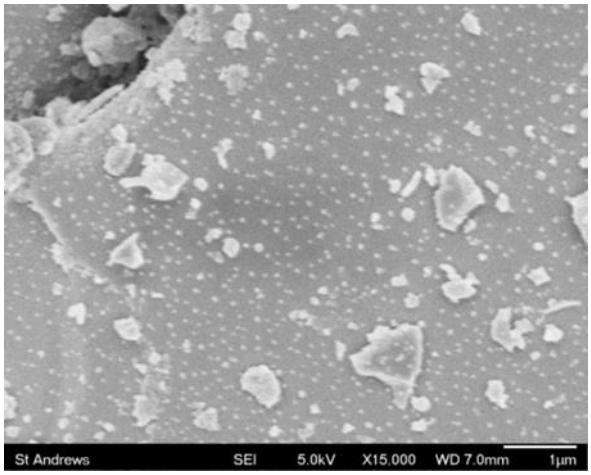

Figure 6-45 Micrograph of the A-site deficient titanates showing exsolved metal particles in **a,** $La_{0.8}Ce_{0.1}Ni_{0.4}Ti_{0.6}O_{3\pm\delta}$ **b**, $La_{0.5}Sr_{0.4}Fe_{0.1}Ni_{0.1}Ti_{0.8}O_{3\pm\delta}$ **c,** $La_{0.4}Sr_{0.2}Ca_{0.3}Ni_{0.1}Ti_{0.9}O_{3\pm\delta}$, **d,** $La_{0.7}Ce_{0.1}Fe_{0.3}Ni_{0.1}Ti_{0.6}O_{3\pm\delta}$ **e,** $La_{0.8}Ca_{0.1}Cr_{0.2}Ni_{0.2}Ti_{0.6}O_{3\pm\delta}$ **f,** $La_{0.6}Ce_{0.05}Sr_{0.1}Ni_{0.1}Ti_{0.9}O_{3\pm\delta}$ **g,** $La_{0.7}Ce_{0.1}Co_{0.3}Ni_{0.1}Ti_{0.6}O_{3\pm\delta}$

6.4.4 Lattice defect chemistry, exsolution and catalytic behaviour of the nickel-based A-site deficient titanate catalyst systems in glycerol steam reforming

Catalytic behaviour of the materials was evaluated at 700 ^{o}C using pure glycerol at atmospheric pressure and steam-to-carbon ratio of 3 on 50mg of the catalyst. 2.60 x 10^{-4} mole/min molar flow rate of glycerol-water solution was used and WHSV of 28 h^{-1}.The result of the screening test is as reported in Figure 6-46 and Table 6-18 and 6-19. The Figure 4-46 shows products generated from the test in mole per mole of glycerol fed to the reactor. It is evident the catalysts are active and selective to the only gaseous products H_2, CH_4, CO and CO_2 detected during the steam reforming of glycerol. The products distribution shows that H_2 and CO are the predominant gases with all the catalyst systems. The H_2/CO_2, H_2/CO ratios and hydrogen produced per mole of glycerol analysis of Table 6-18 and high CO selectivity relatively of Table 6-19 all attests to these observations. In Table 6-18, the H_2/CO_2 ratio shows a higher value than H_2/CO. This suggests more CO was generated perhaps facilitated by the catalyst effective gasification and oxidation of the glycerol decomposition carbonaceous products as well as via reactions such as reverse WGSR and glycerol rapid pyrolysis due to kinetics and nickel contents. Those reactions are known to produce CO as seen

in Eqn. 2-13 to 2-18 as well as Eqn. 2-6 and 2-3 respectively. This is corroborated by their excellent carbon deposition suppression reported in Figure 6-49 as well as the comparison of the products ratios and hydrogen produced per mole of glycerol with equilibrium composition in Table 6-18. What is also common to all the catalyst systems is their propensity for gaseous CO_2. The CO_2, H_2 yield and selectivity as seen in Table 6-18 might be partly due to water-gas-shift reaction most probably due to their nickel content. Though not much hydrogen production and selectivity was achieved compared to what we have seen with samples prepared by wet impregnation, redox lattice rearrangement and combustion methods, the samples shows support for WGSR. The factors that might have contributed to the low hydrogen production could be method of preparation, surface area and perhaps the reduction process. It is also clear that the H_2 production was also limited by the reverse WGSR which the catalysts systems seem to favour. Reactions that lead to formation of acrolein and perhaps carbonyl compounds would have also reduced the hydrogen yield. Too much throughput due low catalyst bed thickness and contact time also contributed to the low yield. Nonetheless, the catalysts could be quite useful for syngas production.

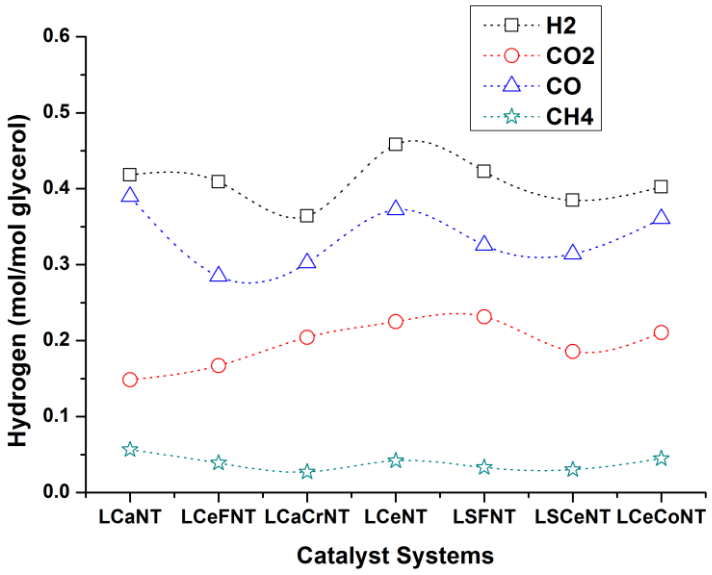

Figure 6-46 products distribution in mol/mol glycerol against the respective catalyst systems. The test was carried out at 700 ^{o}C, S/C ratio of 3 and glycerol molar flow rate of 8.2 x 10^{-5} moles/min and 7.3 x 10^{-4} moles/min of water and WHSV of 28 h^{-1}

The hydrogen produced was within 6-8% of the equilibrium composition as seen in Figure 6-46 while the CO is 29-39% of the equilibrium composition (see Table 2A-2 of appendix 2). Other gaseous products such as CO_2 and CH_4 are also within 8-12% and 28-40 % of the equilibrium composition respectively.

The catalyst systems were further analysed for activity by considering products in mole/min in comparison with glycerol conversion as shown in Figure 6-47. Glycerol conversion to gaseous products >17% was achieved with all the samples and glycerol conversion ≥20% was recorded with four of those sample i.e. $La_{0.8}Ce_{0.1}Ni_{0.4}Ti_{0.6}O_{3\pm\delta}$ (LCeNT), $La_{0.4}Sr_{0.2}Ca_{0.3}Ni_{0.1}Ti_{0.9}O_{3\pm\delta}$ (LSCaNT), $La_{0.7}Ce_{0.1}Co_{0.3}Ni_{0.1}Ti_{0.6}O_{3\pm\delta}$ (LCeCoNT) and $La_{0.5}Sr_{0.4}Fe_{0.1}Ni_{0.1}Ti_{0.8}O_{3\pm\delta}$ (LSFNT). The COx selectivity of the samples in Table 6-19 has further strengthened the extent of steam reforming achieved with these samples as most of them achieved COx selectivity of 0.2 which is very reasonable considering the amount of catalyst used for the catalytic test and low contact time due small catalyst bed.

Table 6-18 Comparison of products from the experiment with equilibrium composition based on glycerol pyrolysis

	Temp. (°C)	Conv.= Conversion (C basis)	H_g= H_2/Glyc. (mol/mol)	H_g/Conv.	H_2/CO	H_2/CO_2
Equilibrium	700	-	6.0	-	6.00	3.00
$La_{0.4}Sr_{0.2}Ca_{0.3}Ni_{0.1}Ti_{0.9}O_{3\pm\delta}$	700	0.20	0.42	2.10	1.07	2.82
$La_{0.7}Ce_{0.1}Fe_{0.3}Ni_{0.1}Ti_{0.6}O_{3\pm\delta}$	700	0.17	0.41	2.41	1.44	2.45
$La_{0.8}Ca_{0.1}Cr_{0.2}Ni_{0.2}Ti_{0.6}O_{3\pm\delta}$	700	0.18	0.36	2.00	1.21	1.78
$La_{0.8}Ce_{0.1}Ni_{0.4}Ti_{0.6}O_{3\pm\delta}$	700	0.21	0.46	2.19	1.23	2.04
$La_{0.5}Sr_{0.4}Fe_{0.1}Ni_{0.1}Ti_{0.8}O_{3\pm\delta}$	700	0.20	0.42	2.10	1.30	1.83
$La_{0.6}Ce_{0.05}Sr_{0.1}Ni_{0.1}Ti_{0.9}O_{3\pm\delta}$	700	0.18	0.39	2.17	1.23	2.07
$La_{0.7}Ce_{0.1}Co_{0.3}Ni_{0.1}Ti_{0.6}O_{3\pm\delta}$	700	0.21	0.40	1.91	1.12	1.91

It is actually very difficult from this test to correlate defect due to A-site deficiency to the observed performance of the catalysts conclusively. But what is understood is that the high CO gas generated virtually with all the catalyst systems could be attributed to enhanced oxidation of the carbon containing residues by the catalyst due to good oxygen mobility in them as a results of their defect due to A-site deficiency. It is observable that those catalysts with the deficiency of 20% and above gave the least

performance except the LCeCoNT. Therefore it seems better to be moderate rather than to overstretch the deficiency or excess limit.

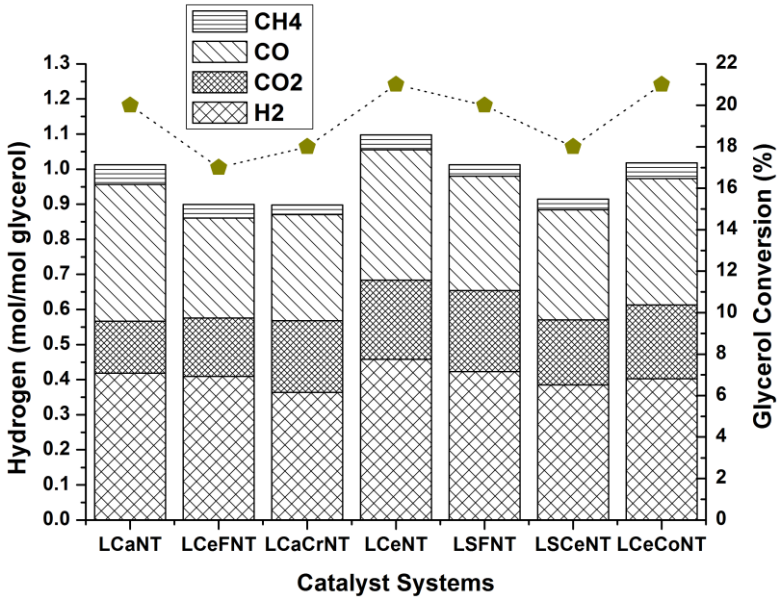

Figure 6-47 Catalyst performance evaluation showing catalytic activity as amount of reformate produced and glycerol conversion to gaseous products. The test was carried out at 700 ^{o}C, S/C ratio of 3 and glycerol molar flow rate of 8.2 x 10^{-5} moles/min and 7.3 x 10^{-4} moles/min of water and WHSV of 28 h^{-1}

While the other samples were prepared by solution and combustion method, these samples were prepared by solid state method. Generally all the samples recorded hydrogen selectivity of >20% and CO selectivity >50% attributable to acidic-basic as well as oxygen storage-release properties of ceria and strong basic behaviour of Sr and Ca which are known to enhance gasification and oxidation of carbon containing residues.

Table 6-19 Catalytic performance characteristics of the catalyst materials

Catalyst	Lattice Defect (%)	H_2 Selectivity (%)	CO Selectivity (%)	Glycerol Conversion (%)	COx Selectivity (%)
$La_{0.4}Sr_{0.2}Ca_{0.3}Ni_{0.1}Ti_{0.9}O_{3\pm\delta}$	10	30	66	20	0.18
$La_{0.7}Ce_{0.1}Fe_{0.3}Ni_{0.1}Ti_{0.6}O_{3\pm\delta}$	20	36	58	17	0.15
$La_{0.8}Ca_{0.1}Cr_{0.2}Ni_{0.2}Ti_{0.6}O_{3\pm\delta}$	10	29	57	18	0.17
$La_{0.8}Ce_{0.1}Ni_{0.4}Ti_{0.6}O_{3\pm\delta}$	10	31	58	21	0.20
$La_{0.5}Sr_{0.4}Fe_{0.1}Ni_{0.1}Ti_{0.8}O_{3\pm\delta}$	10	31	55	20	0.19
$La_{0.6}Ce_{0.05}Sr_{0.1}Ni_{0.1}Ti_{0.9}O_{3\pm\delta}$	25	31	59	18	0.17
$La_{0.7}Ce_{0.1}Co_{0.3}Ni_{0.1}Ti_{0.6}O_{3\pm\delta}$	20	28	59	21	0.19

Therefore defect chemistry and both A-site and B-site metal doping could be tailored to enhance B-site metal catalyst cation exsolution for effective gasification and reforming of glycerol decomposition production for syngas production.

6.4.5 Time on stream and stability testing

The Stability of the samples to deactivation from agents of catalyst deactivation such carbon deposition, sintering or catalyst poisoning due to prolonged usage was investigated by monitoring glycerol conversion as well as hydrogen production per mole of glycerol over time for 10 hours. The test was performed at 700 ^{o}C using continuous flow of pure glycerol-water mixture at 2.60 x 10^{-4} mol/min of steam-to-carbon ratio of 3:1 at atmospheric pressure and WHSV of 28 h^{-1}. The result obtained is as shown in Figure 6-48a and b respectively. The catalyst systems have shown remarkable resistance to catalyst deactivation as no evidence of serious loss of performance was recorded. The $La_{0.7}Ce_{0.1}Fe_{0.3}Ni_{0.1}Ti_{0.6}O_{3\pm\delta}$ catalyst performance stood out among all the catalyst with the highest loss of performance. This clearly reflects the same behaviour by same catalyst in the TGA analysis in section 6.4.1. Despite its ceria content which is known for oxidation of carbonaceous products due to their oxygen storage-release properties, the catalyst showed greater tendency to deactivation relatively. This is attributable to possible segregation or decomposition after reduction though not quite visible from the XRD pattern of the reduced sample in Figure 6-39 above which might have affects its integrity as perovskite. What is remarkable about the entire catalysts is that they had almost maintained the same performance throughout the duration of the test though $La_{0.6}Ce_{0.05}Sr_{0.1}Ni_{0.1}Ti_{0.9}O_{3\pm\delta}$ perovskite with the 25 % deficiency behaved a little bit differently. Despite its convoluted performance, the $La_{0.6}Ce_{0.05}Sr_{0.1}Ni_{0.1}Ti_{0.9}O_{3\pm\delta}$ catalyst was also stable.

Hydrogen production per mole of glycerol also shows some stability over time. The $La_{0.8}Ce_{0.1}Ni_{0.4}Ti_{0.6}O_{3\pm\delta}$ and $La_{0.5}Sr_{0.4}Fe_{0.1}Ni_{0.1}Ti_{0.8}O_{3\pm\delta}$ despite their initial good performance, the hydrogen yield reduced rapidly within the first few hours before stabilizing. Both $La_{0.7}Ce_{0.1}Fe_{0.3}Ni_{0.1}Ti_{0.6}O_{3\pm\delta}$ and $La_{0.6}Ce_{0.05}Sr_{0.1}Ni_{0.1}Ti_{0.9}O_{3\pm\delta}$ also seem to show similar behaviour. The drop in hydrogen could be as a result of the much activity they attracted to their surfaces as corroborated by weight loss recorded for the used

catalysts in section 6.4.6. Generally, the hydrogen production seems fairly stable with other catalyst systems over time.

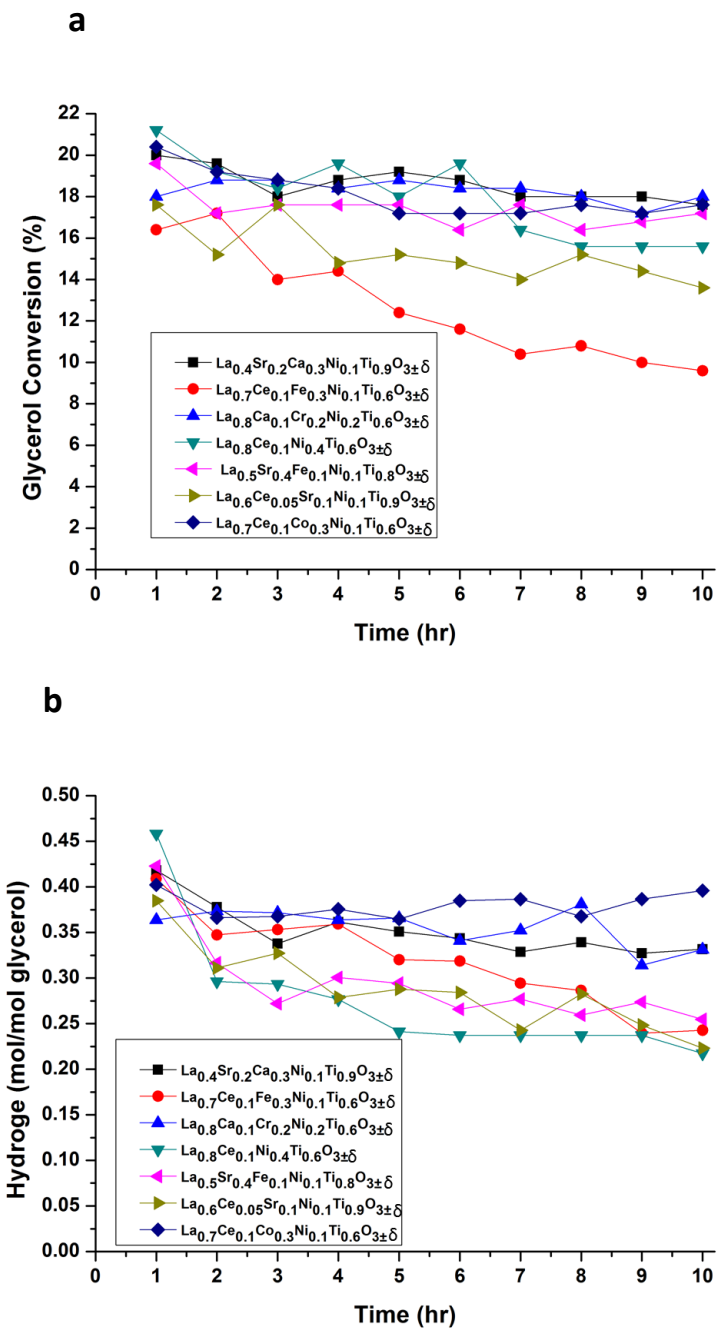

Figure 6-48 Time on stream (TOS) test showing how glycerol conversion changes over time and stability of the materials. The test carried out at temperatures of 700^{o}C, S/C ratio of 3 and glycerol molar flow rate of 8.2 x 10^{-5} moles/min and 7.3 x 10^{-4} moles/min of water and WHSV of 28 h^{-1}

What is common to all catalyst systems investigated is their A-site deficiency, it is believed that defect structures enhance oxygen ion mobility which facilitate oxidation of carbonaceous decomposition products from glycerol pyrolysis and consequently

hinder deactivation by coking activity. It is interesting to note in this regard that having A-site deficiency of 10% or stretching it to the maximum of 20% or even beyond (25%) does not seem to have negative consequences on the stability of the catalyst. This can be proved comparing the performance of the two samples with 20 % A-site deficiencies. Although $La_{0.7}Ce_{0.1}Fe_{0.3}Ni_{0.1}Ti_{0.6}O_{3\pm\delta}$ with 20 % A-site deficiencies had the worst performance, $La_{0.7}Ce_{0.1}Co_{0.3}Ni_{0.1}Ti_{0.6}O_{3\pm\delta}$ was one of the best performing catalyst which also has the same 20 % A-site deficiency. The disparity between them could relate to their constituent chemical species or dopants. Moreover, both showed good exsolution in their microstructure. Therefore, the possible reason as to why $La_{0.7}Ce_{0.1}Co_{0.3}Ni_{0.1}Ti_{0.6}O_{3\pm\delta}$ was found catalytically more active than $La_{0.7}Ce_{0.1}Fe_{0.3}Ni_{0.1}Ti_{0.6}O_{3\pm\delta}$ could be their difference in chemical constituent. Consequently, suffice it to say defect chemistry and constituent metals or dopants could play an important role in tailoring perovskite structures for better catalytic behaviour.

6.4.6 Lattice defect chemistry, exsolution and carbon deposition in glycerol steam reforming

To investigate possible coking activity or carbon deposition during the steam reforming on the catalyst surfaces, the used catalysts after ten hours of reforming were subjected to temperature programmed oxidation in oxygen atmosphere. The carbon deposited on the catalyst surface was characterised completely by identifying their nature or type, location and extent of the coking by the temperature programmed oxidation. The TGA profile in Figure 6-49 represents the extent of carbon deposition whilst the CO_2 peaks indicates the temperature at which bulk of the carbon oxidised which depends on the nature and location of the carbon on the catalyst surface.

Interestingly, it is evident from the gentle weight loss in the TGA profile that all the catalyst effectively suppressed carbon deposition and had only a mild coking. The $La_{0.6}Ce_{0.05}Sr_{0.1}Ni_{0.1}Ti_{0.9}O_{3\pm\delta}$ and $La_{0.8}Ce_{0.1}Ni_{0.4}Ti_{0.6}O_{3\pm\delta}$ recorded the highest weight loss of 3.56% (0.72mg) and 2.80% (0.99 mg) respectively. This attributable to their populated nickel surfaces due to the excellent exsolution they exhibited which attracts a lot of surface reactions hence more tendencies for coking. The corresponding CO_2

peaks due to the entire catalyst show bulk of the coke was oxidised at intermediate temperature (550-600 ^{o}C) which depicts polymeric or graphitic carbon deposited at metal-support interphase.

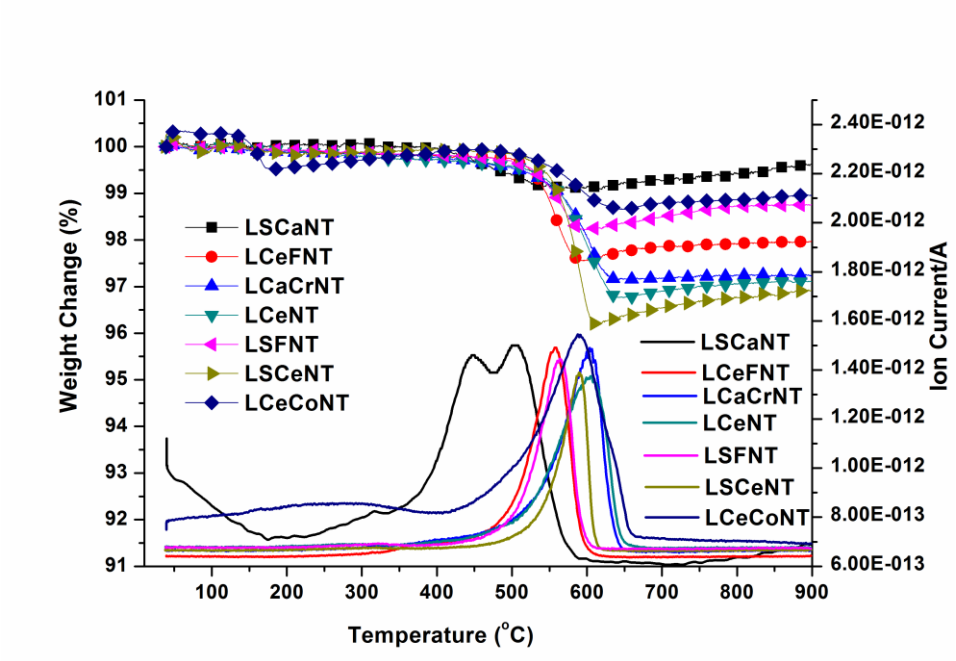

Figure 6-49 Change in weight due to oxidation of carbon from surface of the metal substituted A-site deficient titanate perovskite used catalyst samples in oxidising atmosphere monitored in parallel with CO_2 as a function of temperature. The CO2 peak indicate the temperature at which carbon oxidised which depends on the nature and location of the carbon whilst the TGA profile shows the extent of coking

Generally, titinates are known for their stability and redox property which enhances oxidation of carbonaceous chemical species from glycerol decomposition on the catalyst surface. The constituent dopants were also carefully selected and tailored as A-site deficient to facilitate oxidation of carbon containing products to limit carbon deposition. Furthermore, oxides of Ce, Ca and Sr increase the basic property of the materials which is an important property in oxidation of carbonaceous products that could cause carbon deposition. The ceria's redox property and its oxygen storage-release property was an added advantage to some of the materials. Although is difficult to discern amongst the catalysts system any correlation between the coking activity and A-site deficiency or defect, it is believed the defect enhances oxygen mobility in the lattice which facilitates oxidation of the carbonaceous products and therefore limits carbon deposition. The $La_{0.4}Sr_{0.2}Ca_{0.3}Ni_{0.1}Ti_{0.9}O_{3\pm\delta}$ titinate stood out

among them by almost completely hindering carbon deposition perhaps due to its strong basic character attributed to the strongly basic alkaline earth metal Ca and Sr dopants in it. The nature and location of its carbon was also different relatively. Its carbon was oxidised at lower temperature (400-500 ^{o}C) which depicts an easy-to-oxidise amorphous carbon deposited on the catalyst metal surface.

6.5 Conclusions

Redox lattice reorganisation and Redox exsolution phenomena were successfully demonstrated in the preparation of oxide-supported nickel-based catalyst in spinel and proveskites oxides respectively for utilisation in glycerol steam reforming.

In this new phenomenon called redox lattice reorganiaton, catalyst metal particle size on the surface, population and extent of dispersion as well the size of the micro channels could be tailored for effective catalyst activity by careful choice of reduction temperature. The population of the reduced metal catalysts on the surface was also found to be related to the mobility of the catalyst particle across the bulk to the surface. The mobility differs from one metal to another as shown by the nickel and only iron containing catalysts respectively. The mobility of the particles was also influenced by the reduction temperature. All the catalyst systems were found to be active in steam reforming of both pure and by-product glycerol and carbon deposition was almost hindered. Hydrogen selectivity was significantly enhanced with the nickel substituted derivatives.

B-site metal doping and substitution with transition metals in a chromite based perovskite $La_{0.75}Sr_{0.25}Cr_{0.5}X_{0.5}O_{3\pm\delta}$ (X=Mn, Fe and Co) catalysts had significant influence on structural and catalytic properties of the material in steam reforming of pure and by-product glycerol. It also influences the catalyst ability to suppress coking. All the catalyst systems were found active and selective with Fe-substituted catalyst slightly more active. Hydrogen production per mole of glycerol and coke suppression was better with the Mn-substituted catalyst which was also structurally more stable in fuel environment. Impregnation of Ni into the lattice structures of the pre-reacted both A-site and B-site stoichiometric catalysts by reaction with nickel nitrate solution have modified the systems. The subsequent redox exsolution of Ni nano particles supported

on the oxide surface of the materials has significantly improved the hydrogen production by enhancing glycerol decomposition and WGSR. Thermo gravimetric analysis and SEM revealed that metal-support interaction and reducibility of the Ni-impregnated catalysts was better than what was observed with nickel supported catalysts prepared by wet impregnation. Moreover, exsolution was achieved preferentially on the surface with Mn and Co substituted stoichiometric perovskite catalyst as compared to Fe substituted catalyst whose exsolution perhaps was more in the bulk.

The titanate perovskites $(LaM)_{1-\alpha}(ZNi)_xTi_{1-x}O_{3\pm\delta}$ (where M= Ca, Sr, and Ce and Z= Fe, Co and Cr while α was limited to 10-25%) tailored to be A-site deficient were successfully synthesised. The work revealed that A-site deficiency can be tailored by using suitable constituent metals or dopants to enhance B-site exsolution and improve catalytic activity. All the materials have exhibited some varying degree of exsolution of B-site metal nano particles consisting of Ni and possible Ni-Fe, Ni-Cr and Ni-Co alloys. The particles were preferentially dispersed on the catalyst surface and were found to be stable to redox cycling and active in steam reforming of glycerol. The exsolution of B-site metal catalysts was better facilitated with A-site ceria-doped catalyst system than non-ceria-containing catalysts. The performance of the catalysts is attributable to enhanced metal catalyst-support interaction, metal reducibility and lattice defect. Lattice defect enhance oxygen ion mobility which facilitate oxidation of carbonaceous decomposition products from glycerol pyrolysis and consequently hinder deactivation by coking activity.

Suffices to say, catalysts prepared by both redox lattice reorganisation and redox exsolution exhibited superior structural properties such as better metal-support interaction and reducibility of the nickel particles compared to those prepared by wet impregnation. Catalyst deactivation by agglomeration and carbon deposition was effectively suppressed due to their improved structural properties unlike the impregnated nickel particles that were marred with carbon deposition, agglomeration and phase transformation which led to rapid catalyst deactivation.

However, it is also evident that the small amount of catalyst (0.05g) used for the catalytic test has yielded low gas products and glycerol conversion due to much throughput.

References

1. Lin, Y. Catalytic valorisation of glycerol to hydrogen and syngas, *international journal of hydrogen energy* **38,** 2678-2700 (2013)

2. Vaidya, P. D. and Rodrigues, A. E. Glycerol reforming for hydrogen production: A Review: *Chem. Eng. Technol.* ***32***(10) 1463–1469 (2009)

3. Pinna, F. Supported metal catalyst preparation. *Catalysis Today* **41,** 129-137 (1998)

4. Rerego, C. and Villa, P. Chapter 3 Catalyst preparation methods. *Catalysis Today* **34**, 281–305 (1997)

5. Neagu, D. and Irvine, J. T. S. Structure and properties of $La_{0.4}Sr_{0.4}TiO_3$ ceramics for use as anode Materials in solid oxide fuel cells. *Chem. Mater.* **22**, 5042–5053 (2010)

6. Neagu, D.; Tsekouras, G.; Miller, D. N.; Me´nard, H. and Irvine, J. T. S. *In situ* growth of nanoparticles through control of non-stoichiometry. *Nature Chemistry* **5**, 916-923 (2013)

7. Jiang, S. P. Development of lanthanum strontium manganite perovskite cathode materials of solid oxide fuel cells: A review. *J. Mater. Sci.* **43**, 6799–6833 (2008)

8. Stefan, E.; Connor, P. A. and Irvine, J. T. S. Development and performance of $MgFeCrO_4$ – based electrodes for solid oxide fuel cells. *J. Mater. Chem. A*, **1**, 8262-8269 (2013)

9. Mawdsley, J. R. Krause, T. R. Rare earth-first-row transition metal perovskites as catalysts for the autothermal reforming of hydrocarbon fuels to generate hydrogen. *Applied Catalysis A: General* **334** 311–320 (2008)

10. McIntosh, S. and Gorte, R. J. Direct hydrocarbon solid oxide fuel cells**.** *Chem. Rev.* **104**, 4845-4865 (2004)

11. Accessed on nptel.ac.in/courses/113104005/lctures3/3_9.htm

12. Stefan, E. and Irvine, J. T. S. Synthesis and characterization of chromium spinel as potential electrodes support materials for intermediate temperature solid oxide fuel cell. *J. Mater. Sci.* **4**, 7191-7197 (2011)

13. Fergus, J. W. Lanthanum chromite-based materials for solid oxide fuel cell interconnect. *Solid State Ionics* **171,** 1 –15 (2004)

14. Yokokawa, H.; Sakai, N.; Kawada, T. and Dokiya, M. Thermodynamic stabilities of perovskite oxides for electrodes and other electrochemical materials. *Solid State Ionics* **52**, 43–56 (1992)

15. Sfeir, J.; Buffat, P. A.; Mo¨ ckli, P.*;* Xanthopoulos, N.*;* Vasquez, R.; Mathieu, H. J.*;* Van herle, J. and Thampi, K. R. Lanthanum chromite based catalysts for oxidation of methane directly on SOFC anodes. *Journal of Catalysis* **202,** 229–244 (2001)

16. Tao, S. and Irvine, J. T .S. Synthesis and characterization of $La_{0.75}Sr_{0.25}.Cr_{0.5}Mn_{0.5}O_{3-\delta}$, a redox-stable, efficient perovskite anode for SOFCs. *Journal of The Electrochemical Society* **151** (2), A252-A259 (2004)

17. Tao, S. and Irvine, J. T .S. Catalytic properties of the perovskite oxide $La_{0.75}Sr_{0.25}Cr_{0.5}Fe_{0.5}O_{3-\delta}$ in relation to its potential as a solid oxide fuel cell anode material. *Chem. Mater.* **16***,* 4116-4121 (2004)

18. http://abulafia.mt.ic.ac.uk/shannon-/ptable.php

19. Inoue, T.; Eguchi, K.; Setoguchi, T. and Arai, H. Cathode and anode materials and the reaction kinetics for the solid oxide fuel cell. *Solids State Ionics* **40**(41), 407-410 (1990)

20. Badwal, S. P. S. Jiang, S. P. Love, J. Nowotny, J. Rekas, M. and Vance, E. R. Chemical diffusion in perovskite cathode of solid oxide fuel cell: The Sr-doped LaMn-xMxO3 (M=Co and Fe). *Ceramic international* **27**, 419-429 (2001)

21. Oishi, M.; Yashiro, K.; Sato, K.; Mizusaki, J. and Kawada, T. Oxygen non-stoichiometry and defect structure analysis of B-site mixed perovskite-type oxide (La,Sr)(Cr, M)$O_{3-\delta}$ (M =Ti, Mn and Fe). *Journal of Solid State Chemistry* **181**, 3177–3184 (2008)

22. Fatsikostas, A. N. and Verykios, X. E. Reaction network of steam reforming of ethanol over Ni-based catalysts. *Journal of Catalysis* **225,** 439–452 (2004)

23. Profeti, L .P. R.; Ticianelli, E. A. and Assaf, E. M. Production of hydrogen via steam reforming of biofuels on Ni/CeO_2–Al_2O_3 catalysts promoted by noble metals. *International journal of hydrogen energy* **34,** 5049– 5060 (2009)

24. Newnham, J.; Mantri, K.; Amin, M. H.; Tardio, J. and Bhargava, S. K. Highly stable and active Ni-mesoporous alumina catalysts for dry reforming of methane. *International journal of hydrogen energy* **37,** 1454-1464 (2012)

25. Wu, G.; Zhang, C.; Li, S.; Han, Z.; Wang, T.; Ma, X. and Gong, J. Hydrogen production via glycerol steam reforming over Ni/Al_2O_3: Influence of nickel precursors. *ACS Sustainable Chem. Eng*. **1** 1052−1062 (2013)

26. Neagu, D. and Irvine, J. T. S. Enhancing electronic conductivity in strontium Titanates through correlated A and B-Site doping *Chem. Mater.* **23**, 1607–1617 (2011)

27. Nishihata, Y.; Mizuki, J.; Akao, T.; Tanaka, H.; Uenishi, M.; Kimura, M.; Okamoto,T. and Hamada, N. Self-regeneration of a Pd-perovskite catalyst for automotive emissions control *Nature* **418**, 164-167 (2002)

28. Tanaka, H.; Uenishi, M.; Taniguchi, M.; Tan, I.; Narita, K.; Kimura, M.; Kaneko, K.; Nishihata, Y. and Mizuki, J. The intelligent catalyst having the self-regenerative function of Pd, Rh and Pt for automotive emissions control *Catalysis Today* **117**, 321–328 (2006)

7.0 SUMMARY

7.1 Summary, discussion and general conclusion

Catalyst development for the transesterification reaction of Sunflower oil to biodiesel and gasification of pure and by-product glycerol phase from biodiesel synthesis to hydrogen-rich gases as alternative, sustainable and renewable fuel resource to the fast depleting fossil-based hydrogen for fuel cell utilisation was successfully explored.

This work, demonstrates for the first time the potentials of tricalcium aluminate (C3A) water uptake at elevated temperature and formation of basic products which enhanced its surface basic strength for use as transesterification reaction catalyst in biodiesel production. The hydration temperature and the surface basic strength were optimised and 1000 ^{o}C and 1200 ^{o}C which gave the highest biodiesel yield of 96% and 92% respectively were found to be the optimum hydration temperatures. Hydration temperature of 900 ^{o}C gave only 43% biodiesel yield. The high basic properties of C3A-1100 ^{o}C did not translate to it having the highest performance perhaps affected by the high water content. Furthermore, basic alkaline earth metal oxides such as MgO, SrO and transition metal oxide ZnO are known to catalyse transesterification reaction but suffered significant deactivation due to profuse leaching of the active phase. These metals were doped and incorporated into the non-hydrated C3A lattice structure. The Sr-doped C3A had the strongest basic surface and gave the highest biodiesel yield of 94% and Zn-doped catalyst had the least performance with 88% biodiesel yield. A leaching test performed has revealed no leaching tendencies of the doped active phases. Therefore, this work has demonstrated that unlike what happens with the use of bulk catalyst or impregnation of active phase in supported catalysts, incorporation of the active phase into the lattice structure of the bulk material could prevent catalyst deactivation by leaching of the active phase during transesterification reaction. Generally, hydrated and non-hydrated doped C3A were found to be very promising catalysts but the hydrated C3A is slightly more active. If both were subjected to hydration process, the doped C3A would likely be a better catalyst because the work has revealed that the doping enhanced water uptake which in turn affects basic surface properties.

This work has revealed that nickel-based Ni/Al_2O_3 catalyst could be made better active and stable through the use of promoters such as ceria (CeO_2) and LSCM ($La_{0.75}Sr_{0.25}Cr_{0.5}Mn_{0.5}O_{3-\delta}$) and alternative supports such as samarium-doped ceria ($Ce_{0.8}O_{0.2}O_{2-\delta}$) and zirconia-doped ceria ($Ce_{0.75}Zr_{0.25}O_2$). This led to the development of new catalyst Ni-$La_{0.75}Sr_{0.25}Cr_{0.5}Mn_{0.5}O_{3-\delta}$ / $Ce_{0.75}Zr_{0.25}O_2$ (Ni-LSCM/Ce-Zr) which was found to be active and offered much better suppression of carbon deposition and agglomeration hence catalyst deactivation was minimised. The steam reforming reaction was influenced by many factors and calcination and reaction temperature of 500 ^oC and steam-to-carbon ration ratio of 3 at atmospheric pressure was found to be the optimum condition. Reasonable catalyst amount of 2-5g is required to achieve maximum glycerol conversion to gaseous products.

This work has demonstrated for the first time the use of a new phenomenon called redox lattice reorganisation and already known redox exsolution as alternative methods to wet impregnation in the preparation of oxide-supported nickel-based metal catalysts for glycerol steam reforming. The reorganisation provides good surface morphology such as strong metal-support interaction, uniform dispersion of metal particles and reduced tendency for catalyst deactivation by agglomeration. It also offers effective coking suppression and good catalytic behaviour. The work has shown that particle size population, metal-support interaction, size of the channels in redox lattice rearrangement can all be tailored for better catalytic behaviour by simple control of reduction temperature. The work revealed further that redox exsolution in perovskite; particle size and distribution, metal-support interaction and general morphology of the catalyst surface could be tailored for good catalytic performance though careful choice of dopant metal and defect chemistry in glycerol steam reforming. The exsoluted catalyst systems were found to be not only active and selective towards the desired products but have also demonstrated great potentials to suppress carbon deposition. The little amount of catalyst used (0.05g) has limited glycerol conversion to gaseous products. Reasonable quantity (2-5g) could drive the system to maximum conversion.

Therefore the hydrated C3A is the best catalyst for transesterification reaction to biodiesel and the catalyst system Ni-$La_{0.75}Sr_{0.25}Cr_{0.5}Mn_{0.5}O_{3-\delta}$ / $Ce_{0.75}Zr_{0.25}O_2$ was found

the best amongst the catalyst prepared by wet impregnation. The nickel-based $MnNi_xFe_{1-x}CrO_4$ (x = 0, 0.3, 0.5) spinel series represents the best from lattice reorganisation with spinels while from defect chemistry, $La_{0.4}Sr_{0.2}Ca_{0.3}Ni_{0.1}Ti_{0.9}O_{3\pm\delta}$, $La_{0.8}Ce_{0.1}Ni_{0.4}Ti_{0.6}O_{3\pm\delta}$, $La_{0.7}Ce_{0.1}Co_{0.3}Ni_{0.1}Ti_{0.6}O_{3\pm\delta}$ and $La_{0.5}Sr_{0.4}Fe_{0.1}Ni_{0.1}Ti_{0.8}O_{3\pm\delta}$ catalyst systems showed a remarkable performance.

Appendices

Appendix 1

Methodology for calculation of the weight of methanol required to get the vegetable oil-to-methanol molar ratio required for transesterification reaction of vegetable oil to biodiesel.

$$W_{mt\ req} = \frac{W_{veg\ req} \times M_{r.\ req} \times M_{mm}}{M_{veg}}$$

$W_{mt\ req}$ = Weight of methanol required for the transesterification

$W_{veg\ req}$ = Weight of vegetable oil required

$M_{r.\ req}$ = Methanol ratio required

M_{mm} = Molar mass of methanol

M_{veg} = Molar mass of the vegetable oil

E.g. using 10g sunflower oil (molar weight =880 g/mol) for transesterification with methanol (molar weight 32.04 g/mol) at 1:18 vegetable oil-to-methanol ratio, the amount (weight) of alcohol required would be:

$$\text{Weight of methanol required} = \frac{10g \times 18 \times 32.04\ g/mol}{880g/mol}$$

$$= 6.6g$$

Appendix 2

The general methodology for the quantification of gaseous products detected during glycerol steam reforming is presented below. Specific details on this can be found in chapter three of this work under experimental.

Calibration plots for the CO, CO_2 and CH_4 gases were obtained by flowing different proportions of gas i.e. 5, 20, 35, etc. vol. % of say CO on the GC in a total volume flow rate of 100 ml/min providing the balance with nitrogen. Each vol. % of the gas e.g. CO gives a corresponding peak on the GC and the peak areas were plotted against the vol. % to get the standard gas plots as shown below for CO, CO_2 and CH_4 respectively. The peak area of CO, CO_2 and CH_4 gases produced from the standardisation experiments were collected on the GC and their corresponding response factors obtained using equation of the line of the corresponding gas standard plot as exemplified in Table 2A-1. Subsequent conversion of vol.% to ml/min of the gas products was done as shown below, moles/min of the gas products and products mol/mol of glycerol was obtained by dividing the vol. flow rate (ml/min) with molar volume of gas at NTP at 25 ^{o}C (24000 cm^3) and glycerol-water molar flow rate respectively as shown by the calculation below.

1. CO

Area	Vol. %
145.11	5
409.36	20
835.4	35
1236.8	50
1691.8	65
2115.5	80
2550.8	95
2646.7	100

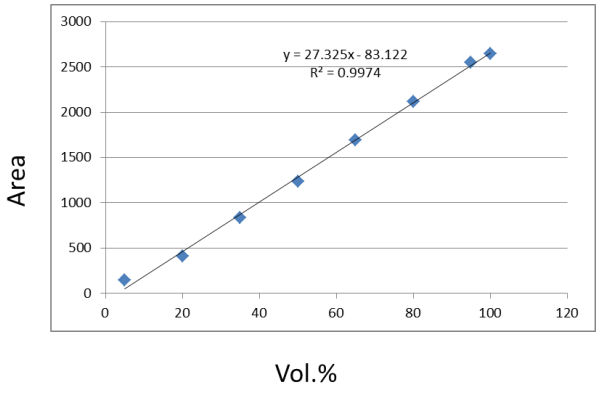

2. CO_2

Area	Vol. %
517.74	10
1030.40	25
1473.50	40
1912.60	55
2364.70	70
2841.20	85
3334.40	100

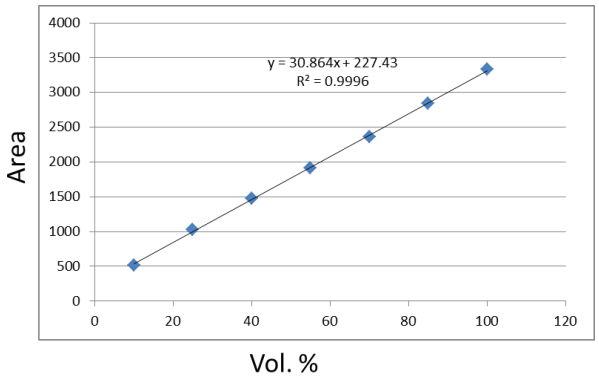

3. CH_4

Area	Vol. %
129.24	5
449.86	20
775.20	35
1114.00	50
1469.00	65
1754.10	80
2093.70	95
2203.20	100

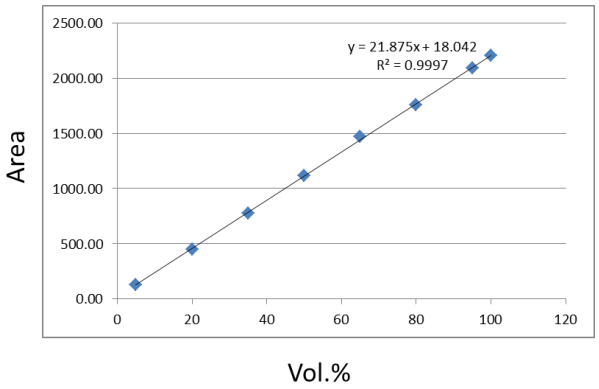

Mass spectrometry rather than gas chromatography was utilised to determine hydrogen. The standardisation for H_2 gas was produced by flowing different volume of hydrogen i.e. 2, 4, 6 etc. vol. % on mass spectrometer in a total volume flow rate of 100 ml/min providing the balance with nitrogen. The corresponding ion current value for each volume was used to obtain the standard plot by plotting ion current against vol. % as seen in plot 4 below. H_2 ion current from the experiment was collected and corresponding vol. % was obtained by using equation of the line from the standard gas plot shown below. Subsequent conversion to moles/min H_2 produced and moles H_2 per moles of glycerol was same as explained for other gases above.

4. H_2

Ion Current	Vol. %
452.0	2
841.0	4
1103.3	6
1480.0	8
1646.7	10

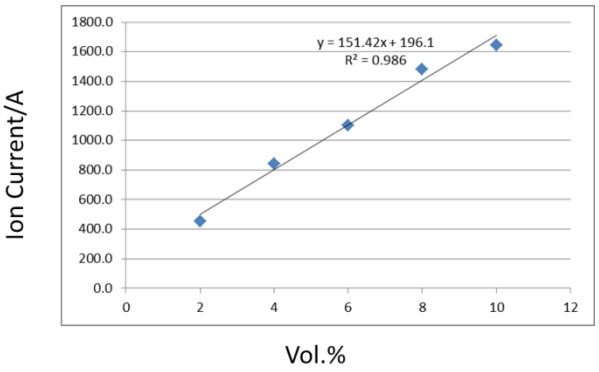

An example of how data were analysed and interpreted is presented in the following. Reformates (products) data collected from glycerol steam reforming at 500 ^{o}C, 3:1 steam to carbon ratio and glycerol molar flow rate of 8.2 x 10^{-5} moles/min and 7.3 x 10^{-4} moles/min of water in a volume flow rate of 5.9 x 10^{-3} cm^3/min of glycerol and 1.3 x 10^{-2} cm^3/min of water using Ni/Al_2O_3 catalyst is shown in Table A1. The test was done by continuous injection of glycerol solution with a syringe pump to a vapouriser at 250 ^{o}C and the vapour produced was conveyed to the reactor with helium gas flowing at 40 ml/min. Gaseous products CO, CO_2 and CH_4 generated from the reaction in the reactor were analysed by GC while H_2 was analysed by mass spectrometry. The calculated data as explained in above is as shown in Table A2-1.

Table A2-1 Experimental data for the reforming products

Glycerol solution	Volume of the gaseous products (Vol. %)			
S/C ratio	H_2	CO_2	CO	CH_4
3:1	18.66	7.04	4.73	0.36

Volume % of gases

H_2: H_{2Vp} = 18.66 %

CO_2: CO_{2Vp} = 7.04 %

CO: CO_{Vp} = 4.73 %

CH_4: CH_{4Vp} = 0.36 %

The vol.% were converted to volume gas flows by assuming a total flow rate of 40 ml/min output, based on gas input rate.

$$H_{2vF} = \frac{H2Vp \times 40}{100} = \frac{18.66 \times 40}{100} = 7.47 \text{ ml/min}$$

$$CO_{2vF} = \frac{CO_{2Vp} \times 40}{100} = \frac{7.04 \times 40}{100} = 2.82 \text{ ml/min}$$

$$CO_{vF} = \frac{CO_{Vp} \times 40}{100} = \frac{4.73 \times 40}{100} = 2.00 \text{ ml/min}$$

$$CH_{4vF} = \frac{CH_{4Vp} \times 40}{100} = \frac{0.36 \times 40}{100} = 0.15 \text{ ml/min}$$

Molar flow rate gaseous products (mol/min) were obtained by dividing the volume flow rate of products by molar volume of gas at NTP at 25 ^{o}C (24000 cm^3) as shown below.

$$H_{2MF} = \frac{H_{2Vf}}{24000} = \frac{7.47}{24000} = 3.11 \times 10^{-4} \text{ moles/min}$$

$$CO_{2MF} = \frac{CO_{2Vf}}{24000} = \frac{2.82}{24000} = 1.18 \times 10^{-4} \text{ moles/min}$$

$$CO_{MF} = \frac{CO_{Vf}}{24000} = \frac{2.00}{24000} = 8.3 \times 10^{-5} \text{ moles/min}$$

$$CH_{4MF} = \frac{CH_{4Vf}}{24000} = \frac{0.15}{24000} = 6.3 \times 10^{-6} \text{ moles/min}$$

Products in mole/mole of glycerol from glycerol molar flow rate of 8.2 x 10^{-5} mole/min and 7.3 x 10^{-4} moles/min molar flow rate of water and glycerol volume flow rate of 5.9 x 10^{-3} cm^3/min and 1.3 x 10^{-2} cm^3/min volume flow rate of water equivalent to total glycerol-water solution volume flow rate of 0.019 cm^3/min (2.6 x 10^{-4} mole/min molar flow rate of glycerol-water solution) was obtained by dividing the products in mole/min by the glycerol-water molar flow rate thus:

$$\frac{H_{2M}}{C_3H_8O_{3M}} = \frac{3.11 \text{ X } 10^{-4}}{2.60 \text{ X } 10^{-4}} = 1.2 \text{ mole/mole glycerol}$$

$$\frac{CO_{2M}}{C_3H_8O_{3M}} = \frac{1.18 \text{ X } 10^{-4}}{2.60 \text{ X } 10^{-4}} = 0.45 \text{ mole/mole glycerol}$$

$$\frac{CO_{MF}}{C_3H_8O_{3M}} = \frac{8.3 \text{ X } 10^{-5}}{2.60 \text{ X } 10^{-4}} = 0.32 \text{ mole/mole glycerol}$$

$$\frac{CH_{4MF}}{C_3H_8O_{3M}} = \frac{6.3 \text{ X } 10^{-6}}{2.60 \text{ X } 10^{-4}} = 0.03 \text{ mole/mole glycerol}$$

Equilibrium composition for the gaseous products at the reforming temperatures most studied in this work.

Table A2-2 Equilibrium composition of the gaseous products at different temperatures

		Equilibrium Composition (mol/mol glycerol)			
S/C Ratio	Temperature (^{o}C)	H_2	CO_2	CO	CH_4
3	500	4	2.0	0.4	0.8
3	600	5.5	2.2	0.8	0.2
3	700	6	2	1.0	0.1

Table A2-3 H_2 to glycerol, CO and CO_2 equilibrium composition ratios

Reaction	Eqn.	H_2 /glycerol	H_2/CO	H_2/CO_2
$C_3H_8O_3 \rightarrow 3CO + 4H_2$	2-3	4	1.33	0
$C_3H_8O_3 \rightarrow C_3H_6O_2 + H_2O$	2-4	0	0	0
$C_3H_8O_3 \rightarrow C_3H_6O_3 + H_2$	2-5	1	0	0
$C_3H_8O_3 + 3H_2O \leftrightarrow 3CO_2 + 7H_2$	2-7	7	0	2.33
	Temp/^{o}C			
Equilibrium	500	4	5	2
Equilibrium	600	5.5	6.9	2.5
Equilibrium	700	6	6	3

In this work, the input was designed to deliver a ratio of glycerol to water to He of 2:18:40 with a helium carrier of 40 ml/min in a total flow rate of 60ml/min. In the output stream, volume % of CO, CO_2, H_2 and CH_4 and all that could have been detected if produced such as ethane and ethene or even carbonyl compounds, carboxylic acid and alcohols were measured. However the water content and unreacted glycerol was condensed out before entering the GC and MS and not measured. Therefore, the output depends upon the overall reaction in the catalytic rig. For instance the maximum output flow that would be given by the glycerol steam reforming at equilibrium at 600 ^{o}C would be:

Output: 2.75 ml/min (H_2), 1.1 ml/min (CO_2), 0.4 ml/min (CO) and 0.1 ml/min (CH_4)

So the total gas output would be 40 + 4.35ml/min = 44.35ml/min for equilibrium conversion. Hence we might expect the gas output to be in the range 40-44 ml/min depending on the degree of conversion.

In converting measured volume % to ml/min produced, a flow rate of 40ml/min was assumed, hence the reported results may in fact be around 10% underestimated as the equilibrium conversion suggests a total flow of 44ml/min. As the total flow was

not measured and there may be some coking or similar losses, this possible underestimate seemed appropriate. The alternative of compensation by adding 10% might unreasonably increase the reported results. Overall the flow of glycerol was fairly dilute minimising degree of error.

Furthermore, analysis based on carbon balance from some experiments representing different conditions and catalysts systems could be used to show the maximum error that have occurred. The carbon balance analysis as shown below indicates a maximum of 5-10 % error in the above quantification.

Table A2-4 Analysis based on carbon balance using Ni/Al_2O_3 as a function of temperature

Temperature (^oC)	Total carbon **IN** (moles/min)	Total carbon **OUT** (moles/min)	CO **OUT** (moles/ min)	CO_2 **OUT** (moles/min)	CH_4 **OUT** (moles/ min)
500	7.8×10^{-4}	2.1×10^{-4}	8.3×10^{-5}	1.2×10^{-4}	6.1×10^{-6}
600	7.8×10^{-4}	2.0×10^{-4}	8.2×10^{-5}	1.2×10^{-4}	7.5×10^{-7}
700	7.8×10^{-4}	2.6×10^{-4}	9.5×10^{-5}	1.6×10^{-4}	-
800	7.8×10^{-4}	3.0×10^{-4}	8.8×10^{-5}	2.1×10^{-4}	-

Table A2-5 Analysis based on carbon balance as function of temperature using Ni-LSCM/Ce-Zr

Temp.(^oC)	Total carbon **IN** (moles/min)	Total carbon **OUT** (moles/min)	CO **OUT** (moles/ min)	CO_2 **OUT** (moles/ min)	CH_4 **OUT** (moles/ min)
300	7.8×10^{-4}	5.7×10^{-5}	5.5×10^{-5}	1.3×10^{-6}	2.4×10^{-7}
400	7.8×10^{-4}	1.2×10^{-4}	5.7×10^{-5}	4.4×10^{-5}	1.5×10^{-5}
500	7.8×10^{-4}	3.0×10^{-4}	6.2×10^{-5}	1.8×10^{-4}	3.5×10^{-5}
600	7.8×10^{-4}	1.6×10^{-4}	7.8×10^{-5}	8.0×10^{-5}	5.7×10^{-6}

Table A2-6 Analysis based on carbon balance as function of reduction in spinels

Catalyst System	Reduction Temp. (^oC)	Total C **IN** (moles/ min)	Total C **OUT** (moles/ min)	CO **OUT** (moles/ min)	CO_2 **OUT** (moles/ min)	CH_4 **OUT** (moles/ min)
$MnFeCrO_4$	1200	7.8×10^{-4}	2.0×10^{-4}	9.6×10^{-5}	7.6×10^{-5}	1.6×10^{-5}
$MnFe_{0.5}Ni_{0.5}CrO_4$	900	7.8×10^{-4}	2.7×10^{-4}	8.0×10^{-5}	1.7×10^{-4}	2.3×10^{-5}
$MnFe_{0.5}Ni_{0.5}CrO_4$	1000	7.8×10^{-4}	2.7×10^{-4}	7.8×10^{-5}	1.7×10^{-4}	1.7×10^{-5}
$MnFe_{0.5}Ni_{0.5}CrO_4$	1200	7.8×10^{-4}	2.4×10^{-4}	8.9×10^{-5}	1.2×10^{-4}	2.9×10^{-5}

Table A2-7 Influence of metal dopant substitution on carbon loss

Catalyst System	Reaction Temp.(^oC)	Total C **IN** (moles/min)	Total C **OUT** (moles/ min)	CO **OUT** (moles/ min)	CO_2 **OUT** (moles/ min)	CH_4 **OUT** (moles/min)
LSCM-Ni	700	7.8×10^{-4}	2.7×10^{-4}	9.4×10^{-5}	1.7×10^{-4}	1.3×10^{-5}
LSCF-Ni	700	7.8×10^{-4}	2.5×10^{-4}	8.6×10^{-5}	1.6×10^{-4}	9.4×10^{-6}
LSCC-Ni	700	7.8×10^{-4}	2.4×10^{-4}	8.0×10^{-5}	1.5×10^{-4}	8.6×10^{-6}

Appendix 3

Methodology for calculation of weight hourly space velocity (WHSV) and contact time

1. $$\text{WHSV} = \frac{\text{Density of the feed (kg/m}^3\text{) X Volumetric flow rate (m}^3\text{/h)}}{\text{Mass of the catalyst taken (kg)}}$$

Glycerol density = 1.261 g/cm^3 = 1261kg/m^3

Volumetric flow rate = Glycerol flow rate + He flow rate

Helium flow rate = 40 ml/min

Glycerol flow volume rate = 0.019 ml/min

Mass flow rate = 0.019 ml/min x 1.261g/cm^3 = 0.023959 g/min = 1.44 x 10^{-3} g/hr

=1.44 x 10^{-3} kg/hr

$$\text{WHSV} = \frac{1.44 \times 10^{-3}\ \text{kg/h}}{5 \times 10^{-5}\ \text{kg}}$$

= 28.8 h^{-1}

2. $$\text{Contact (residence) time} = \frac{\text{Catalyst volume (m}^3\text{)}}{\text{Volumetric flow rate (m}^3\text{/h)}}$$

Catalyst volume = Area x thickness

Reactor inner diameter = 8mm, r = 4mm

Area = πr^2 =3.14 x 16 = 50 mm^2 = 50 x 10^{-6} m^2

Catalyst bed thickness = 3mm = 3 x 10^{-3} m

Volume of catalyst = 5 x 10^{-5} m^2 x = 3 x 10^{-3} m = 1.5 x 10^{-8} m^3

Volumetric flow rate = 2.78 x 10^{-3} m^3/hr (from above)

$$\text{Contact time} = \frac{1.5 \times 10^{-8}\ \text{m}^3}{2.78 \times 10^{-3}\ \text{m}^3\text{/hr}}$$

= 5.39 x 10^{-6} h^{-1}

Appendix 4

Different formulas used for the calculation H_2 yield and selectivity in the literature review.

1. Hydrogen Selectivity (S_{H2}):

$$S_{H2} = \frac{H_2 \text{ mol. Produced}}{\text{Total mol C products produced}} \times \frac{1}{RR} \times 100 \quad \text{.....Eqn. A4-1}$$

2. Hydrogen yield (Y_{H2}):

$$Y_{H2} = \frac{H_2 \text{ mol. produced}}{3 \times 7 \times \text{glycerol soln molar flow rate}} \times 100 \quad \text{.....Eqn. A4-2}$$

Appendix 5

Methodology for calculation of molar mass of by-product glycerol from percentage composition obtained from elemental analysis.

Table A5-1 Molar mass calculation of by product glycerol from percentage composition using data from elemental analysis

	% Composition	Mole ratio	Whole number mole ratio	Empirical formula	Molecular formula
C	39.40	39.40/12 = 3.28	3.28/3.24 = 1		92.09/31 = 3
H	8.75	8.75/1 = 8.75	8.75/3.24 = 3	**CH_3O = 31**	**(CH_3O)3 = $C_3H_9O_3$ = 93**
O	51.85	51.85/16 = 3.24	3.24/3.24 = 1		M.M = **93**